Development of Micro Analytical Devices

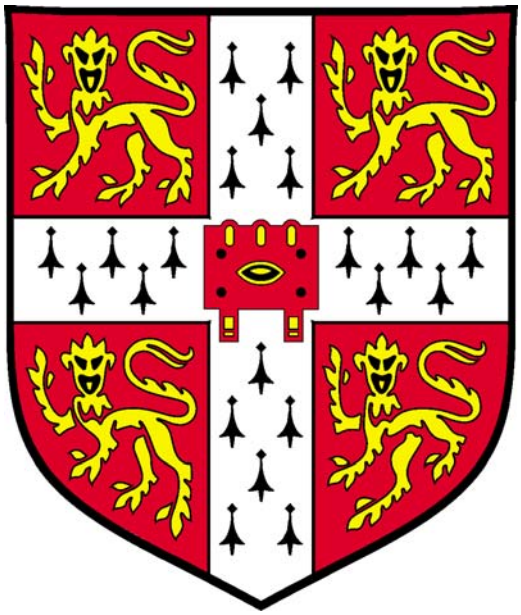

Abhishek Girish Sunila Deshpande

Trinity Hall

Department of Chemical Engineering and Biotechnology
University of Cambridge

2009

This dissertation is submitted for the degree of Doctor of Philosophy

Preface

The work presented in this thesis was carried out in the Department of Chemical Engineering and Biotechnology, University of Cambridge between October 2005 and April 2009. This thesis is the result of my own work and includes nothing which is the outcome of work done in collaboration except where specifically indicated in the text. The work presented has not previously been submitted for any other degree, diploma or qualification. This thesis contains less than 150 figures and 65,000 words including appendices, references, tables and equations.

Summary

Development of Micro Analytical Devices

Abhishek Girish Sunila Deshpande

This thesis describes the design and development of novel micro analytical devices for application in on-line process analytics. The work describes the design, development, numerical simulation and application of these devices for two specific cases: (i) electrochemical detection of bio(chemical) species at micro-scale and (ii) separation and purification of biological reagents using immobilised metal affinity chromatography at micro-litre scale.

Chapter 1 provides a general overview and background to the field of process analytics, microreactors and theory related to the mass transfer inside the electrochemical microfluidic devices and meso-chromatography columns. Chapter 2 provides an overview of microfabrication methods and the numerical simulations employed for the development of micro analytical devices used in this thesis.

Chapter 3 describes an experimental voltammetric study of enzyme cofactors in batch and hydrodynamic systems and also provides a numerical investigation of mass transfer over electrodes inside microreactors. Chapter 4 investigates the effect of hydrodynamic focusing within a microfluidic device in detail, using experimental and numerical techniques. The quantification of the results was carried out using a pseudo two-dimensional, steady state backward implicit finite difference model. A series of studies, interrogating the effects of volumetric flow rate, volume ratio and lead-in length, were carried out to quantitatively investigate hydrodynamic focusing.

Chapter 5 details the development and fabrication of patterned photopolymerised and electrochemically polymerised (conducting) monoliths with dimensions in the range of 100-1000 μm. The photopolymerised monoliths were characterised using hydrodynamic methods in order to study the flow profile. Electrochemical techniques were used to characterise the conducting monoliths and its composites, using N,N,N',N'-tetramethyl-p-phenylenediamine. Chapter 6 describes an application of the photopatterned monoliths. A meso-chromatography column was fabricated and immobilised metal affinity chromatography at meso and micro-litre scale was studied inside these columns. Proteins with polyhistidine tags were shown to be successfully separated, purified and quantified under batch and hydrodynamic conditions.

Acknowledgments

I would like to acknowledge the following people who have contributed towards this thesis in various ways.

My supervisor, Professor Nigel Slater for his guidance and support over the past three years. I am extremely grateful to Dr Adrian Fisher who also assisted and guided me throughout my PhD.

Dr Kamran Yunus for his helpful discussions and knowledge concerning the design and development of most of the electrochemical sensors.

Dr Sinead Matthews, Korakot Sombatmankhong, Yungfeng Gu and Paolo Bombelli from CREST laboratory for their "enlightening and entertaining" discussions.

Samantha Gooneratne, Helder Barbosa, Dr Gabi Kaminski and other members from CUBE for their valued contributions.

Surinder Sall, John Gannon and Zlatko Saracevic and all other support staff at the Department of Chemical Engineering and Biotechnology for their assistance in obtaining equipment, materials and general advice.

Cambridge Commonwealth Trust, Trinity Hall and Bombay Cambridge Trust for the Scholarship.

Mum, Dad, Jaydeep and my closest friends-Thanks!

Publications

- Deshpande, A. G.; Gu, Y.; Matthews, S. M.; Yunus, K.; Slater, N. K. H.; Brennan, C. M.; Fisher A. C. *Chem. Eng. J.* **2009**, 149, 428-434.

- Deshpande, A. G.; Barbosa, H.; Cheeks, M. C.; Yunus, K.; Fisher, A. C.; Slater, N. K. H. *J. Chromatogr. B*, *To be Submitted* (**2009**).

Abbreviations

Abbreviation	Meaning
AGE	Allyl Glycidyl Ether
BDDE	Boron Doped Diamond Electrode
BI	Backward Implicit
CV	Cyclic Voltammetry
DBC	Dynamic Binding Capacity
EBC	Equilibrium Binding Capacity
EGDMA	Ethyleneglycol Dimethacrylate
EMB	Electrochemical Micro-Biosensors
FAD	Flavin Adenine Nucleotide
FDM	Finite Difference Method
FMN	Flavin Mononucleotide
FTIR	Fourier Transform Infrared
GCE	Glassy Carbon Electrode
GE	Gold Electrode
HEMA	2-Hydroxyethyl Methacrylate
His	Histidine
HPIDA	2,2'-{[2-Hydroxy-3-(prop-2-en-1-yloxy)propyl]imino}Diacetate
IDA	Iminodiacetic Acid
IMAC	Immobilised Metal Affinity Chromatography
LSV	Linear Sweep Voltammetry
MIC	Metal Ion Capacity
NADH	Nicotinamide Adenine Dinucleotide (Reduced)
NMR	Nuclear Magnetic Resonance
PDMS	Poly(dimethylsiloxane)
PE	Platinum Electrode
SEM	Scanning Electron Microscopy
SDS PAGE	Sodium Dodecyl Sulfate-Polyacrylamide Gel Electrophoresis
TMPD	Tetramethyl-P-Phenylenediamine
UV	Ultra-violet

Common Symbols

Symbol	Definition	Units
n	Number of electrons transferred	-
F	Faraday's constant	C mol^{-1}
x,y,z	Cartesian co-ordinates	-
i,j,k	Counters in z, y, x directions	-
$a_{i,j,k}$	Normalised concentration of species A at position i,j,k	-
D	Diffusion coefficient	cm^2 s^{-1}
w_e	Width of electrode	cm
d_d	Width of channel	cm
h_2	Height of channel	cm
R	Universal gas constant	J K^{-1} mol^{-1}
V_f	Volume flow rate	cm^3 s^{-1}
T	Temperature	T
J_0	Diffusional flux	mol m^{-2} s^{-1}
C	Concentration	mol dm^{-3}
C_i	Initial concentration	mol dm^{-3}
C_f	Final concentration	mol dm^{-3}
C^*	Normalised concentration	-
t	Time	s
v	Scan rate	V s^{-1}
ΔEp	Peak potential difference	V
η	Over Potential	V
x_{Diff}	Diffusion layer thickness	cm
k_{ox}	Oxidation rate constant	Order Dependent
k_{red}	Reduction rate constant	Order Dependent
ρ	Density	kg m^{-3}
P	Pressure	Pa
μ	Viscosity	Pa s
u	Velocity in the x direction	cm s^{-1}
t_R	Retention time	s
t_M	Mobile phase time	s
$w_{1/2}$	Width at half peak	s
$[A]$	Concentration of species A	mol dm^{-3}
$[A]_0$	Initial concentration of species A	mol dm^{-3}
$[A]_{eq}$	Concentration of species A at equilibrium	mol dm^{-3}
$[A]_{bulk}$	Bulk concentration of species A	mol dm^{-3}
$[R]$	Concentration of species R	mol dm^{-3}
$[P]$	Concentration of species P	mol dm^{-3}
$[FMN]$	Concentration of FMN	mol cm^{-3}
$[FAD]$	Concentration of FAD	mol cm^{-3}
$[NADH]$	Concentration of NADH	mol cm^{-3}
$[Vitamin\ B_{12}]$	Concentration of Vitamin B_{12}	mol cm^{-3}
$[K_4Fe(CN)_6]$	Concentration of Ferrocyanide	mol cm^{-3}

Symbol	Definition	Units
$[K_3Fe(CN)_6]$	Concentration of Ferricyanide	mol cm^{-3}
$[BSA]$	Concentration of Bovin Serum Albumin	
D_{FMN}	Diffusion coefficient of FMN	$cm^2\ s^{-1}$
D_{NADH}	Diffusion coefficient of NADH	$cm^2\ s^{-1}$
$D_{Ferrocyanide}$	Diffusion coefficient of Ferrocyanide	$cm^2\ s^{-1}$
$D_{Ferricyanide}$	Diffusion coefficient of Ferricyanide	$cm^2\ s^{-1}$
Φ	Electronic potential	V
ϕ_i	Potential of a charged surface	V
u	Ionic mobility	$cm^2\ s^{-1}\ V^{-1}$
Z	Distance down channel	cm
Y	Distance across channel	cm
K_E	Equilibrium constant	-
$HETP$	Height equivalent of theoretical plates	cm
i_L	Mass transport limited current	A
E	Standard reduction potential	V
x_e	Length of electrode	cm
x_l	Length of channel	cm
x_o	Counter at the start of the electrode in the x direction	-
z_o	Counter at the start of the electrode in the z direction	-
x_f	Counter at the end of the electrode in the x direction	-
z_f	Counter at the end of the electrode in the z direction	-
J_{int}	Position of the interface	-
N_J	Number of grid points in y direction	-
N_K	Number of grid points in x direction	-
N_I	Number of grid points in z direction	-
V_o	Superficial velocity	cm s^{-1}
D_p	Diameter of packing particle	cm
ϕ_s	Particle sphericity	-
ε	Bed voidage	-
q^*	Concentration of protein adsorbed on the adsorbent	µg ml^{-1}
q_M	Maximum capacity of adsorbent	µg ml^{-1}
K_D	Langmuir adsorption constant	µg ml^{-1}
$[C^*]$	Equilibrium concentration of adsorbate	µg ml^{-1}

Symbol	Definition	Units
q_D	Amount of protein adsorbed at a given time	µg
w	Width of chromatography column	cm
d_p	Diameter of porogen particle	cm
h	Height of chromatography channel	cm
l	Length of the chromatography channel	cm
L	Length of the monolith	cm
κ	Permeability	cm^2
$Vpore$	Pore velocity	$cm\ s^{-1}$
r_H	Hydraulic radius	cm
d_{pore}	Diameter of pore	cm
$M_{Protein}$	Mass of protein	µg
$\overline{v}$	Wave number	cm^{-1}

Contents

Chapter 1

An Introduction to Micro Analytical Devices

1.1 INTRODUCTION

This thesis describes the development and fabrication of novel, micro analytical devices for the detection and purification of (bio)chemical reagents, using electrochemical and chromatographic techniques.

Analysis of chemical reagents before, during and after a chemical process is essential in all chemical engineering operations. There are many analytical methods at macro-scale such as pressure measurement, optical detection, chromatography or electrochemical sensing that may be used for examining a vast number of chemical or biochemical analytes [1, 2]. However, they require laboratories that are well-equipped and staff that is specialised in operating the requisite instruments. Today, an analytical tool for biomedical or fine chemical applications should satisfy several requirements, such as high selectivity for the analyte, address high percentage of chemical reagent of interest, minimisation of the sample and reagent volume, and a potential for acceptation by non-professional users [1].

Miniaturisation of clinical diagnostics instrumentation has been carried out over the last few decades [3, 4]. Today many new technologies such as photolithography, micromachining and molecular self assembly are being used to fabricate devices for analytical applications with sub

micro-litre volumes [5]. Micro analytical devices have the inherent benefits of faster, easier, inexpensive and more convenient analyses and hence are extremely popular in the pharmaceutical industry for drug discovery [5]. Many analytical techniques such as mass spectrometry and electrophoresis have also been successfully implemented on microchips made from silicon, glass, or plastic [6, 7]. Developing a user-friendly interface between a human and a microchip, by combining these techniques on a single device, promises a new future for analytical science.

This chapter outlines the methods currently used for the analysing biochemical reagents at macro-scale. The need for micro-scale devices and the advantages of miniaturisation will be discussed. Current industrial examples of micro analytical devices and integration of analytical methods on a single chip to fabricate a micro-total analytical system or lab-on-a-chip device will be investigated in detail in this chapter [8]. Techniques used for the experimental quantification of these analytical techniques at micro-scale, will also be covered in brief.

1.2 PROCESS ANALYTICS

Chemical and biochemical processing plants comprise of several unit operations converting raw materials into valuable products. Measurements are continuously taken at various stages during the operation using either simple sensors such as temperature, pressure and flow or sophisticated chemical analysers (measurement of composition or concentration of one or more chemical streams) [1]. These measurements provide a snapshot of the operation and can be used to control the process to ensure the plant operates efficiently and safely (refer Figure 1-1).

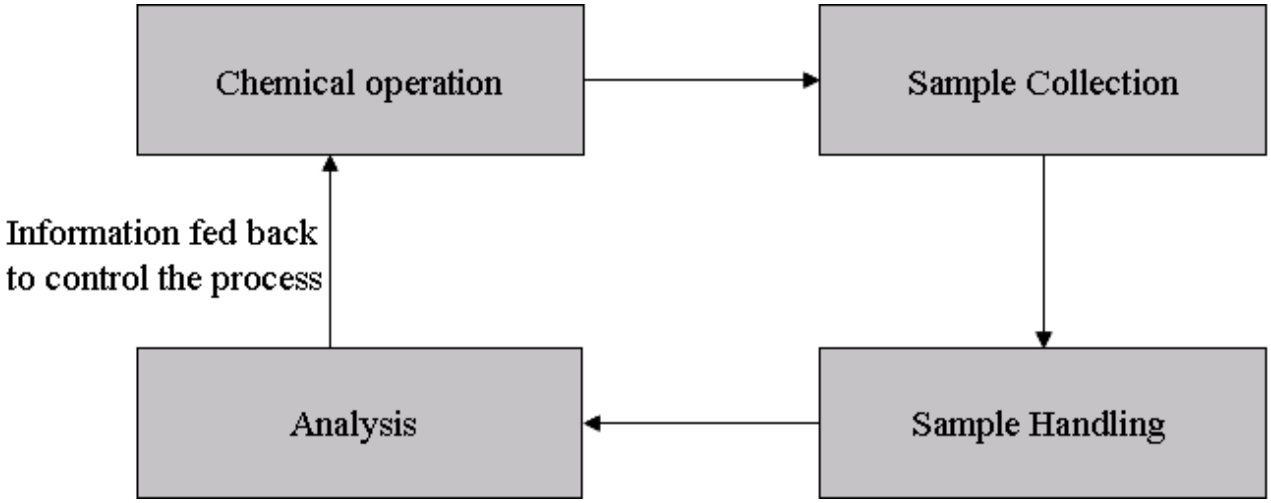

Figure 1-1 Off-line analytical measurement in a chemical process industry

In the past, most of the measurements were commonly made offline by analysing the samples collected from the process in the laboratory. Very few measurements such as temperature and pressure were made on the plant. With the advent of advanced analysers in the eighties, there was a rapid development in process analytics and a new discipline called process analytical chemistry (PAC) emerged, which combined chemical engineering and analytical chemistry [1, 9].

Process analytical chemistry is most commonly used in extractive sampling. Extractive sampling involves removing a representative portion of the stream from the flow or process vessel, either continuously or periodically [10]. The samples are sent to the process handling system and then transported to an analyser, where the chemical composition or the intrinsic physical properties of the process fluids (vapours and liquids) are measured. In the industrial plants, the majority of sample systems and their related analysers are installed in analyser houses [9, 11].

The process sample handling system is an important component of an effective process analytics system. Sample systems are used to influence or adjust the sample conditions (pressure, amount of particulate allowed, temperature and flow) to a level suitable for use with an analyser [9]. If the process sample is not delivered to the process analyser in a condition that is representative of the

process, errors will occur in the analysis. There are numerous analytical techniques used in the process industry, some of which have been explained in detail below.

1.2.1 Analytical Techniques

Analytical techniques that are commonly used in process analytics measurements include chromatography, spectrophotometry, electrochemical detection, optical measurements, electron microscopy, electron spin resonance and IR spectroscopy [12-22]. Applications of some of these techniques in the chemical industry have been described in brief below.

1.) Chromatography

Chromatography is an analytical and separation technique used to isolate two components in a mixture and measure their relative proportions based on their physiochemical properties such as charge, size or affinity. Although chromatography is frequently used in biochemical research, it is also well suited to petrochemical or environmental monitoring [12]. In addition, chromatography has applications in analytical chemistry where it is used to detect concentrations of acrylonitrile (carcinogen) in the air [13], and also useful for therapeutic purposes where a combination of chromatographic processes can be used for purification and fractionation of human blood plasma, albumin [14].

2.) Spectrophotometry

Spectrophotometry is the quantifiable study of electromagnetic spectra which includes visible light, near-ultraviolet, and near-infrared [15]. The first industrial application of spectrophotometry and colorimetry was in the paint industry, primarily used to minimise differences when touching up paintwork by keeping batches of paint as similar as possible. Similarly, spectrophotometry is used in printers, to ensure that reprints are identical to the original [16]. Another application of

spectrophotometer is in diagnostics, for example in determination of the amount of haemoglobin in blood [17].

3.) Electrochemical Analysis

In electrochemical analysis a chemical reaction is driven by an external applied voltage (*e.g.* electrolysis). This type of analysis deals with situations where oxidation and reduction reactions are measured in space or time, connected by an external electric circuit to understand each process [18]. Electrochemical analysis is commonly used in the pharmaceutical industry to measure the hydrogen ion concentration of a solution *i.e.* the pH. Furthermore, electrochemical detection is also used in combination with liquid chromatography (LCEC), to measure the amount of analyte that is separated from other electroactive species when reverse phase or ion exchange chromatography is applied to a sample [19].

1.2.2 Disadvantages of Macro-Scale Analysers

Most of the modern analysers or sampling systems are quite large, cumbersome, and expensive. Figure 1-2 depicts an image of a large gas chromatography system used in chemical industries [13].

Figure 1-2 A setup of gas chromatography system for detecting acrylonitrile in air [13]

In pharmaceutical industries, large volumes of expensive biochemical reagents for sampling and analysis can make the whole process uneconomical. Hence there is a drive for miniaturisation of

the analytical devices that are able to handle small sample volumes, provide a rapid and reliable analysis and that are easily portable within various points of a process [5].

1.3 MICRO-SCALE ANALYTICAL DEVICES

Miniaturisation has contributed significantly to the emergence and development of new research areas in chemical analysis, especially in bioanalysis [23]. Portable miniaturised devices enable real time *in situ* on-line monitoring [5]. The recent drive to make most of the measurements on-line, stems from the potential benefits of a significantly quicker analysis, without any time lag associated with sample handling, transport and processing. Moreover, the process can be monitored and corrected in real time by using feed-back or feed-forward control loops, in order to maintain the desired high standards of the final product, as well as to ensure operational safety [24]. Additionally, unlike macro-scale analytical systems, there is no need for skilled operators or special equipment, thus facilitating decentralisation of analyses [25].

Performing process analytics at micro- or nano- scale is the next step in diagnostic studies and has become an important area of research and development in clinical laboratories. Analysers such as AGA Autochemist and Technicon SMAC have been successfully scaled down from self-standing to bench top and are now also available as handheld devices [26]. Micro and nano-metre sized devices represent the next step in this progression.

1.3.1 Microfluidic Devices

Microfluidic devices comprise of simple or complex networks of channels with typical channel dimensions in the region of sub micrometer to sub millimeter [5]. In these devices it is possible to control the flow and reaction of minute amounts of liquids or gases. Some advantages of microfluidic devices include:

- Amount of reagent addressed could be as small as few pico-litres, which is of particular interest in fine chemical industries where reagents are extremely expensive. Using small amounts will not only make the process economical but also reduce the amount of waste produced.
- Low Reynolds number resulting in well defined laminar flow enabling more accurate prediction of mass transport from computational models (Equation 1.1)

$$Re = \frac{\rho U_0 L_0}{\eta} \tag{1.1}$$

- Easy interface with analytical devices for the quantification of species.
- Well-controlled chemical synthesis reactions, including the control over unwanted side reactions.
- Easy scale-up by parallelisation.
- Provide a large specific interfacial area.
- Efficient heat dissipation where heat exchange is required.
- Faster mixing times compared to traditional hydrodynamic techniques, thus allowing the study of much faster reaction kinetics.
- Easier to handle and manipulate, reduces the power requirements and offers the possibility of high-density testing and integration of individual steps in a multistep analytical process

Due to the above advantages, microfluidic or miniaturised devices have a huge demand in areas such as point-of-care testing, high throughput drug discovery, detection of biological warfare agents and astrobiology [27-31]. Miniaturisation allows for the fabrication of small, lightweight, and portable analysers with low power requirements. Some of the new generation microminiature analysers and their applications have been discussed in detail, in the next section.

1.3.2 Micro Analytical Devices: Types and Applications

Various types of microfluidic devices are used extensively for applications ranging from quantitative analysis inside microchannels to high throughput screening [29, 32]. Depending on the type of application, several micro analytical devices have been developed; such as high density arrays for studying combinatorial synthesis, which involves testing thousands of candidate drugs against thousands of biological targets; or simple microchips for sensing biological reagent of pharmaceutical significance [33]. The following section describes three main areas of applications which are: (1) high throughput screening, (2) sensing and detection and (3) separation [29, 34, 35].

1.3.2.1 High Throughput Drug Discovery

High throughput drug discovery involves screening vast number of candidate drugs against an equally large number of biological targets [29]. It is essential to have rapid, automated and simultaneous testing of drug compounds in an analytical drug discovery process. Additionally, due to the limited availability of reagents used in drug screening assays and combinatorial synthesis, conservation of valuable compounds is imperative. The micro plate provides a viable solution to the drug discovery assays (refer Figure 1-3). It is readily integrated into an automated process and allows for multiple, simultaneous testing on a simple disposable device [36]. Two commonly used methods for drug discovery are immunoassays and gene expression which are described below [37, 38].

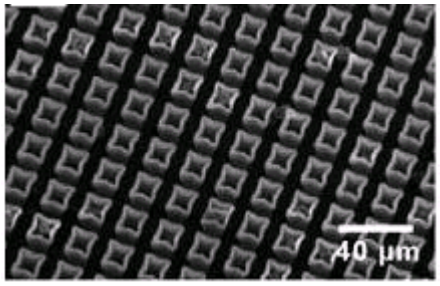

Figure 1-3 SEM image of glass tube array [39]

i) *Immunoassays*

Ekins and coworkers have successfully demonstrated the use of microarrays for immunoassay studies [37]. Microfabricated arrays were used for simultaneous measurement of an unlimited number of analytes in a small biological sample such as a drop of blood. High assay sensitivities were obtained by confining a small number of sensor antibody molecules onto a small area in the form of a micro spot, and measuring their occupancy by an analyte, using high-specific activity antibody probes.

Mendoza and colleagues have developed an array of 144 elements in each well of a 96- well micro plate, which can perform multiplex screening of different samples against each array set [40].

One of the next steps in the development of high-content microarrays comprises the production of arrays by high-density spotting of bacteria onto nitrocellulose filters [41]. In these microarrays, the bacteria expressed and secreted antibody fragments that were subjected to a filter-based ELISA. This was used for the identification of antibody fragments that were specific to the tested antigens.

ii) *Gene Expression*

DNA microarrays can be used to measure, in parallel, the expression patterns of thousands of genes, generating clues to gene function that can help to identify appropriate targets for therapeutic intervention. They can also be used to monitor changes in gene expression in response to drug treatments.

Recently, microchips of area 1–2 cm^2 with surface microarrays of nucleic acids and proteins at discrete locations have been reported by Lockhardt *et al.* [38]. They have developed an approach that is based on hybridisation to small high-density arrays containing tens of thousands of synthetic oligonucleotides. The arrays were designed based on sequence information alone and were synthesised *in situ* using a combination of photolithography and oligonucleotide chemistry. RNAs

present at a frequency of 1:300,000 were unambiguously detected at over three orders of magnitude. This method allowed simultaneous monitoring of tens of thousands of genes because of the combinatorial nature of the chemistry and the ability to synthesise small arrays containing hundreds of thousands of specifically chosen oligonucleotides.

1.3.2.2 Detection and Measurement

Microfluidic devices are used for analyte detection and measurement due to their ability to process volumes as low as pico-litres. Sensing and detection in these devices is generally carried out using electrochemical techniques, chromatography or spectrophotometry [35, 42, 43]. Two common detection applications which are of commercial importance have been described below.

i) *Glucose Monitoring*

Recently microchips have been used to detect chemical and biochemical reagents. One common application of such microchip is glucose monitoring, where a glucose sensor continuously monitors glucose levels in diabetic patients. In one implementation, the biosensor is an implantable electrochemical sensor array that monitors the current related to the rate of reaction occurring between glucose and a redox polymer, with the catalyst glucose oxidase [44].

The sensor is fabricated using photolithography, which is used to develop electrodes with sensing elements (redox polymer and glucose oxidase), encapsulated within a poly (ethylene glycol) (PEG) hydrogel (see Figure 1-4 for illustration).

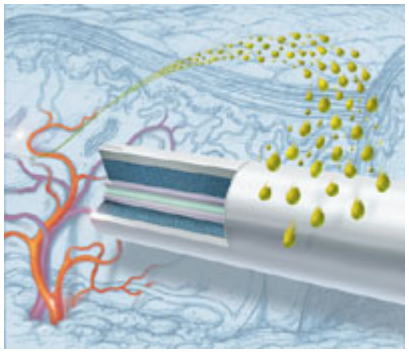

Figure 1-4 Implantable glucose biosensor

The success of this particular technology highlights the potential for micro-scale based electrochemical devices.

ii) *Cofactor Regeneration*

Another example of electrochemical detection is via redox electrochemistry, as used in cofactor regeneration. Cofactors are commonly used in fine chemical industries for stereoselective transformations. However, due their high costs, the cofactors need to be recycled. This can be achieved by fabricating an electrode band inside a microfluidic channel and performing *in situ* regeneration. Yoon *et al.* have described the electrochemical regeneration of reduced nicotinamide adenine dinucleotide (NADH) that is required for the conversion of pyruvate to L-lactate inside an electrochemical microreactor [33].

1.3.2.3 Separation

Scaling separations by using micro-scale devices is yet another breakthrough in microfluidics. Separations could be carried out using electrophoresis, porous gel or simple obstacles. The inclusion of these obstacles or different sized side channels into the microchannel has been used for size-based separation [45]. Passive techniques, such as the H-filter, as well as active techniques based on electric or magnetic field susceptibilities have also been reported [46, 47]. The latter has been extended to a number of electrophoretic techniques; for instance isoelectric focusing (IEF) has

been combined with capillary electrophoresis to separate biological samples [48, 49]. Zone electrophoresis has also been incorporated into microfluidic devices by pre-treating surfaces within the microchannel, for protein separation [50].

Östman *et al.* have developed an atmospheric pressure chemical ionisation (APCI) microchip which combines a gas chromatograph (GC) to a mass spectrometer (MS) as illustrated in Figure 1-5 [51, 52]. The chip includes a capillary insertion channel, a stopper, a vaporiser channel, a nozzle, a nebuliser gas inlet fabricated on the silicon wafer and a platinum heater sputtered on a glass wafer.

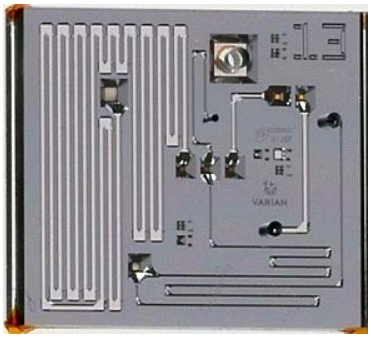

Figure 1-5 Image of a micro gas chromatograph [52]

1.3.3 Microfabrication Methods

Some common methods of microfabrication include photolithography, soft lithography, laser ablation/drilling, electrodischarge, injection molding, polymer casting, printing, and lithographie galvanoformung abformung (LIGA) [5, 53]. With the help of photolithography and soft lithography, structures of dimensions up to 50 μm are easily achieved. These two techniques have been explained in detail in Chapter 2. Ablation or drilling with a laser offers a simple, one-step process for fabrication of features <30 μm on a range of materials [5]. These techniques are particularly useful in cutting curved and/or irregular shapes that are more challenging for conventional etching methods.

Another emerging method to make plastic microchips is hot embossing (stamping of a pattern into a polymer, softened by raising the temperature of the polymer just above its glass transition

temperature). This method would enable a high volume, low cost, continuous production of micro devices, and would be easier to implement than batch etching silicon wafers, for silicon-based microchips [54].

1.3.4 Drawbacks of Down-scaling of Analytical Devices

The increasingly popular use of microfluidics in research laboratories and fine chemical industries, has led a number of analytical chemists to regard these devices as the solution to all issues related to macro analysis, and hence may use them unnecessarily. The surface to volume ratio of a microfluidic device with a characteristic length of 1 μm is 10^6 m^{-1}, as compared to a device with a characteristic length of 1 m, giving a surface to volume ratio of 1 m^{-1}. This million fold increase in the surface area relative to the volume will dramatically affect transfer of mass, momentum and energy. Inertial forces will be small, whilst surface friction and viscous effects will increasingly dominate the fluid motion. As a consequence, most microfluidic systems operate in the laminar regime. However, while performing flow simulations for these devices, the small length scales often invalidate the continuum hypothesis of the Navier-Stokes equations, giving inaccurate results. Particularly at fluidic channel dimensions below 100 nm, the liquid cannot be considered a continuum proper, but should instead be viewed as an ensemble of individual molecules. On these scales, the surface to volume ratio is very high, non-slip boundary conditions hold incompletely, and fluid constitutive relations are strongly affected by the presence of a boundary [55, 56].

Another drawback of scaling down devices is the inaccuracy of the representative sample. Successive reductions in the amount of sample used for analysis in a micro analytical device could hamper the measurement of the analyte either because measurement limit of the analytical method is exceeded, or because the sample is no longer representative of the bulk specimen.

1.4 MICRO-TOTAL ANALYTICAL SYSTEM

A variety of analytical techniques have been used to quantify events occurring within microchannels, which have been discussed in detail, later in this chapter. An important development has been the integration of analytical devices onto the micro-total analytical system (μTAS) device, creating a true 'lab-on-a-chip' [57]. This not only allows performing more than one function on a single chip, but is also more efficient in terms of time, cost and compactness. Examples of such a system/device include UV spectroscopy with light emitting diodes (LED) for excitation and photodiodes for detection, optical coherence tomography, Fourier transform infra red spectroscopy (FTIR), electrochemical detection and nuclear magnetic resonance (NMR) spectroscopy [49, 58, 59, 60, 61].

A wide range of components such as pumps, valves, lamps, filters, heaters, refrigeration, ion-selective electrodes, capillary electrophoresis, and electronic control circuitry have been miniaturised, and are available to be used as building blocks for fully integrated analysers [62]. Most devices integrate the different analytical structures through interconnections on the surface of the chip. Three-dimensional integration can be achieved by stacking or by fabricating chips into interconnected layers [63]. Unifluidics^{TM} Technology, Bayer Corp have miniaturised bench-top analysers by machining entire fluidic modules into transparent plastic blocks on a single chip. These systems have important applications, such as the UniFluidics hydraulics module, which is used as a core component of the Bayer Advia 120 blood analysing system. The module integrates liquid pathways, valves, reaction chambers, heaters, optical cuvettes, connections, and plug-in interfaces into a precision-designed system.

In addition to scaling down, integrating the sample preparation step with the analysis stage required in an analytical procedure is another important goal [64]. Water *et al.* have developed a monolithic micro device that can perform functions such as cell lysis, multiple PCR amplification and

electrophoretic analysis on a single chip [65]. El-Ali and coworkers have demonstrated tissue organisation, culture and analysis, all on a single microchip for pharmacological applications as illustrated in Figure 1-6 [57].

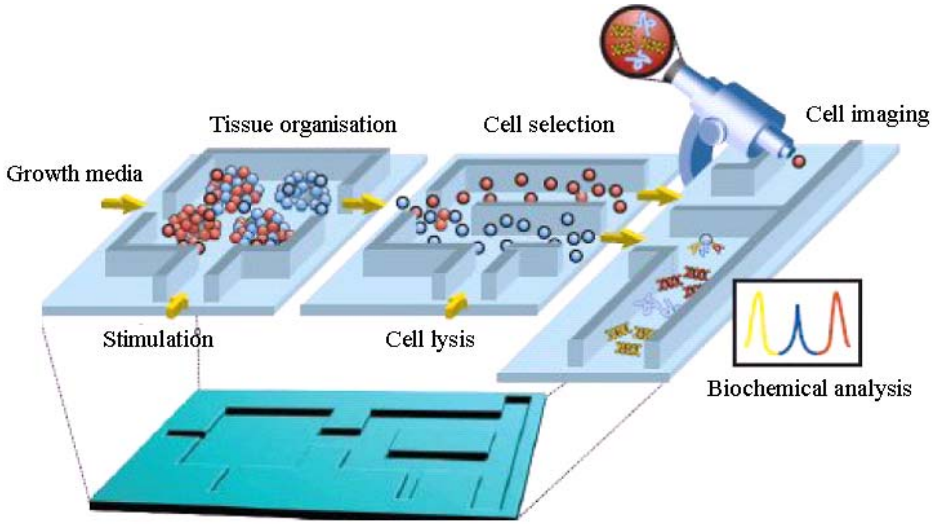

Figure 1-6 Tissue organisation, culture and analysis in micro systems [57]

Although various analytical techniques have been demonstrated inside a micro-total analytical system, many techniques are yet to be reported in depth and numerous related applications are still to be studied. Two such analytical techniques used in this thesis were electrochemical analysis and chromatography. Before describing the development of these techniques, the fundamental principles governing these two analytical techniques have been reviewed in detail. The next section discusses some of the theoretical aspects related to the study of electrochemical sensing and chromatography.

1.5 ELECTROCHEMICAL ANALYSIS AT MICRO-SCALE

Electrochemical analysis at micro-scale, compared to traditional electrochemical analysis, is one in which analysis is carried out using microelectrodes of dimensions in the range of 10 µm - 500 µm. The electrical signal (current) produced due to redox reactions of electroactive reagents over these electrodes is then measured to determine conversions and selectivities. The use of microelectrodes

in electrochemical techniques offers several advantages over macroelectrodes. They exhibit large current densities, but low total currents so that steady state currents are easily achieved in the absence of added supporting electrolyte, which is not usually possible with macroelectrodes.

The basic principle behind electrochemical detection involves electron transfer at the solution electrode interface. A large range of factors can control the rate of an electron transfer reaction at the solid-liquid interface. These include the rate of charge transfer across the interface as a function of applied potential, the transport of material between the bulk solution and electrode, the reactivity of the solution species, the nature of the electrode surface and the structure of the interfacial region where the electron transfer takes place [18].

1.5.1 Electron Transfer at the Solution Electrode Interface

In the absence of adsorption, the mechanism by which an electroactive species undergoes a reversible single-electron oxidation and reduction reaction at the electrode surface is given by the following equation.

$$R_{(aq)} + e^-_{(m)} \underset{k_{ox}}{\overset{k_{red}}{\rightleftharpoons}} P_{(aq)} \qquad (1.2)$$

There are six steps involved in the solid-liquid electrochemical process.

1. Diffusion of the species R from the bulk solution to the region where the reaction occurs.
2. Rearrangement of the ionic atmosphere at the double electric layer.
3. Reorientation of the solvent dipoles.
4. Alterations of the distances between the central ions and ligands.
5. Electron transfer.
6. Transport of the species away from the interfacial region, and diffusion to the bulk solution.

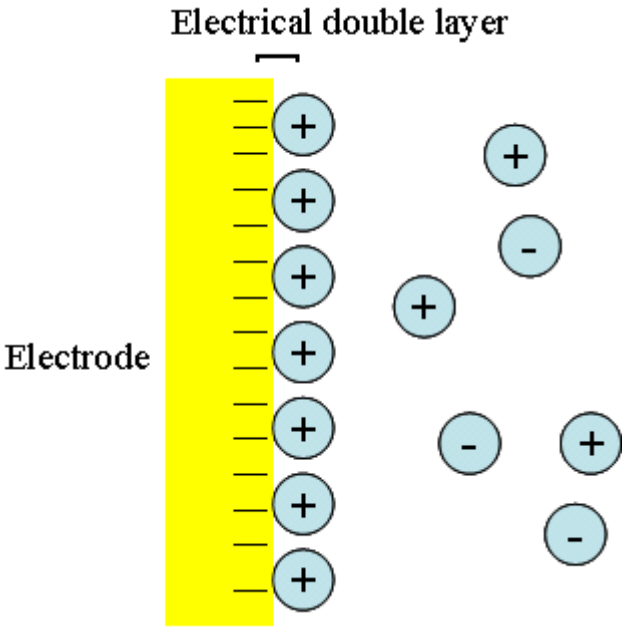

Figure 1-7 Illustration of electrical double layer

The current derived as a result of this redox reactions can be predicted using Equation 1.3.

$$i_a = -nFAk_{red}[R] \text{ or } i_c = nFAk_{ox}[P] \qquad (1.3)$$

Where i_a is the anodic current, i_c the cathodic current, n the number of electron transferred, F the Faraday constant (96500 C mol^{-1}), A the electrode surface area (cm^2) and k_{red} and k_{ox} are rate constants for reduction and oxidation steps.

1.5.2 Rate of Electron Transfer

The rate of the electron transfer reaction at the electrode surface can be varied by changing the applied voltage. It is expressed in terms of the Butler-Volmer equation, which relates the observed current as a function of the over potential and the transfer coefficient as follows [66]:

$$i = i_o\left(\frac{[P]_o}{[P]_{bulk}}\exp\left\{\frac{(1-\alpha)F\eta}{RT}\right\} - \frac{[R]_o}{[R]_{bulk}}\exp\left\{\frac{-\alpha F\eta}{RT}\right\}\right) \qquad (1.4)$$

Where η is the over potential (E-E_e, where E is applied potential and E_e is voltage established by the mixture of (R) and (P) at equilibrium), α the transfer coefficient, F is the Faraday constant, R the universal gas constant, T the absolute temperature, $[R]_{bulk}$ and $[P]_{bulk}$ the bulk solution concentration of species R and P, $[R]_o$ and $[P]_o$, the electrode surface concentrations and i_o is the exchange current (A).

1.5.3 Cell Time Constant - Kinetics of Fast Reactions

Cell time constant is the measure of the speed at which a microelectrode system will return to steady state after a current or voltage perturbation. The product of electrolyte resistance and electrode capacitance gives the cell time constant. The cell time constant limits the accessible time domain for an electrochemical experiment. Any process occurring faster than the cell time constant will not be observable. But since the value of cell time constant in the case of microelectrodes is very small, fast kinetic reactions can be studied easily.

1.5.4 Mass Transport

During an electrolysis reaction, the rate of reaction is influenced not just by the cell potential difference, but also by the rate of transport of electroactive species to the electrode surface. Rate of mass transport, can at times, even dominate the overall reaction rate. The following section describes the three most significant processes that influence the current derived from an electrode.

1.5.4.1 Diffusion

As a faradic reaction progresses, reactants in the immediate vicinity of the electrode are consumed. The consumption of reactants produces a concentration gradient, encouraging more reactants to diffuse in from the surrounding region to further feed the reaction. Often the diffusion of the reactants to the reaction sites is the limiting factor to the overall speed of the reaction process. If

diffusion is slow, the reaction will also be slow, even if faradic process itself is fast. It can be expressed using Fick's first law that states that the diffusional flux of a species, J_o, is defined (in one-dimension) as:

$$J_o = -D\left(\frac{\partial C}{\partial x}\right) \tag{1.5}$$

Where D is the diffusion coefficient and C is the concentration of the species. However, it is more useful to know how the concentration of a species changes with time as defined by Fick's second law (in three-dimensions):

$$\frac{\partial C}{\partial t} = D\left(\frac{\partial^2 C}{\partial x^2}\right) + D\left(\frac{\partial^2 C}{\partial y^2}\right) + D\left(\frac{\partial^2 C}{\partial z^2}\right) \tag{1.6}$$

1.5.4.1.1 *Diffusion Layer*

If a reactant is continually consumed at a surface, the depleted region through which new reactant must diffuse to reach the surface will steadily increase with time. This depleted region is known as diffusion layer. The diffusion layer grows with square root of time and is expressed as:

$$x_{Diff} = A\sqrt{Dt} \tag{1.7}$$

Where x_{Diff} is the diffusion layer thickness (cm), A is the geometric constant, D is the diffusivity ($cm^2\ s^{-1}$) and t is time (s).

For microelectrode systems, the diffusion layer can easily grow to be the same size or even larger than the microelectrode itself, during experimental timescales. As the diffusion layer grows larger than the microelectrode dimensions, a transition from planar to spherical diffusion occurs. Hence mass transport to and from these electrodes is much faster compared to macro electrodes, where planar diffusion tends to pre-dominate.

1.5.4.2 Convection

The application of force on the solution results in convection. Convection within a solution exists in two forms (i) natural convection generated by the difference in density due to thermal gradients and (ii) forced convection generated by an external action or force such as pumping. Natural convection can be neglected in an electrochemical cell if forced convection is introduced, as forced convection is several orders of magnitude greater than natural convection.

The applied external force produces two forms of flow characteristics over the electrode; laminar and turbulent. For laminar flow profile, the one-dimensional mass transport equation is predicted by:

$$\frac{\partial C}{\partial t} = -u_x \left(\frac{\partial C}{\partial x} \right) \tag{1.8}$$

Where C is the concentration of the species in solution and u_x is the central velocity profile in the x direction, which can be calculated by solving the appropriate form of Navier-Stokes equation [67].

1.5.4.3 Migration

Migration is an electrostatic effect produced when a voltage is applied to an electrode, creating a charged interface. Any charged species near the interface will either be attracted to or repelled from it due to electrostatic forces, depending on the charge they possess.

The migration of a species is dependent on the potential of the charged surface, ϕ, and the ionic mobility, u, by the following equation:

$$\frac{\partial C}{\partial t} = -uC \left(\frac{\partial \phi}{\partial x} \right) \tag{1.9}$$

This does not account for effects such as ion solvation, ion pairing or the electrical double layer. Migration can be neglected by adding an excess amount of background (supporting) electrolyte. The background electrolyte does not undergo electrolysis itself, but helps to shield the reactants

from migratory effects. Another advantage of adding an electrolyte is that it acts as a conductor to aid the passage of current through the solution.

Some additional benefits of microelectrodes over macroelectrodes include:

(i) Reduced surface area results in a significant reduction in transient current, allowing fewer effects from capacitive charging, thereby enabling the potential to be ramped at a higher scan rate.
(ii) Reduction in the occurrence of Ohmic drop, where the experimental measurements of the resistive solution lead to distortions in the current/voltage curves.

1.5.5 Electrochemical Techniques

Electrochemical techniques such as potential step chronoamperometry, cyclic voltammetry and linear sweep voltammetry, are used to elucidate kinetic and mechanistic information about an electroactive species in a solution [18]. In this thesis, cyclic and linear sweep voltammetric measurements were carried out in stagnant solution and within hydrodynamic devices respectively.

1.5.5.1 Cyclic Voltammetry

Cyclic voltammetry is a widely employed electrochemical technique that uses a triangular potential perturbation (Figure 1-8). A fixed potential range is applied, and voltage is scanned from initial value V1 (where it is thermodynamically unfavourable for the electrochemical reaction to proceed) to a final value V2 (where it is thermodynamically favourable for the reaction to occur), and back. The cyclic voltammogram obtained is a function of various factors such as rate of electron transfer, chemical reactivity and voltage scan rate.

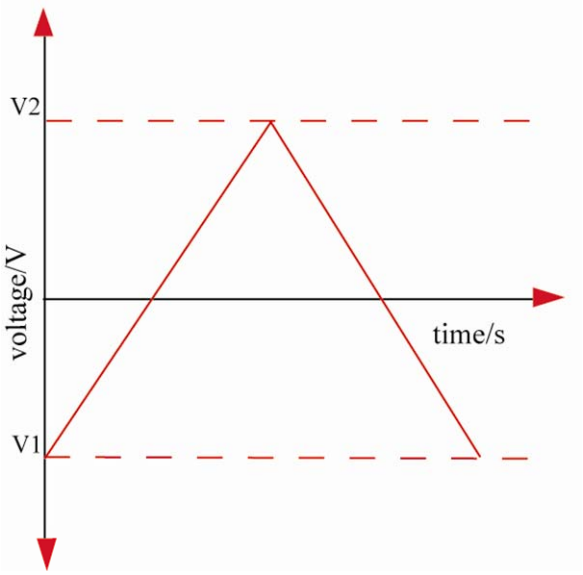

Figure 1-8 Application of cyclic voltammetry

Consider a one-electron reduction of *R* to *P* (refer Equation 1.2). When a reduction potential is applied, *R* starts getting depleted over the electrode and equilibrium is established between *R* and *P*. This equilibrium can be predicted using the Nernst equation [18]:

$$E = E^{o} - \frac{RT}{nF} ln \frac{[P]}{[R]} \qquad (1.10)$$

Where *F* is the Faraday constant, *n* the number of electrons transferred, *R* the universal gas constant, *T* the temperature and E^{O} the standard potential. The reverse of oxidation reaction is similar but in opposite direction.

In a typical measurement, a three electrode cell containing a solvent, reagent (usually in low concentration) and background electrolyte is used. If sufficient electrolyte is present, migratory transport may be neglected and the current response observed can then be characterised in terms of the diffusion, natural convection and the fundamental electron transfer/coupled chemical reactions occurring within the cell.

A typical set of cyclic voltammograms observed for a reversible, one-electron transfer redox reaction, as a function of scan rates is shown in Figure 1-9.

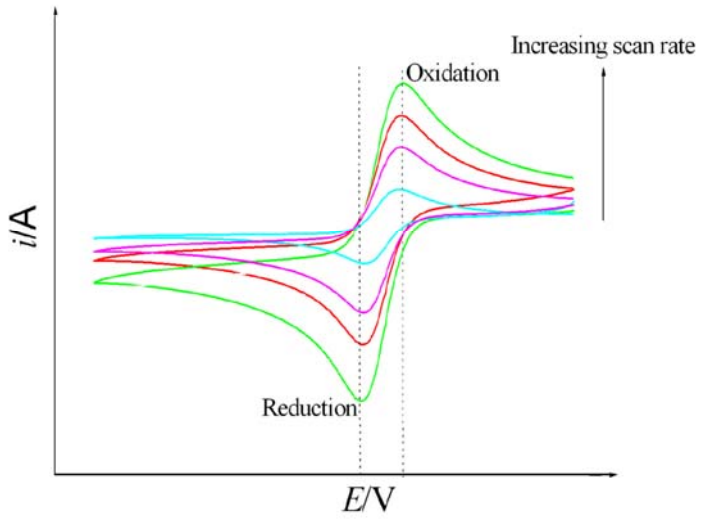

Figure 1-9 Current response from application of cyclic voltammetry at different scan rates

Each voltammogram shows a characteristic peak current, which for the reversible system, occurs at a specific potential. Another characteristic of a reversible system is that the oxidation and reduction peak current should be of equal magnitude, while the peak potential for an ideal case, should be separated by approximately 57 mV, and is independent of the scan rate. The peak current varies linearly with the square root of scan rate, which is also known as Randles-Sevcik equation [18].

$$i = 2.69 \times 10^5 n^{1.5} A D^{0.5} [R] v^{0.5} \qquad (1.11)$$

Where n is number of electron transfer, A is active electrode surface area, D is diffusion coefficient and $[R]$ is bulk concentration of electroactive species.

For an irreversible or quasi reversible system, the current response will vary from that for an ideal reversible case discussed above, due to different values of the reduction and oxidation rate constants.

1.5.5.2 Hydrodynamic Techniques

Methods involving the introduction of convective mass transport to promote the transport of reactants/products to and from the electrode are called hydrodynamic techniques. Some of the popular hydrodynamic techniques (within a much larger subset) include: the dropping mercury electrode, the rotating disc electrode, the wall jet electrode and the channel electrode [18].

Hydrodynamic methods have proved popular due to some key advantages over traditional measurements performed in stagnant solutions. First, the ability to perform measurements under steady state conditions removes potential restrictions due to capacitative charging, which may arise during rapid scan techniques. Second, the ability to vary the residence time of a reagent near the electrode by a forced convection component provides a powerful method for mechanistic studies. Finally the enhanced transport, to and from the surface over stagnant conditions, leads to higher current densities and results in an improved signal to noise performance.

Recently, the benefits of hydrodynamic techniques have been combined with the microreactor approaches. These are discussed in more detail below.

1.5.5.2.1 Linear Sweep Voltammetry in Microreactors

Linear sweep voltammetric (LSV) measurements have recently been exploited for microreactor applications. The experimental conditions typically employed, ensure that well defined laminar flow conditions are observed. Channel electrode geometries with large aspect ratios ($h_2 < d_d$) typically have a uniform flow profile across a centrally sited electrode and negligible edge effects. Electrolyte is pumped through the microreactor, where the smooth walls and low Reynolds numbers ensure that an essentially parabolic velocity is induced, with the maximum value of the parabolic flow velocity being at the centre of the channel as illustrated in Figure 1-10.

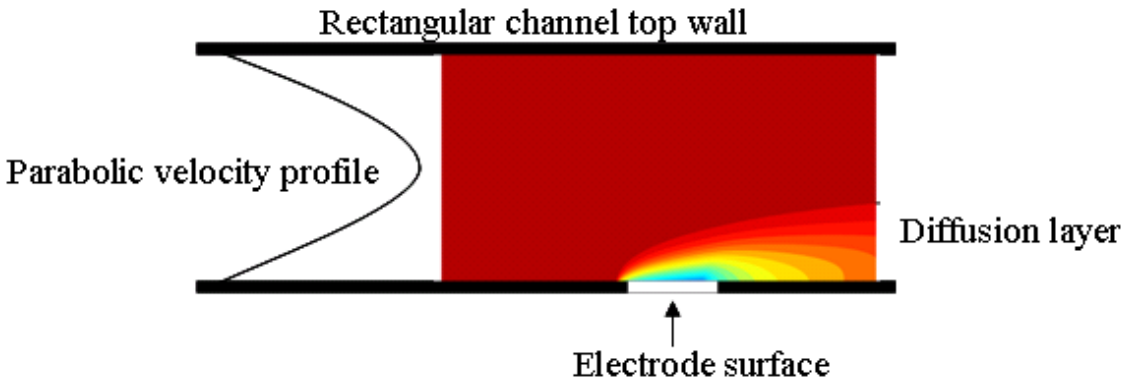

Figure 1-10 Schematic of parabolic flow and diffusion layer formation on an electrode surface inside a microchannel

In LSV, the potential is swept at a constant rate from an initial potential V1 (thermodynamically unfavourbale) to a final value V2 (thermodynamically favourable) (refer to Figure 1-11).

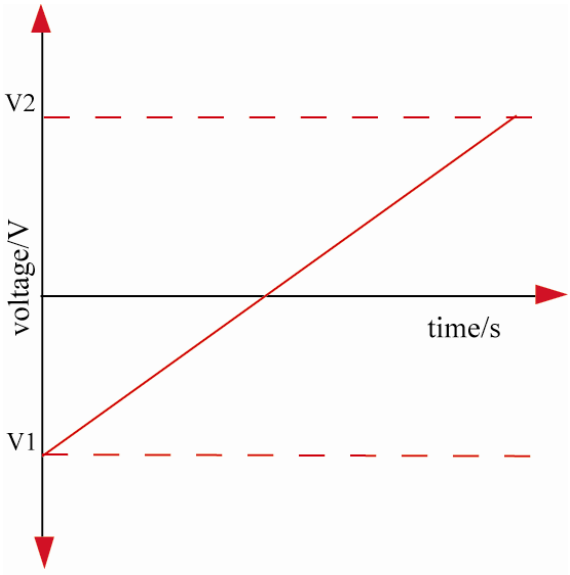

Figure 1-11 Application of linear sweep voltammetry

In comparison to the CV behaviour noted in Section 1.5.5.1, it is apparent that a steady state response is observed, with no distinguishable peak. Typically in a channel electrode, the potential is held at a value whereby all *R* are reduced to *P*; the flow of solution over the electrode constantly replenishes the depleted material at the electrode surface resulting in a stable diffusion layer (see Figure 1-10), which in turn generates a steady state limiting current (i_L) as illustrated in

Figure 1-12. Unlike in a stagnant system, the thickness of the diffusion layer can be controlled using flow rate.

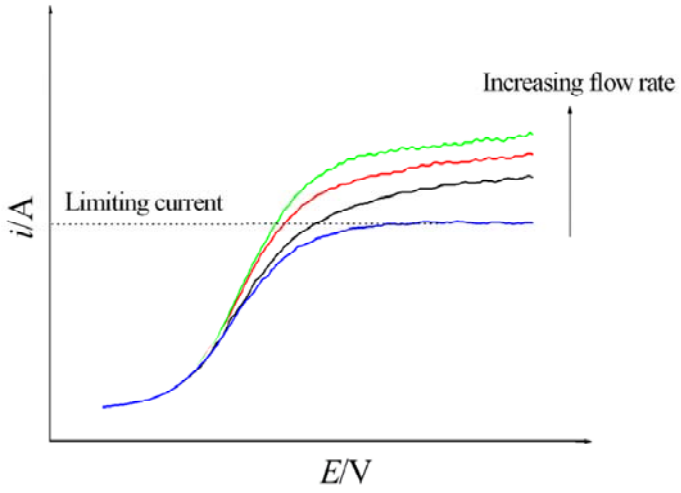

Figure 1-12 Current response from application of linear sweep voltammetry for different flow rates

The limiting current is dependent only on the transport of material to the electrode surface; a change in the flow rate alters the rate at which the material at the electrode surface is replenished, which in turn affects the resultant steady state current. The variation of the transport limited current as a function of the volume flow rate was found to follow a cube root relationship, also known as the Levich equation [68].

$$i_L = 0.925nF[R]_{Bulk} w_e \left(\frac{D_A^2 V_f x_e^2}{h^2 d_d} \right)^{\frac{1}{3}} \tag{1.12}$$

Where h is half the cell height, d_d the cell width, w_e the electrode width, x_e the electrode length, and V_f is the volume flow rate. According to Levich, axial diffusion can be neglected, so that the only contributions to mass transport to the electrode arise from axial convection and normal diffusion (diffusion is perpendicular to the walls).

1.6 MICRO-CHROMATOGRAPHIC SEPARATION

Micro-chromatography is a technique used to separate two components in a mixture and to measure their relative proportions at micro-scale. Due to its ability to analyse few micro-litres of reagents, it is extremely popular in the pharmaceutical industry and biomedical research laboratories, where high cost and low availability of biological reagents of industrial significance can make the whole process on a macro-scale, unviable. Working at micro-scale also reduces the waste generated during the process. Like traditional chromatography, it is used for preparative purposes, particularly for the isolation of relatively small amounts of materials that have comparatively high intrinsic value. Micro-chromatography is probably the most powerful and versatile technique available to the modern analyst. In a single step process, it can separate a mixture into its individual components and simultaneously provide a quantitative estimate of each constituent. Samples may be gaseous, liquid or solid in nature and can range in complexity from a simple blend of two enantiomers to a multi-component mixture containing widely differing chemical species.

1.6.1 Chromatography Theory

Chromatography is a physical method of separation in which the components to be separated are distributed between two phases; stationary phase and mobile phase. The mobile phase (gas, liquid or supercritical fluid) consists of the sample being separated, and the solvent that carries the sample through the column. The mobile phase interacts with the stationary phase and the analytes are separated based on size (size exclusion chromatography), special interaction (ion exchange chromatography) or affinity for the stationary phase (metal affinity) [12].

1.6.2 Distribution of Analyte Between Phases

When a sample is injected through the chromatography column, the distribution of the analyte in the sample between mobile and stationary phases can often be described quite simply by equilibrium.

$$A_{mobile} \rightleftharpoons A_{stationary} \tag{1.13}$$

The equilibrium constant, K_E, also termed as the partition coefficient, is defined as the molar concentration of analyte in the stationary phase divided by the molar concentration of the analyte in the mobile phase.

The performance of separation can be calculated using the theoretical plate model. The plate model assumes that the chromatographic column contains a large number of separate layers called theoretical plates (refer Figure 1-13). Separate equilibrations of the sample between the stationary and mobile phase occur in these plates. The analyte moves down the column by the transfer of equilibrated mobile phase from one plate to the next.

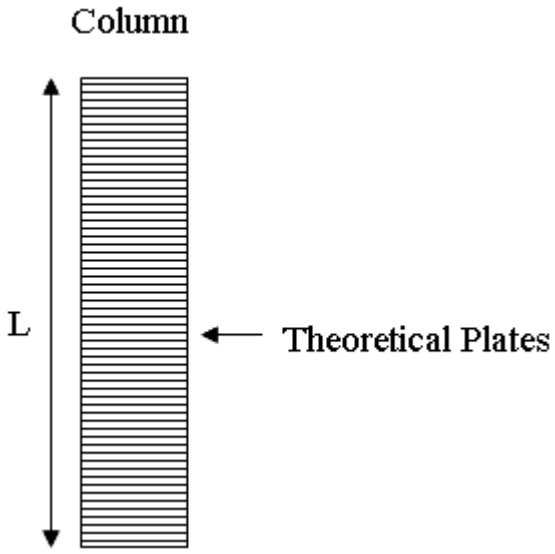

Figure 1-13 Schematic of theoretical plates in chromatography column.

The height equivalent of a theoretical plate (HETP) is expressed as [12]:

$$HETP = \frac{L}{N} \tag{1.14}$$

Where, L is the length of the column (cm) and N the number of theoretical plates. N can be expressed as [12]:

$$N = \frac{5.55 t_R^2}{w_{1/2}^2} \tag{1.15}$$

Where $w_{1/2}$ (s) is the peak width at half height, t_R is the time measured between injecting a sample and an analyte peak being detected at the end of the column and is termed the retention time (t_R). Retention time is specific to each analyte in the sample. The time taken for the mobile phase to pass through the column is called t_M as seen in Figure 1-14.

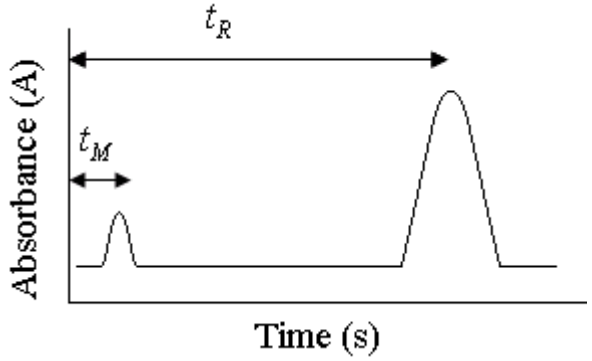

Figure 1-14 Retention time for a solute in the mobile phase

1.6.3 Peak broadening

As the reagent passes through the column, each individual pulse corresponding to various analytes in the initial reagent becomes broader because of mass transfer resistances, axial diffusion and the departure from plug flow. To obtain optimal separations, sharp and symmetrical chromatographic peaks must be obtained. Various factors contributing towards peak broadening have been discussed in detail below.

1.6.3.1 Eddy Diffusion

Eddy diffusion is caused by the difference in the residence time of the solute molecules in the mobile phase. When the mobile phase moves through the column packed with stationary phase, solute molecules take different paths through the stationary phase at random. This causes broadening of the solute peak, as each path exhibits a different length.

1.6.3.2 Longitudinal Diffusion

At low volume flow rates, the concentration of the analyte is less at the edges of the analyte band in the column, than at the center. The analyte diffuses out from the center to the edges, causing band broadening. If the velocity of the mobile phase is high then the analyte spends less time on the column, which decreases the effects of longitudinal diffusion.

1.6.3.3 Resistance to Mass Transfer

This occurs when the analyte has a strong affinity for the stationary phase. The analyte when passed through the column, takes a certain amount of time to equilibrate between the stationary and mobile phase. If the velocity of the mobile phase is high, then the analyte in the mobile phase will move ahead of the analyte in the stationary phase. This leads to the broadening of the analyte band in the column and hence causing peak broadening. The higher the velocity of mobile phase, the worse the broadening becomes.

1.6.3.4 Wall Effect

At low aspect ratios of the tube-to-particle diameter (d_t/d_p), a strong porosity distribution is observed, with an increased porosity near the membrane wall. Due to higher porosity near the wall, the liquid essentially tends to flow out of the packings or the porous bed and down the walls. This

is known as channeling and leads to a substantial amount of the reagent bypassing the column without being processed, also contributing to peak broadening.

To facilitate mass transfer, diameter of the particle or the pore diameter can be reduced so as to attain better resolution. In doing so, the interstitial distance is reduced thus lowering the diffusion path length for the species in consideration. While this improves the efficiency/performance of the chromatography column, it also results in an increase in the pressure drop, which increases the operating cost of the process.

1.6.4 Pressure Drop Calculation

Pressure drop measurements inside a chromatography column not only help in determining the operational flow rate range for the process, but also help understand the flow profile. Pressure drop inside a packed bed chromatography column can be predicted using the Ergun equation [12]:

$$\frac{\Delta P}{L} = \frac{150 V_s \mu (1-\varepsilon)^2}{\phi_s^2 D_p^2 \varepsilon^3} + \frac{1.75 \rho V_s (1-\varepsilon)}{\phi_s D_p \varepsilon^3} \tag{1.16}$$

Where $\frac{\Delta P}{L}$ is the pressure gradient (Pa cm^{-1}), V_s is the superficial velocity (cm s^{-1}), μ is the fluid viscosity, ρ is the fluid density (g cm^{-3}), D_p is the diameter of the packing particles (cm), ϕ_s is the packing particle sphericity and ε is the bed voidage.

In case of porous beds, pressure drop can be calculated either using Darcy's law or Hagen-Poiseulle approximation which has been explained in detail in Chapter 5 [12].

1.7 QUANTIFICATION OF MICROFLUIDIC DEVICES: NUMERICAL METHODS

One of the major advantages of microfluidic devices over macro-scale analysers is the enhanced control of experimental conditions, such as temperature, pH, electrical and concentration gradients along a channel [69-72]. The effects of these conditions can easily be quantified using a number of analytical techniques. Chromatography and electrochemical methods are two such quantitative analytical techniques that have been utilised in this research in order to develop a micro bioanalytical device.

Apart from these standard quantitative methods, numerical simulations are also commonly used to study flow profiles, concentration gradient or adsorption front predictions. The simulations are particularly helpful when it is difficult to explain or understand a complex reactions system based on experimental or standard analytical results. In the past, one and two-dimensional numerical models have been extensively used to study the rate of mass transfer and electron transfer at the electrode, measuring rate constants of fast kinetics reactions; to understand diffusion between two parallel streams inside a microchannel and also for improved design of reactors. Recently Henley *et al.* demonstrated a complete three-dimensional simulation of fluid flow and the concentration distribution in low aspect ratio ducts [73].

Many numerical methods exist today to solve complex problems, as digital simulations of processes occurring in hydrodynamic devices have expanded. In numerical simulations, the problem is discretised into a number of sequentially solved steps. Various methods for discretisation have been developed including the finite difference (FDM), finite element (FEM) and boundary element methods (BEM) [74-76]. In this thesis, FDM was used for the quantification and verification of electrochemical microreactors.

1.8 THESIS STRUCTURE

The thesis has the following structure.

Chapter 2 discusses some of the micro-scale fabrication techniques used in order to construct the devices evaluated within this thesis. It also describes the voltammetric and numerical methods used for electrochemical quantification.

Chapter 3 describes the development and analysis of an electrochemical micro-biosensor with applications in fine chemical industries. Various electrode materials were characterised to obtain an electrode which was most sensitive to biological reagents. Numerical models were used to understand the diffusion patterns over the electrode surface inside a micro-biosensor.

Chapter 4 describes the development of a confluence electrochemical sensor for the voltammetric study of hydrodynamic focusing. It also describes a numerical model used to investigate hydrodynamic focusing, and its accuracy is assessed using well-established analytical theory. Finally, the numerical model is compared with experimental results.

Chapter 5 describes the development and characterisation of patterned conducting and non conducting monoliths for application in meso-chromatography and electrochemical micro-biosensors. Porosity of these monoliths was studied in detail using NH_4Cl salt and silica particles as porogen. Various physical methods were used to characterise these monoliths.

Chapter 6 describes the development and fabrication of photopatterned monoliths inside a mesochannel for applications in affinity chromatography. The chapter also discusses the meso-chromatography column developed, which was used to study and separate histidine tag proteins selectively from rest of the impurities in the cell lysate.

1.9 REFERENCES

[1] Baughman, E. *Process Analytical Chemistry: Introduction and Historical Perspective In: Process Analytical Technology: Spectroscopic Tools and Implementation Strategies for the Chemical and Pharmaceutical Industries* **2005**, Ed. Bakeev, K. A., Wiley-Blackwell, Oxford, pp.1-80.

[2] Yan, B. *Analytical methods in combinatorial chemistry* **1999**, Technomic Publishing Company, Inc, Lancaster, pp.1.

[3] Garcia, C. D.; Henry, C. S. *Analyst* **2004**, 129, 579-584.

[4] Colyer, C. L.; Mangru S. D; Harrison, D. J. *J. Chromat. A* **1997**, 781, 271-276.

[5] Ehrfeld, W.; Hessel, V.; Löwe, H. *Microreactors: New Technology for Modern Chemistry* **2000**, Wiley-VCH, Mainz, pp.1.

[6] Rohner, U.; Benz, W.; Whitby, J. A.; Wurz, P.; Schulz, R.; Romstedt, J. *Tools and Technologies for Future Planetary Exploration In: Proceedings of the 37th ESLAB Symposium* **2004**, Ed. Battrick, B., Noordwijk, The Netherlands, pp.131-138

[7] Landers, J. P. *Handbook of Capillary and Microchip Electrophoresis and Associated Microtechniques* **2007**, Taylor and Francis Group, Boca Raton, pp.1.

[8] Kricka, L. J. *Clin. Chim. Acta* **2001**, 307, 219-223.

[9] Koch, K. H. *Process Analytical Chemistry: Control, Optimisation, Quality, Economy* **1997**, Springer-Verlag, Berlin, pp.1

[10] Achá, V.; Naveau, H.; Meurens, M. *Analysis* **1998**, 26, 157-163.

[11] Mullinger, P.; Jenkins, B. I*ndustrial and Process Furnaces* **2008**, Butterworth-Heinemann, Oxford, pp.1.

[12] McCabe, W. L.; Smith, J. C.; Harriott, P. *Unit Operations of Chemical Engineering* **2001**, McGraw-Hill, New York, 6th Edition, pp. 157 - 161.

[13] Bartlett, L., http://visualsonline.cancer.gov/details.cfm?imageid=2020.

[14] Matejtschuk, P.; Dash, C. H.; Gascoigne, E. W. *Br J Anaesth* **2000**, 85 (6), 887–95.

[15] Rendina, G. *Experimental Methods in Modern Biochemistry* **1976**, W. B. Saunders Company, Philadelphia, pp. 46-55.

[16] Bernd, U.; Werner, H. *Colorimetry and Spectrophotometry: Cutting-Edge Tools for the Print Media Industry* **2005**, Graphic Arts Technical Foundation.

[17] Khalifa, A. A.; Salah, M. K. *Nature* **1951**, 168, 915 – 916.

[18] Bard, A. J.; Faulkner, L. R. *Electrochemical methods: fundamentals and applications* **1980**, John Wiley, USA, pp.119-336.

[19] Norris, B. J. Electrochemical Methods of Analysis In: *Encyclopedia of Pharmaceutical Technology: Economic Characteristics of the R&D-Intensive Pharmaceutical Industry to Fermentation Processes* **1992**, Ed. Swarbrick, J.; Boylan, J. C., Marcel Dekker Inc. New York, Vol 5, pp. 89.

[20] Kastening, B. *Anal. Chem.* **1967**, 224, 196.

[21] Dohrmann, J. K.; Galluser, F.; Wittchen, H. *Faraday Discuss. Chem. Soc.* **1973**, 56, 350.

[22] Webster, R. D.; Dryfe, R. A. W.; Eklund, J. C.; Lee, C. W.; Compton, R. G. *J. Electroanal. Chem.* **1996**, 402, 167.

[23] Kricka, L. J.; Nozaki, O.; Wilding, P. *J. Int. Fed. Clin. Chem.* **1994**, 6, 54-59.

[24] Luque de Castro, M. D.; Priego Capote, F. *Anal. Bioanal. Chem.* **2008**, 390 (1), 67-69.

[25] Ríos, A.; Escarpa, A.; González, M.C.; Crevillén, A. G. *Trends Anal. Chem.* **2006**, 25, 467–479.

[26] Westgard, J. O.; Carey, R. N.; Feldbruegge, D. H.; Jenkins, L. M. *Clin. Chem.* **1976**, 22, 489-496.

[27] Paul, B. K. *Microenergy and Chemical Systems and Multiscale Fabrication In: Micromanufacturing and Nanotechnology: Fundamentals, Techniques, Platforms, and Experiments* **2006**, Ed. Mahalik, M. P., Springer-Verlag, Heidelberg, pp.323.

[28] Dirks, J. L. *AACN Clin. Issues* **1996**, 7, 249-259.

[29] Devlin, J. P. *High throughput screening* **1997**, Marcel Dekker, New York, pp.673.

[30] Barnaby, W. *Med. Confl. Surviv.* **1997**, 13, 301-313.

[31] Smith, J. M.; Szathmary, E. *Nature* **1996**, 384, 107.

[32] Deshpande, A. G.; Gu, Y.; Matthews, S. M.; Yunus, K.; Slater, N. K. H.; Brennan, C. M.; Fisher, A. C. *Chem. Eng. J.* **2009**, 149, 428-434.

[33] Yoon, S. K.; Choban, E. R.; Kane, C.; Tzedakis, T.; Kenis, P. J. A. *J. Am. Chem. Soc.* **2005**, 127, 10466.

[34] Matson, R. S.; Rampal, J.; Pentoney, S. L.; Anderson, P. D.; Coassin, P. *Anal. Chem.* **1995**, 224, 110-116.

[35] Bruns, M. W. *Erdol Kohle Erdgas* **1994**, 47, 80-84.

[36] Sasaki, N. *Hokkaido J. Med. Sci.* **1997**, 72, 249-259.

[37] Ekins, R.; Chu, F. W. *Clin. Chem.* **1991**, 37, 1955-1967.

[38] Lockart, D. J.; Dong, H.; Byrne, M. C.; Follettie, M. T.; Gallo, M. V.; Chee, M. S.; Mittmann, M.; Wang, C.; Kobayashi, M.; Horton, H.; Brown, E. L. *Nat. Biotechnol.* **1996**, 14, 1675-1680.

[39] Sato, H.; Homma, T.; Mori, K.; Osaka, T.; Shoji, S. *Electrochim. Acta* **2005**, 51 (5), 844-848.

[40] Mendoza, L. G.; McQuary, P.; Mongan, A.; Gangadharan, R.; Brignac, S.; Eggers, M. *Biotechniques* **1999**, 27, 778–788.

[41] De Wildt, R. M.; Mundy, C. R.; Gorick, B. D.; Tomlinson, I. M. *Nat. Biotechnol.* **2000**, 18, 989–994.

[42] Aauroux, P. A.; Iossifidis, D.; Reyes, D R.; Manz, A. *Anal. Chem.* **2002**, 74, 2637.

[43] Roulet, J. C.; Fluri, K.; Verpoorte, E.; Wolkel, R.; Herzig, H. P.; De Rooij, N. F.; Dandliker, R. *Proc. Mic. Tot. Anal .Sys.* **1998**, 287.

[44] Henry, C. *Anal. Chem.* **1998**, 594A-598A.

[45] Huang, L. R.; Cox, E. C.; Austin, R. H.; Sturm, J. C. *Sci.* **2004**, 304, 987-990.

[46] Subramanian, K. R. V.; Saifullah, M. S. M.; Tapley, E.; Kang, D.-J.; Welland, M. E.; Butler, M. *Nanotechnol.* **2004**, 15, 158-162.

[47] Pamme, N.; Manz, A. *Anal. Chem.* **2004**, 76, 7250-7256.

[48] Cui, H. C.; Horiuchi, K.; Dutta, P. I.; Ivory, C. F. *Anal. Chem.* **2005**, 77, 7878-7886.

[49] Hong, S. M.; Kim, S. H.; Kim, J. H.; Hwang, H. I. *J. Phys. Conf. Ser* **2006**, 34, 656-661.

[50] Kaniansky, D.; Masar, M.; Dankova, M.; Bodor, R.; Rakocyova, R. *J. Chromatogr. A* **2004**, 1051, 33-42.

[51] Östman, P.; Luosujärvi, L.; Haapala, M.; Grigoras, K.; Ketola, R. A.; Kotiaho, T.; Franssila, S.; Kostiainen, R.; *Anal. Chem.* **2006**, 78 (9), 3027–3031.

[52] http://www.xensor.nl/txtfiles/projects/xi-proj/injec.htm

[53] Jackman, R. J.; Wilbur, J. L.; Whitesides, G. M. *Sci.* **1995**, 269, 664-666.

[54] Becker H.; Heim, U. *Sens. Actuators A: Phys.* **2000**, 83, 130–135.

[55] Eijkel, J. C. T.; van den Berg, A. *Microfluid. Nanofluid.* **2005**, 1, 249–267.

[56] Hu, G.; Li, D. *Chem. Eng. Sci.* **2007**, 62, 3443–3454.

[57] El-Ali, J.; Sorger, P. K.; Jensen, K. F.; *Nature* **2006**, 442, 403.

[58] Xi, C. W.; Marks, D. L.; Parikh, D. S.; Raskin, L.; Boppart, S. A. *Proceedings Of The National Academy Of Sciences Of The United States Of America* **2004**, 101, 7516-7521.

[59] Herzig-Marx, R.; Queeney, K. T.; Jackman, R. J.; Schmidt, M. A.; Jensen, K. F. *Analytical Chemistry* **2004**, 76, 6476-6483.

[60] Amatore, C.; Belotti, M.; Chen, Y.; Roy, E.; C.Sella; Thouin, L. *Journal Of Electroanalytical Chemistry* **2004**, 573, 333-343.

[61] Wensink, H.; Benito-Lopez, F.; Hermes, D. C.; Verboom, W.; Reinhoudt, D. N. G. H.; Berg, A. V. D. *Lab Chip* **2005**, 5, 280-284.

[62] Kricka, L. J.; Wilding, P. *Micromechanics and Nanotechnology In: Handbook of Clinical Automation Robotics and Optimisation* **1996**, Ed. Kost, G. J., John Wiley & Sons, New York, pp. 45-77.

[63] van der Schoot, B. H.; Verpoorte, E.; Jeanneret, S.; Manz, A.; de Rooij, N. F. *Microsystems for Analysis in Flowing Solutions In: Micro Total Analytical Systems* **1995**, Ed. van den Berg, A.; Bergveld, P., Kluwer Academic Publishers, Dordrecht, pp.181-190.

[64] Jacobson, S. C.; Ramsey, J. M. *Anal. Chem.* **1996**, 68, 720-723.

[65] Waters, L. C.; Jacobson, S. C.; Kroutchinina, N.; Khandurina, J.; Foote, R. S.; Ramsey, J. M. *Anal. Chem.* **1998**, 70, 158-162.

[66] Volmer, M.; Weber, A.Z..; *Phys. Chem.* **1926**, 119, 277.

[67] Bird, R. B.; Stewart, W. E.; Lightfoot, E. N. *Transport Phenomenon* **2002**, John Wiley and Sons, New York, 2nd Edition.

[68] Levich, V. G. *Physicochemical Hydrodynamics*; **1962**, Prentice-Hall: New Jersey.

[69] Mao, H. B.; Yang, T. L.; Cremer, P. S. *J.Am. Chem. Soc.* **2002**, 124, 4432-4435.

[70] Cabrera, C. R.; Finlayson, B.; Yager, P. *Anal. Chem.* **2001**, 73, 658-666.

[71] Benninger, R. K. P.; Koc, Y.; Hofmann, O.; Requejo-Isidro, J.; Neil, M. A. A.; French, P. M. W.; deMello, A. J. *Anal. Chem.* **2006**, 78, 2272-2278.

[72] Yang, M.; Yang, J.; Li, C. W.; Zhao, J. L. o. a. C., 2002, 2, 158-163 *Lab Chip* **2002**, 2.

[73] Henley, I. E.; Yunus, K.; Fisher, A. C. *J. Phys. Chem. B* **2003**, 109, 7843-7849.

[74] Richardson, L. F. *Philosophical Transactions of the Royal Society A* **1911**, 210, 307-357.

[75] Clough, R. W. *Proc. 2nd ASCE Conf. Electron. Computa.* **1960**, Pittsburg.

[76] Banerjee, P. K.; Butterfield, R. *Boundary Element in Engineering Science* **1981,** McGraw-Hill, New York.

Chapter 2

Methods and Techniques

2.1 INTRODUCTION

This chapter reviews the various microfabrication methods, electrochemical techniques and numerical methodology used to quantify analytical systems currently used in the industry. This chapter has been divided into two sections. The first section describes some of the methods commonly employed in the fabrication of micro analytical devices. It also discusses some of the techniques that were used to fabricate the electrochemical micro-sensor and micro-chromatography columns, used during the research. The second section details the numerical methods that were employed to quantify the electrochemical devices.

2.2 MICROFABRICATION

2.2.1 Photolithography

Since its inception, photolithography is the most widely used form of lithographic techniques [1, 2]. It is used to fabricate polymer structures of micron and sub micron dimensions, onto silicon substrates. In this process, a pattern is transferred to a photosensitive polymer (photoresist) by exposure to an ultraviolet light (UV) source through a photomask. The pattern in the photoresist is then transferred to the underlying substrate using etching techniques. The combination of accurate

positioning of successive photomasks and exposure of these successive patterns to UV light, gives multilayered structures. The various factors that determine and affect the resolution of micro structures produced by photolithographic process are explained in detail below.

1. *Wafer Cleaning*: Contaminants such as dust, inorganic and organic impurities can hinder the photolithographic process by interrupting the light, disturbing the surface uniformity of the resist or by reacting with the photoresist. This problem is magnified when working with features of sub micron dimensions. A variety of cleaning methods are available to prepare a glass wafer for the photolithographic process. Some of the cleaning methods include: using a hydrofluoric acid (HF) dip or Piranha solution (3:1 ratio of concentrated sulphuric acid to 32 (vol%) hydrogen peroxide).
2. *Photomask*: A photomask is an optical mask consisting of opaque patterns on a transparent support. These masks are prepared using either computer aided design (CAD) or adobe illustrator. For resolutions up to 5 μm, the photomasks can be printed on thin transparent films. For less than 5 μm, chrome or iron oxide masks are used.
3. *Photoresist*: A photoresist is a UV light sensitive polymer. It is available in two forms: positive and negative photoresists. In the case of negative photoresist, the exposed regions are intact during the development stage; whereas the exposed regions of positive photoresists are washed away during the development stage. This variation is explained by the different changes in physical properties of the two polymers during the UV light exposure stage. The typical composition of a positive photoresist consists of a mixture of diazonaphthoquinone (DNQ) and novolac resin. Under normal conditions, DNQ prevents the dissolution of the Novolac resin [3]. However, when exposed to UV light, the DNQ increases the dissolution rate, thereby allowing the region that was exposed to be removed from the unexposed regions during development. An example of a commercially available positive photoresist is Shipley 1800 series, produced by Chestech Ltd. In the case of a

negative photoresist, an epoxy polymer mixed with an appropriate photoinitiator is used. During the UV light exposure, the epoxy based polymer gets cross-linked, leaving the unexposed regions to be etched away easily. Film thicknesses obtained using negative resist are in the range of 1 μm to 1 mm. A commercially available negative photoresist is SU8 manufactured by MicroChem.

4. *Light Source*: A mask aligner is used as the light source for the photoresist. The mask aligner helps in transferring the pattern from the photolithographic mask to the photoresist on the substrate. Ultra-violet (UV) light, at a wavelength typically in the range of 250 nm to 578 nm, is used to initiate the reaction in the photoresist. Some other commonly used energy sources include electron-beams (e-beam) and proton beams [4, 5]. A correct light exposure time is extremely critical in order to obtain sharp features.
5. *Development*: This final stage of the photolithographic process can also affect the resolution of the micropatterned structures, in case the structures are left underdeveloped or get overdeveloped. Positive photoresists are typically developed in aqueous alkaline solutions; while negative are developed using organic solvents.

A schematic of photolithographic process is shown in Figure 2-1.

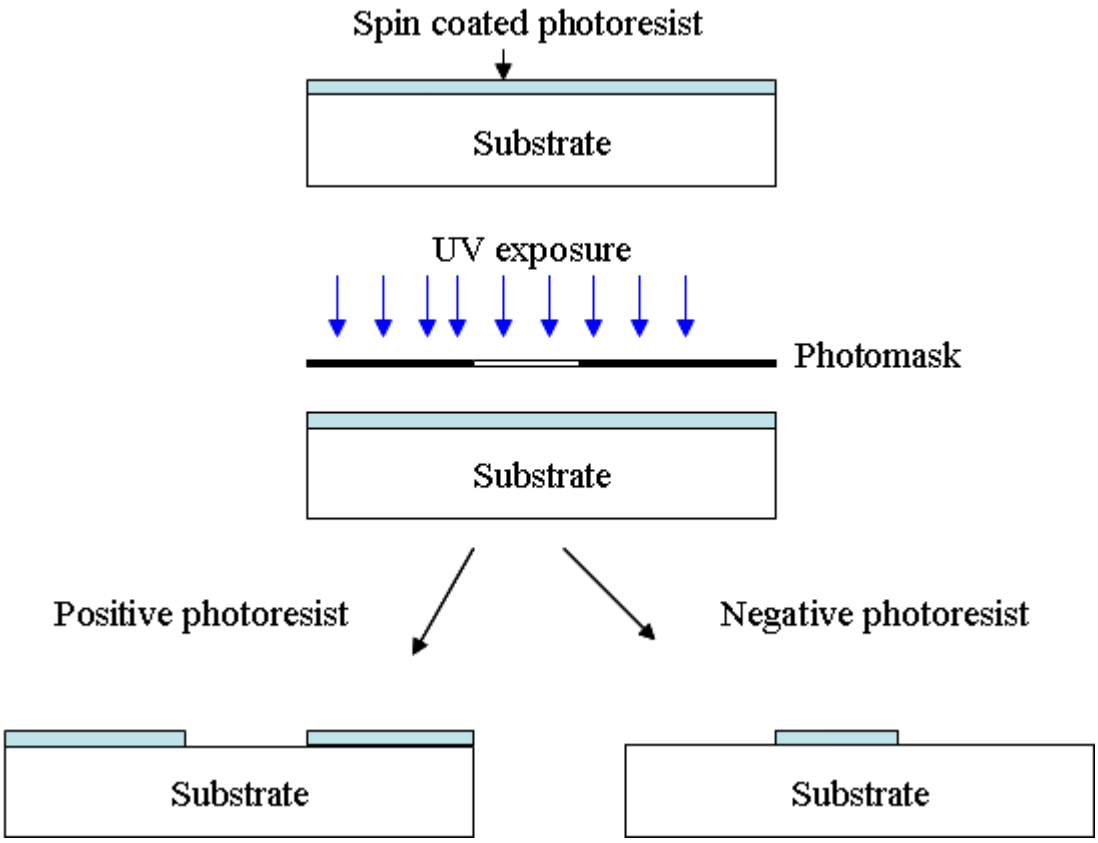

Figure 2-1 Schematic of photolithographic process

Substrate materials other than silicon or glass that are currently used or are being investigated for use in microfabrication process includes: polymers, ceramic, biomaterial and carbon [1]. However, to date, glass remains the preferred choice of substrate. Optical transparency of glass is essential for a number of imaging techniques and its efficient heat transfer is useful, both during the fabrication process as well as the subsequent applications of the devices.

2.2.2 Etching

There are two types of etching processes:

1. Wet etching where the material is dissolved when immersed in a chemical solution.
2. Dry etching where the material is sputtered or dissolved using reactive ions or a vapor phase etchant.

1.) *Wet Etching*: This method uses a chemical (etchant) such as buffered hydrofluoric acid (HF) that dissolves subsequent layers of substrate material to form predefined micropatterned structures [6]. Wet etching requires a mask that dissolves or at least etches much slower than the material to be micropatterned. There is however a disadvantage of using this process. Some single crystal materials, such as silicon, exhibit anisotropic etching in certain chemicals. Anisotropic etching in contrast to isotropic etching means different etch rates in different directions in the material. This leads to the appearance of crystal plane side walls in the silicon wafer, when etched in potassium hydroxide. On the other hand, an isotropic process causes the undercutting of the mask layer by the same distance as the etch depth [7]. An illustration of anisotropic and isotropic wet etching of a hole in a silicon wafer is shown in Figure 2-2. Another example of wet etching is the hydrofluoric acid etch of Foturan glass exposed to UV light through a photomask [8]. Microcrystallites are formed in the exposed areas of glass which are more susceptible to HF than the non-exposed glass, resulting in microstructures at least 25 μm in depth.

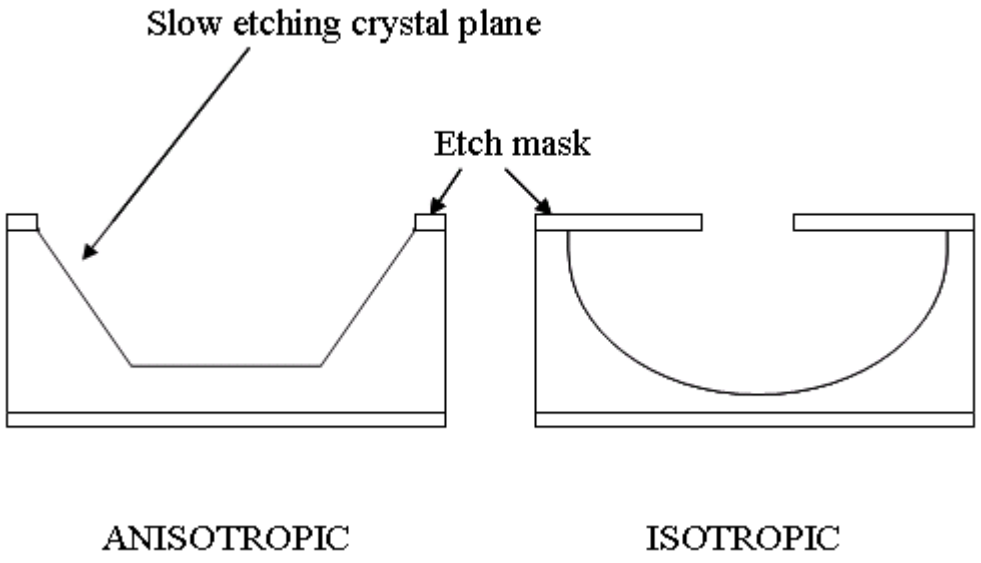

Figure 2-2 Illustration of wet etching techniques

2.) *Dry Etching*: Two popular dry etching methods are: reactive ion etching (RIE) and deep reactive ion etching (DRIE). In RIE, etch depths of hundreds of microns can be achieved with almost

vertical sidewalls. Reactive ions generated using plasma are accelerated towards the substrate and made to react with it [9]. This is chemical type of RIE. In the physical method, accelerated ions with high enough energy are used to knock out atoms from the surface of the substrate, etching it in the process.

In the case of DRIE, an anisotropic etch procedure is employed by sputtering two compositions of gas at the substrate. The first gas composition creates a polymer on the surface of the substrate which protects the side walls, while the second gas composition physically etches the substrate. Using this technique, etching aspect ratios of 50 to 1 can be achieved.

2.2.3 Laser Ablation

In laser ablation, high-power laser pulses are used to evaporate matter from a target surface. As a result, a supersonic jet of particles is ejected normal to the target surface. The depth of the cut is controlled by the length of the laser pulse and can be used to obtain depths of up to several hundred microns. Clean edge profiles are produced as the laser pulse removes material rapidly, giving little time for the surrounding material to absorb heat, hence avoiding distortions [10].

2.2.4 Soft Lithography

Soft lithography is a method in which the topography of a surface defines the patterns created on a substrate. A soft polymeric stamp is used to reproduce a desired pattern (see Figure 2-3) directly on a substrate [11]. The main advantage of this method is its short turnaround time *i.e.* time taken from design to production is less than 24 hours.

The polymeric stamp is often made up of poly(dimethylsiloxane) (PDMS) (refer Figure 2-3 for chemical structure). High aspect ratio microfluidics can be fabricated using a SU8 negative photoresist mould, as discussed earlier. PDMS is prepared by mixing the PDMS elastomer with a

curing agent, typically in the ratios of 4:1 to 10:1, as recommended by manufacturer's guidelines. The PDMS mixture is then poured onto the SU8 mould. It is cured, removed and then sealed onto a flat surface, typically glass. A schematic of the soft lithographic process is shown in Figure 2-4.

One of the advantages of using PDMS in soft lithography is that PDMS devices can be cut to size with standard surgical steel blades, and inlet/outlet holes can be easily punched for tubing and other device inputs. For tubing inputs, a needle hole, slightly smaller than the outer diameter, is drilled to provide adequate sealing for typical fluidic pressures. Another useful property of PDMS is that its surface can be chemically modified in order to obtain permanent bonding between the PDMS and the glass, prior to sealing. This is done by exposing the PDMS to oxygen plasma. By doing so, the surface Si-CH_3 groups along the PDMS backbone, are transformed into Si-OH groups by the reactive oxygen species in the plasma. These silanol surfaces easily form permanent bonds with Si on glass surface [12].

Due to the biocompatibility of PDMS, these devices can be used for biological applications such as patterning cells or proteins with the help of self assembled monolayers (SAM) [13]. Its use can also be extended to act as membranes in biological systems, to selectively pass the desired gas through the device [14].

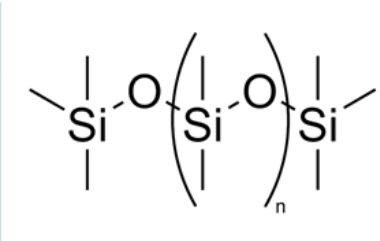

Figure 2-3 Chemical Structure of poly(dimethylsiloxane)

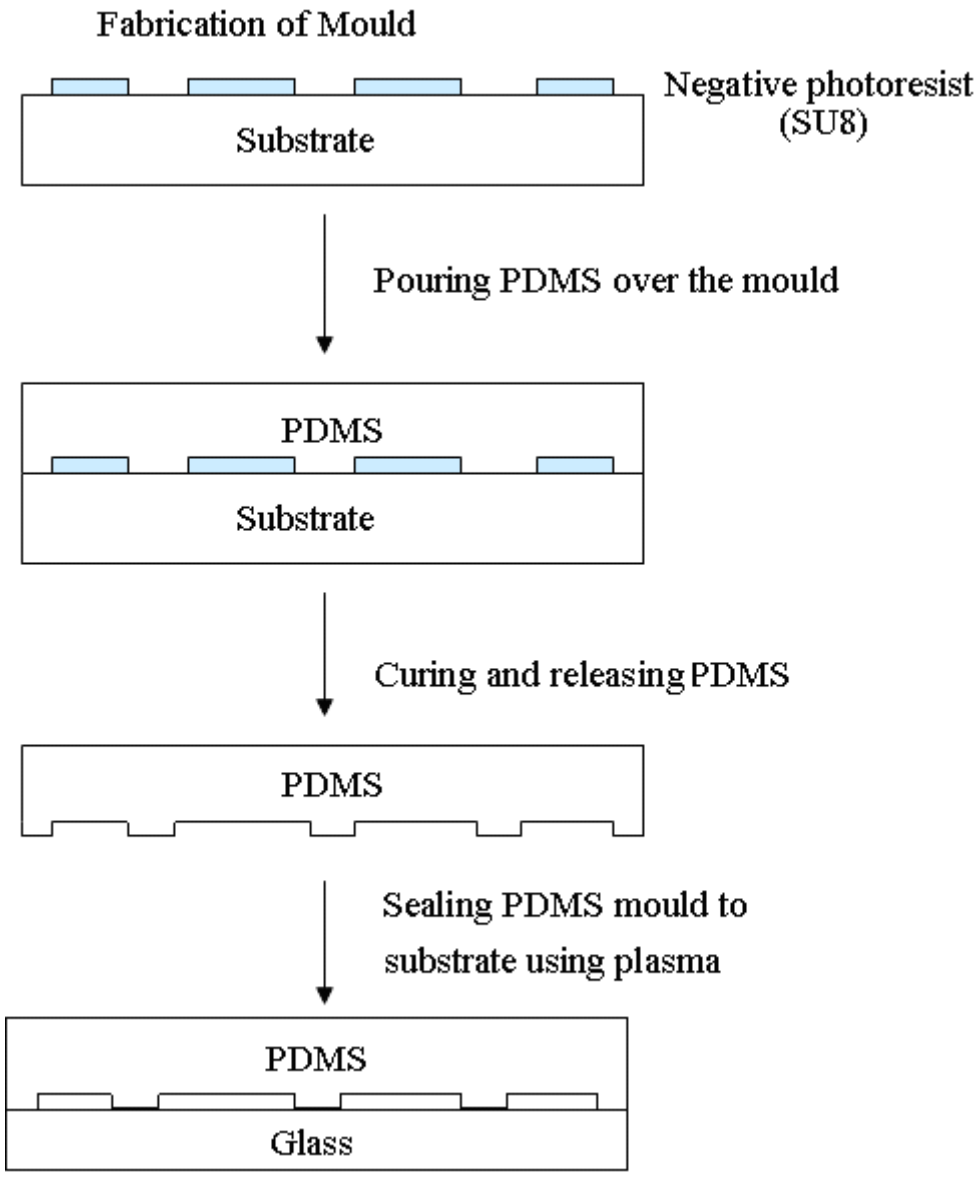

Figure 2-4 Fabrication of poly(dimethylsiloxane) channels from SU8 mould

2.2.5 Micromachining

Micromachining is carried out using standard methods such as sawing, milling and turning, using machining components with micro dimensions. The resolution that can be achieved using this method is up to 80 μm. A variety of materials such as steel, glass, teflon can be used for machining micro structures into them [15]. These materials offer better mechanical strength, chemical resistance and tolerance to high temperatures and pressures. The development time from start to the end product is shorter than any lithographic technique.

2.2.6 Sub Micron Patterning

1.) *Focused Ion Beam Lithography*

This technique is used to fabricate features with dimensions as small as 10 nm. It uses accelerated high energy gallium ions (5-50 keV), focused through an electrostatic lens to sputter atoms from a defined region of substrate surface. This also leads to the deposition of a thin layer of gallium ions in the region where the ions were focused. Figure 2-5 illustrates the high precision features of sub micron dimension obtained using this technique [16].

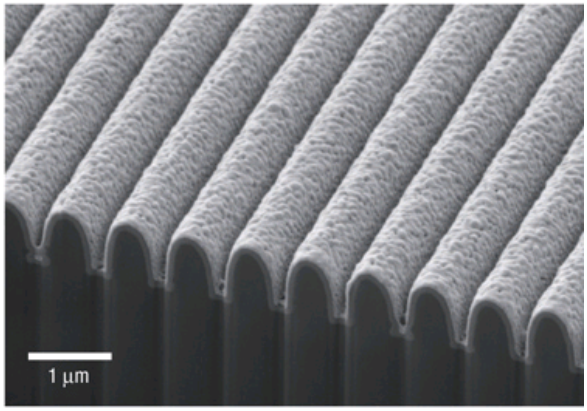

Figure 2-5 Typical features obtained through application of focused ion beam lithography [16]

2.) *Electron Beam Lithography*

Electron beam (E-Beam) lithography is the technique of obtaining patterned features by focusing a beam of electrons onto a surface covered with resist, allowing either the exposed or the non-exposed regions of the resist to be selectively removed. The micropatterned structures thus created in the resist are then transferred into another material for a variety of applications in research laboratories. The use of a focused electron beam means that the diffraction limit of light can be surpassed in order to produce sub micron features as illustrated in Figure 2-6 [17]. Features of dimensions up to 25 nm can be obtained. The key limitation of electron beam lithography is the long time required to expose an entire silicon wafer or glass substrate. A long exposure time leaves the user vulnerable to beam drift or instability which may occur during the exposure.

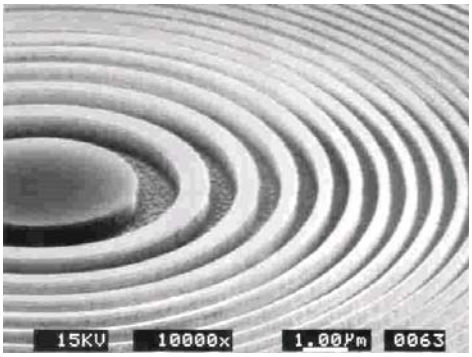

Figure 2-6 Typical features obtained using E-Beam lithography [17]

2.3 MICROFABRICATION - EXPERIMENTAL PROCEDURE

The electrochemical micro-(bio)sensor (EMB) developed during the experiment, was based on a sandwich micro structure, where the counter electrode was sited on one of the walls of the microchannel, while the working electrode was placed on the opposite wall (see Figure 2-7 for schematic). Fabrication details for the thin metal electrodes and the microchannel, have been outlined in the following section.

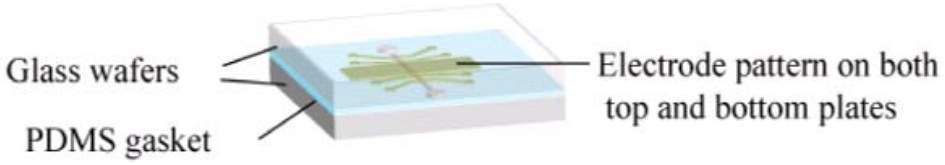

Figure 2-7 Schematic of electrochemical micro-biosensor setup

2.3.1 Fabrication of Thin Metal Electrode

The steps involved in the fabrication of the thin metal electrode from wafer preparation to development, are listed below.

1. *Wafer Preparation*: The glass wafer was cut to the desired size, using a diamond cutter. Using a solution of Piranha acid, the wafer was then cleaned from any impurities and organic residues on the surface of the glass. The cleaned wafer was rinsed thoroughly in milli-Q water several times before being dried in a clean supply of nitrogen. The glass wafer

was dehydrated at 200 ^{o}C in a commercial temperature controlled oven for approximately 2 hours.

2. *Spin Coat*: 2 ml of the positive photoresist, S 1828, was dispensed in the centre of the wafer, before being spin coated at 4000 rpm for 60 seconds at high acceleration, using a commercial spin coater. A photoresist layer thickness of approximately 2.5 μm was obtained. The photoresist coated wafer was then subjected to a soft bake at 115 °C for 60 seconds to remove the solvent within the resist layer.
3. *UV Light Exposure*: The soft baked substrate was exposed to an UV light source (340 nm - 430 nm), which was projected through a predesigned photomask using a standard mask aligner for 16 seconds (150-250 mJ cm^{-2}).
4. *Development*: After the exposure process, the photoresist coated wafer was then subjected to a development process. The exposed regions of the photoresist were developed away in an aqueous developer solution (AZ 351). A development time of 60 seconds was required to remove all the exposed photoresist, leaving the desired micro features on the glass wafer. After development, the wafer was rinsed in milli-Q water before being blow dried in a clean supply of nitrogen.
5. *Evaporation:* The patterned glass wafer was then put in a thermal metal evaporator, and a thin film of titanium (Ti: approx. 20 nm thick) and then gold (Au: approx. 150 nm thick) were deposited over the wafer and photoresist. The evaporation is typically carried out in vacuum chamber with a controlled pressure of $1x10^{-6}$ mbar to allow easier vapourisation of gold, while preventing the oxidation of the titanium layers prior to gold coating. The gold plated wafer was removed from the evaporator and then immersed in acetone to dissolve and lift off the photoresist, leaving the desired pattern of the metal film.

2.3.2 Fabrication of PDMS Microchannel

The fabrication of the PDMS microchannel was divided into two steps: (1) SU8 template preparation, (2) PDMS microchannel preparation.

2.3.2.1 SU8 Template Preparation

1. *Wafer Preparation*: The glass wafer onto which the PDMS microchannel was to be fabricated, was cleaned and dried using protocol described previously in Section 2.3.1.
2. *Spin Coat*: Negative photoresist SU8 2100 was spin coated onto the clean glass wafer. The thickness of SU8 2100 could be adjusted by varying the spinning speed; conditions for which have been tabulated in Table 2-1. After spin coating the photoresist, a two stage soft baking procedure was used (see Table 2-1).
3. *UV Light Exposure*: After subsequent drying by heating the coated glass wafer on a hot plate, the photoresist was exposed to UV light, while placed under the desired photomask, using a mask aligner. After exposure, the wafer was further heated to ensure a complete polymerisation reaction, in order to obtain well defined features. The details of UV light exposure time and the post exposure bake times are given in Table 2-1.
4. *Development:* The exposed glass wafer was then placed into a developer solution (EC solvent), in order to develop away the unexposed regions from the masked pattern.

Thickness (µm)	**Spin Speed (rpm)**	**Acceleration**	**Duration (s)**	**Pre Exposure Bake Time @ 65 °C (min)**	**Pre Exposure Bake Time @ 95 °C (min)**	**Exposure Time (s)**	**Post Exposure Bake Time @ 65 °C (min)**	**Post Exposure Bake Time @ 95 °C (min)**	**Development Time (min)**
100	500	9	10	5	20	25	1	10	10
	3000	4	30						
140	500	9	10	5	35	28.5	1	15	15-18
	2000	4	30						
250	500	9	10	12	60	5 x 10 s with 1 min interval	1	15	20-25
	1000	4	30						

Table 2-1 Protocol using SU8 2100 photoresist

2.3.2.2 PDMS Gasket Channel Fabrication

A modified form of standard soft lithographic process was used, where PDMS was spin coated rather than poured, to form a microchannel in a thin PDMS gasket. The microchannel, when clamped between two glass wafers, consisted of two PDMS walls and two glass walls. This design allowed electrodes and inlets to be sited on both the top and the bottom walls of the device.

The height of the PDMS gasket could be adjusted by varying the spin speed. Table 2-2 gives various thicknesses obtained at respective speeds. Following deposition of PDMS on a glass wafer, the wafer was baked at 45 ˚C on a hotplate for 1 minute and at 60˚C in an oven for 2 hours, to enhance the curing process. The gasket on the micropatterned glass wafer was then put through a lift off process, where they were released by floating off in 1,2-dichloroethane.The gasket channel

was then dried and aligned with the electrode features and the inlet and outlet holes in the two glass wafers. The device was sealed by placing it in a mechanical Perspex clamp, which also contained features to provide fluid flow to the inlets and outlets. This method provided a seal capable of withstanding significant pressures within the channel.

Acceleration: 9; Duration: 60 s	
Speed (rpm)	**Thickness (µm)**
250	240
300	210
350	200
500	140
1000	70

Table 2-2 Variation of PDMS thickness with spin speed

A schematic outlining the fabrication procedure for the thin metal electrode and the PDMS microchannel has been illustrated in Figure 2-8 below.

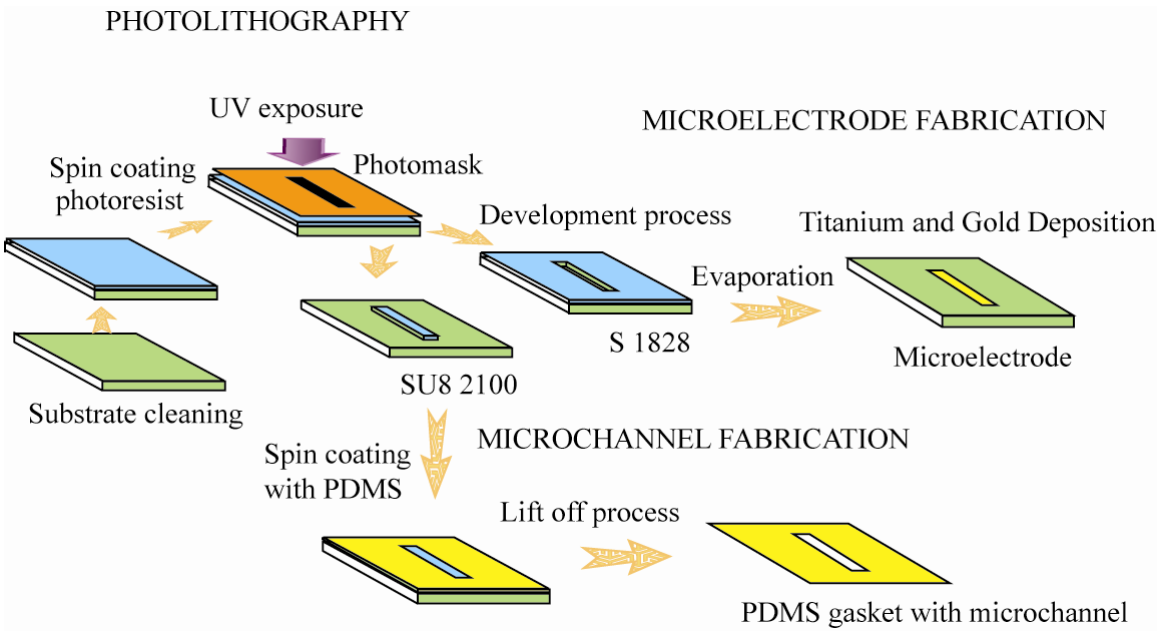

Figure 2-8 Illustration of microfabrication procedure for thin metal electrode and PDMS microchannel

2.3.3 Fabrication of Microchannel Using Micromachining

Microchannels used to study micro-chromatography were fabricated using micromachining. Using a commercially available milling machine, channels of dimensions in the range of 100-800 μm were fabricated. After milling the microchannel in the glass wafer, inlets and outlet were drilled using a commercially available diamond drill. The glass wafers were then cleaned in Piranha acid, and rinsed several times in milli-Q water, before being dried in a clean supply of nitrogen. The wafer with the microchannel was then sealed with another glass substrate using epoxy glue.

2.4 SOLUTION FLOW AND EXPERIMENTAL SETUP

Fluid flow in all experiments was either pressure driven, using a syringe pump or under gravitational force, with typical flow rates between 1.66 x 10^{-4} cm^3 s^{-1} (0.01 ml min^{-1}) and 6.6 x 10^{-2} cm^3 s^{-1} (4 ml min^{-1}). A setup of the flow system using the syringe pump is shown in Figure 2-9.

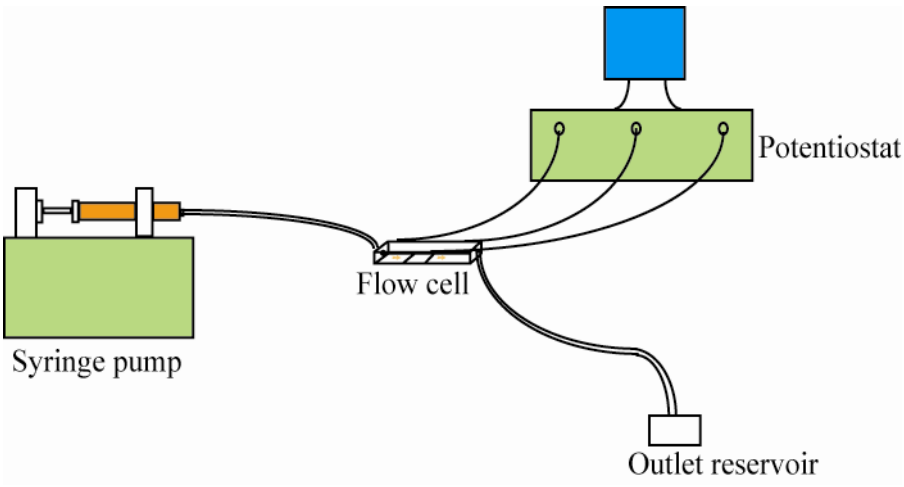

Figure 2-9 Experimental setup for microelectrode system

2.5 REAGENTS

The chemical reagents and other materials used for the fabrication of the microfluidic devices and for the experimental studies are listed in Table 2-3 together with their supplier and analytical grades.

Reagent	**Supplier**	**Grade**
Acetone	Aldrich	HPLC
Acetonitrile	Aldrich	HPLC
AZ 351 Developer	Shipley	Clean Room Quality
1,2-Dicholoroethane	Aldrich	HPLC
EC solvent	MicroChem	Clean Room Quality
Ethanol	Fisher	Absolute
Gold	Advent Materials	99.99%
Hydrogen peroxide	Aldrich	35wt.%
Microposit S1828	Shipley	Clean Room Quality
Poly(dimethylsiloxane)	Dow Corning	N/A
Platinium	Advent Materials	99.99%
Potassium chloride	Aldrich	99.999%
Potassium ferricyanide	Aldrich	99%
Potassium ferrocyanide	Aldrich	99%
SU8-2100	MicroChem	Clean Room Quality
Sulphuric acid	BDH	95%
Titanium	Advent Materials	99.99%
Boron doped diamond electrode	Windsor Scientific	1.1 x 1.1 cm chips 0.2 x 0.5 cm chips
Epoxy resin	Struers	N/A
Nicotineamide dinucleotide (NADH)	Sigma Aldrich	N/A
Flavin mononucleotide (FMN)	Sigma Aldrich	N/A
Flavin adenine dinucleotide (FAD)	Sigma Aldrich	N/A
Ascorbic acid	Fisher Scientific	N/A
Phytic acid	Fluka	N/A
Sodium iminodiacetate dibasic hydrate (IDA)	Aldrich	98%
Alyllglycidyl ether (AGE)	Sigma Aldrich	N/A
Phosphate buffer	Sigma Aldrich	N/A
Tris HCl	Melford Lab.	N/A
Imidazole	Sigma Aldrich	99%
Phenylmethylsulfonyl fluoride (PMSF)	Sigma Aldrich	N/A
2,2-Dimethoxy 2-phenyl acetophenone (DMPA)	Sigma Aldrich	99%
2-Hydroxyethyl methacrylate (HEMA)	Sigma Aldrich	98%
Ethylene glycol dimethacrylate (EGDMA)	Sigma Aldrich	98%
Comassie protein assay	Thermo scientific	N/A
BL21 competent cells	Stratagene	N/A
Bovin serum albumin	Thermoscientific	N/A
β-lactoglobulin	Sigma Aldrich	N/A

Reagent	**Supplier**	**Grade**
Copper(II) Sulphate	Sigma	N/A
Gel-reducing agent, marker, loading agent	Invitrogen	N/A
Silica: Syloid CP4-7358 (36μm),CP4-7051(94μm)	Grace Davidson	N/A
Glass	Soham Scientific	N/A
LB agar and LB broth	Sigma Aldrich	N/A
Sodium Hydroxide (NaOH)	Fisher Scientific	N/A
Ethylenediaminetetraacetic acid (EDTA)	Aldrich	N/A
Methanol	Sigma Aldrich	Anhydrous, 99.8%
N, N, N', N'-Tetramethyl-p-pentylendiamine	Aldrich	98%
Tetrabutylammonium perchlorate	Fluka	N/A
Ammonium chloride	Sigma Aldrich	N/A
Pyrrole	Sigma Aldrich	ACS reagent, 99.5%
Methylene blue	Sigma Aldrich	ACS reagent, 99.5%
Platinum diamminedinitrite	Johnson Matthey	N/A
Disodium hydrogen phosphate dihydrate	Fisher Scientific	N/A
Diammonium hydrogen phosphate	Fisher Scientific	N/A
Sodium chloride	Sigma Aldrich	N/A
Sodium phosphate	Sigma Aldrich	N/A
Sodium carbonate	Sigma Aldrich	N/A

Table 2-3 Reagents list

2.6 EQUIPMENT

The fabrication of the devices and subsequent experimental measurements were performed using the following equipment:

Apparatus	**Supplier**	**Model**
Spin Coater	Karl Suss	Delta 10 TT
Analytical Balance	Ohaus	Galaxy 160D
Diamond Band Saw	Diamond Tech	DL 3000 XL
Evaporator	BOC Edwards	Auto 306
Mask Aligner	Karl Suss	MJB3 340 nm 10 W cm^{-2}
PCB Drill	Proxxon	TBM220
Milling Machine	Warco	ZX45
Photographic Film Masks	Circuit Graphics	N/A
Potentiostat	Autolab	PGSTAT 100
Syringe Pump	Harvard Apparatus	PHD 2000
Technical Drawing Software	Adobe	Illustrator v11
Spin Coater	Karl Suss	Delta 10 TT
Confocal	Leica	TCS SP5
FTIR Spectrometer	Thermo Nicolet	N/A
Solid State NMR	Varian VNMRS	N/A
NMR	Brucker Avance	500 MHz NMR

Apparatus	Supplier	Model
Elemental Analyser	Exeter Analytical	CE440
UV-vis spectrophotometer	Thermospectronic	UV1
Centrifuge	DuPont	Sorvall RC-5B
Hg Porosimeter	Micromeritics	Autopore IV
BET analyser	Micromeritic	BET Tristar 3000
Laser particle sizer	Beckman Coulter	LS230
Particle Sieve	Endecoth	EVS1
Pulveriser	Fritsch GmBH	Pulverisette 6
SEM	Cral Zeiss	FE-SEM
ESEM	Philips	XL30 ESEM
Air Plasma	Electronic Diener	N/A
Xcell Surelock Electrophoresis Cell	Biorad	PowerPac 300
Incubator	New Brunswick Scientific	N/A
Sonicator	Heat Systems	XL 2020
Oven	Memmert	100-800 series
Pressure drop sensor	Digitron Instrumentation	N/A

Table 2-4 Equipment list

2.7 NUMERICAL METHODS

Numerical simulations were performed in this thesis, to quantify the electrochemical reactions occurring inside the microfluidic device under hydrodynamic conditions. Many numerical methods, such as finite element modelling (FEM) and finite difference method (FDM), have been developed in the past to predict reaction kinetics and transport rates of an electroactive species undergoing redox reactions in macro and micro environments as mentioned in Chapter 1 [18, 19]. In the following section, the most commonly used approaches to model mass transport and reaction kinetics within electrochemical microreactors have been described.

The aim of numerical simulations of microfluidic devices is to solve the convective diffusion equation, used to describe the movement of species in up to three dimensions. The equation is as follows:

$$\frac{\partial C}{\partial t} = D\frac{\partial^2 C}{\partial x^2} + D\frac{\partial^2 C}{\partial y^2} + D\frac{\partial^2 C}{\partial z^2} - u\frac{\partial C}{\partial x} \qquad (2.1)$$

Where, C is the concentration of the species in the solution, D the diffusion coefficient, x, y and z the Cartesian co-ordinates and u_x the velocity in the x direction.

The finite difference method can be used to solve this equation inside a rectangular duct microchannel containing an electrode sited at the centre of this conduit, as illustrated in Figure 2-10.

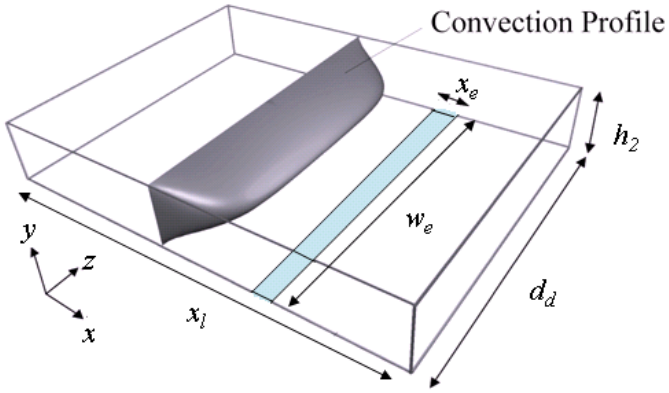

Figure 2-10 Schematic of a rectangular duct

2.7.1 Finite Difference Method

Finite difference method is a technique used to solve partial differential equations. This technique has been reported in the past for simulating coupled kinetics, hydrodynamics or linear sweep experiments [20, 21]. FDM consists of transforming the continuous domain of the state variables such as concentration and temperature, by a network or mesh of discrete nodal points. The partial differential equation (PDE) is then converted into a set of finite difference equations that can be solved subject to the appropriated boundary conditions by performing a Taylor's expansion around the nodal points of known values.

The governing principles of the finite difference technique can be explained using the time dependent evolution of a two-dimensional concentration distribution perpendicular to a solid surface as described by Fick's second law of diffusion:

$$\frac{\partial a}{\partial t} = D\frac{\partial^2 a}{\partial x^2} + D\frac{\partial^2 a}{\partial y^2} \tag{2.2}$$

Where a is the normalised concentration of species *A* ($a = \left(\frac{[A]}{[A]_{Bulk}}\right)$) which undergoes a transport limited reduction at an electrode fabricated on one wall of a rectangular duct (refer Figure 2-10).

The simulation domain can be discretised into a series of points, *i*, with a position, x_i as shown in Figure 2-11. .

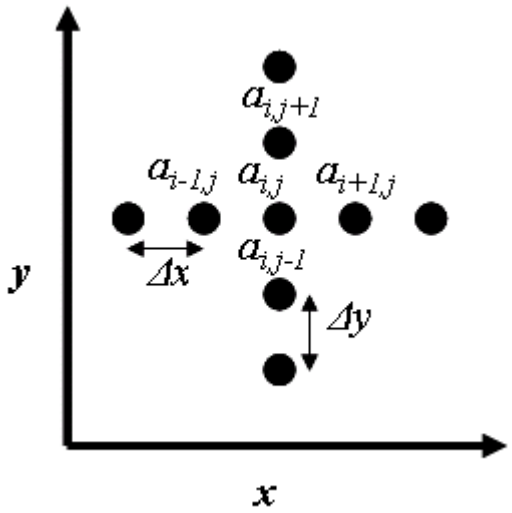

Figure 2-11 Illustration of the discretisation of the two-dimensional simulation domain

The first derivative or gradient of the concentration profile at a given point, (*i,j*), can be estimated by one of three methods; backward difference method, central difference method or forward difference method.

Backward Difference

$$\left(\frac{da}{dx}\right)_{i,j} = \frac{a_{i,j} - a_{i-1,j}}{\Delta x}$$
$$\left(\frac{da}{dy}\right)_{i,j} = \frac{a_{i,j} - a_{i,j-1}}{\Delta y} \tag{2.3}$$

Central Difference

$$\left(\frac{da}{dx}\right)_{i,j} = \frac{a_{i+1,j} - a_{i-1,j}}{2\Delta x}$$
$$\left(\frac{da}{dy}\right)_{i,j} = \frac{a_{i,j+1} - a_{i,j-1}}{2\Delta y} \tag{2.4}$$

Forward Difference

$$\left(\frac{da}{dx}\right)_{i,j} = \frac{a_{i+1,j} - a_{i,j}}{\Delta x}$$
$$\left(\frac{da}{dy}\right)_{i,j} = \frac{a_{i,j+1} - a_{i,j}}{\Delta y} \qquad (2.5)$$

The difference between the forward and backward difference methods is often used as the second derivative of the gradient:

$$\left(\frac{d^2a}{dx^2}\right)_{i,j} \approx \frac{a_{i+1,j} - 2a_{i,j} + a_{i-1,j}}{(\Delta x)^2}$$
$$\left(\frac{d^2a}{dy^2}\right)_{i,j} \approx \frac{a_{i,j+1} - 2a_{i,j} + a_{i,j-1}}{(\Delta y)^2} \qquad (2.6)$$

The variation of the concentration over a time period, Δt, is formulated in a similar manner to give the expression:

$$\left(\frac{da}{dt}\right)_{i,j} = \frac{a_{i,j}^{t+\Delta t} - a_{i,j}^{t}}{\Delta t} \qquad (2.7)$$

Where $a_{i,j}^{t}$ represent the normalised concentration of species *A* at the coordinate (*i*,*j*) at time, *t* and $a_{i,j}^{t+\Delta t}$ is the concentration of species *A* at time $t+\Delta t$. Fick's second law (Equation 2.2) can be rewritten according to the relationships defined above to give Equation 2.8:

$$\frac{a_{i,j}^{t+\Delta t} - a_{i,j}^{t}}{\Delta t} = D\frac{a_{i+1,j}^{t} - 2a_{i,j}^{t} + a_{i-1,j}^{t}}{(\Delta x)^2} + D\frac{a_{i,j+1}^{t} - 2a_{i,j}^{t} + a_{i,j-1}^{t}}{(\Delta y)^2} \qquad (2.8)$$

This can be rewritten as:

$$a_{i,j}^{t+\Delta t} = \left(\lambda_x a_{i-1,j}^{t} + (1-2\lambda_x)a_{i,j}^{t} + \lambda_x a_{i+1,j}^{t}\right) + \left(\lambda_y a_{i,j-1}^{t} + (1-2\lambda_y)a_{i,j}^{t} + \lambda_y a_{i,j+1}^{t}\right) \qquad (2.9)$$

Where $\lambda_x = \frac{D\Delta t}{(\Delta x)^2}$ and $\lambda_y = \frac{D\Delta t}{(\Delta y)^2}$.

λ_x or λ_y can be considered as the distance the material can travel in a single time step. In the two-

dimensional simulation, the requirement for λ_x or λ_y is to remain below 0.25, in order to remain stable. If it were to exceed 0.25, the simulation will become unstable, creating oscillations in the calculated concentration values, which would proliferate through the simulation domain over each subsequent time step.

The finite difference procedure described above is an explicit method to calculate the normalised concentration at time $t+\Delta t$., as the equation is solved in a single calculation. It is also possible to use implicit methods, where the time at which the differential equations are solved, is changed. Implicit methods are applied to the simulations of electrochemical measurements due to their enhanced stability compared to explicit methods. There are two commonly used implicit techniques; the Crank-Nicolson (CN) and the Backward Implicit (BI) approaches [22, 23]. BI method was used in this thesis and has been described in the following section.

2.7.2 Backward Implicit Method

Backward implicit method provides a stable solution to numerical simulations for electrochemical systems involving large changes such as at the electrode during potential step experiment. In using other numerical methods such as Crank Nicholson, such changes often produce large errors oscillating about zero. In channels with a large aspect ratio (height: width), it can be assumed that the velocity profile is constant across the width of the microchannel; and velocity in the x direction as a function of the cell height, u, is given by [24]:

$$u = u_0\left(\frac{1 - y'^2}{h^2}\right) \tag{2.10}$$

Where u_0 is the central velocity, h the half height of the channel and $y' = h - y$.

In this thesis, some of the rectangular ducts (microchannel) used also had low aspect ratios. For low aspect ratio microchannels, the velocity profile across the width of the channel is non-uniform and

hence must be accounted for. Under conditions of laminar flow, the three-dimensional solution velocity, u_x, can be predicted analytically, provided a sufficient lead-in length is present to enable the flow to become fully developed [25].

$$u_{i,j,k} = \frac{16\beta^2}{\pi^4} \sum_{l\,(odd)}^{\infty} \sum_{p\,(odd)}^{\infty} \frac{\sin\left(l\pi\frac{\xi}{d_d}\right)\sin\left(p\pi\frac{\eta}{h_2}\right)}{lp\left(\beta^2 l^2 + p^2\right)} \tag{2.11}$$

Where $u_{i,j,k}$ is the finite difference three-dimensional velocity term used in formulation, d_d is the channel width, h_2 is the channel height, β is the height: width ratio, ξ is the position along the z axis and η is the position along the y axis. The summation is performed using l = 1, 3, 5…. and p = 1, 3, 5 ….

Using the analytically predicted velocity profile, finite difference techniques can then be employed to solve the steady-state convection-diffusion equation in two-dimensions:

$$\frac{\partial a}{\partial t} = D\frac{\partial^2 a}{\partial y^2} - u\frac{\partial a}{\partial x} = 0 \tag{2.12}$$

The relevant boundary conditions for flow in a microfluidic device are shown in Table 2-5. A no flux boundary condition is applied at each wall of the microchannel to ensure no material is 'lost' at these solid-liquid interfaces.

$x > 0$	$y = 0$	$0 < z < d_d$	$\frac{\partial[A]}{\partial y} = 0$
$x > 0$	$y = h_2$	$0 < z < d_d$	$\frac{\partial[A]}{\partial y} = 0$
$x > 0$	$0 < y < h_2$	$z = 0$	$\frac{\partial[A]}{\partial z} = 0$
$x > 0$	$0 < y < h_2$	$z = d_d$	$\frac{\partial[A]}{\partial z} = 0$

Table 2-5 Boundary conditions applied for simulation of microchannel

Using the finite difference approach outlined in Section 2.7.1, the convection-diffusion equation becomes:

$$\frac{D_A}{(\Delta y)^2}\left(a_{i,j-i,k+1} - 2a_{i,j,k+1} + a_{i,j+i,k+1}\right) = \frac{u_{i,j,k}}{\Delta x}\left(a_{i,j,k+1} - a_{i,j,k}\right) \tag{2.13}$$

Equation 2.13 can be rearranged to express the equation in terms of the unknown:

$$a_{i,j,k} = -\lambda_{i,j,k} a_{i,j-1,k+1} + (2\lambda_{i,j,k} + 1)a_{i,j,k+1} - \lambda_{i,j,k} a_{i,j+1,k+1} \tag{2.14}$$

Where, $\lambda_{i,j,k} = \frac{D_A \Delta x}{u_{i,j,k} \Delta y^2}$. This can be solved simultaneously using Thomas algorithm (the Thomas algorithm is reported in more detail in the Appendix 1 (A.1.1) [26].

$$\begin{bmatrix} \lambda_{i,1,k} & 2\lambda_{i,1,k}+1 & \lambda_{i,1,k} & & \\ & \ddots & & & \\ & & \ddots & & \\ & & & & \\ & \lambda_{i,4,k} & 2\lambda_{i,4,k}+1 & \lambda_{i,4,k} & \end{bmatrix} \begin{bmatrix} a_{i,1,k+1} \\ a_{i,2,k+1} \\ a_{i,3,k+1} \\ a_{i,4,k+1} \end{bmatrix} = \begin{bmatrix} a_{i,1,k} \\ a_{i,2,k} \\ a_{i,3,k} \\ a_{i,4,k} \end{bmatrix} \tag{2.15}$$

The BI programme was written in f77 gcc version 3.3.3 and run on Linux Fedora Core 2.6. Typical run times for the simulations were 5 – 10 minutes.

2.8 SUMMARY

An overview of some of the microfabrication techniques currently used in industry was presented in this chapter. The microfabrication protocol used to fabricate microfluidic devices used in this thesis, was reported. A modification of the soft lithographic technique to fabricate PDMS gasket channel was also discussed. This approach allowed a higher degree of freedom in adapting and modifying the microreactor design, especially when integrating electrodes in certain orientations.

Numerical techniques used in this thesis were described in detail. Some of the numerical methods available for the simulation of diffusion and convection within microfluidic devices were reviewed. The theory underlying the backward implicit finite difference method developed for the purpose of this thesis was detailed.

The remainder of this thesis described the development of microfabricated devices for micro analytical applications including electrochemical detection of enzyme cofactors and affinity meso-chromatography.

2.9 REFERENCES

[1] Zaouk, R.; Park, B. Y.; Madou, M. J. *Introduction to Microfabrication Techniques In: Microfluidic Techniques: Reviews and Protocols* **2005**, Ed. Minteer, S. D., Humana Press Inc., New Jersey, pp. 5-15.

[2] Madou, M. J. *Fundamentals of Microfabrication: The Science of Miniaturisation* **2002,** CRC Press, Boca Raton, 2nd Edition.

[3] Van Steenwinckel, D. *J. Vac. Sci. Tech. B* **2006**, 24, 316.

[4] Vieu, C.; Carcenac, F.; Pepin, A.; Chen, Y.; Mejias, M.; Lebib, A.; Manin-Ferlazzo, L.; Couraud, L.; Launois, H. *Applied Surface Science* **2000**, 164, 111-117.

[5] Gomez-Morilla, I.; Abraham, M. H.; de Kerckhove, D. G.; Grime, G. W. *J. Micromech. Microeng.* **2005**, 15, 706-709.

[6] Paulus, A. *Proc.Micro. Tech.* **2000**, 2, 499.

[7] Sheeja, D.; Tay, B. K.; Yu, L. J.; Chua, D. H. C.; Milne, W. I.; Miao, J.; Fu, Y. Q. *Diamond and Related Materials* **2003**, 12, 1495.

[8] Dietrich, T. R.; Ehrfeld, W.; Lacher, M.; Krämer, M.; Speit, B. *Microelectronic Engineering* **1996**, 30, 497.

[9] Hamzah, A. A.; Majlis, B. Y.; Ahmad, I. *J. Electrochem. Soc.* **2006**, 16, 1143.

[10] Vaidya, R.; Tender, L. M.; Bradley, G.; O'Brien II, M. J.; Cone, M.; Lopez, G. P. *Biotechnol. Prog.* **1998**, 14, 371-377.

[11] Whitesides, G. M.; Ostuni, E.; Takayama, S.; Jiang, X.; Ingber, D. E. *Annu. Rev. Biomed. Eng*. **2001**, 3, 335-373.

[12] Arkles, B. C.; Larson, G. L. *Silicon Compounds: Silanes and Silicones* **2004**, Gelest, Inc., Morrisville, PA, pp. 560.

[13] Duffy, D. C.; McDonald, J. C.; Schueller, O. J. A.; Whitesides, G. M. *Anal. Chem.* **1998**, 70, 4974-4984.

[14] Eddings, M. A.; Gale, B. K. *J. Micromech. Microeng.* **2006**, 16, 2396.

[15] Morgan, C. J.; Vallance, R. R.; Marsh, E. R. *J. Micromech. Microeng.* **2004**, 14, 1687.

[16] Rill, M. S.; Plet, C.; Thiel, M.; Staude, I.; Von Freymann, G.; Linden, S.; Wegener, M. *Nature Materials* **2008**, 7, 543-546.

[17] Padeste, C. *http://lmn.web.psi.ch/mntech/ebeam.htm?forprint.*

[18] Yang, C.; Li, D. Q. *J. Colloid Interface Sci.* **1997**, 194, 95-107.

[19] Mengeaud, V.; Josserand, J.; Girault, H. H. *Anal. Chem.* **2002**, 74, 4279-4286.

[20] Randles, J. E. B. *Trans. Faraday Soc.* **1948**, 44, 327-338.

[21] Feldberg, S. W.; Auerbach, C. *Anal. Chem.* **1964**, 36, 505-509.

[22] Crank, J.; Nicolson, P. *Proc. Cambridge Phil. Soc.* **1947**, 43, 50-67.

[23] Laasonen, P. *Acta Math.* **1949**, 81, 309-317.

[24] Levich, V. G. *Physicochemical Hydrodynamics* **1962**, Prentice-Hall: New Jersey.

[25] Spiga, M.; Morini, G. *International Communications in Heat and Mass Transfer* **1994**, 21, 469-475.

[26] Lapidus, L.; Pinder, G. F. *Numerical Solution of Partial Differential Equations in Science and Engineering* **1982**, Wiley, New York.

Chapter 3

Development of Electrochemical Micro-Biosensor to Study Cofactors

3.1 INTRODUCTION

This chapter describes the development and fabrication of electrochemical micro-biosensors (EMB) for continuous detection of electroactive cofactors of industrial significance, at micro-scale. Electrochemical biosensors have found potential applications in fields ranging from drug discovery to continuous reagent monitoring, in a chemical process [1-3]. One of the most widely studied applications of electrochemical biosensor is the continuous glucose monitoring, with the help of electrochemical cofactor detection, in pharmaceutical industry [4]. Combining biosensing with microfluidics renders handling of electrochemical cofactors at volumes as low as few pico-litres and at same time high conversions (>95%) can be achieved [5, 6]. The following sections investigate the sensitivity of cofactors towards a variety of electrode materials and concentration profiles inside EMB, using electrochemical techniques and numerical simulations.

3.1.1 Cofactor Biosensor

Accurate detection, quick analysis and achieving high selectivity as well as conversions are of prime importance in fine chemical industries [7]. Fine chemical industries are continuously designing biosensors that could detect the smallest amount of impurities or could accurately determine the slightest change in conversions and selectivities during upstream and downstream processing. A biosensor is an analytical device which converts a biological response into an electrical signal [8]. It could be based on electrochemical, photometric or even piezoelectric sensing [9, 10]. The electrochemical detection technique in particular, offers the precise measurement of electroactive species at a concentration as low as pico-moles. The current corresponding to the amount of electroactive species, reduced or oxidised, can be measured and used to calculate reaction conversions as well as product concentration [11]. Oxido-reductive cofactors are commonly used electroactive species in electrochemical detection, due to their ability to transfer electrons.

Cofactors are non-protein chemical compounds that are bound (either tightly or loosely) to an enzyme and are required during biocatalysis [12]. They can be considered as "helper molecules/ions" that assist in biochemical transformations. Since some of the cofactors can be reduced or oxidised, they can be used for shuttling electrons between the transducer and the enzyme [13]. For example, oxido-reductases are enzymes that catalyse the asymmetric reduction of carbonyl groups to alcohols and amines or promote the oxygenation of C-H bonds, in the presence of cofactors such as nicotinamide adenine dinucleotide (NAD^+) that act as mediators [14]. During the catalysis, NAD^+ gets reduced to NADH, which can be oxidised back using a transducer (*e.g.* an electrode). A schematic of this reaction is shown in Figure 3-1. Cofactors can be divided into two broad groups: coenzymes and prosthetic groups. Coenzymes are small organic non-protein molecules that carry chemical groups between enzymes. These molecules are not bound tightly by

enzymes and are released as a normal part of the catalytic cycle. In contrast, prosthetic groups form a permanent part of the protein structure [12].

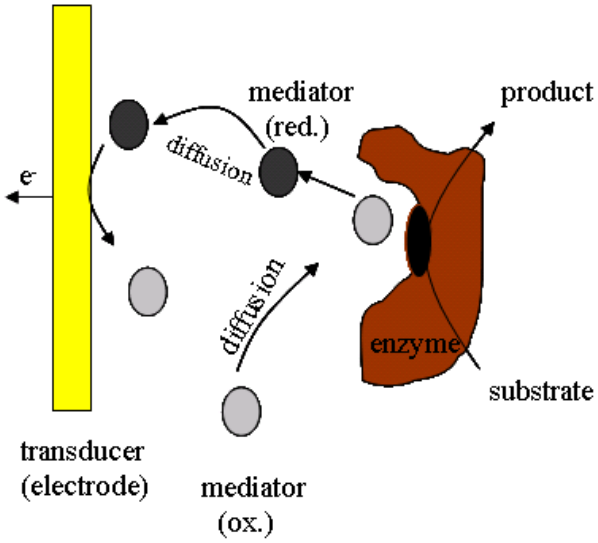

Figure 3-1 Schematic of electron transfer between an electrode and a cofactor in a biocatalytic reaction

The ability of all these cofactors to help transfer electrons in a biochemical reaction has been exploited in biosensing applications. Today cofactor based biosensors are regularly used in glucose monitoring, biocatalytic conversions, cofactor regeneration, studying whole cell metabolism, ligand binding and the antibody-antigen reaction [15-19]. Some of these applications have been explained in detail below.

3.1.2 Applications of Cofactor Biosensor

1.) *Glucose Monitoring*: Glucose monitoring is important in medicine as a clinical indicator of diabetes [20]. An electrochemical blood glucose biosensor uses the enzyme glucose oxidase to break blood glucose down [21]. In order to work as a catalyst, glucose oxidase requires a cofactor (prosthetic group), flavin adenine dinucleotide (FAD). The enzyme first oxidises glucose and uses two electrons to reduce the cofactor FAD (a component of the enzyme) to its reduced form $FADH_2$. This in turn is oxidised at the electrode (donating two electrons to the electrode), as illustrated in Figure 3-2. The resulting current is a measure of the concentration of glucose [21].

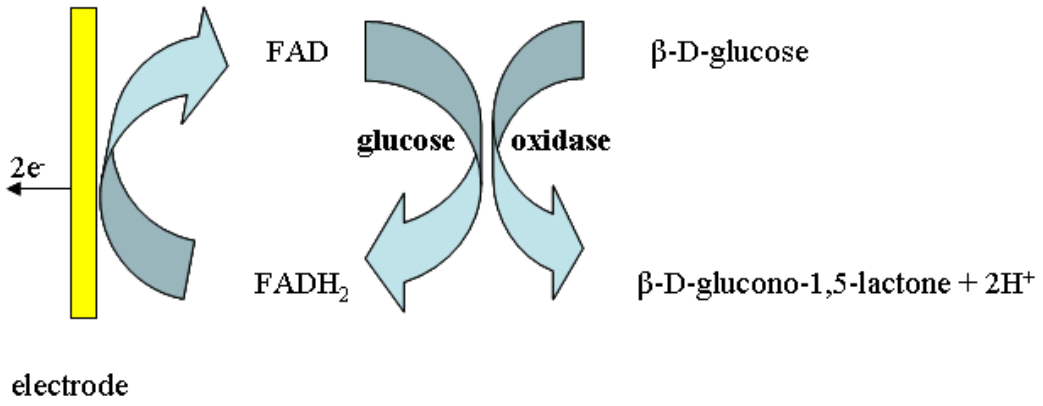

Figure 3-2 Illustration of continuous glucose detection using cofactor FAD

2.) *Biocatalysis*: In certain biocatalytic reactions, a biosensor can be used to measure the amount of conversions and simultaneously regenerate the cofactors that drive these reactions. For example, the stereo-selective enzymatic transformations of pyruvate to L-lactate takes place in the presence of cofactor NADH and enzyme lactate dehydrogenase (LDH), as seen in Figure 3-3 [22]. L-lactate, amongst the isomers of lactate, is important in pharmaceutical industries for production of ringers solution (an aqueous solution containing the chlorides of sodium, potassium and calcium used in physiological experiments or to correct dehydration) and also in polymers industries for manufacturing polylactide (PLA), which is a biodegradable polymer [23]. Pyruvate to L-lactate reaction, however, requires NADH in stoichiometric amounts; making the whole process economically unfeasible. NADH can be regenerated continuously from its reduced form NAD^+, over the electrode. But due to slow electron transfer between NAD^+ and electrode, even at a potential where the reduction of NAD^+ into NADH is thermodynamically favourable, it is avoided [24]. Bergel *et al.* have demonstrated the use of another cofactor FAD that can shuttle electrons between electrode and enzyme flavin dehydrogenase (FDH), following Michaelis-Menten kinetics (see Figure 3-3) more quickly [25]. By doing so, the biosensor was used not just to detect the amount of substrate conversion but also to perform continuous regeneration of cofactor NADH.

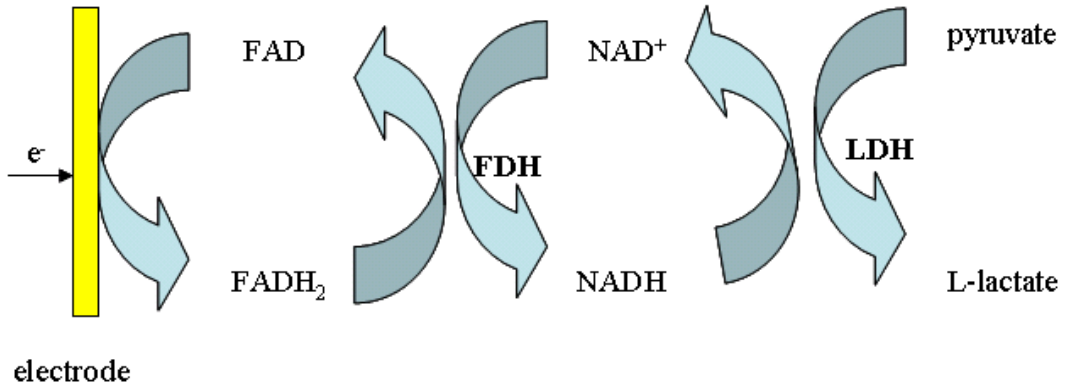

Figure 3-3 Biocatalytic conversion of pyruvate to L-lactate with a continuous NADH regeneration using FAD as the mediator

However there are three main limitations that affect the performance of electrochemical biosensors based on cofactors. They have been explained in detail below.

i) *Diffusion Limitation*: The amount of reagent that can be addressed at the electrode, at any given time, is controlled by diffusion. Due to electrochemical reaction, diffusion layer is formed over the electrode surface and the concentration gradient can be calculated using Fick's Law [26]. In a lab-scale batch reactor, this could affect the overall substrate conversion. For example, in the cofactor regeneration application described above, $FADH_2$ is electrochemically regenerated at the electrode, hence forming a concentration gradient over the electrode surface as illustrated in Figure 3-4. This affects the amount of $FADH_2$ available in the bulk phase to drive the NADH regeneration reaction. Low concentrations of $FADH_2$ in bulk phase drive the equally favourable reversible reaction between NADH and FAD reaction, hence consuming NADH [3]. This contributes to low conversion of pyruvate to L-lactate.

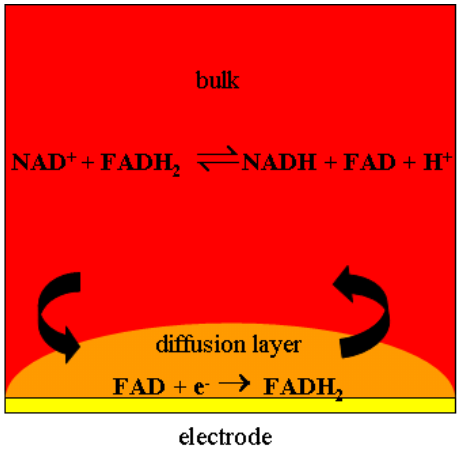

Figure 3-4 Schematic of diffusion layer formation over the electrode surface due electrochemical reduction of cofactor FAD

To overcome this problem, Bergel *et al*. regenerated NADH at a smaller scale, at an initial rate of 12 μM min^{-1}, in a non flowing thin layer electrochemical cell. However, most of industrial scale regeneration processes need a continuous flow system for higher turnovers [27].

Miniaturisation could be a feasible alternative in terms of performing cofactor regeneration in a continuous flow system. It is also a very lucrative option for fine chemical industries (in process development) as less quantity (pico-litres) of reagents is required and less wastage makes it environmentally friendly. Microreactors are extremely efficient and have the advantage of easier scale-up of production capacity by parallelisation, as described in detail in Chapter 1 [28]. Yoon *et al.* have reported the conversion of pyruvate to L-lactate inside a rectangular duct and have reported the *in situ* regeneration of NADH from NAD^+ electrochemically, over the electrode [3]. Due to shorter mixing lengths, the diffusion of reagents over the electrode is quick. The absence of a bulk phase in the microreactor prevents the undesired reverse reaction (NADH oxidation due to FAD) from occurring, while its continuous flow characteristics allow for high throughput operation.

ii) *Electrode Deactivation*: Even after using microreactors, the conversions for biocatalytic reactions, such as pyruvate to L-lactate, were still quite low (around 50%) [3, 29]. Deactivation of

electrode surface contributes to low conversions, by blocking the electroactive species from reaching the electrode surface. Gold electrodes, used by Yoon *et al.*, are easily deactivated by biological reagents due to adsorption of biological reagents on them [3]. This affects the current response from these electrodes, making them less reliable. Glassy carbon electrode and boron doped diamond electrode have been shown to give good response to biological reagents [30]. Polycrystalline diamond electrodes are highly doped with boron, in order to act as metallic conductors. They display a much wider potential window compared to gold and platinum electrodes. Boron doped diamond electrodes also provide other advantages for electrochemical studies including low capacitance, extreme electrochemical stability, high resistance to deactivation via fouling and insensitivity to dissolved oxygen [31, 32].

iii) ***Interference Effect***: Finally, electrochemical response of one cofactor could also affect the response of another electroactive species in the system, hence contributing to error in calculating total current and the conversions. For example, the interference of ascorbic acid is a major problem during the electrochemical determination of certain biological species such as dopamine and NADH. One electroactive component could suppress or enhance the electrochemical response of other electroactive reagent, if their redox potentials are very close. Rao *et al.* have reported that by taking an equimolar mixture of both ascorbic acid and NADH, the interference due to ascorbic acid could be corrected [33].

Although the development and application of microreactor as an electrochemical micro-biosensor has expanded rapidly over recent years, the qualitative and quantitative current/voltage relationships with flow rate still remains less well explored. The aim of this chapter was to develop and fabricate an electrochemical micro-biosensor and study two parameters that affect its performance: sensitivity of electrode material and diffusion. Electrochemical techniques (cyclic voltammetry (CV) and linear sweep voltammetry (LSV) - refer Section 1.5.5) were used to study the current

response for four industrially significant cofactors (FMN, FAD, Vitamin B_{12}, NADH) over platinum, gold, glassy carbon and boron doped diamond electrodes, in batch and flow systems [26, 34]. Computer-aided designs, developed using numerical models, enabled studying the concentration gradient and flow profile inside microchannel and understand diffusion layer formation as well as reagent transfer over the electrode [17]. Numerical models were also used to compare the simulated results with experimental data.

3.2 COFACTOR ELECTROCHEMISTRY - THEORY

Cofactors can undergo single or multiple electron transfer oxidation-reduction reactions. In order to analyse their electrochemical response, it is essential to understand the electrochemistry of each cofactor. Electrochemistry of four cofactors, FMN, FAD, Vitamin B_{12} and NADH, has been described in brief below.

3.2.1 Flavin Adenine Dinucleotide

Flavin adenine dinucleotide (FAD) is a redox cofactor which is involved in several reactions in metabolism, such as oxidative phosphorylation in the mitochondria. It can exist in two different states and is required by many oxido-reductases (*e.g.* flavoproteins) as a prosthetic group for electron transfer. FAD has an isoalloxazine ring as a redox-active component. The reduction of FAD (oxidised quinine form) to $FADH_2$ (fully reduced hydroquinone form) (refer Figure 3-5) over an electrode is reversible, when a redox potential is applied [35]. At pH 7, intermediate semiquinone is also present.

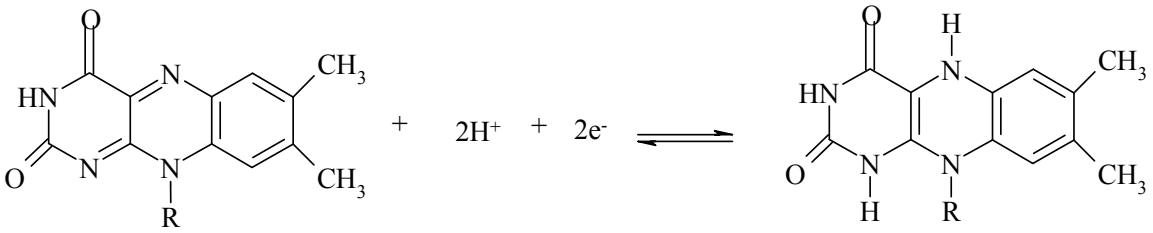

where,

$R = C_{15}H_{22}O_{13}N_5$

Figure 3-5 Schematic of FAD redox reaction

3.2.2 Flavin Mononucleotide

Flavin mononucleotide (FMN) is produced from riboflavin (Vitamin B_2) and also functions as a prosthetic group for various oxido-reductases, such as NADH dehydrogenase. It has an important role as mediator in the electron transport chain. It undergoes a two-electron reduction to $FMNH_2$ in two steps. It is first reduced to semiquinone ($FMNH^{\bullet}$), which is further reduced to $FMNH_2$. Figure 3-6 below depicts the FMN reversible reduction chemistry over an electrode [36].

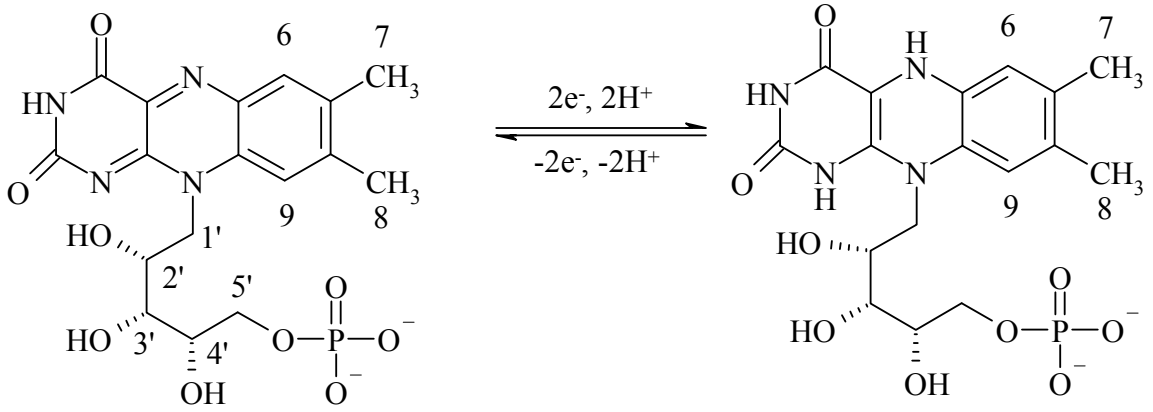

oxidised FMN reduced FMN

Figure 3-6 Schematic of FMN redox reaction

3.2.3 Vitamin B_{12}

Vitamin B_{12} is a water soluble vitamin, with a rich redox chemistry centered on a Cobalt ion (refer Figure 3-7). It is used for Vitamin B_{12} deficiency and as a treatment for cyanide poisoning. Vitamin B_{12} can undergo a reduction reaction, where Aquocob(III)alamin (B_{12a}) (Figure 3-7) can be reduced to Cob(II)alamin (B_{12r}) and Cob(I)alamin (B_{12s}). In aqueous media, the Co(II) and Co(I) complexes can exist in "base-on" or "base-off" forms, the latter having protonated benzimidazole side chains. Electron transfer from an electrode is significantly faster for the base-off form of Cob(II)alamin below pH 2.9. At pH greater than 5, electron transfer from electrode is higher for base-on form [37].

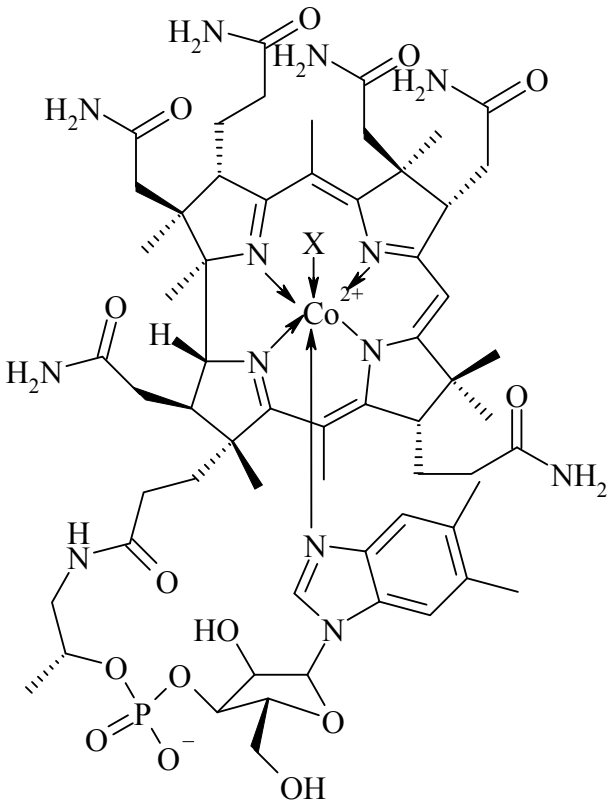

Figure 3-7 Structure of Aquo(III)cobalamin where X:H_2O

3.2.4 Nicotinamide Adenine Dinucleotide

Nicotinamide adenine dinucleotide (NADH) is the reduced form of NAD^+. NAD^+ is a coenzyme found in all living cells and helps in electron transfer during metabolism. The compound is a dinucleotide, since it consists of two nucleotides joined through their phosphate groups; with one nucleotide containing an adenine base, and the other containing nicotinamide. NADH is a reducing agent and can readily donate electrons to get oxidised to NAD^+. Figure 3-8 illustrates the two-electron oxidation of NADH at electron surface [38].

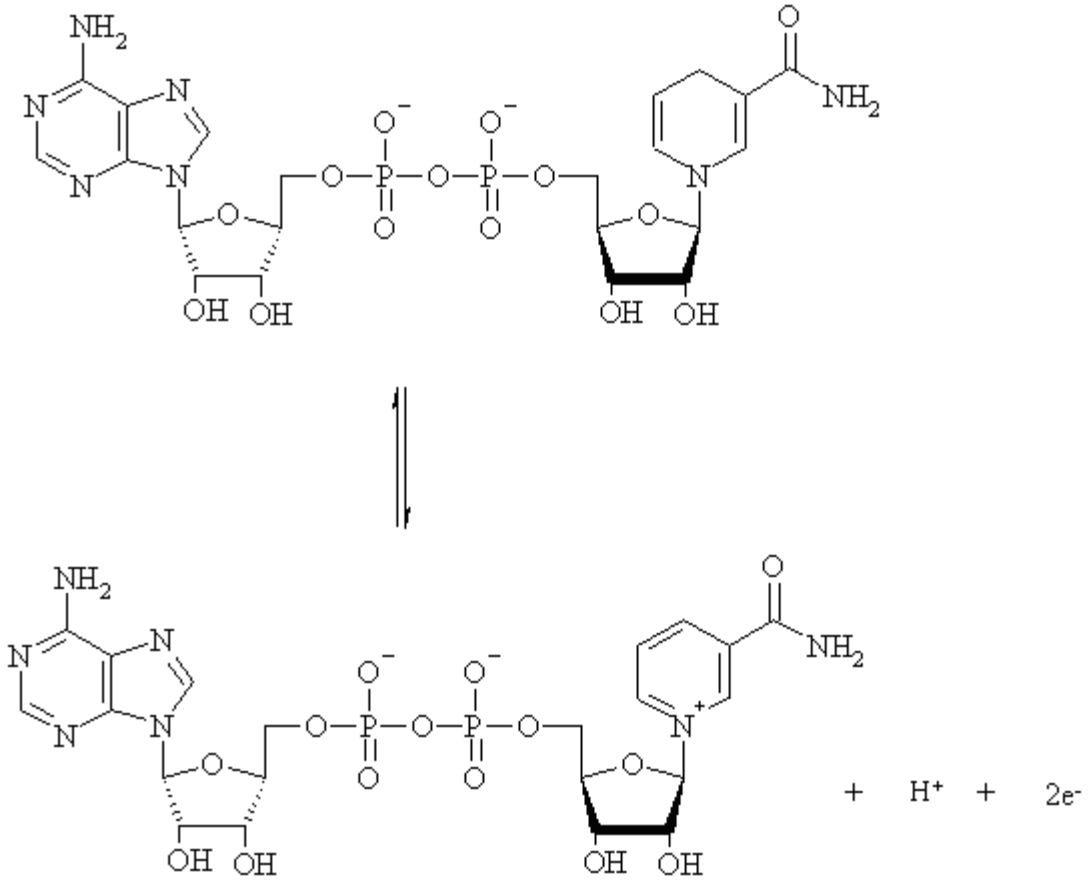

Figure 3-8 Schematic of NADH redox reaction

3.3 NUMERICAL SIMULATIONS

Numerical simulations were carried out to predict the current response in hydrodynamic microreactor and to study the concentration and flow profile over a centrally sited electrode in the bottom wall of a microchannel. To do this, backward implicit finite difference method (BI-FDM) was employed. The theory of the BI method is described in Section 2.7. In brief, it is a two-dimensional, steady state solution to the convection-diffusion equation, where the diffusion in the *z* direction (lateral diffusion) is omitted. Due to the steady state nature of the simulation, the BI method used is not iterative and consequently far more computationally efficient [39]. A schematic of the two-dimensional mesh adopted to simulate the coupled mass transfer and electrolysis reaction is shown in Figure 3-9. The simulation was conducted only over the electrode and not for the whole channel (whole channel simulations are used when working at extremely low flow rates or with reagents with very high diffusion coefficient value).

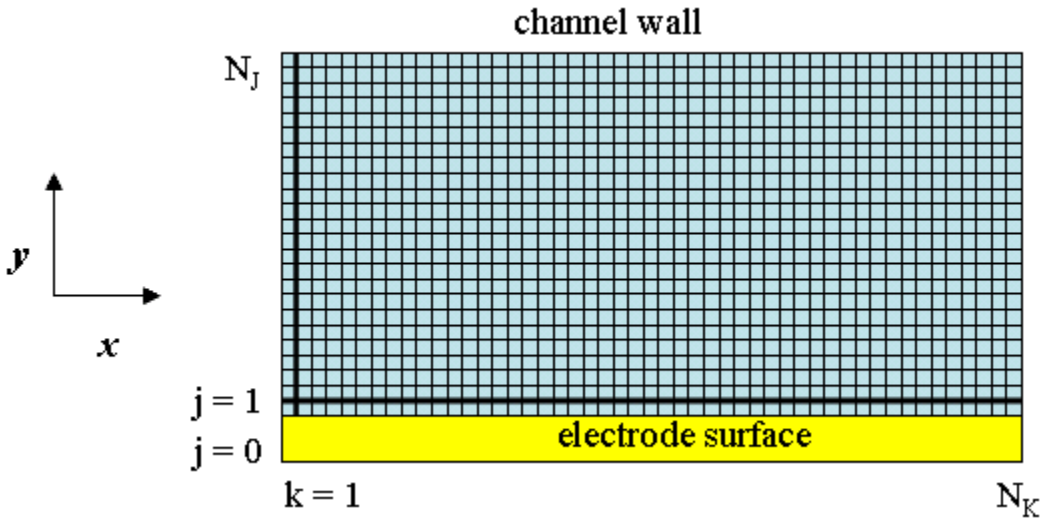

Figure 3-9 Schematic of two-dimensional grid employed for numerical simulations over the electrode surface

3.3.1 Boundary Conditions

Boundary conditions at the channel walls and for an electrolysis reaction occurring at the electrode surface, as defined in Figure 3-9, were appropriate for a potential step experiment (or linear sweep

voltammetry) at steady state. In the potential step experiment, the potential was stepped from initial value where there is zero electron transfer, to a second value where there is complete depletion of species *A* ($A + e^- \rightarrow B$) at the electrode surface, as seen in the Table 3-1. It was assumed that sufficient electrolyte was present in solution to neglect transport effects induced by migration and that the diffusion coefficients of species *A* and *B* are matched.

t = steady state

$0 < x < N_K$	$y = 0$	$[A] = 0$
$x < 0$	$y = 0$	$\frac{\partial [A]}{\partial y} = 0$
$x > N_K$	$y = 0$	$\frac{\partial [A]}{\partial y} = 0$
all x	$y = h_2$	$\frac{\partial [A]}{\partial y} = 0$
$x = 0$	$0 < y < h_2$	$[A] = 1$
$x = N_K$	$0 < y < h_2$	$\frac{\partial [A]}{\partial y} = 0$
$0 < x < N_K$	$y = 0$	$^t i = F x_e w_e D \left(\frac{\partial [A]}{\partial y} \right)_{y=0}$

Table 3-1 Boundary conditions for electrochemical simulations

Where start and end of the electrode corresponds to 0 and N_K, in the *x* direction (see Figure 3-9). The current measure by electrode was calculated using the following equation:

$$i = F D_A w_e [A]_{bulk} \frac{\Delta x}{\Delta y} \sum_{k=0}^{k=N_K} ({}^t a_{1,k} - {}^t a_{0,k}) \qquad (3.1)$$

As the height to width ratio of channel used to study cofactor was sufficiently large, the velocity profile was assumed to be constant across the width of microchannel and velocity (u) in x direction as a function of the cell height is given by

$$u = u_o\left(\frac{1-y'^2}{h^2}\right) \tag{3.2}$$

Where u_o is the central velocity and h half the cell height and $y'=h - y$.

3.4 EXPERIMENTAL

3.4.1 Sample Preparation for Stagnant System Studies

Cofactors FAD, FMN and Vitamin B_{12} were studied in stagnant system. Solutions of concentrations 1 x 10^{-6} mol cm^{-3}, 0.8 x 10^{-6} mol cm^{-3}, 0.6 x 10^{-6} mol cm^{-3} and 0.4 x 10^{-6} mol cm^{-3} (1M = 10^{-3} mol cm^{-3}) were prepared for each of the four cofactors (FAD, FMN and Vitamin B_{12}) in a pH 7.4 phosphate buffer solution (phosphate buffered saline giving concentrations of 0.1 x 10^{-3} mol cm^{-3} phosphate, 0.0027 x 10^{-3} mol cm^{-3} potassium chloride and 0.137 x 10^{-3} mol cm^{-3} sodium chloride). The solution was deoxygenated with nitrogen prior to use, to remove dissolved oxygen.

3.4.2 Sample Preparation for Hydrodynamic System Studies

The analyte solutions considered for hydrodynamic system studies were 1.17 x 10^{-6} mol cm^{-3} potassium ferrocyanide ($K_4Fe(CN)_6$), 0.9 x 10^{-6} mol cm^{-3} FMN and 60 x 10^{-9} mol cm^{-3} NADH. Low concentration of NADH was selected to test the sensitivity of the electrochemical microreactor for low amounts of reagents. The background electrolyte used in the experiments was 0.1 x 10^{-3} mol cm^{-3} potassium chloride (KCl) for potassium ferrocyanide system and phosphate buffered solution for FMN and NADH, to minimise the migration effects. The sample was then deoxygenated using nitrogen.

3.4.3 Electrode Configuration for Cyclic Voltammetry Analysis

A three electrode configuration was also used for stagnant system cyclic voltammetric analysis, with reference electrode as silver/silver chloride (Ag/AgCl), counter electrode as platinum mesh and working electrodes as gold (diameter = 0.05 cm), platinum (diameter = 0.02 cm), boron doped diamond (0.5 cm x 0.2 cm) and glassy carbon (diameter = 0.295 cm) electrode respectively.

Gold and platinum electrodes were used during the stagnant system studies, as their electrochemical response for biological systems is widely reported and is well understood [3, 25]. On the other hand, glassy carbon and boron doped diamond electrodes were selected for their high resistance to fouling due to biological reagents, and they also offer a wider potential window [30]

3.4.4 Electrode Configuration for Linear Sweep Voltammetry Analysis

Linear sweep voltammetric studies of cofactors were conducted in an EMB constructed using microfabrication techniques. The microfabrication procedure consisted of two stages:

(i) Fabrication of gold pseudo-reference and counter electrodes of length (x_e) 500 µm and 1 cm respectively, on the glass wafer.
(ii) Fabrication of a poly(dimethylsiloxane) (PDMS) microchannel gasket of height (h_2): 250 µm, width (d_d): 500 µm and length (x_l): 3 cm, with single inlet and outlet.

The fabrication procedure for electrodes and channels is detailed in Section 2.3. A boron doped diamond (1.1 cm x 1.1 cm) was used as a working electrode. It was placed inside a Perspex block and sealed using an epoxy resin. The electrical connections to the electrode were made using a silver epoxy resin. The working and reference electrodes were at a distance of 1 cm from the inlet. An extra external platinum counter electrode was also provided downstream. The EMB was assembled by sandwiching the PDMS microchannel between the glass wafer containing a gold

pseudo-reference and a counter electrode and the perspex with an embedded boron doped diamond electrode (BDDE) (see Figure 3-10). This way, the PDMS microchannel defined the channel sidewalls.

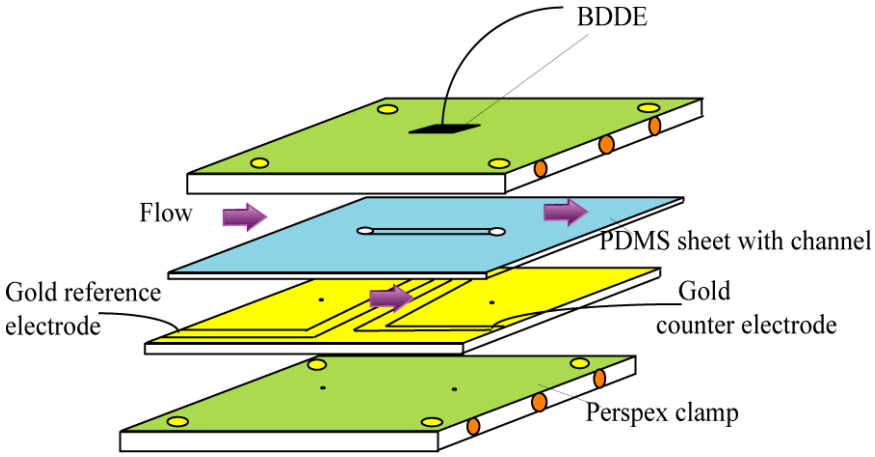

Figure 3-10 Schematic of an electrochemical micro-biosensor

The electrodes and channel were aligned before placing them between the perspex clamp. Because a perspex clamp was used in this case, only aqueous systems were studied, as perspex is not suitable for organic solvent. Prior to the experiments, boron doped diamond electrode was cleaned thoroughly with ethanol and treated with phytic acid to improve its conductivity [40]

Voltammetric measurements were carried out using a computer controlled potentiostat. The fluid flow was controlled using two syringe pumps, with a typical flow rates between 1 x 10^{-4} cm^3 s^{-1} and 0.4 cm^3 s^{-1}.

3.5 RESULTS AND DISCUSSION

The objective of this work was to study different enzyme cofactors and to develop and fabricate a highly sensitive EMB that could potentially be used in detecting biochemical reagents for high turnover applications. Electrochemical characterisation of four enzyme cofactors (FAD, FMN, Vitamin B_{12}) was carried out in stagnant system using cyclic voltammetry. Response of all four cofactors was studied over platinum electrode (PE), gold electrode (GE), glassy carbon electrode

(GCE) and boron doped diamond electrode (BDDE). The results from stagnant system were used to develop a hydrodynamic system: an EMB with BDDE as the working electrode. Linear sweep voltammetry was performed in EMB and variation of limiting current versus total volume flow rate was investigated using three electrochemical systems (potassium ferrocyanide, FMN and NADH). Numerical simulations were performed to study the concentration profiles and compare numerical results with experimental data.

3.5.1 Cyclic Voltammetry in Stagnant System

3.5.1.1 Effect of Scan Rate

Using a three electrode configuration, cyclic voltammetry (CV) was performed at six different scan rates (0.02, 0.05, 0.1, 0.2, 0.3 and 0.4 V s^{-1}). Described below are cyclic voltammograms obtained for FAD, FMN and Vitamin B_{12}.

1.) *Response for FAD*

Cyclic voltammetry was performed by scanning voltage from -0.8 V to 0.6 V at a variety of scan rates mentioned above. The sample voltammograms obtained for 0.6 x 10^{-6} mol cm^3 FAD solution over BDDE, GCE, GE and PE respectively can be seen in Figure 3-11. The voltammograms clearly depict sharp two-electron oxidation and reduction peaks for FAD at -0.25 V and -0.6 V respectively. As is evident from the CVs, the peak current was seen to increase with scan rate (SR). At higher voltage scan rates, a higher flux of the fresh reactant is obtained at the electrode surface, thus resulting in a higher peak current. This behaviour suggests a diffusion controlled redox process [41].

It was noted that the voltammograms obtained using BDDE and GCE as working electrodes were well defined and reproducible. There was a slight variation in difference in peak potentials (ΔE_p) with increasing scan rate, indicating slow electron transfer kinetics and also the onset of kinetic

irreversibility. These are characteristics of an electrochemical quasi-reversible system, as discussed in Section 1.5.5.

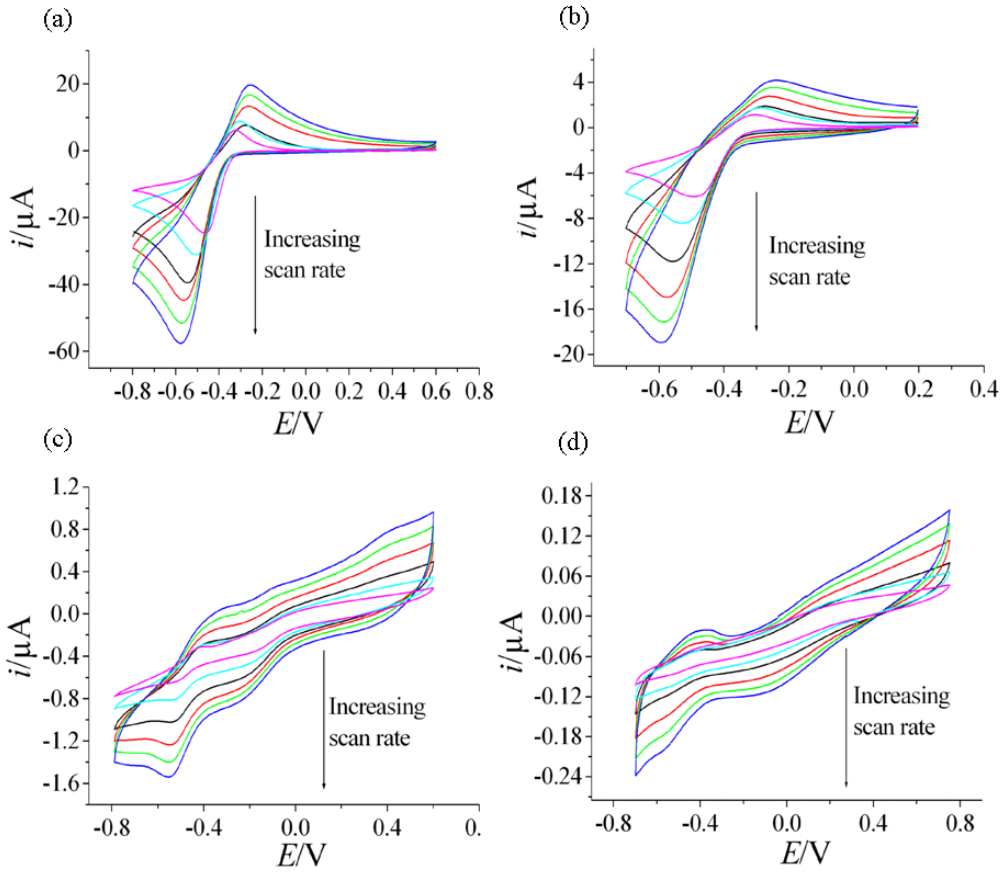

Figure 3-11 Sample cyclic voltammograms of 0.6 x 10^{-6} mol cm^{-3} FAD solution in 0.1 x 10^{-3} mol cm^{-3} phosphate buffer at scan rates (v) of 0.02, 0.05, 0.1, 0.2, 0.3 and 0.4 V s^{-1} over (a) BDDE, (b) GCE, (c) GE and (d) PE

PE and GE however, exhibited very poor reproducibility. The oxidation and reduction peaks were found to be broader and new peaks were observed at approximately -0.2 V. The new peaks were due to the reorientation of the adsorbed isoalloxazine and adenine groups in FAD molecule at negative potential, as explained by Birss *et al.* [42].

Adsorption of cofactor affects the kinetics of cofactor reaction at electrode, hence causing peak broadening. It also leads to increase in current response after first scan, due to reaction of both adsorbed species and the FAD molecules diffusing to the electrode surface from the solution [42].

This was seen to be avoided to a great extent for both BDDE and GCE, proving their resistance to cofactor adsorption.

A linear relationship between the peak current and the square root of scan rate, as defined by Randles-Sevcik equation, was observed for each of the four electrodes [43]. A sample Randles-Sevcik plot (peak current versus square root of scan rate) over BDDE is given in Figure 3-12. Refer Appendix 2 (A.2.1) for Randles-Sevcik plots for GCE, GE and PE. Using this correlation, the diffusion coefficient for 0.6 x 10^{-6} mol cm^{-3} FAD solution in 0.1 x 10^{-3} mol cm^{-3} phosphate buffer was calculated to be 6.05 x 10^{-6} cm^2 s^{-1}, which is similar to values reported in the literature [44].

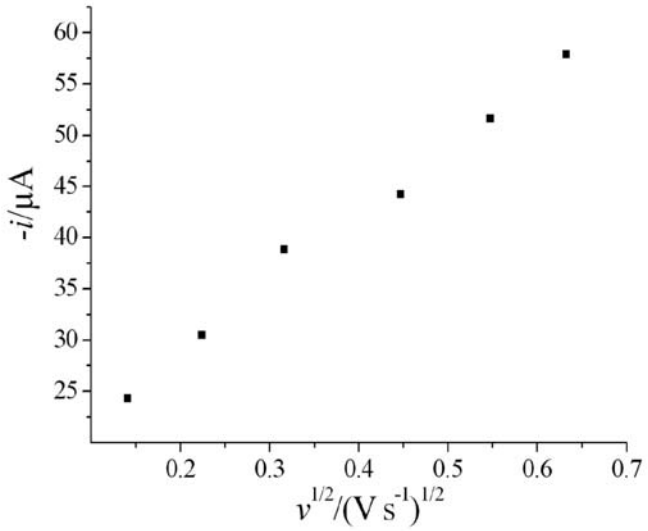

Figure 3-12 Randles-Sevcik plot of 0.6 x 10^{-6} mol cm^{-3} FAD solution in 0.1 x 10^{-3} mol cm^{-3} phosphate buffer over BDDE

2.) *Response for FMN*

FMN, like FAD, also undergoes a two-electron oxidation-reduction reaction thereby giving a similar voltammetric response with GE, PE, BDDE and GCE. A sample CV obtained over BDDE for FMN with a concentration of 0.6 x 10^{-6} mol cm^{-3} in 0.1 x 10^{-3} mol cm^{-3} phosphate buffer is shown in Figure 3-13a. The rest of the plots are reported in Appendix 2 (A.2.1). The trends observed for all four electrodes were quasi-reversible. In the case of GE and PE, the CV were not

reproducible and new peaks were observed, which can be explained due to the reorientation of isoalloxazine group of the adsorbed FMN monolayer. These peaks were absent in BDDE and GCE, suggesting the absence of adsorbed FMN.

Figure 3-13b depicts the variation of peak current with square root of scan rate for BDDE and was found to be linear, as given by the Randles-Sevcik correlation. This indicated diffusion controlled reaction system [45, 46]. The diffusion coefficient for FMN, calculated from the slope of this plot, was 1.38 x 10^{-5} cm^2 s^{-1}.

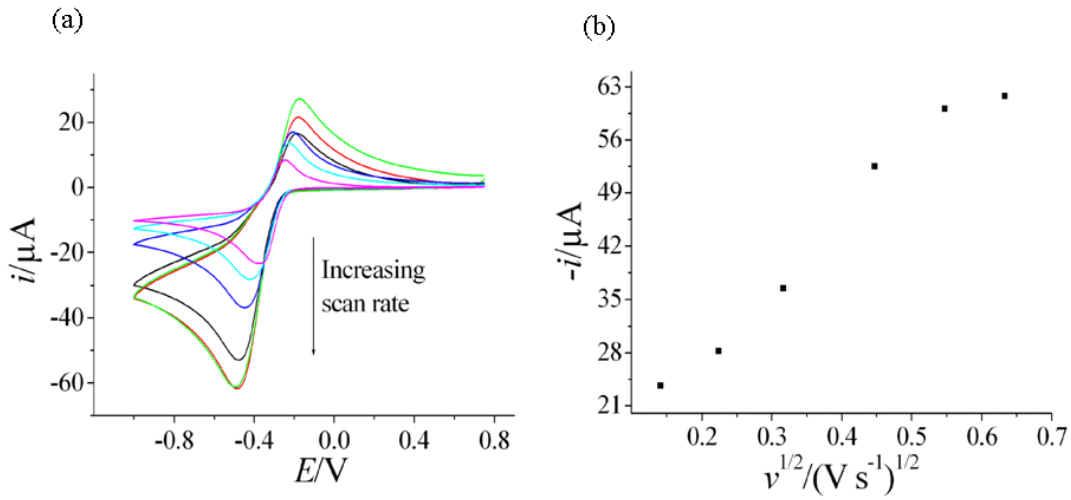

Figure 3-13 (a) Sample cyclic voltammograms of 0.6 x 10^{-6} mol cm^{-3} FMN solution in 0.1 x 10^{-3} mol cm^{-3} phosphate buffer and (b) corresponding Randles-Sevcik plot over BDDE at scan rates (v) of 0.02, 0.05, 0.1, 0.2, 0.3 and 0.4 V s^{-1}

3.) *Response for Vitamin B_{12}*

Vitamin B_{12} exhibited a reproducible voltammetric response when using BDDE and GCE as working electrodes. The voltammetric response obtained was an indication of an irreversible reaction, which was expected at pH values greater than 3, as reported by Lexa *et al.* [47]. At high pH Co(I) that is reduced at the electrode during reduction cycle reacts with Co(III) to recycle Co(II) back into the solution. In Figure 3-14, the slow base-on Cobalamine(III)/Cobalamine(II) reaction is suppressed by relatively fast base-on Cobalamine(II)/base-off Cob(I)alamine reaction (refer Section

3.2.3). The voltammograms obtained for PE and GE were not reproducible due to the adsorption of Vitamin B_{12} on the electrode surface. A sample voltammogram obtained for 0.8 x 10^{-6} mol cm^{-3} Vitamin B_{12} in 0.1 x 10^{-3} mol cm^{-3} phosphate buffer, at a variety of scan rates over BDDE is shown in Figure 3-14a below. CV for GCE, PE and GE are reported in Appendix 2 (A.2.1). Figure 3-14b shows linear variation of peak current with square root of scan rate (Randles-Sevcik plot). The diffusion coefficient for vitamin B_{12} calculated from the slope of this plot was 3.29 x 10^{-6} cm^2 s^{-1} and was found comparable to the value reported by Connor *et al.* for an aqueous system [35].

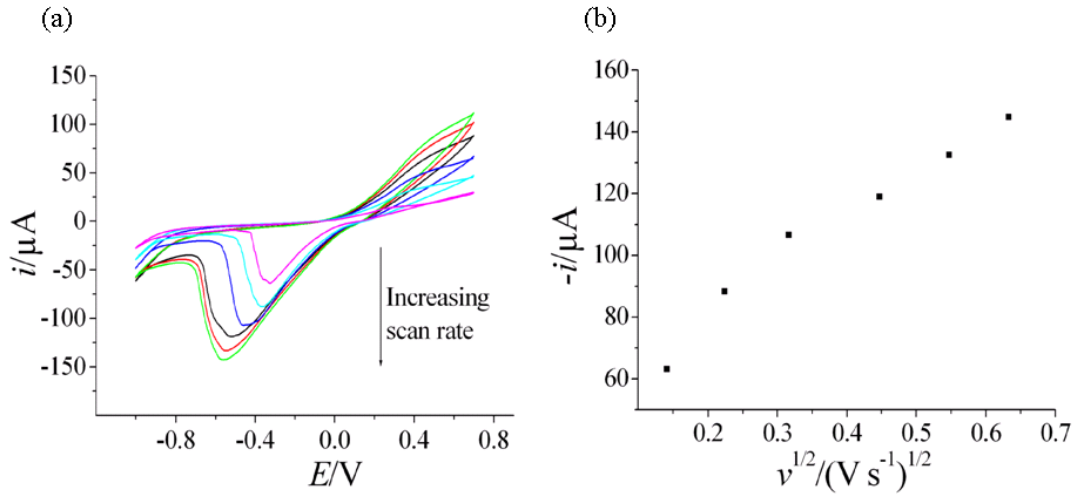

Figure 3-14 (a) Sample cyclic voltammograms of 0.6 x 10^{-6} mol cm^{-3} Vitamin B_{12} solution in 0.1 x 10^{-3} mol cm^{-3} phosphate buffer and (b) corresponding Randles-Sevcik plot over BDDE

3.5.1.2 Effect of Concentration

The effect of concentration on the peak current values was studied using BDDE, GCE, PE and GE as the working electrodes. The voltammetric responses of each of the cofactors, FMN, FAD and Vitamin B_{12}, for concentrations of 0.4 x 10^{-6} mol cm^{-3}, 0.6 x 10^{-6} mol cm^{-3}, 0.8 x 10^{-6} mol cm^{-3} and 1 x 10^{-6} mol cm^{-3} were obtained at a scan rate of 0.4 V s^{-1}. The peak current was found to vary proportionally with concentration for all four working electrodes, as expected (refer Appendix 2 (A.2.2). Figure 3-15 a-c illustrates the voltammograms obtained at various concentrations of FAD

over BDDE and a corresponding plot of peak current versus concentration. The plots for GCE, GE and PE are reported in Appendix 2 (A.2.2).

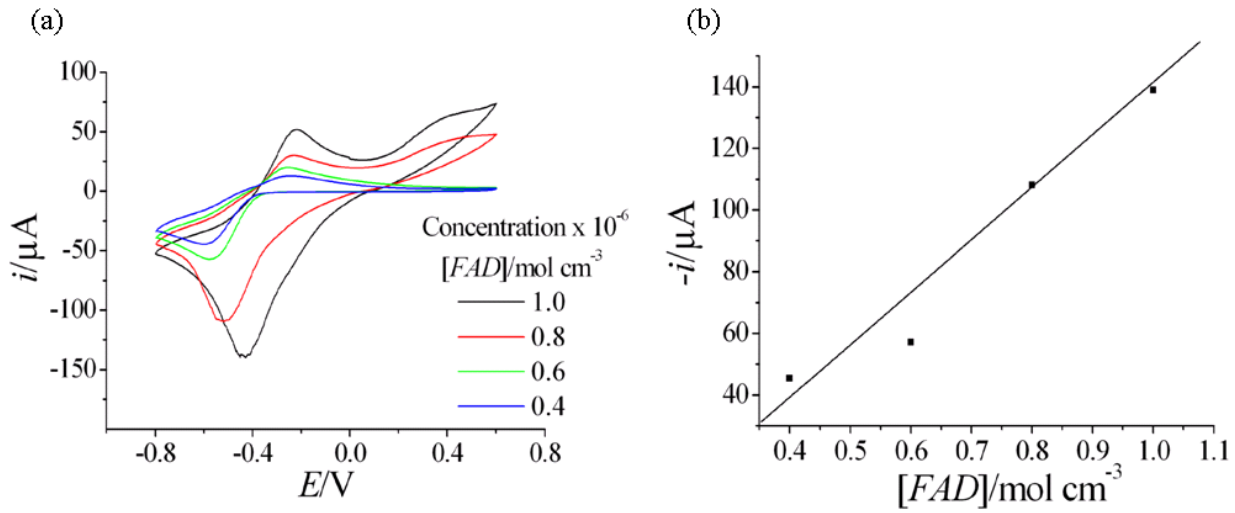

Figure 3-15 (a) Sample cyclic voltammograms of cofactor FAD over BDDE at a scan rate of 0.4 V s^{-1} and for concentrations of 0.4, 0.6, 0.8 and 1 x 10^{-6} mol cm^3 in 0.1 x 10^{-3} mol cm^{-3} phosphate buffer (b) Plot of variation of peak current versus FAD concentration

3.5.2 Linear Sweep Voltammetry in Hydrodynamic Systems

In the previous section, it was noted that BDDE is an ideal electrode material for the electrochemical investigation of cofactors. In the following section, an EMB fabricated with BDDE as working electrode, was electrochemically characterised using a well reported system of potassium ferrocyanide [48]. It was then used to study the electrochemical response of cofactors, FMN and NADH, at different flow rates using linear sweep voltammetry (LSV) at a scan rate of 0 1 V s^{-1}.

3.5.2.1 *Characterisation of EMB using Potassium Ferrocyanide*

The reaction for reversible one-electron oxidation of potassium ferrocyanide is given below:

$$Fe(CN)_6^{4-}(s) \underset{k_{red}}{\overset{k_{ox}}{\rightleftharpoons}} Fe(CN)_6^{3-}(s) + e^-(m) \qquad (3.3)$$

Linear sweep voltammograms obtained (ν = 0.1 V s^{-1}) for 1.17 x 10^{-6} mol cm^{-3} potassium ferrocyanide solution in 0.1 x 10^{-3} mol cm^{-3} KCl, at various flow rates, are illustrated in Figure 3-16a. A linear variation of limiting current versus cube root of flow rate was observed, thus demonstrating a Levich type behaviour (refer to Figure 3-16b) [49]. The experimental data was compared with analytically calculated current using Levich equation (refer Section 1.5.5) and a good agreement was observed between the two. The diffusion coefficient considered for calculating analytical value of limiting current was 6.5 x 10^{-6} cm^2 s^{-1} (see Appendix 2 (A.2.3) for diffusion coefficient calculations).

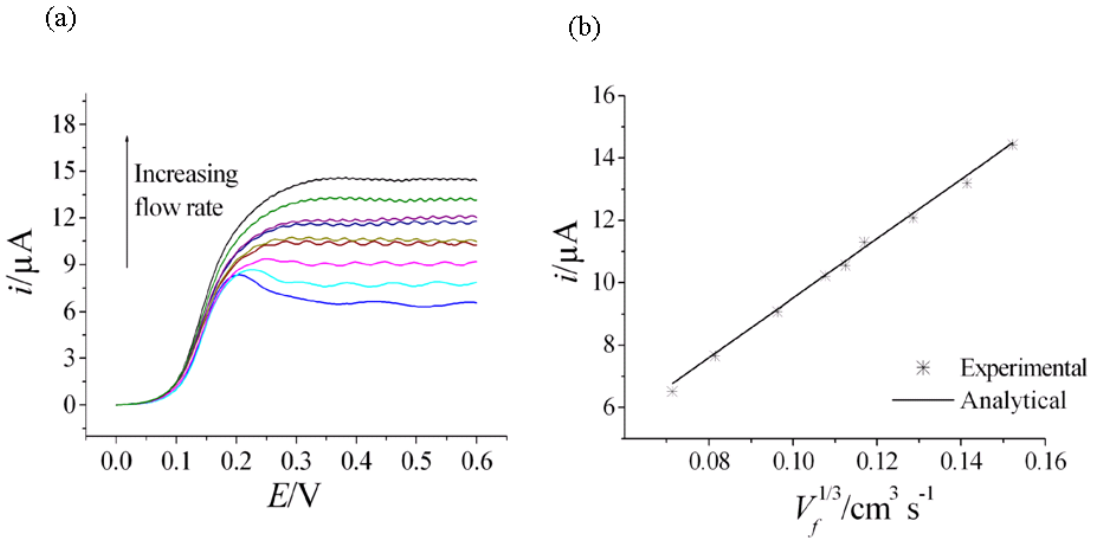

Figure 3-16 (a) Sample linear sweep voltammograms of 1.17 x 10^{-6} mol cm^{-3} potassium ferrocyanide solution in 0.1 x 10^{-3} mol cm^{-3} KCl and (b) corresponding Levich plot over BDDE, inside EMB, at total volume flow rates (V_f) of 0.0003, 0.0005, 0.0008, 0.0012, 0.0013, 0.0015, 0.0020, 0.0027 and 0.0033 cm^3 s^{-1}

3.5.2.2 *Response for FMN*

Having successfully characterised the EMB using potassium ferrocyanide, the EMB was then used to study FMN. LSV obtained for 0.9 x 10^{-6} mol cm^{-3} FMN solution in 0.1 x 10^{-3} mol cm^{-3} phosphate buffer are shown in Figure 3-17a and a Levich plot of limiting current versus cube root of flow rate is shown in Figure 3-17b. The linear relationship between the steady state current and cube root of volume flow rate demonstrates that the system is mass transfer limited. It also confirms that BDDE can be used successfully to analyse cofactors like FMN in hydrodynamic conditions. The experimental limiting current values were compared with the analytical data. The diffusion coefficient value of 1.38 x 10^{-5} cm^2 s^{-1} was considered (refer Section 3.5.1.1(2)), when calculating analytical current values. The experimental data was found to deviate from the analytical values, particularly for lower flow rates. This could be due to deactivation of electrode surface due to adsorbed FMN.

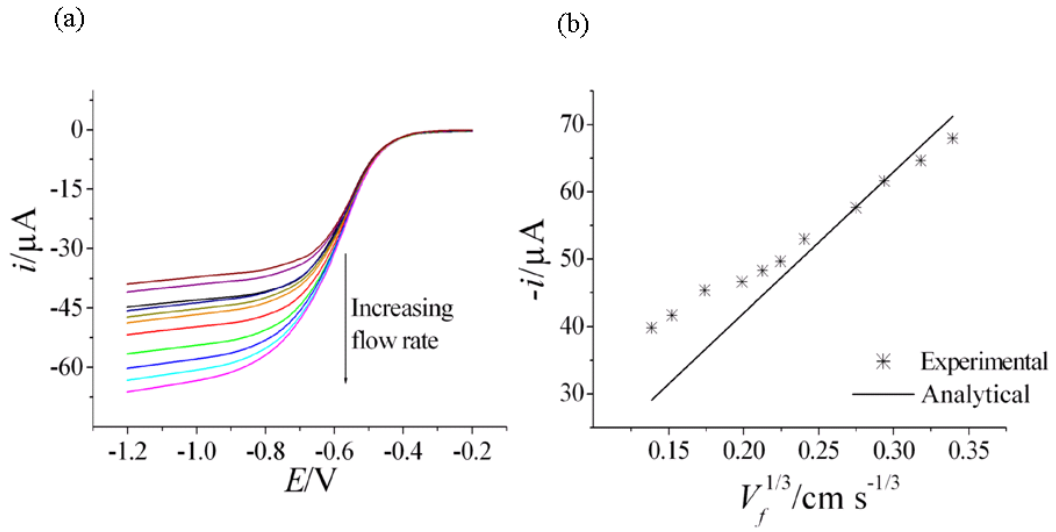

Figure 3-17 (a) Sample linear sweep voltammograms of 0.9 x 10^{-6} mol cm^{-3} FMN solution in 0.1 x 10^{-3} mol cm^{-3} phosphate buffer and (b) corresponding Levich plot over BDDE, inside EMB, at total volume flow rates (V_f) of 0.0025, 0.0033, 0.0050, 0.0075, 0.0092, 0.0108, 0.0133, 0.0200, 0.0244, 0.0311 and 0.0377 cm^3 s^{-1}

3.5.2.3. *Response for NADH*

Another cofactor, NADH, was used to study hydrodynamic voltammetry inside EMB. NADH, unlike FMN or FAD, undergoes single step two-electron oxidation. Figure 3-18a illustrates the LSV obtained for 60 x 10^{-9} mol cm^{-3} NADH solution in 0.1 x 10^{-3} mol cm^{-3} phosphate buffer. From the data it was clear that the voltammetric response for NADH is consistent with analytical values of current, which was obtained using Levich equation (refer Figure 3-18b). The EMB was noted to be very sensitive to low concentrations of the cofactor, which is necessary in many biosensor applications, as discussed earlier. Diffusion coefficient considered in analytical current calculations was 2.9 x 10^{-5} cm^2 s^{-1} (refer Appendix 2 (A.2.3) for diffusion coefficient calculations).

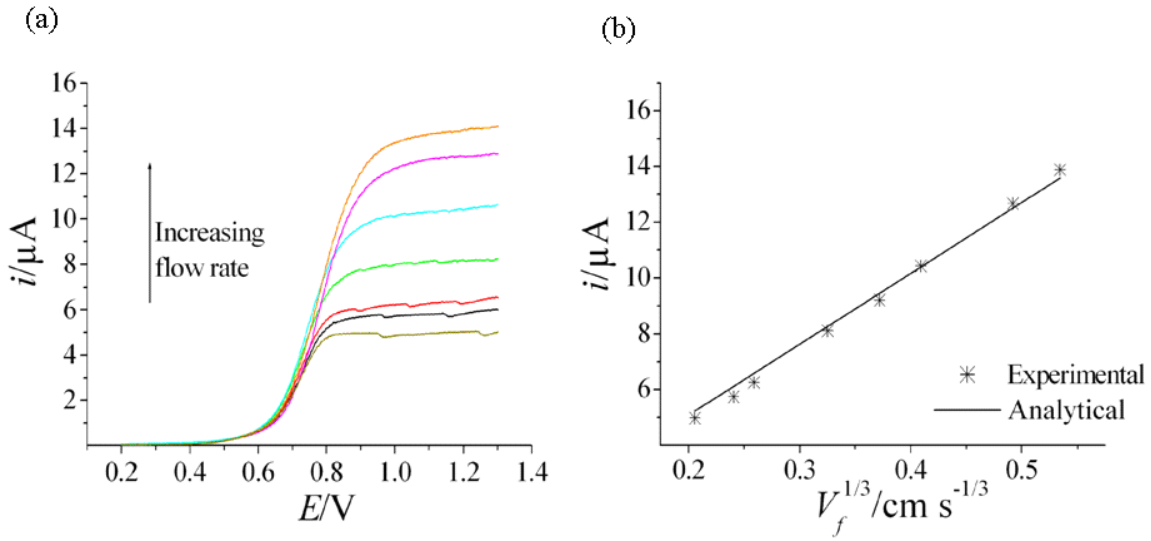

Figure 3-18 (a) Sample linear sweep voltammograms of 60 x 10^{-9} mol cm^{-3} NADH solution 0.1 x 10^{-3} mol cm^{-3} phosphate buffer and (b) corresponding Levich plot over BDDE, inside EMB, at total volume flow rates (V_f) of 0.0087, 0.0139, 0.0173, 0.0344, 0.0685, 0.1192 and 0.1528 cm^3 s^{-1}

3.5.3 Numerical Simulation Results

The numerical codes developed were tested by examining a system of potassium ferrocyanide in a cell of same geometry as the one used for experiments. A 1.1 cm x 1.1 cm electrode was sited centrally within the bottom face of a duct of width 0.05 cm and height 0.025 cm. Figure 3-19 shows the predicted response for a microfluidic device employing the following parameters: $[K_4Fe(CN)_6]$ = 1.17 mol cm^{-3}, $D_{Ferrocyanide}$= 6.5 x 10^{-6} cm^2 s^{-1}, N_J = 250, N_K = 500, V_f = 0.0003 – 0.0033 $cm^3\ s^{-1}$.

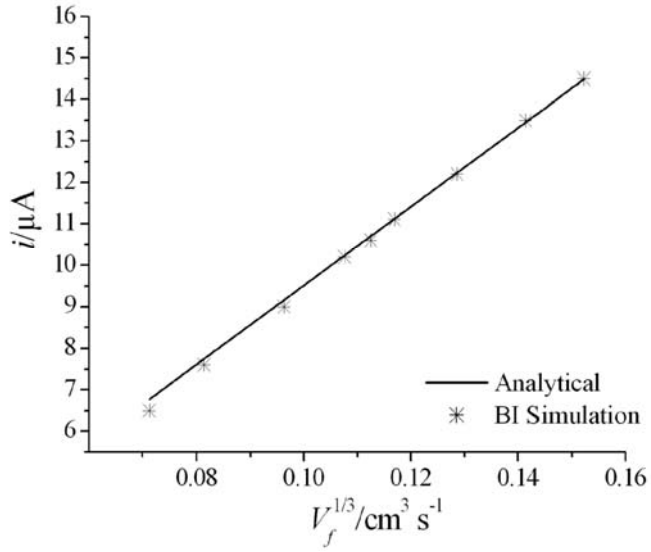

Figure 3-19 Comparison of transport limited current predicted by BI simulation and analytical methods

Under these conditions, it was established that axial convection and diffusion normal to the electrode surface are the dominant transport characteristics and therefore control the mass transport limited current [50]. Also presented in Figure 3-19 is the current predicted on the basis of the Levich equation. Agreement is observed between the two approaches.

Similarly, BI numerical model was used to simulate the experimental response for NADH and FMN. The parameters used were: h_2 = 0.025 cm, $w_e = d_d$ = 0.05 cm, x_e = 1.1 cm, N_J = 250, N_K = 500, V_f = 0.0003 – 0.16 $cm^3\ s^{-1}$, D_{FMN} = 1.38 x 10^{-5} $cm^2\ s^{-1}$, D_{NADH} = 2.9 x 10^{-5} $cm^2\ s^{-1}$,

[*FMN*] = 0.9 × 10^{-6} mol cm^{-3} and [*NADH*] = 60 × 10^{-9} mol cm^{-3}. Figure 3-20 compares numerically predicted and experimental responses for (a) potassium ferrocyanide, (b) FMN and (c) NADH. Also illustrated in Figure 3-21, Figure 3-22 and Figure 3-23 are the concentration profiles obtained for potassium ferrocyanide (V_f =0.0003, 0.0013, 0.0033 cm^3 s^{-1}), FMN (V_f = 0.0025, 0.0133, 0.0377 cm^3 s^{-1}) and NADH (V_f = 0.0087, 0.0685, 0.1528 cm^3 s^{-1}) respectively, over the entire BDDE.

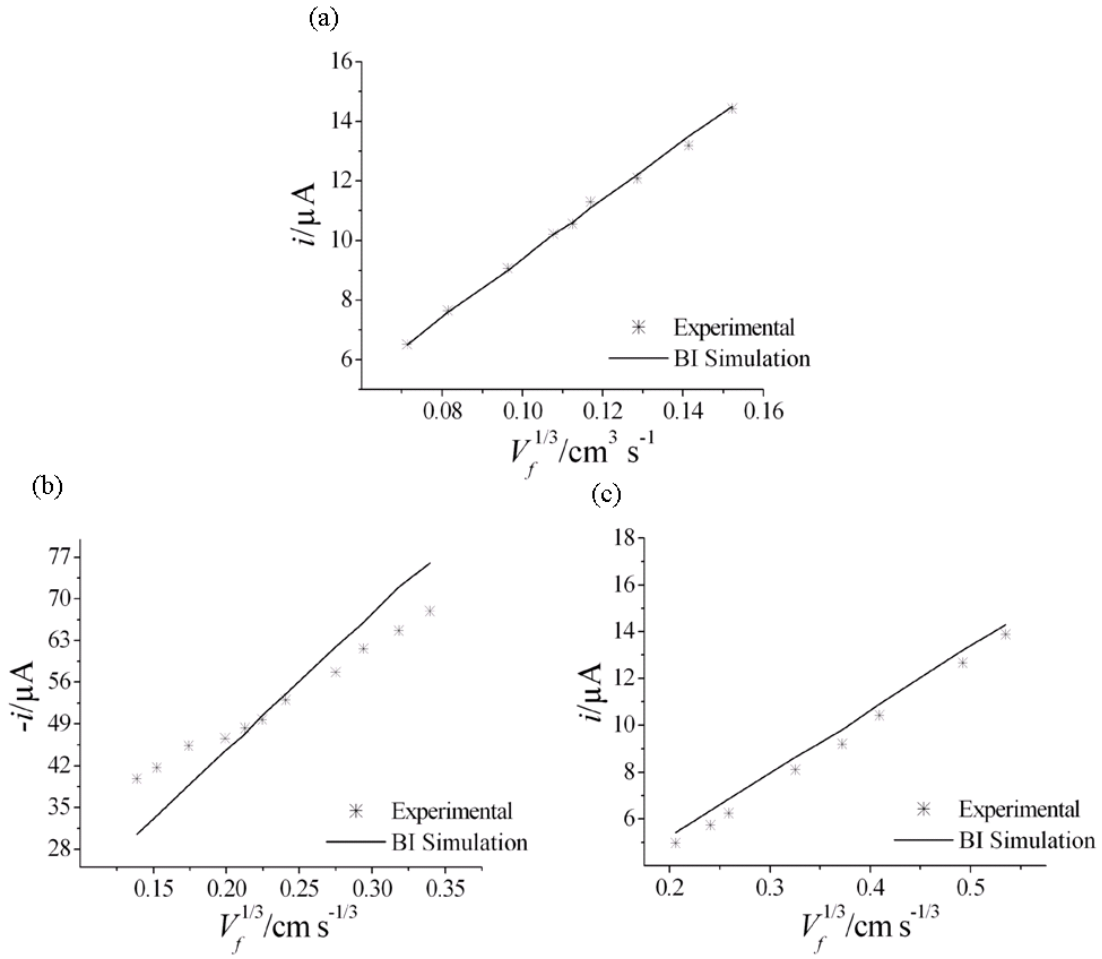

Figure 3-20 Comparison of experimental and simulated limiting currents for (a) 1.17 x 10^{-6} mol cm^{-3} potassium ferrocyanide in 0.1 x 10^{-3} mol cm^{-3} KCl (b) 0.9 x 10^{-6} mol cm^{-3} FMN in 0.1 x 10^{-3} mol cm^{-3} phosphate buffer and (c) 60 x 10^{-9} mol cm^{-3} NADH in 0.1 x 10^{-3} mol cm^{-3} phosphate buffer

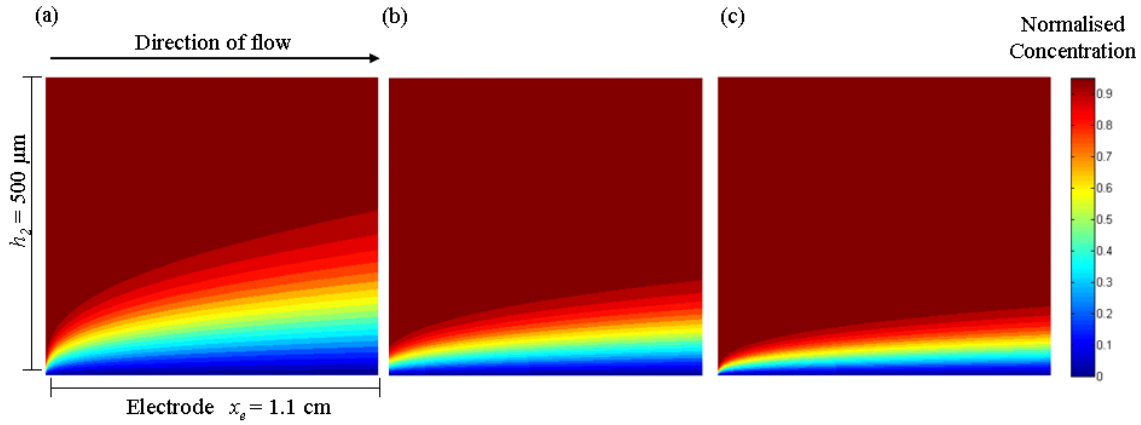

Figure 3-21 Concentration profiles of 1.17 x 10^{-6} mol cm^{-3} potassium ferrocyanide in 0.1 x 10^{-3} mol cm^{-3} KCl at volume flow rates of (a) 0.0003 (b) 0.0013 and (c) 0.0033 cm^3 s^{-1} over BDDE, inside EMB

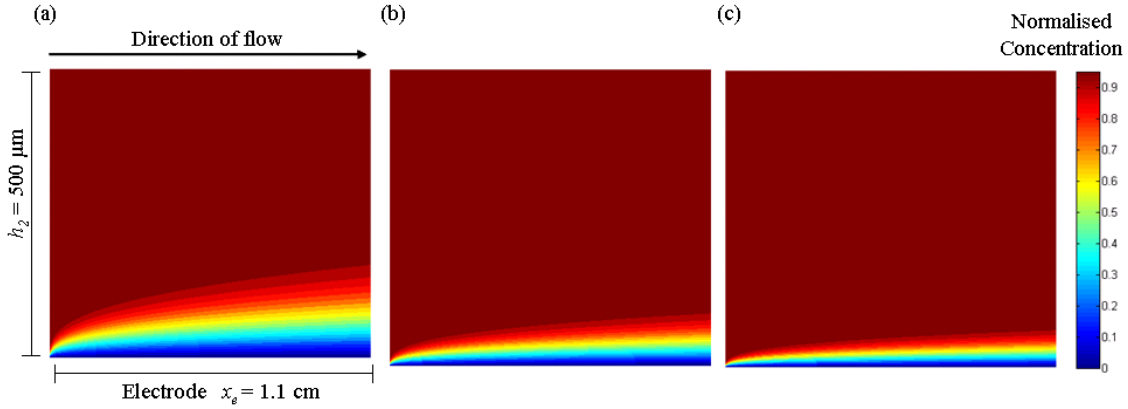

Figure 3-22 Concentration profiles of 0.9 x 10^{-6} mol cm^{-3} FMN in 0.1 x 10^{-3} mol cm^{-3} phosphate buffer at volume flow rates of (a) 0.0025 (b) 0.0133 and (c) 0.0377 cm^3 s^{-1} over BDDE, inside EMB

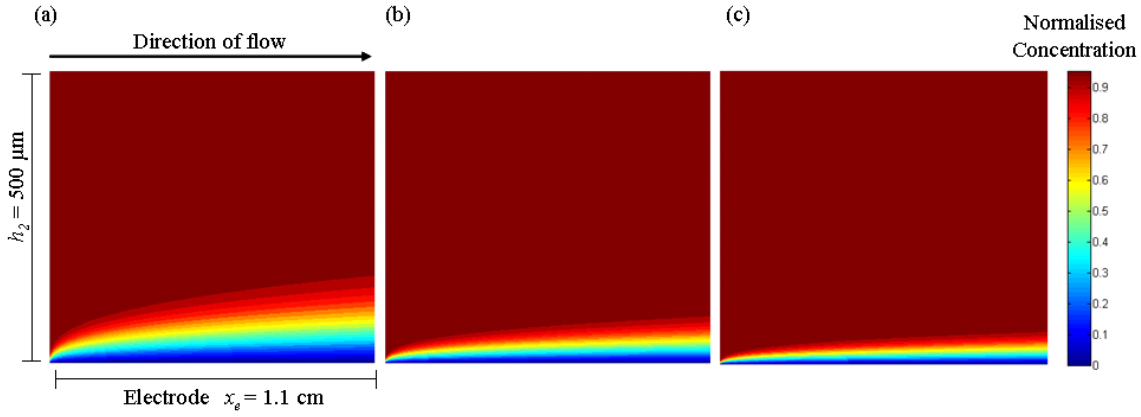

Figure 3-23 Concentration profiles of 60 x 10^{-9} mol cm^{-3} NADH in 0.1 x 10^{-3} mol cm^{-3} phosphate buffer at volume flow rates of (a) 0.0087 (b) 0.0685 and (c) 0.1528 cm^3 s^{-1} over BDDE, inside EMB

The experimental data was found to be in good qualitative agreement with the numerical values. There was however a slight deviation in case of FMN, which could be attributed because of the experimental errors (flow rate and concentration measurements, diffusion coefficient calculations) and due to deactivation of BDDE, over a long period of time. Also, the Levich analysis and the numerical model do not account for the two step reduction of FMN.

It was confirmed from the concentration profiles of potassium ferrocyanide, NADH and FMN that a large amount of reagent was passing over the electrode surface unaddressed. As reported by Matysik *et al.*, roughly 11% is electrochemically converted over microelectrodes [51]. This was one of the main reasons for low overall conversions in biocatalytic reactions.

3.6 CONCLUSIONS

In this chapter, electrochemical response of cofactors FAD, FMN and Vitamin B_{12} was studied using various electrodes and at different concentrations, in batch. It was found that BDDE gave the most reproducible voltammograms in comparison to GE, PE and GCE and also had a wider potential window to work in. Better electrochemical response for BDDE was due to less or no adsorption of the electroactive species on the electrode surface, during electrochemical reaction. Biological molecules adsorbed easily on other electrodes compared to BDDE.

An EMB with integrated BDDE was developed and fabricated. Hydrodynamic electrochemical studies of potassium ferrocyanide, FMN and NADH were performed inside the EMB. The transport limited current as a function of the cube root of volume flow rate gave a linear response, which is consistent with studies shown for traditional channel electrodes and electrochemical microreactors in literature. The numerical simulation data showed good qualitative agreement with analytical values of current, but they varied with experimental values by approximately 8%.

The concentration profile clearly demonstrated, the reduction in the amount of reagent being addressed over the electrodes with increasing flow rates. This was noted as one of the reasons for low conversions in biocatalytic reactions. Hence a method to reduce the amount of electroactive reagent passing over the electrode unaddressed needs to be developed. In the next chapter, a technique known as hydrodynamic focusing has been applied, to reduce the amount of unreacted analyte passing over the electrode. Numerical models have been developed to qualitatively and quantitatively compare the results of the effect of hydrodynamic focusing.

3.7 REFERENCES

[1] Linder, V.; Sia, S. K.; Whitesides, G. M. *Anal. Chem.* **2005**, 77 (1), 64.

[2] Zheng, B.; Ismagilov R. F. *Angewandte Chem. Int.* **2005**, 44 (17), 2520-2523.

[3] Yoon, S. K.; Choban, E. R.; Kane, C.; Tzedakis, T.; Kenis, P. J. A. *J. Am. Chem. Soc.* **2005**, 127, 10466.

[4] Rishpon, J.; Shabtai, Y.; Rosen, I.; Zibenberg, Y.; Tor, R.; Freeman, A. *Biotechnol*. *Bioeng*. **2004**, 35 (1)**,** 103-107.

[5] BjoÈrefors, F.; Strandman, C.; Nyholm, L. *Electroanal.* **2000**, 12 (4), 255-261.

[6] Lambrechts, M.; Sansen, W. M. C. *Microelectrochemical Devices In: Biosensors* **1992**, Taylor and Francis Group, LLC, Boca Raton.

[7] Kwakye, S.; Goral, V. N.; Baeumne, A. J.; *Biosens. Bioelectron.* **2006**, 21 (12), 2217-2223.

[8] McNaught, A. D.; Wilkinson, A. *Compendium of Chemical Terminology* **1997**, (The "Gold Book"), Blackwell Scientific Publications, Oxford, 2nd Edition.

[9] Lowe, C. R. *Biosens*. **1985**, 1, 4.

[10] Kumar, A. *J O M*-e **2000**, 52 (10).

[11] Basheer, C.; Vetrichelvan, M.; Suresh, V.; Lee, H. K. *Tetrahed. Lett.* **2006**, 47, 957–961.

[12] Bezkorovainy, A.; Rafelson Jr., M. E. *Concise Biochemistry: International Edition* **1996**, Marcel Dekker Inc., New York, pp.114-120.

[13] Habermüller, K.; Mosbach, M.; Schuhmann, W.; Fresenius, J. *Anal. Chem*. **2000**, 366, 560–568.

[14] Kometani, T.; Yoshii, H.; Matsuno, R. *J. Mol. Catal. B: Enzymatic* **1996**, 1 (2), 45-52.

[15] Muramatsu, H.; Dicks, J. M.; Tamiya E.; Karube, I.; *Anal. Chem.* **1987**, 59, 2760-2763.

[16] Hafner, F. *Biosens. Bioelectron*. **2000**, 15 (3-4), 149-158.

[17] Choban, E. R.; Waszczuk, P.; Kenis, P. J. A.; Tzedakis, T.; Yoon, S. K.; Kane, C. *Microfluidic device and synthetic methods* **2007**, US Patent No.7273541.

[18] Wentholt, I. M.; Vollebregt, M. A.; Hart, A. A.; Hoekstra, J. B.; DeVries, J. H. *Diabetes Care* **2005**, 28, 2871–2876.

[19] Steil, G.M.; Rebrin, K.; Mastrototaro, J.; Bernaba, B.; Saad, M. F. *Diabet. Technol. Ther*. **2003**, 5, 27-31.

[20] Wilhelm, B.; Forst, S.; Weber, M. M.; Larbig, M.; Pfûtzner, A.; Forst, T. *Diabet. Technol. Ther*. **2006**, 8, 146-155.

[21] http://www.lsbu.ac.uk/biology/enztech/amperometric.html

[22] Schmid, A.; Dordick, J. S.; Hauer, B.; Kiener, A.; Wubbolts, M.; Witholt, B. *Nature* **2001**, 409, 232−240.

[23] Akao, S.; Tsuno, H.; Cheon, J. *Water Research*, **2007**, 41, 1774 – 1780.

[24] Durliat, H.; Barrau, M. B.; Comtat, M. *Bioelectrochem. Bioenerg.* **1988**, 19, 413−423.

[25] Bergel, A.; Comtat, M. *Bioelectrochem. Bioenerg.* **1992**, 27, 495−500.

[26] Bard, A.J.; Faulkner, L.R.. *Electrochemical Methods: Fundamentals and Applications* **1980**, John Wiley, USA, p.119-336.

[27] Bergel, A.; Comtat, M. *J. Electroanal. Chem.* **1991**, 302, 219−231.

[28] Schwalbe, T.; Autze, V.; Hohmann, M.; Stirner, W. *Org. Proc. Res. Dev 8* **2004**, p. 440ff.

[29] DiCosimo, R.; Wong, C. H.; Daniels, L.; Whitesides, G. M. *J. Org. Chem.* **1981**, 46, 4622−4625.

[30] Popa, E.; Notsu, H.; Miwa, T.; Tryk, D. A.; Fujishima, A. *Electrochem. Solid-State Lett*. **1999**, 2, 49.

[31] Baur, J. B.; Kristensen, E. W.; May, L. J.; Wiedemann, D. J.; Wightman, R. M. *Anal. Chem*. **1988**, 60, 1268.

[32] DeClements, R.; Swain, G. M. *J. Electrochem. Soc*. **1997**, 144, 856.

[33] Rao, T. N.; Yagi, I.; Miwa, T.; Tryk, D. A.; Fujishima, A. *Anal. Chem.* **1999**, 71, 2506-2511.

[34] Yunus, K.; Fisher, A. C. *Electroanal*. **2003**, 15, 1782-1786.

[35] Lin, K-C.; Chen, S-M. *J. Electroanal. Chem.* **2005**, 578, 213–222.

[36] Butterfield, S. M.; Goodman, C. M.; Rotello, V. M.; Waters, M. L. *Angew. Chem. Int. Ed.* **2004**, 43, 724 –727.

[37] Connors, T. F.; Arena, J. V.; Rusling, J. F. *J. Phys. Chem.* **1988**, 92 (10), 2810-2816.

[38] Lin, H. *Org. Biomol. Chem.* **2007**, 5, 2541-2554.

[39] Matthews, S. M.; Elder, A. D.; Yunus, K.; Kaminski, C. F.; Brennan, C. M.; Fisher, A. C. *Anal. Chem.* **2007**, 79, 4101-4109.

[40] Visbal, H.; Sugita, S.; Ishizaki, C.; Ishizaki, K. *J. Mat. Sci.*, **2006**, 2, 1-10.

[41] Yamashit, M.; Rosatto, S. S.; Kubota, L. T. *J. Braz. Chem. Soc.* **2002**, 13 (5), 635-641.

[42] Birss, V. I.; Elzanowska, H.; Turner, R. A. *Can. J. Chem.* **1988**, 66, 86-96.

[43] Bard, A. J.; Faulkner, L. R. *Electrochemical Methods: Fundamentals and Applications* **1980,** John Wiley, New York, 2nd Edition, pp.136-140.

[44] Honeychurch, M. J.; Ridd, M. J. *Electroanal.* **1996**, 8 (4), 362-369.

[45] Suzuki, M.; Matsui, M.; Kihara, S. *J. Electroanal. Chem.* **1997**, 438, 147-151.

[46] Takamura, K.; Mori, A.; Kusu, F. *Chem. Pharm. Bull.* **1981**, 29 (11), 3083-3089.

[47] Lexa, D.; Saveant, J. M. *J. Am. Chem. Soc.* **1976**, 98, 9.

[48] Thompson, M. D. K. *Theoretical and Applied Electrochemistry* **1939**, The Macmillan and Co. Madison, 3rd Edition.

[49] Levich, V. G. *Physicochemical Hydrodynamics* **1962**, Prentice-Hall: New Jersey.

[50] Matthews, S. M. *A Microfluidic Investigation of Interfacial Reaction Kinetics* (PhD Thesis) **2008.**

[51] Matysik, F-M.; Björefors, F.; Nyholm, L. *Anal. Chim. Acta* **1999**, 385 (1-3), 409-415.

Chapter 4

Hydrodynamic Focusing Studies in Microreactors using Voltammetric Analysis: Theory and Experiment

4.1 INTRODUCTION

In the previous chapters, characterisation of electrochemical microreactors based on various cofactors and electrode material was presented. Using simulations it was observed that only small amount of electrochemical reagent was actually addressed at the electrode surface [1]. In fine chemical industries, high conversion is necessary due to the high reagent cost [2]. Also, the amount of reagent addressed and high sensitivity is of paramount importance in biosensor applications, described in Chapter 3 [3]. Hence in this chapter, the problem of low conversion has been addressed by applying a technique called hydrodynamic focusing [4]. This chapter describes a numerical and experimental investigation of the voltammetric response observed within small scale electrochemical reactors under hydrodynamic conditions.

4.1.1 Hydrodynamic Focusing

A potential limitation of the traditional "hydrodynamic voltammetry in microchannel reactors" approach results from the necessity for reagent transport to and from the electrode surface, due to diffusion layer formation as seen in Chapter 3. This can result in a low percentage of the

electroactive reagent being available over the electrode surface at high throughput rates. One way of making a higher percentage of reagent available over the electrode has been demonstrated by Horii *et al.*, in which a thin microchannel was employed, with channel heights close to the diffusion layer thickness [5]. This method is not totally effective, as reduction in channel height leads to increase in fluid velocity and therefore decreases the height of the diffusion layer further. More recently, there has been a considerable interest in hydrodynamic focusing. Hydrodynamic focusing is a technique by which a sample (analyte) is confined into a narrow stream, by the use of a second liquid stream which acts to drive the sample stream closer to one wall of the microchannel [6]. Figure 4-1 shows a schematic of an analyte stream being focused by a carrier stream inside a rectangular duct. The thickness of the analyte stream can be varied by varying the velocity of carrier stream relative to the analyte stream. By applying higher flow rateS of carrier stream, thickness of the analyte stream can be reduced significantly [4]. This reduces the total quantity of reagent employed, while retaining cell geometries, which permit high throughput characteristics. Another advantage of hydrodynamic focusing is the ability to increase the surface to volume ratios, without physically modifying the microreactor. Yoon *et al.* have demonstrated the focusing of reagent streams close to an electrode by using a buffer stream of same phase [7]. Lee *et al.* have studied the effect of hydrodynamic focusing of a central analyte stream by using two carrier streams in rectangular microchannels [8]. They have developed two models that can predict the width of focused stream in symmetric and asymmetric hydrodynamic focusing in microchannel of varying aspect ratios. Due to these advantages, it has found application in areas such as flow cytometry, studying rate kinetics and biocatalysis, some of which are described in more detail below [7, 9, 10].

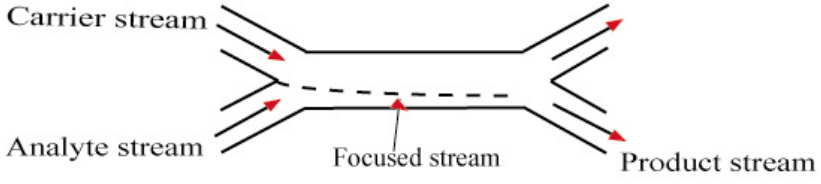

Figure 4-1 Schematic of hydrodynamic focusing inside a microfluidic device

4.1.2 Applications of Hydrodynamic Focusing

1.) *Flow Cytometry*

Flow cytometry is a technique used for continuous counting and physical analysis of cells and other similar particles such as microbes in solution. Using hydrodynamic focusing techniques, the cell stream can be controlled so that a single cell passes through a detector at a given time [9].

Kruger *et al.* injected suspended cells in a laminar flow stream and hydrodynamically focused a flow of single cells to pass under a beam of monochromatic light [11]. Wolff *et al.* have developed a chimney-like sheathing structure in a microchannel for focusing of the cell sample [12]. Yamada *et al.* have fabricated a 45 μm height channel by UV laser ablation technique and by using hydrodynamic focusing from two opposite sides they have developed a high precision blood cell counter (refer Figure 4-2) [13]. Another novel method of focusing has been addressed by Fu *et al.* where the focusing of particles and liquids into a narrow beam was achieved using high voltages [14].

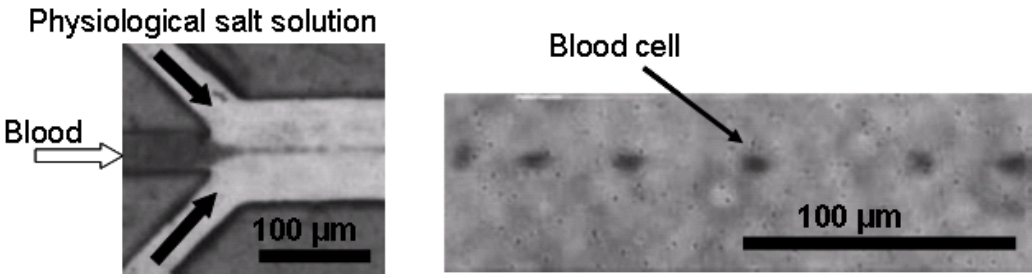

Figure 4-2 Blood path through three-pronged channel. The image on the right shows the downstream blood cell counting [13]

2.) *Fast Kinetic Studies*

Mixing of chemical species is limited by the time required for molecular diffusion across a finite length scale and diffusion time scales as the square of diffusion length [15, 16]. This makes it very difficult to study fast kinetics reactions, such as structural events in protein folding which occur at microsecond time scale [9]. Diffusion lengths can be reduced greatly with turbulent fluid

motion, but this requires high flow rates to achieve high Reynolds numbers [17]. Instead Hertzog *et al.* have employed hydrodynamic focusing technique for reducing diffusion lengths in microfluidic devices in order to decrease mixing times and enable the study of faster reaction kinetics [18]. Typically these devices use one analyte stream and two carrier streams to increase the surface area to volume ratio. By using this approach, they were able to report protein folding events with mixing times of 8 μs.

3.) *Cofactor Regeneration*

An application of hydrodynamic focusing relevant to this chapter is found in cofactor regeneration reaction. One classical reaction in biochemistry is the conversion of pyruvate to L-lactate (refer Section 3.1.2), which requires nicotinamide adenine dinucleotide (NADH) as a cofactor [6, 19]. Stoichiometric use of cofactors such as NADH could be cost prohibitive. Hence there is a need for its regeneration, to make the process economically viable and at the same time increase the conversion of pyruvate to L-lactate. Durliat *et al.* have shown that NADH can be regenerated electrochemically from NAD^+, using flavin adenine dinucleotide (FAD) as a mediator that shuttles electrons from a cathode to the enzyme [20]. However this reaction is reversible and hence the equilibrium is not completely favourable in the desired direction, as seen in Chapter 3. This leads to lower percentage of regeneration of NADH. Yoon *et al.* have performed the same reaction inside a microreactor and have tried to address the low conversions by applying hydrodynamic focusing technique [6]. The analyte stream was focused very close to the electrode surface, where the electrochemical reaction occurred by using higher flow rates of carrier stream. The relative flow rates of the two streams determined the proportion of the channel occupied by each stream. This resulted in a significantly higher conversion using the focusing approach, compared to standard biocatalytic methods reported previously.

Chen *et al.* have developed this system further and reported a membrane reactor with porous

graphite electrode with immobilised enzyme that could perform *in situ* regeneration of cofactor whilst converting pyruvate to L-lactate, giving conversions upto 70 % [19].

The ability to manipulate fluids at micro- or nano-litre scale offers significant potential for these combined microreactor/electrochemical devices in the fields of analysis and electrosynthesis [21]. In this chapter, an electrochemical microreactor was developed, fabricated and tested for electrochemical sensitivity. Hydrodynamic focusing technique was employed to focus the analyte stream closer to the working electrode and hence potentially reducing the amount of reagent that gets wasted due to its unavailability at the electrode surface. A widely reported system of potassium ferricyanide over gold electrode was used as a one-electron transfer system for the experiments [22]. A numerical model was developed to study the various hydrodynamic parameters affecting the limiting current values, and using these models best experimental conditions were employed. Numerical models were also used to modify the design of the electrochemical microreactor in order to achieve high conversions.

4.2 HYDRODYNAMIC VOLTAMMETRY- CHANNEL ELECTRODES

Hydrodynamic voltammetry is a well understood and established technique. It has been widely used in continuous chemical monitoring, high throughput screening and the mechanistic analysis of electrolysis processes [23-25]. Hydrodynamic voltammetry in microfluidic systems can be conducted by placing a working electrode smoothly into the wall of a rectangular duct and passing electrolyte solution through the cell under laminar flow conditions [26]. Well defined mass transport conditions can be obtained by careful design of the channels, enabling analysis of the current/transport rate response of a specific system [27]. Other voltammetric methods under hydrodynamic conditions have been discussed in detail in Section 1.5.5.

The development and application of microfluidic devices incorporating electrochemical sensors has expanded rapidly over recent years, although qualitative and quantitative current/voltage

relationships with flow rate remain less well explored [28-30]. In this chapter, a new confluence electrochemical microreactor was developed in which the analyte stream could be hydrodynamically focused to minimise the volume of analyte passing over the electrode unconverted, due to the formation of diffusion layer [31]. Using voltammetric techniques, the effect of three variables on the efficacy of hydrodynamic focusing was studied.

(i) *Lead-in Length*: This is the distance between the point where the carrier stream meets the analyte stream and the leading edge of the electrode, as illustrated in Figure 4-3. By varying the lead-in length, diffusion between the two streams is varied before the analyte stream can be processed over the electrode.

(ii) *Focusing Ratio*: It is the ratio of carrier stream flow rate to analyte stream flow rate. By either increasing or decreasing the focusing ratio, the interface between the two streams can be either brought closer to the electrode or taken away from it.

(iii) *Total Volume Flow Rate*: This is the combined flow rates of the analyte and carrier streams. The electrochemical limiting current response is significantly affected by this parameter. Furthermore, it also affects the contact time between the two streams prior to electrochemical detection.

Figure 4-3 illustrates the variables described above. The studies presented in this chapter examine the influence of stream velocity, lead-in length and focusing stream ratios on the electrolytic current induced.

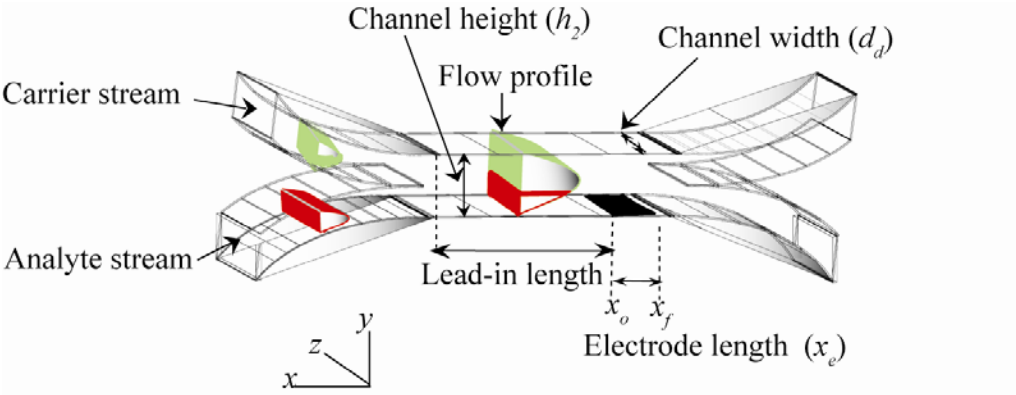

Figure 4-3 Schematic of hydrodynamic focusing in a microchannel

4.3 NUMERICAL SIMULATIONS

A numerical model was developed to describe the variation of current as a function of volume flow rate, lead-in length and focusing stream ratios. An electrochemical cell in which two streams (analyte and carrier) were introduced was simulated using a finite difference model in order to determine the response of the device to hydrodynamic focusing. Analyte stream contained an electrochemically active species, *A*, which was not present in the carrier stream.

A schematic of a rectangular duct used for the reduction of species *A* at an electrode ($A + e^- \rightarrow B$), fabricated inside it, has been illustrated in Section 2.7. As described in Chapter 2, it was assumed that sufficient electrolyte was present in solution to neglect transport effects induced by migration and that the diffusion coefficients of species *A* and *B* are matched. In this way, we may either simulate reactant (*A*) or product (*B*) subject to application of appropriate boundary conditions at the inlet and electrode surface.

A finite difference scheme was adopted to simulate the coupled mass transfer and electrolysis reaction. A pseudo- two dimensional form of the backwards implicit (BI) scheme (refer Section 2.7 for brief theory), which has been reported previously by Matthews *et al.* for three-dimensional simulations with microreactors, was employed [32]. A schematic of the mesh is shown in Figure 4-4. It simulates the voltammetric behaviour of a centrally sited electrode in the bottom wall

of a microchannel. Due to the steady state nature of the simulation, the BI method used is not iterative and consequently far more computationally efficient.

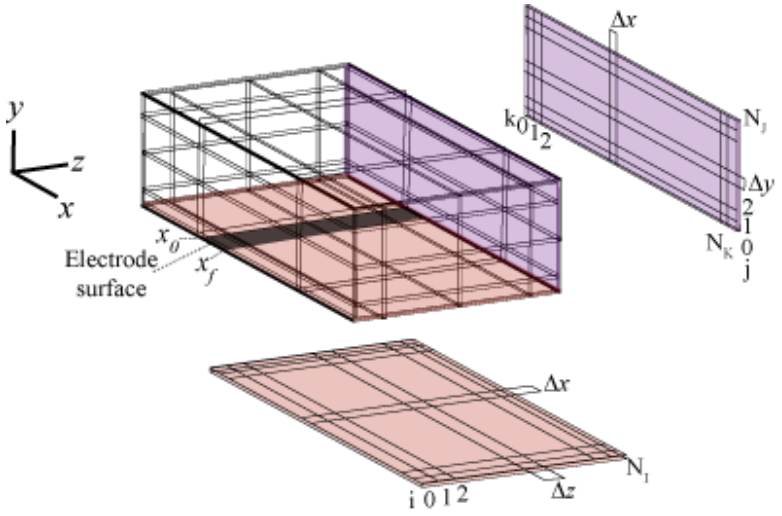

Figure 4-4 Schematic of three-dimensional grid employed for numerical simulations

4.3.1 Boundary Conditions

Standard boundary conditions at the channel walls are described in Section 2.7. The relevant boundary conditions for an electrolysis reaction occurring at the electrode surface as defined in Figure 4-4 were appropriate for a potential step experiment at steady state. In the potential step experiment, the potential was stepped from initial value where there is zero electron transfer to a second value where there is complete depletion of species *A* at the electrode surface, as seen in the Table 4-1.

t = steady state

$x_0 < x < x_f$	$y = 0$	$z_0 < z < z_f$	$[A] = 0$
$x_0 < x < x_f$	$y = 0$	$z_0 < z < z_f$	${}^{t}i = Fx_e w_e D\left(\frac{\partial[A]}{\partial y}\right)_{y=0}$
$0 < x < x_0$	$y = 0$	$0 < z < d_d$	$\frac{\partial[A]}{\partial y} = 0$
$x_0 < x < x_f$	$y = 0$	$0 < z < z_0$	$\frac{\partial[A]}{\partial y} = 0$
$x_0 < x < x_f$	$y = 0$	$z_f + w_e < z < d_d$	$\frac{\partial[A]}{\partial y} = 0$
$x_f < x$	$y = 0$	$0 < z < d_d$	$\frac{\partial[A]}{\partial y} = 0$
$0 < x$	$y = h_2$	$0 < z < d_d$	$\frac{\partial[A]}{\partial y} = 0$
$x > 0$	$0 < y < h_2$	$z = 0$	$\frac{\partial[A]}{\partial z} = 0$
$x > 0$	$0 < y < h_2$	$z = d_d$	$\frac{\partial[A]}{\partial z} = 0$
$x = 0$	$y < J_{int}$	$0 < z < d_d$	$[A] = 1$
$x = 0$	$y > J_{int}$	$0 < z < d_d$	$[A] = 0$

Table 4-1 Boundary conditions for electrochemical simulations

Where x_0 and x_f correspond to the start and end of the electrode in the x direction (see Figure 4-3). J_{int} is the position of the interface. The current measure by electrode was calculated using the following equation:

$$i = F D_A [A]_{Bulk} \frac{\Delta x \ \Delta z}{\Delta y} \sum_{k=k_0}^{k=k_f} \sum_{i=1}^{i=N_I} ({}^{t}a_{i,1,k} - {}^{t}a_{i,0,k}) \qquad (4.1)$$

Where k_o is the counter at the start of the electrode in the x direction, with k_f the corresponding box at the end of the electrode in the x direction.

The choice of flow rates and dimensions of channels ensured the laminar flow throughout the experiments. This ensured position of the interface between the two streams was dependent only on the ratios of the flow rates of the analyte and carrier stream. Using this assumption, the velocity profile could be calculated using the analytical expression described in Section 2.7. By summing the velocity across the width of the channel at each grid point above the bottom channel wall, the position of the interface (J_{int}) could be calculated within the channel. The interface was positioned at the point where the sum equaled the analyte solution flow rate. The analyte stream ($y<J_{int}$) contained a normalised concentration of 1 and the carrier stream ($y>J_{int}$) contained no species *A*.

The results from the numerical simulations were compared to those observed experimentally using microfabricated devices. The numerical models reveal a regime where the finely focused stream of reagent responds in an identical manner to a cell completely full of reagent and also to a regime where diffusional broadening of the reagent stream into the carrier stream becomes significant with a resulting loss in voltammetric sensitivity. In addition, at higher focusing ratios where the reagent occupies a much smaller portion of the channel, full electrochemical depletion of the species is possible at substantially greater throughput rates than is feasible without the focusing arrangement. Experimental studies show qualitative agreement with numerical predictions.

4.4 MICROFABRICATION

Electrochemical microreactors were assembled by sandwiching a poly(dimethylsiloxane) (PDMS) microgasket channel between two electrode plates (Figure 4-5). The working and reference electrodes were fabricated on one of the glass substrates and the counter electrode on the other glass substrate, with PDMS microchannel placed between them to define the channel sidewalls as illustrated in Figure 4-6. The electrodes and channel were aligned before placing them between a

perspex clamp, designed using milling techniques described in Chapter 2. The clamp contained two staggered inlets, one at 90^{o} (for analyte stream) and the other at 45^{o} (for carrier stream) as seen in Figure 4-6b. It was constructed at an angle to ensure smooth confluent region. There was only one outlet. The channel was placed such that three different lead-in lengths of 0.08 cm, 0.16 cm and 0.26 cm could be studied during the experiments.

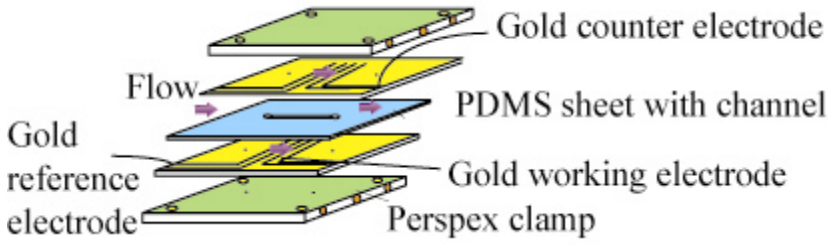

Figure 4-5 Schematic of electrochemical microreactor

The microfabrication procedure consisted of two stages, fabrication of gold microelectrodes and fabrication of a microchannel made from a PDMS microgasket. The fabrication of electrodes and channel is detailed in Section 2.3. The gold pseudo-reference electrode and working electrode on the bottom glass wafer were of length 500 µm and the gold counter electrode on the top wafer was constructed so that it was more than 100 times in length compared to the working electrode, as seen in Figure 4-6a. An extra gold counter electrode on the bottom wafer was also provided downstream from the working and reference electrodes. The PDMS gasket straight channel of dimensions height (h_2): 250 µm, width (d_d): 890 µm and length (x_l): 3 cm with single inlet and outlet was constructed using soft lithographic techniques described in Section 2.3.

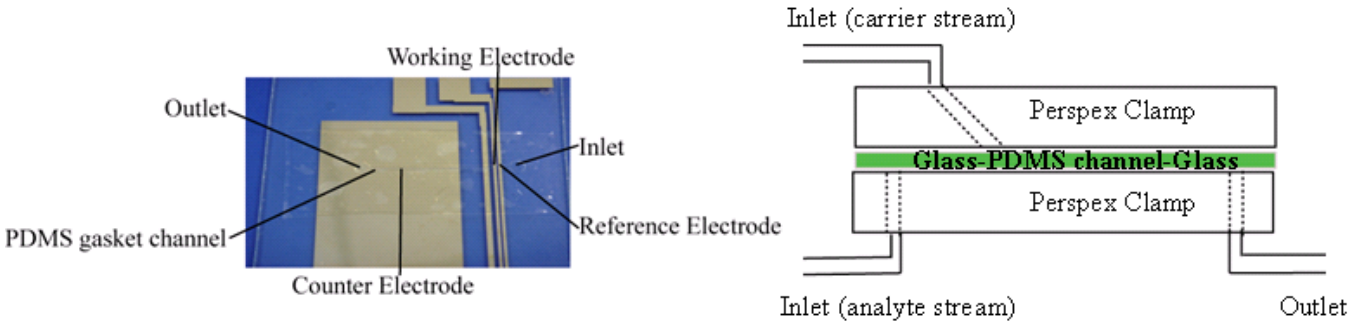

Figure 4-6 (a) Image of gold electrodes with PDMS channel, (b) Illustration of staggered inlet clamp

The analyte stream considered for experimental purpose was potassium ferrricyanide ($K_3Fe(CN)_6$) and potassium ferrocyanide ($K_4Fe(CN)_6$). Potassium ferricyanide and potassium ferrocyanide were used for electrochemical analysis, as they are well established electroactive system. The carrier stream used in the focusing experiments was potassium chloride (KCl) to minimise the migration effects. In order to compare to standard channel electrode behaviour, a control experiment where both streams contained potassium ferricyanide was also performed.

Voltammetric measurements were carried out using a computer controlled potentiostat - standard three-electrode configuration. The fluid flow was controlled using two syringe pumps with a typical flow rates between 1.67×10^{-5} cm^3 s^{-1} and 8.3×10^{-2} cm^3 s^{-1}.

4.5 DIFFUSION COEFFICIENT AND CELL HEIGHT CALCULATION

The diffusion coefficients of potassium ferricyanide and potassium ferrocyanide in aqueous system were calculated using Randles-Sevcik equation (refer Section 1.5.5) by obtaining series of cyclic voltammograms [33]. The experimental conditions and experimental data have been reported in Appendix 2 (A.2.3).

The channel height calibration was performed by using the following parameters $w_e = d_d = 0.089$ cm, $x_e = 0.05$ cm, and 0.1 cm, $V_f = 0.001 - 0.0083$ cm^3 s^{-1}, $D = 6.77$ x 10^{-6} cm^2 s^{-1} and 6.5 x 10^{-6} cm^2 s^{-1} and $C = 0.8 \times 10^{-6}$ mol cm^{-3}(1M = 10^{-3} mol cm^{-3}). The linear sweep voltammograms (LSV) as seen in Figure 4-7a,c,e,g were obtained by sweeping the potential

between 0 to +0.4 V for potassium ferrocyanide and 0 to -0.5 V for potassium ferricyanide, at a scan rate of 0.04 V s^{-1}. Using the LSV, plots of limiting current against flow rate were obtained and compared with analytical values of limiting current calculated using Levich equation (refer Section 1.5.5), as illustrated in Figure 4-7b,d,f,h [34]. The height of the channel was thus calibrated to match the two plots and was calculated as 250 µm.

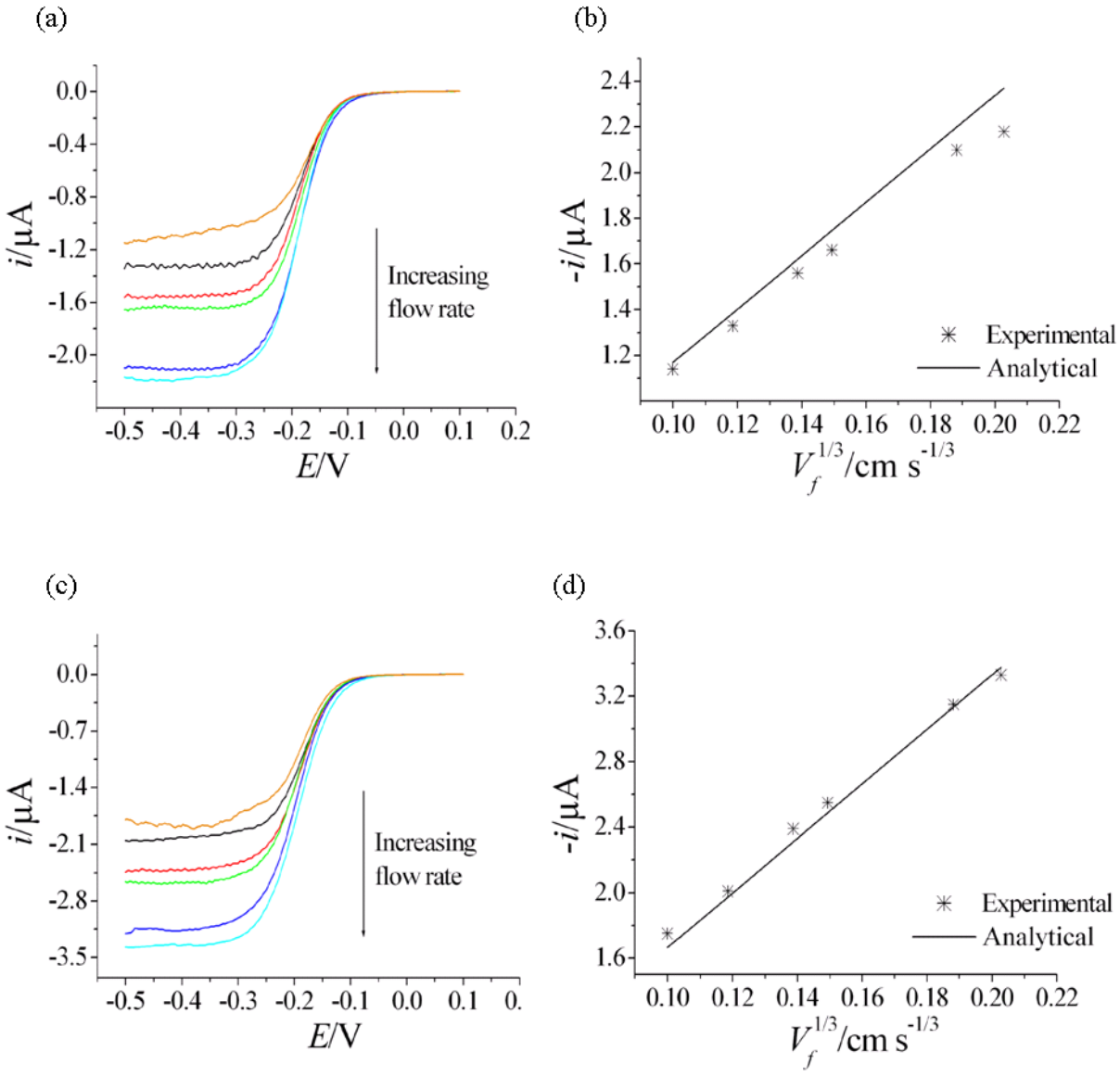

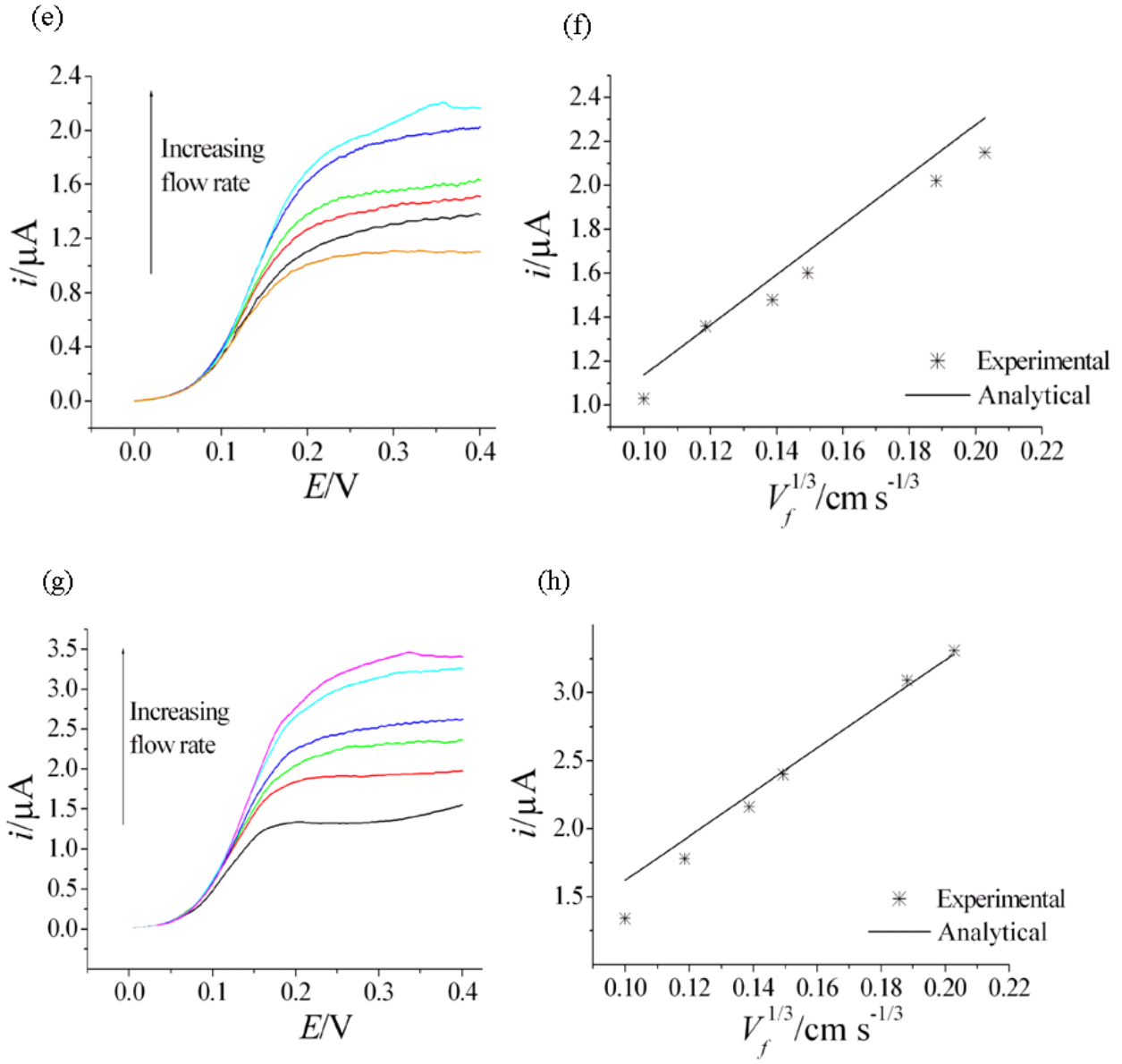

Figure 4-7 Sample linear sweep voltammograms and their corresponding Levich plots obtained for 0.8 x 10^{-6} mol cm^{-3} potassium ferricyanide [$K_3Fe(CN)_6$] and 1 x 10^{-6} mol cm^{-3} potassium ferrocyanide [$K_4Fe(CN)_6$] in 0.1 x 10^{-3} mol cm^{-3} potassium chloride as background electrolyte at a scan rate of 0.04V s^{-1} and flow rates of 0.001, 0.017, 0.0027, 0.0033, 0.0067 and 0.0083 cm^3 s^{-1} (a-b) analyte: $K_3Fe(CN)_6$, x_e = 0.05 cm (c-d) analyte: $K_3Fe(CN)_6$, x_e = 0.1 cm (e-f) analyte: $K_4Fe(CN)_6$, x_e = 0.05 cm (g-h) analyte: $K_4Fe(CN)_6$, x_e = 0.1 cm

4.6 RESULTS AND DISCUSSION

4.6.1 Numerical Simulations of Hydrodynamic Focusing

In order to test the numerical codes developed, a cell of macroscopic geometry where both inlets supply a solution containing the bulk concentration of a species *A* was initially examined. In this case a 0.4 cm x 0.4 cm electrode was sited centrally within the bottom face of a duct of width 0.6 cm and height 0.04 cm. Under these conditions the hydrodynamic boundary layers at the edge of the channel are sufficiently small that they should render the calculation analogous to a two-dimensional channel flow cell calculation and allow comparison of the voltammetric predictions with that expected from the Levich equation. Figure 4-8 shows the predicted response for a microfluidic device employing the following parameters: $[A]_{Bulk} = 10^{-6}$ mol cm^{-3}, $D_A = 10^{-5}$ cm^2 s^{-1}, $N_I = 20$, $N_K = 40$, $N_J = 200$, $V_f = 10^{-1}$–10^{-6} cm^3 s^{-1}.

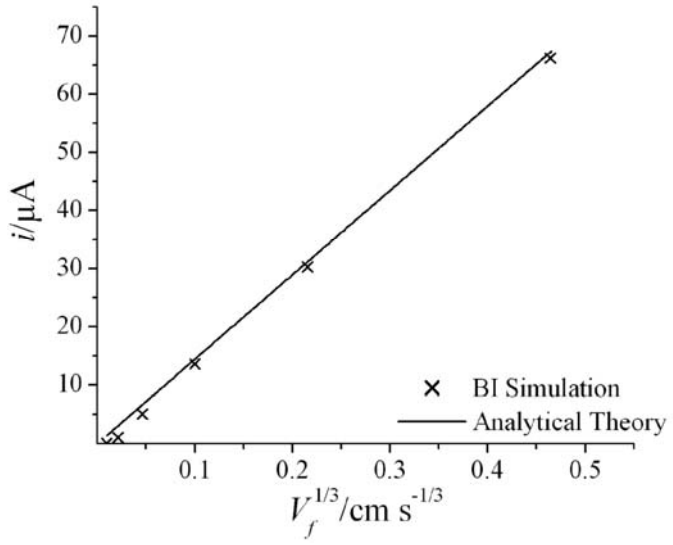

Figure 4-8 Comparison of transport limited current predicted by BI simulation and analytical theory methods

Under these conditions, it is established that axial convection and diffusion normal to the electrode surface are the dominant transport characteristics and therefore control the mass transport limited

current [35]. Also presented in Figure 4-8 is the current predicted on the basis of the Levich equation. An agreement was observed between the two approaches.

Next the BI model was applied to the numerical investigation of variables affecting the performance of a microfluidic device with hydrodynamic focusing. As stated previously, three specific variables were examined: lead-in length, focusing ratio and total volume flow rate.

The effect of lead-in length on the current response was studied using six different lead-in lengths: 0, 0.1, 0.2, 0.3, 0.5 and 1 cm. Four different focusing ratios were simulated: 1:1, 5:1, 10:1 and 20:1 (see Figure 4-9a-d for each lead-in length). An electrode spanning the width of the channel was simulated using the following parameters: $h_2 = w_e = 0.05$ cm, $x_e = 0.025$ cm, $x_l = 0.225$ cm, 0.325 cm, 0.425 cm, 0.525 cm, 0.725 cm and 1.225 cm (for lead-in lengths of 0 cm, 0.1 cm, 0.2 cm, 0.3 cm, 0.5 cm and 1 cm respectively), $N_J = 250$, $N_K = 2600 - 9800$, $N_I = 80$, $[A]_{Bulk} = 10^{-6}$ mol cm^{-3}, $D_A = 10^{-5}$ cm^2 s^{-1}, $V_f = 0.0001 - 0.05$ cm^3 s^{-1}. Figure 4-9a-d show the plots obtained for the different focusing ratios (1:1, 5:1, 10:1 and 20:1).

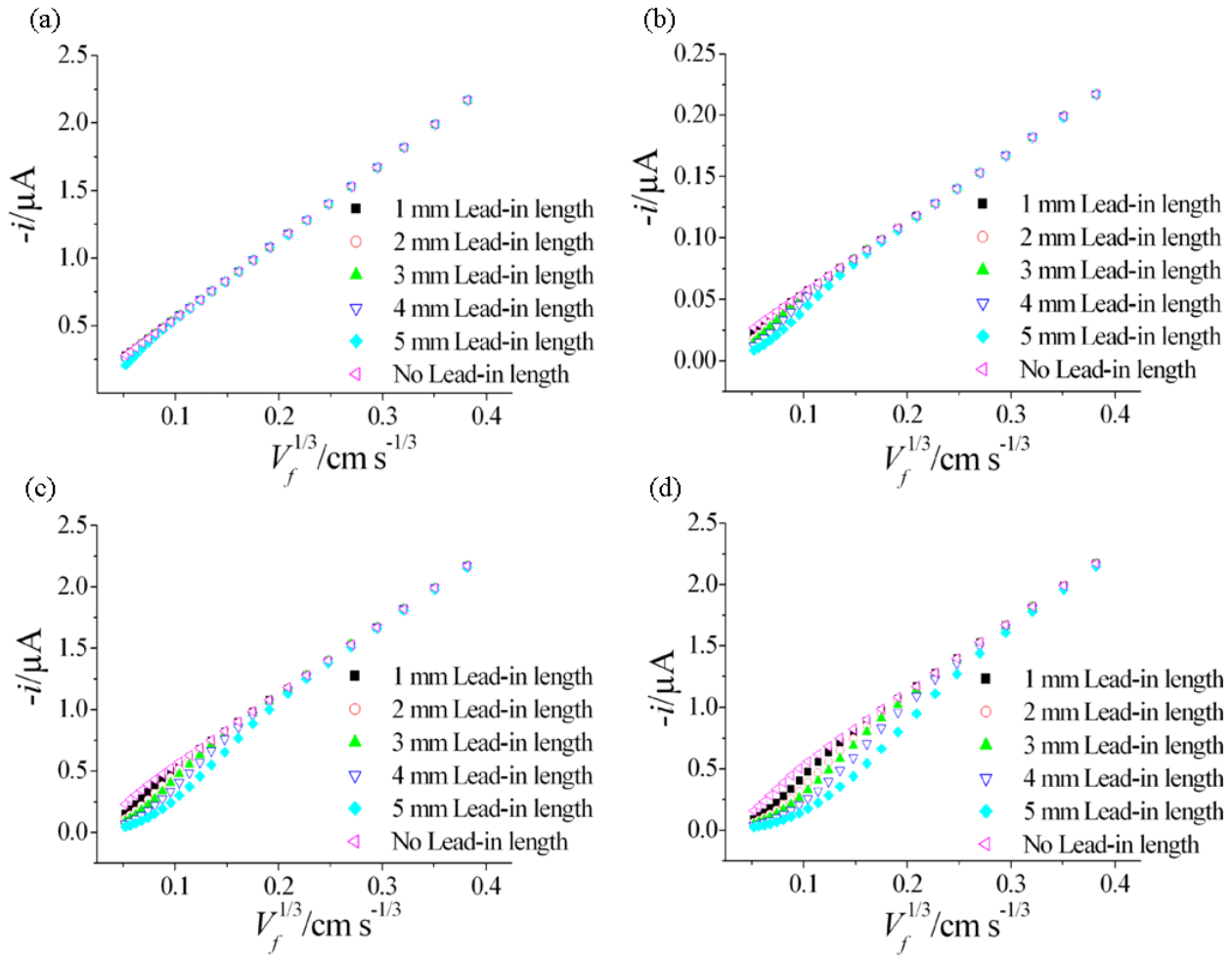

Figure 4-9 Plots of steady state current against cube root of volume flow rate for focusing ratios of (a) 1:1, (b) 5:1, (c) 10:1 and (d) 20:1

At high volume flow rates, the mass transport limited current for all cases converges to that expected for the whole cell filled with an electroactive agent. At lower flow rates, the effect of lead-in length and transport rate show clear deviations resulting from diffusional broadening of the reagent into the carrier stream. A series of concentration profiles taken from the central position (refer Figure 4-10) along the cell for a lead-in length of 1 cm at a total volume flow rate of 10^{-3} cm^3 s^{-1} and demonstrating the effect of focusing ratios can be seen in Figure 4-11a-d. Figure 4-12a-d shows the corresponding effects of volume flow rate at a fixed focusing ratio of 20:1. Both sets of figures clearly demonstrate the effect of diffusional broadening on the reagent concentration within the device.

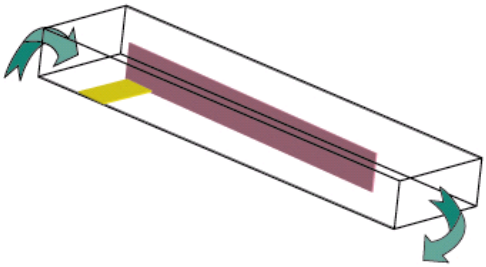

Figure 4-10 Central plane of concentration profile considered for simulation

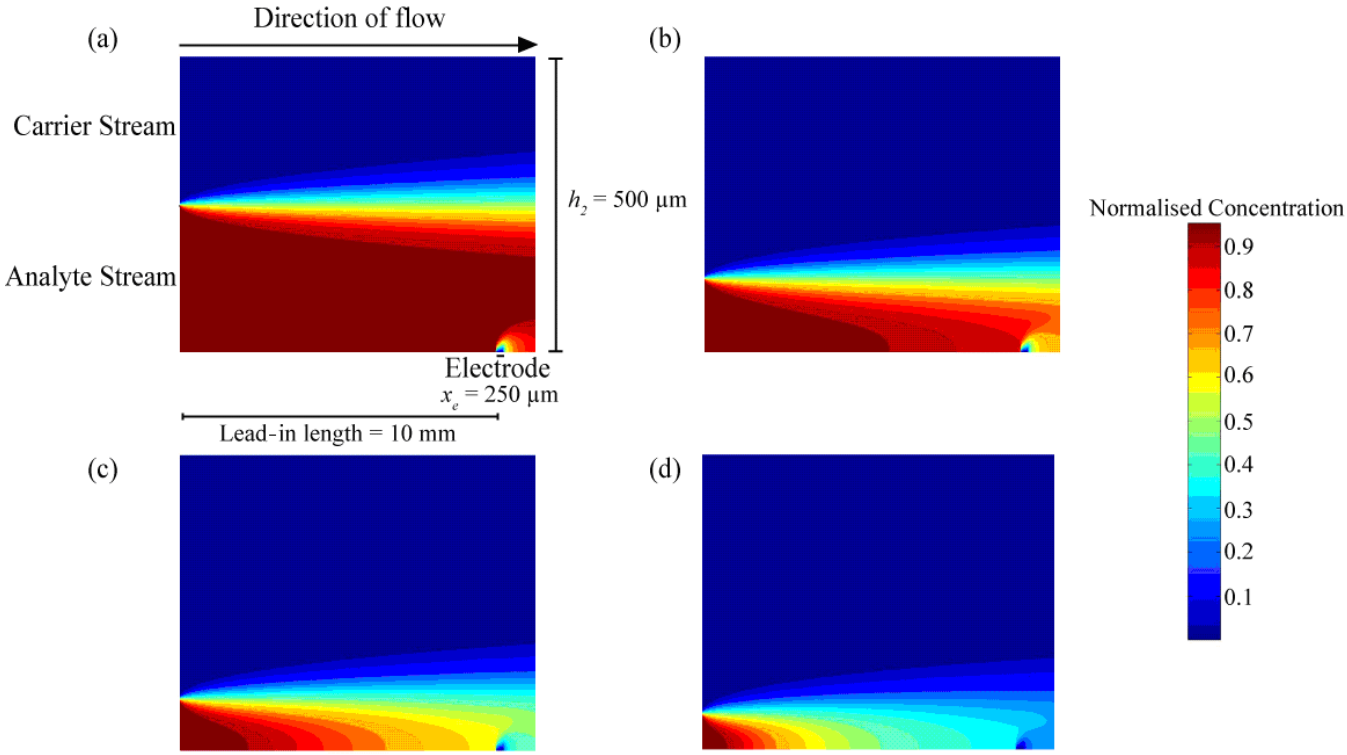

Figure 4-11 Concentration profile taken along the centre of the cell for a lead-in length of 1 cm and focusing ratios of (a) 1:1, (b) 5:1, (c) 10:1 and (d) 20:1

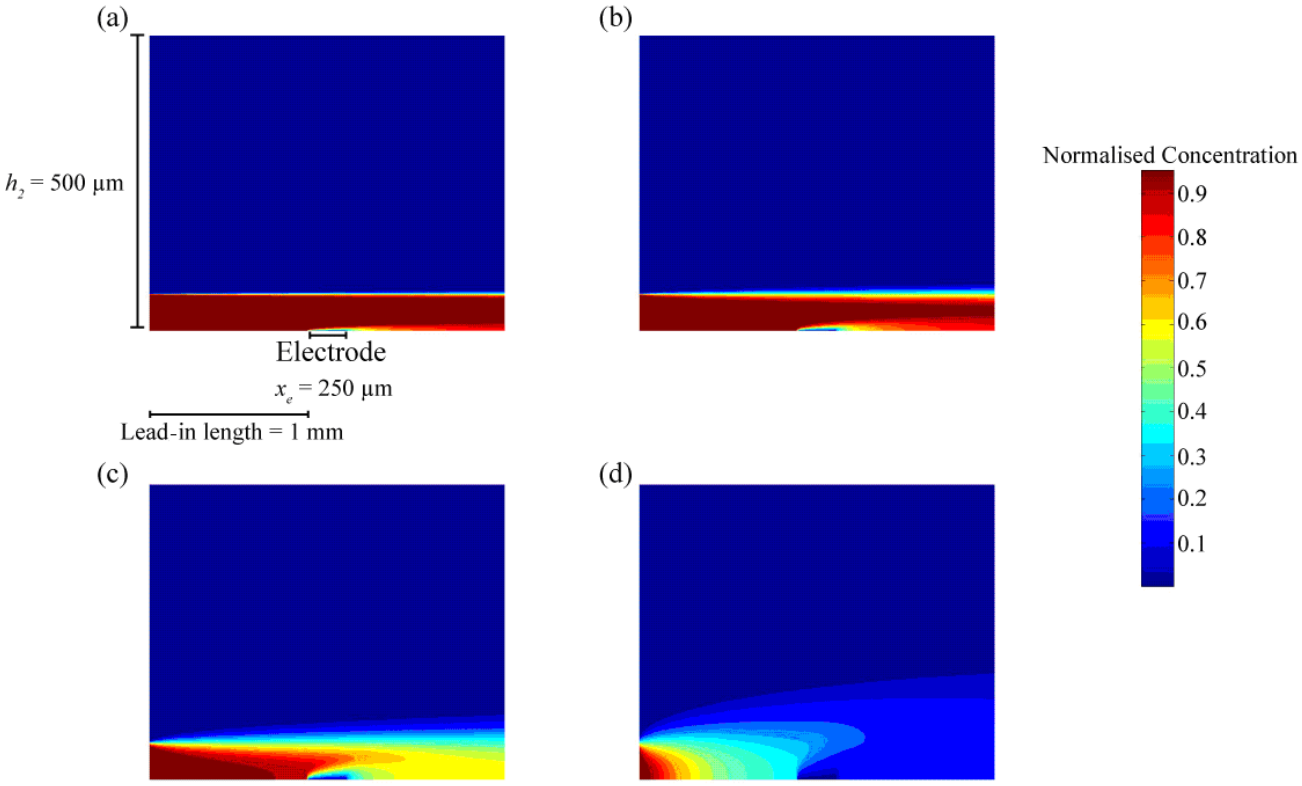

Figure 4-12 Central concentration profiles for volume flow rates of (a) 7.5×10^{-2} $cm^3 s^{-1}$, (b) 1×10^{-2} $cm^3 s^{-1}$, (c) 1×10^{-3} $cm^3 s^{-1}$ and (d) 1×10^{-4} $cm^3 s^{-1}$ with a focusing ratio of 20:1

The numerical simulations illustrate the potential to employ hydrodynamic focusing as a method to reduce the quantity of reagent required within the device, yet obtain a response equivalent to a cell full of reagent thereby offering significant potential for cost and material savings in high throughput devices. In addition, at higher focusing ratios the analyte stream occupies a much smaller portion of the channel, enabling the electrochemical depletion of species *A* to extend to the full height of the analyte stream. It was also now clear from the numerical analysis that the deviation from expected Levich behaviour, as seen at lower flow rates, does not necessarily mean complete conversion but is mostly due to the diffusional broadening of reagent stream into carrier stream. These models are thus vital in ensuring correct experimental conditions are employed to obtain high conversions.

4.6.2 Experimental Hydrodynamic Focusing Studies

Experimental studies were carried out to examine the effect of the three variables investigated using the numerical model: lead-in length, focusing ratio and total volume flow rate. An analyte stream containing 1×10^{-6} mol cm^{-3} potassium ferricyanide in 0.1×10^{-3} mol cm^{-3} potassium chloride solution and a carrier stream containing 0.1×10^{-3} mol cm^{-3} potassium chloride solution were employed for the focusing studies. In order to compare with the standard channel electrode behaviour, a control experiment where both streams contained potassium ferricyanide was also performed.

The flow to the device was controlled using two separate syringe pumps to regulate independently the flow rate of each stream. Three different focusing ratios were studied: 5:1, 12:1 and 15:1. It was difficult to conduct experiments with focusing ratios over 15:1 as it increased the back pressure on the analyte stream, hence resisting it from entering the channel. The voltammetric response of potassium ferricyanide was measured using linear sweep voltammetry. The potential difference was scanned from 0.2 to –0.5 V (vs. gold pseudo-reference electrode) at a rate of 0.04 V s^{-1}. For each experiment, voltammograms were recorded for a series of total volume flow rates between 1×10^{-2} cm^3 s^{-1} and 1×10^{-4} cm^3 s^{-1}. Sample voltammograms obtained using a focusing ratio of 5:1, 12:1 and 15:1 and a lead-in length of 0.205 cm, are shown in Figure 4-13a,c,e. The resulting variations of the transport limited current as a function of the cube root of volume flow rate are shown in Figure 4-13b,d,f. The analytically predicted current is also shown and agreement between the two sets of data was observed.

Figure 4-14 illustrates the comparison studies for all three focusing ratios together. It shows plots of the steady state current against both the cube root of the total volume flow rate and the total volume flow rate for each focusing ratio and the control (unfocused) experiment.

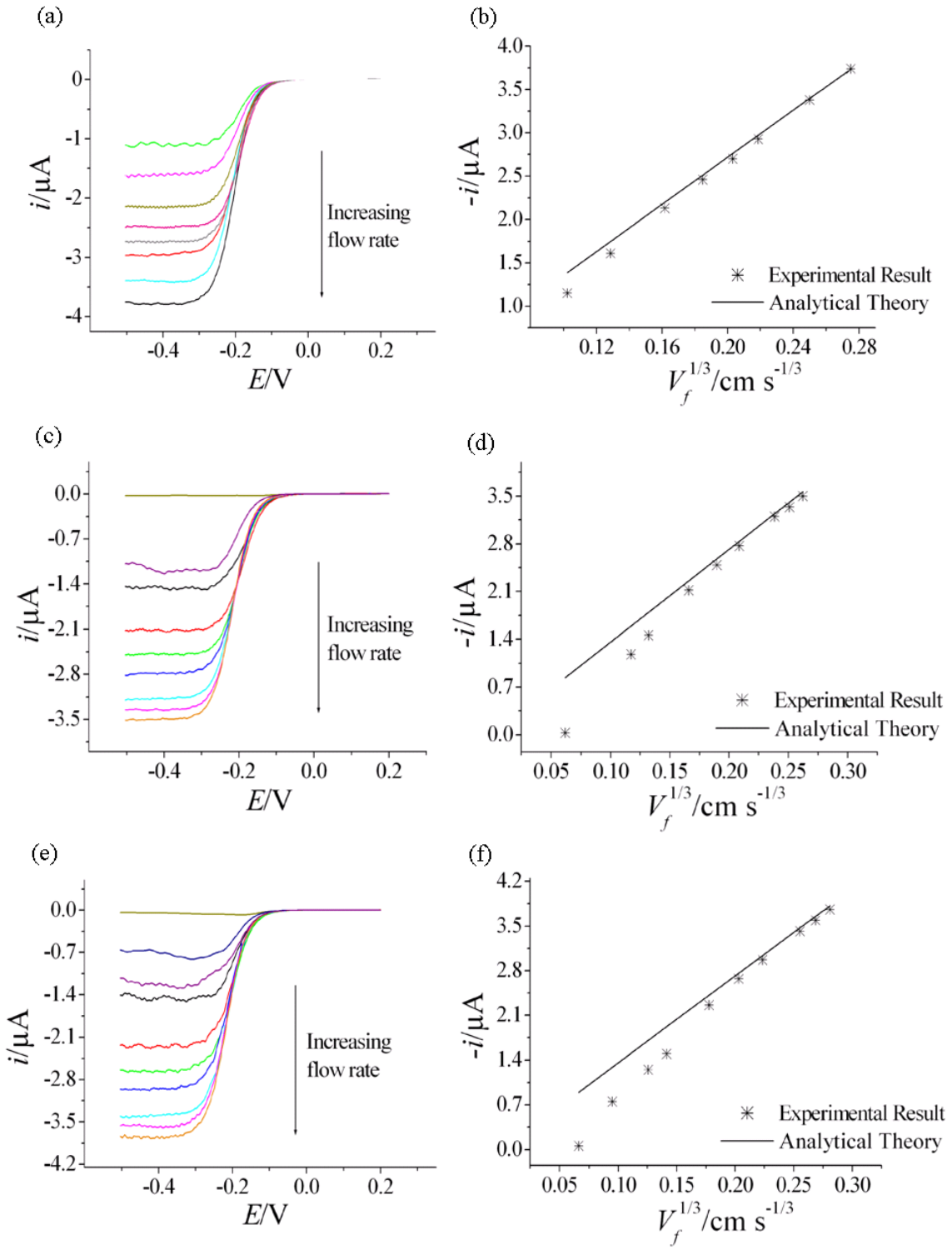

Figure 4-13 Sample linear sweep voltammograms and their corresponding plots of limiting current against the cube root of the total volume flow rate for the focusing ratio experiments with a lead-in length of 2.05 mm and focusing ratios of (a-b) 5:1 (V_f = 0.0003, 0.001, 0.002, 0.004, 0.006, 0.008, 0.01 cm^3 s^{-1}) (c-d) 12:1 (V_f = 0.0002, 0.0015, 0.0022, 0.0044, 0.0065, 0.0087, 0.013, 0.0152, 0.0173 cm^3 s^{-1}) and (e-f) 15:1 (V_f = 0.0003, 0.0008, 0.0018, 0.0026, 0.0053, 0.0081, 0.0107, 0.0161, 0.0187, 0.0213 cm^3 s^{-1})

Figure 4-14b illustrates that at higher volume flow rates, regardless of the focusing ratio, the current varies linearly (typical Levich response) with the cube root of the volume flow rate; indicating a standard voltammetric response. However, at low volume flow rates this linear relationship breaks down and the deviation from the expected response appears to be dependent on the focusing ratio. The lowest ratio (5:1) clearly deviates from the unfocused behaviour the least. The current response for the 12:1 and 15:1 are very similar and overlap at some total volume flow rates (Figure 4-14a), but in general the 15:1 focusing ratio deviates from the linear behaviour more than the 12:1 ratio.

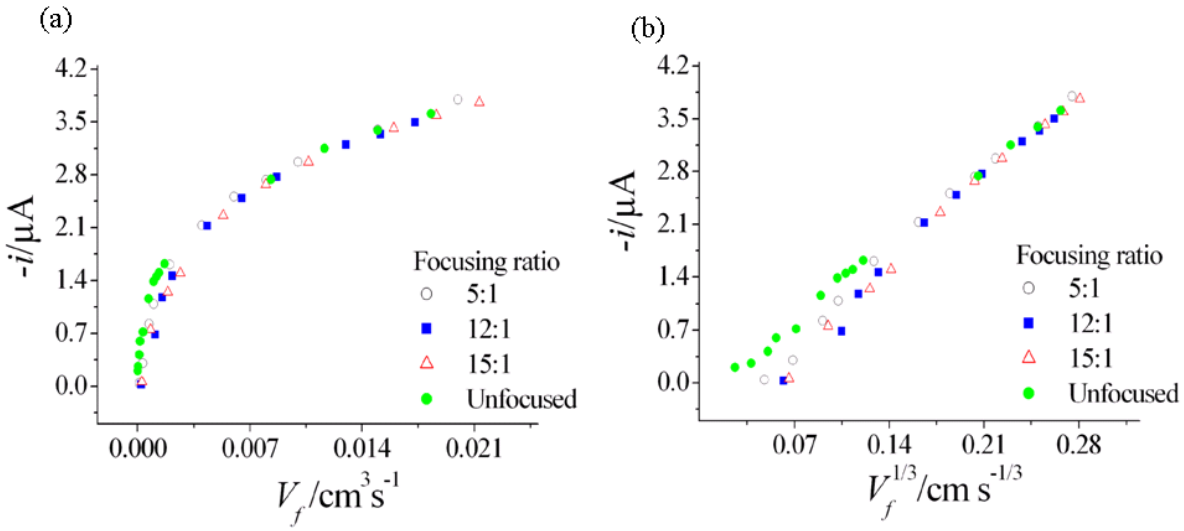

Figure 4-14 Effect of focusing ratio experimental (a) steady state current against volume flow rate (b) steady state current against cube root of volume flow rate

Finally the effect of the lead-in length on the voltammetric response of the system was investigated using three different values: 0.08, 0.16 and 0.26 cm. A focusing ratio of 12:1 was used for the following experiments. The sample voltammograms, obtained using a focusing ratio of 12:1 and a lead-in length of 0.08, 0.16 and 0.26 cm are shown in Figure 4-15a,c,e. Also seen in Figure 4-15b,d,f are their respective plots of limiting current against cube root of volume flow rates. Figure 4-16 compares the plots of steady state current against both volume flow rate and its cube root for all three lead-in lengths.

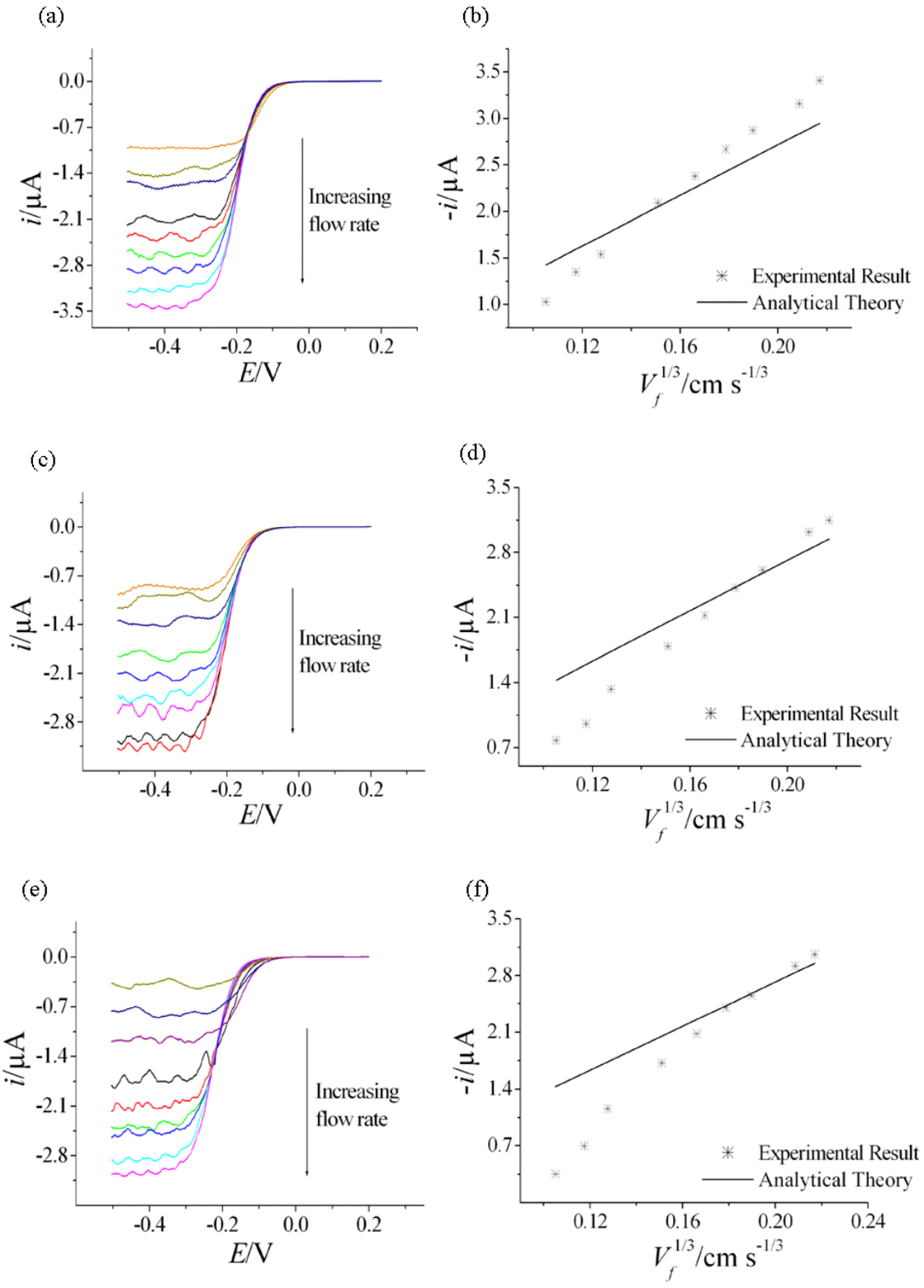

Figure 4-15 Sample linear sweep voltammograms and their corresponding plots of limiting current against cube root of total volume flow rates (V_f = 0.0011, 0.0015, 0.0019, 0.0032, 0.0043, 0.0054, 0.0065, 0.0085, 0.0097 cm^3 s^{-1}) for a cell with a focusing ratio of 12:1 and lead-in lengths of (a-b) 0.08 cm, (c-d) 0.16 cm, (e-f) 0.26 cm

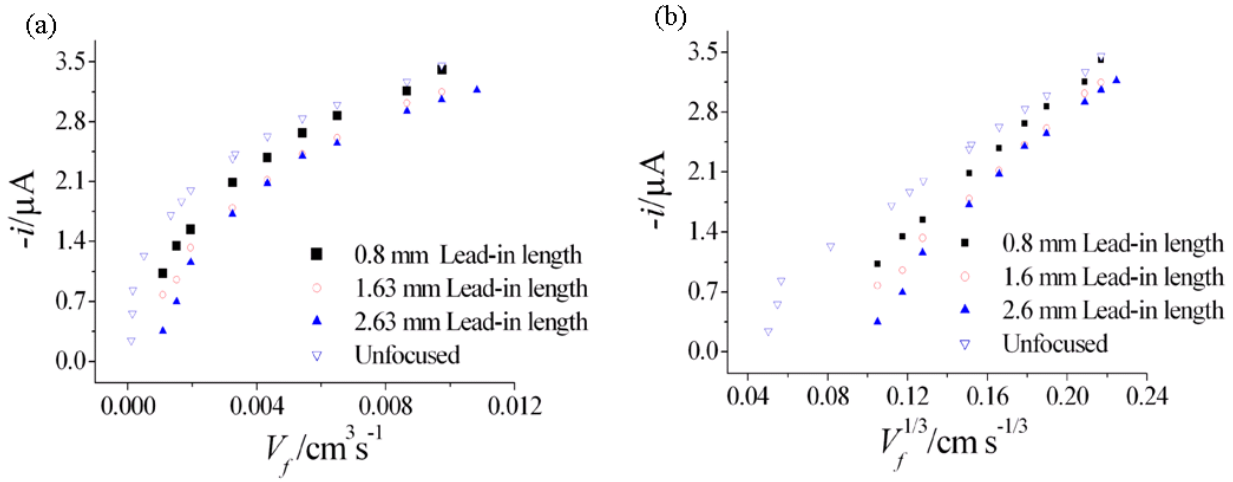

Figure 4-16 Effect of lead-in length (a) steady state current against cube root of volume flow rate (b) steady state current against volume flow rate.

Figure 4-16 shows that the current response varies linearly with the cube root of the volume flow rate. However, with increasing lead-in length the steady state current is reduced compared to the unfocused current. This effect is greatest at lower flow rates and longer lead-in lengths. These general trends are consistent with those predicted by the numerical model; as the lead-in length is increased more diffusive mixing between the streams can occur, reducing the flux of material to the electrode surface and as a result the current response is reduced. Finally, the BI numerical model was used to simulate the experimental hydrodynamic focusing system. The parameters were: h_2 = 0.025 cm, $w_e = d_d$ = 0.089 cm, x_e = 0.05 cm, x_l = 0.285 cm, 0.365 cm and 0.465 cm (for 0.08 cm, 0.16 cm and 0.26 cm lead-in lengths respectively) N_J = 500, N_K = 1000 – 2000 (depending on the lead-in length), N_I = 100, V_f = 0.0002 – 0.02 cm^3 s^{-1}, $D_{Ferricyanide}$ = 6.77 x 10^{-6} cm^2 s^{-1} and [$K_3Fe(CN)_6$]= 1× 10^{-6} mol cm^{-3}. Illustrated in Figure 4-17 are the concentration profiles obtained for various lead-in lengths for the range of flow rates mentioned above.

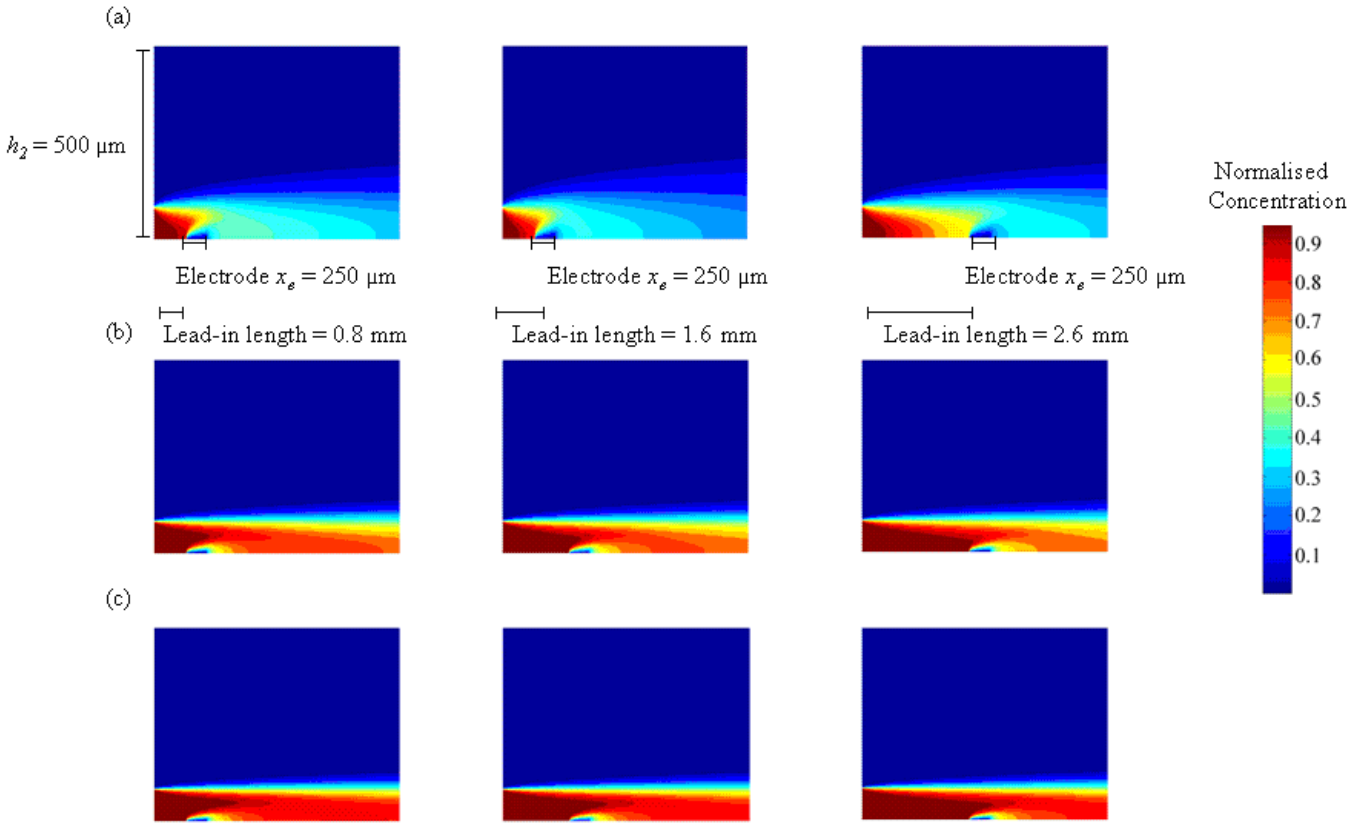

Figure 4-17 Concentration profile taken along the centre at a focusing ratio of 12:1 and for a cell of lead-in lengths of 0.08 cm, 0.16 cm and 0.26 cm at total volume flow rates of (a) 0.001 $cm^3 s^{-1}$ (b) 0.0055 $cm^3 s^{-1}$ (c) 0.0095 $cm^3 s^{-1}$

Figure 4-18a-e compares predicted and experimental responses. The model provides a qualitative description of the variation of current with volume flow rate, although absolute values of current are off-set by ~ 0.5 µA. Though the trend of the plots was adequately described by the simulation, some off-set was seen at higher lead-in lengths. This off-set was due to experimental errors which were propagated and amplified with increasing lead-in lengths. Small errors in diffusion coefficient and concentration measurements could also contribute slightly to the deviation.

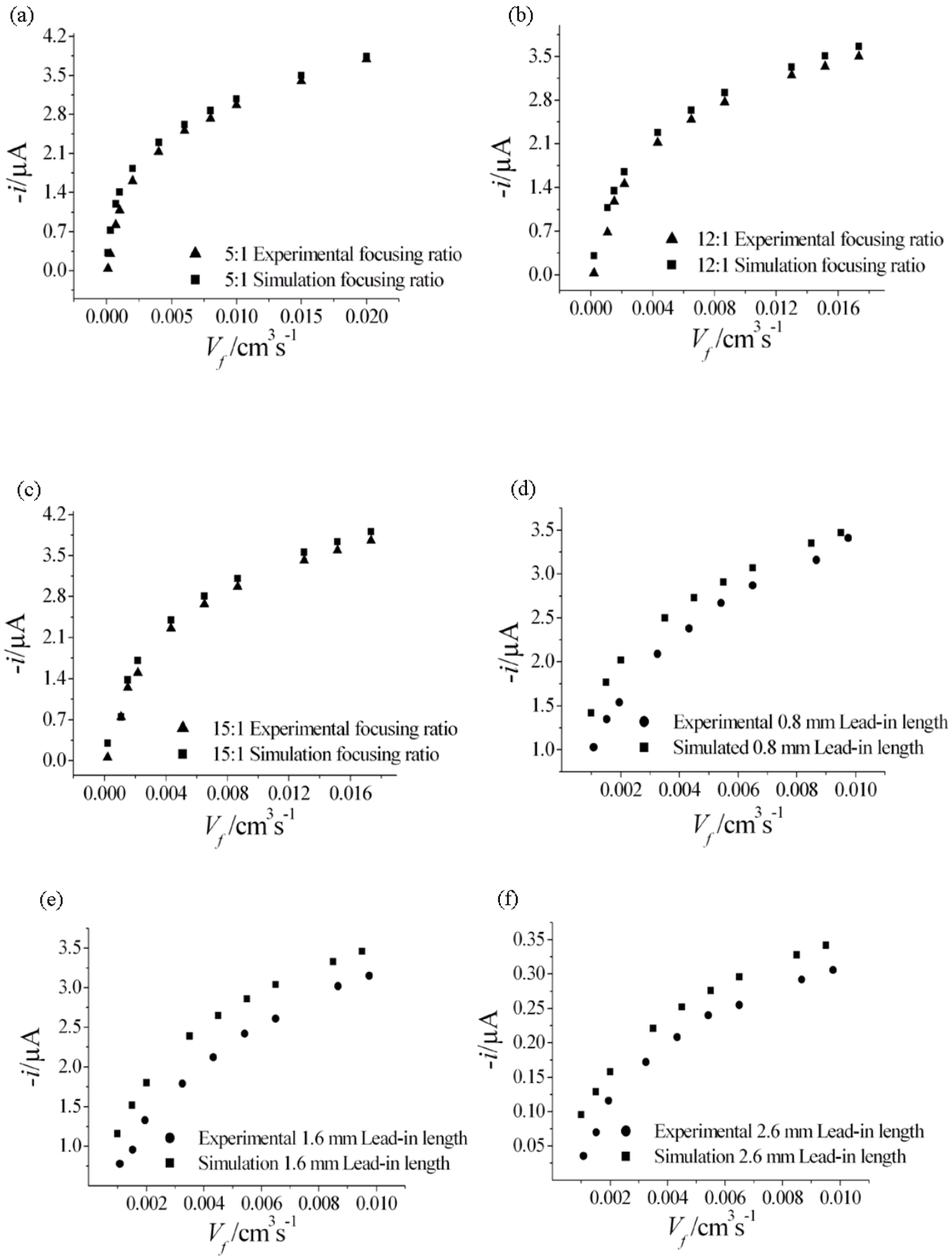

Figure 4-18 Comparison of experimental and simulated steady state currents (lead-in length 2.05 mm) for focusing ratios of (a) 5:1, (b) 12:1, (c) 15:1 and comparison of experimental and simulated steady state currents (focusing ratio 12:1) for lead-in lengths of (d) 0.08 cm, (e) 0.16 cm, (f) 0.26 cm

4.7 CONCLUSIONS

An electrochemical microreactor based on a sandwich like structure was successfully developed, fabricated and employed for hydrodynamic focusing studies. Experimental studies examining the effects of focusing ratio, lead-in length and total volume flow rate on the electrolysis response observed were carried out and compared to results predicted numerically using a finite difference model. Regimes where diffusional broadening of the reagent stream may affect the current response were identified. Diffusional broadening is low at high flow rates and hence electron transfer at the electrode occurs at the same rate as if the entire channel were filled with reactant. In contrast, diffusional broadening due to considerable lead-in lengths and high focusing ratios affect the concentration of reagents at the electrode surface at low flow rates resulting in slower electron transfer.

By applying hydrodynamic focusing, the surface area to volume ratio was effectively increased without physically altering the channel dimensions. It was demonstrated using simulations that at extremely high flow rates and focusing ratios the diffusion layer could be reduced and at the same time the amount of reagent passing over the electrode unaddressed could be minimised.

By replacing the gold electrode with boron doped diamond electrode in electrochemical micro-biosensor, regeneration of cofactors over the electrode can now be carried out more efficiently. Although it is theoretically ideal to employ hydrodynamic focusing in achieving high turnover in biocatalytic reactions but it can be practically difficult to work at the high ratios that are required for such high conversions. Also recovering cofactors from the product stream would be a challenge. Hence a system in which the cofactor or enzyme can be immobilised to channel or a network of channels such as porous electrode can be developed, by which mixing of cofactor with the product stream could be avoided and at the same time the immobilised cofactor can be regenerated electrochemically.

In the next two chapters, another application of biosensor analysis has been developed and discussed in detail. Porous photosensitive and conducting polymers were studied and further developed extensively for application in micro- and meso-chromatography and purification of proteins.

4.8 REFERENCES

[1] Matysik, F-M.; Björefors, F.; Nyholm, L. *Anal. Chim. Acta* **1999**, 385 (1-3), 409-415.

[2] Woodyer, R. D.; Johannes, T. W.; Huimin, Z. *Regeneration of Cofactors for Enzyme Biocatalysis In: Enzyme Technology* **2005**, Ed. Pandey, A.; Webb, C.; Soccol, C. S.; Larroche, C. Asiatech Publishers Inc., New Delhi, pp. 85–103.

[3] Gau, J. J.; Lan, E. H.; Dunn, B.; Ho, C. M. **2000**, http://ho.seas.ucla.edu/publications/conference/2000/MicroTas2000.pdf

[4] Deshpande, A. G.; Gu, Y.; Matthews, S. M.; Yunus, K.; Slater, N. K. H.; Brennan, C. M.; Fisher, A. C. *Chem. Eng. J.* **2009**, 149, 428-434.

[5] Horii, D.; Atobe, M.; Fuchigami, T.; Marken, F. *Electrochem. Comm.* **2005**, 7 (1), 35.

[6] Hung, C. I.; Ke, B. J.; Huang, G. R.; Hwei, B. H.; Lai, H. F.; Lee, G. B. *Journal Of Fluids Engineering Transactions Of The Asme* **2001**, 123, 672-679.

[7] Yoon, S. K.; Choban, E. R.; Kane, C.; Tzedakis, T.; Kenis, P. J. A. *J. Am. Chem. Soc.* **2005**, 127, 10466.

[8] Lee, G. B.; Chang, C. C.; Huang, S. B.; Yang, R. Y. *J. Micromech. Microeng.* **2006**, 16, 1024-1032.

[9] Yang, S. Y.; Hsiung, S. K.; Hung, Y. C.; Chang, C. M.; Liao, T. L.; Lee, G. B. *Measurement Science & Technology* **2006**, 17, 2001-2009.

[10] Brody, J. P.; Yager, P; Goldstein, R. E.; Austin, R. H. *Biophys J.* **1996**, 71, 3430–3441.

[11] Krüger, J.; Singh, K.; O'Neill, A.; Jackson, C.; Morrison, A.; O'Brien, P. *J. Micromech. Microeng.* **2002**, 12, 486.

[12] Wolff, A.; Perch-Nielsen, I. R.; Larsen, U. D.; Friis, P.; Goranovic, G.; Poulsen, C. R.; Kutter, J. P.; Telleman, P. *Lab Chip* **2003**, 3, 22.

[13] Yamada, H.; Yoshida, Y.; Terada, N. *Japanese J. App. Phy.* **2005**, 44 (12), 8739–8741.

[14] Fu, A.Y.; Spence, C.; Scherer, A.; Arnold, F. H.; Quake, S. R. *Nature Biotechnology* **1999**, 17, 1109.

[15] Roder, H. *Proc. Natl. Acad. Sci. USA* **2004**, 101, 1793–1794.

[16] Stroock, A. D; Dertinger, S. K. W.; Ajdari, A.; Mezic, I.; Stone, H. A.; Whitesides, G. M. *Science.* **2002**, 295, 647–651.

[17] White F. M: *Viscous Fluid Flow* **1991**, McGraw-Hill, New York.

[18] Hertzog, D. E.; Michalet, X.; Jager, M.; Kong, X.; Santiago, J. G.; Weiss, S.; Bakajin, O. *Anal. Chem.* **2004**, 76, 7169-7178.

[19] Chen, X.; Fenton, J. M.; Fisher, R. J.; Peattie, R. A. *J. Electrochem. Soc.* **2004**, 151 (2) E56-E60.

[20] Durliat, H.; Barrau, M. B.; Comtat, M. *Bioelectrochemistry And Bioenergetics* **1988**, 19, 413-423.

[21] Horii, D.; Atobe, M.; Fuchigami, T.; Marken, F. *Electrochem. Comm.* **2005**, 7 (1), 35.

[22] Thompson, M. D. K. *Theoretical and Applied Electrochemistry* **1939**, The Macmillan and Co. Madison, 3rd Edition.

[23] Brett, C. M. A. *Electrode Reactions in Microvolumes In*: *Comprehensive Chemical Kinetics* **1999**, Ed. Hancock, G.; Compton, R.G., Elsevier, Chap. 16, Vol. 37.

[24] Brett, C. M. A.; Maria, A. *Comp. Chem. Kinetics* **1986**, 26, 355.

[25] Cooper, J. A.; Compton, R. G. *Electroanal.* **1998**, 10, 141.

[26] Martinelli, M.; Viktorov, V. *J. Micromech. Microeng.* **2009**, 19, 025013.

[27] Ehrfeld, W.; Hessel, V.; Löwe, H. *Microreactors: New Technology for Modern Chemistry* **2000**, Wiley-VCH, Germany, pp. 1-20.

[28] Yunus, K.; Henley, I. E.; Fisher, A. C. *J. Phys. Chem. B* **2003**, 107, 3878.

[29] Sullivan, S. P.; Johns, M. L.; Matthews, S. M.; Fisher, A. C. *Electrochem. Comm.* **2005**, 7, 1323.

[30] Henley, I. E.; Fisher, A. C. *J. Phys. Chem. B* **2003**, 107, 6579.

[31] Choban, E. R.; Waszczuk, P.; Kenis, P. J. A.; Tzedakis T.; Yoon, S. K.; Kane, C. *Microfluidic Device and Synthetic Methods* **2007**, US Patent No.7273541.

[32] Matthews, S. M.; Elder, A. D.; Yunus, K.; Kaminski, C. F. Brennan, C. M.; Fisher, A. C. *Anal. Chem.* **2007**, 79, 4101-4109.

[33] Bard, A. J.; Faulkner, L. R. *Electrochemical Methods: Fundamentals and Applications* **1980,** John Wiley, New York, 2nd Edition , pp.136-140.

[34] Levich, V. G. *Physicochemical Hydrodynamics*; **1962**, Prentice-Hall: New Jersey.

[35] Matthews, S. M. *A Microfluidic Investigation of Interfacial Reaction Kinetics* (PhD Thesis) **2008.**

Chapter 5

Development and Fabrication of Patterned Monoliths

5.1 INTRODUCTION

This chapter describes the development and fabrication of a monolithic micro analytical device for lab-on-a-chip applications. As reviewed in Chapter 1, micro analytical technology offers a range of applications from proteomics to high throughput screening, polymerase chain reaction (PCR), chromatography and fuel cells [1-7]. Most of these applications involve operations such as purification, separation or selective transfer of ions, all of which require a stationary phase [8]. In the context of micro analytics, this means structuring the microchannel so as to generate a high surface area for the analytes to interact with the solid support. Microreactors have the inherent advantage of high surface area to volume ratios compared to macro-scale reactors, thereby rendering enhanced mass transfer as discussed in Chapter 1 [9]. This can be enhanced further by introducing frits or packing particles in a microchannel [10]. However, it is difficult to control the packing density of the particles and they can be a site of bubble generation [11, 12]. An alternative solution is to structure the microchannel using microtechnology techniques by etching pillar-shaped structures inside the microchannel [13]. Nonetheless, this microtechnology based route does not allow for the generation of a surface area that is high enough for the applications mentioned above. A solution to this is the use of monoliths inside microchannels. Monoliths inside microchannels can

offer a variety of functions ranging from product separation to electrochemical detection [14]. The following sections investigate the development, application and fabrication of monolithic reactors in detail.

5.1.1 Monolithic Reactors

Monoliths can be described as interconnected networks of cross-linked porous globules, providing a preferential pathway for fluid-flow through the column, and where molecular interactions take place between the analytes and the stationary phase [15]. These interconnected channels do not have dead ends and the transport of the solute to the surface of the monolith is solely by convection as opposed to diffusion, as observed in conventional media [16, 17]. The monolith approach thus represents an attractive way for the preparation of supports for various applications inside micro analytical systems. Monoliths inside a microchannel would provide devices with even higher surface area to volume ratios, enabling their use in applications requiring high-cost, low-volume reagents, such as cofactors. From a commercial perspective, the inclusion of the porous monoliths within a microchannel eliminates the need for column packing by the customer and the problems arising from bubble formation are avoided [12]. Furthermore, Mihelic *et al*. have reported a 50 percent reduction in pressure drop in CIM disk monolith columns compared to the pressure drop observed in a packed bed of spheres [18]. Figure 5-1 illustrates a photopolymerised monolith inside glass capillaries.

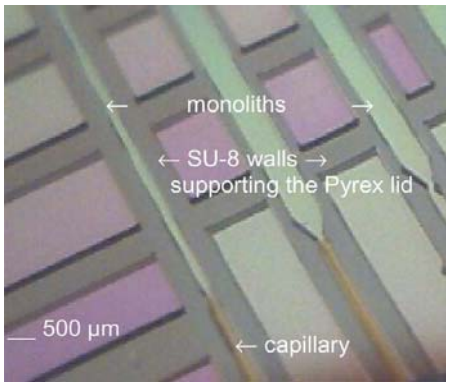

Figure 5-1 Image of a micro system with integrated monolith inside glass capillaries [19]

Monolithic microreactors can be used in downstream analysis of the final product in unit operations such as fermentation [20]. On-line calculation of selectivity and conversion will provide quick valuable assistance in process optimisation [21]. Other significant applications include separation of high value products (*e.g.* biopharmaceuticals) based on affinity or molecule size, peptidic hydrolysis and analyte pre-concentration [19]. Monoliths with conducting properties such as polypyrrole or polyaniline can be used as electrodes in sensors and fuel cells [7]. Fabrication of conducting monoliths is far less expensive than using traditional noble metal electrodes.

Various fabrication methods of monolithic channels have been developed depending on the starting substrate. Oriel and Dufaud *et al*. have investigated a method for the production of porous poly(dimethyl siloxane) (PDMS) beads from cross-linked emulsions [22, 23]. These devices have been used in the fabrication of high surface to volume reactors, valves and filters [24, 25]. Duan *et al.* have carried out *in situ* polymerisation of acrylamide monomers, glycidyl methacrylate (GMA) and ethyleneglycol dimethacrylate (EGDMA), inside a microreactor in the presence of a binary porogenic mixture of dodecanol and cyclohexanol [26, 27]. Apart from PDMS and polyacrylaminde monoliths, Stejskal and coworkers have demonstrated the fabrication of conducting polyaniline from oxidation of aniline hydrochloride with ammonium peroxydisulphate in aqueous medium at ambient temperature [28]. However, these polymers and polymerisation techniques do not have the flexibility of synthesising monoliths of desired dimension and shape, at predetermined location and with variable pore size. In this chapter, two main categories of monoliths were studied in detail with the primary goal of obtaining their micropatterned structures: (i) photopolymerised monolith: poly(2-hydroxyethyl methacrylate-co-ethyleneglycol dimethacrylate), (ii) electrochemically polymerised conducting monolith: polypyrrole. A brief theory and background on these monoliths is presented in the following sections.

5.1.2 Photopolymerised Monoliths

Photopolymerisation is a light-induced chain growth reaction (addition of two monomers having double or triple bonds that can break easily and form a link) that converts a liquid monomer into a solid high molecular weight polymer [29]. The use of light, rather than heat, to drive the reactions leads to a variety of advantages, including solvent-free formulations, very high reaction rates (k = 10^2-10^4 L (mol s)$^{-1}$) at room temperature, spatial control of the polymerisation, low energy input, and chemical versatility (a variety of monomers can be polymerised photochemically) [29-31]. Photopolymerisation takes place in three distinct stages: (i) Initiation (a photoinitiator generates radicals by undergoing decomposition when exposed to UV light (λ~360nm)), (ii) Propagation (the radicals generated induce growth of the macromolecular chain by a kinetic mechanism and repeated addition of a monomer to the growing chain) and (iii) Termination (the kinetic chain is brought to halt by neutralisation or transfer of active centres by the radicals present in the solution).

Unlike commercially available polymer photoresists used in photolithography, monoliths synthesised by photoinitiated polymerisation of methacrylate monomers, such as 2-hydroxyethyl methacrylate (HEMA), can be made porous [32]. Chuda *et al.* have studied the characteristics and fluidic properties of porous poly(HEMA) prepared by radiation induced polymerisation inside glass capillaries (refer Figure 5-1) [19]. They have demonstrated the effect of different monomer concentrations, porogen amounts and ultraviolet (UV) exposure time on monolith properties. Another advantage of poly(HEMA) monoliths is their biocompatibility, hence they can be used in biomedical applications [33]. Carlier *et al.* have demonstrated the digestion of benzoyl arginine ethyl ester by immobilising trypsin on poly(HEMA) monoliths [34].

However, there are two main limitations of the photopolymerised monoliths that have been previously reported. First is the high pressure drop observed in these monoliths, which eventually leads to increase in the operating costs. The second limitation is that due to the low viscosity of the

monomer and the liquid porogen used, these structures can only be formed inside either glass capillaries or microchannel moulds. There is no flexibility or freedom for micropatterning photopolymers of desired shapes and size.

A solution to both these limitations, as reported in this thesis, is the use of a solid porogen such as salt crystals or silica particles. Using a solid porogen would increase the viscosity of poly(HEMA), thereby allowing the fabrication of complex micropatterned structures such as static mixers, porous membrane separating channels or chromatographic columns with high aspect ratios. In addition, pore size and porosities could be controlled by using porogen particles of known dimension. This has been explained in detail in Section 5.3.1.

5.1.3 Electrochemically Polymerised Monoliths

Another monolith that has great potential in micro analytical applications is the conducting monolith. Conducting polymers are conjugated polymers, namely organic compounds, which have an extended p-orbital system, through which electrons can move from one end of the polymer to the other. Classic conductive polymers are typically derivatives of polyacetylene, polyaniline or polypyrrole [35].

Electrochemical synthesis of conducting polymers is a complex process. It involves diffusion of the monomer to the electrode surface, electron transfer between the electrode and the monomer, and complex reactions. As with photopolymerisation, the steps involved in electrochemical polymerisation of pyrrole are (i) Initiation (oxidation of monomer at the electrode to form cation radical), (ii) Propagation (coupling of cation radicals with neutral molecules or other radicals) and (iii) Termination (neutralisation of cation radicals present in the solution) [36].

Conducting polymer electrodes have gained much interest recently in fuel cells. Electrode materials such as gold, copper, carbon cloth, carbon paper or graphite have been commercially used in micro-

fuel cells for over a decade [37]. Some of these materials, such as copper, are unstable and form an insulating oxide film, resulting in a narrow potential window and a low surface area. Most of these materials exhibit limited performance, since they do not meet long term requirements for a viable fuel cell performance, durability and cost [38]. Therefore there is considerable interest in developing alternative electrode materials with a highly porous structure.

Electrochemically micropatterned conducting monoliths provide a new direction in developing and fabricating economical and environmentally friendly fuel cells. Favourable structural and chemical properties of monoliths made from conducting polymers like polyaniline (PolyAni) or polypyrrole (PolyPr) could be used to provide a porous electrode material [39]. A number of studies have focused on developing a method for producing a porous polyPr film. Li *et al.* have reported the synthesis of porous polypyrrole by the electrochemical polymerisation of a mixture of two types of electropolymerisable monomers [40]. Following the polymerisation, one of the polymers was removed from the composite film leaving voids where the polymer had been located, resulting in a highly porous structure. Combining electrochemical polymerisation technique with photolithographic micropatterning will further broaden the scope of application of conducting monoliths.

The main objective of this chapter was to study the development and fabrication of two monoliths that could potentially be used in the development of bio-analytical devices. This chapter has been divided into two sections. In the first section, the development and fabrication of well-defined monolithic micro structures made from photopolymerised poly(HEMA-co-EGDMA) has been reported. Poly(HEMA-co-EGDMA) monoliths were characterised using physical and hydrodynamic techniques. An application of these monolithic columns in meso-chromatography has been discussed in the next chapter in detail. In the second section, an electrochemically polymerised micropatterned monolith (polyPr) with conducting properties was synthesised for

potential application in sensors and fuel cells. Electrochemical characterisation of polyPr and its composites was performed by studying electrochemical analysis of a single-electron oxidation of N,N,N′,N′-tetramethyl-p-phenylenediamine (TMPD) [41].

5.2 METHODS AND TECHNIQUES - EXPERIMENTAL

5.2.1 Photopolymerised Monolith Details

Photopolymer studies were carried out in batch and flow systems. The experimental and fabrication details for both the systems have been described below separately.

5.2.1.1 Batch System

1.) ***Fabrication of Mould***

Sealed and unsealed macro moulds of SU8 2100 epoxy resin (length 3 cm, height 0.025 cm and width 0.03 cm, 0.11 cm,0.15 cm and 3 cm) were fabricated using standard photolithographic techniques (refer Section 2.3) or made on glass (length 3 cm, height 0.055 cm and 0.07 cm and width 3 cm) using heat laminate sheets. The moulds were silanised with 3-aminopropyltrimethoxysilane before being filled with porogen or monomer to facilitate hydrogen binding between polymer and substrate.

2.) ***Monolith Synthesis***

The polymer selected for photopolymer studies was poly(HEMA-co-EGDMA) due to its fast reaction kinetics [42]. Monomer HEMA and cross-linker EGDMA were mixed in 3:2 volume ratio and dimethoxyphenyl acetophenone (DMPA) was added as photoinitiator (1 volume(%)). This mixture was exposed to UV light using a commercial mask aligner through a patterned photomask. Figure 5-2 below illustrates the photopolymerisation reaction scheme.

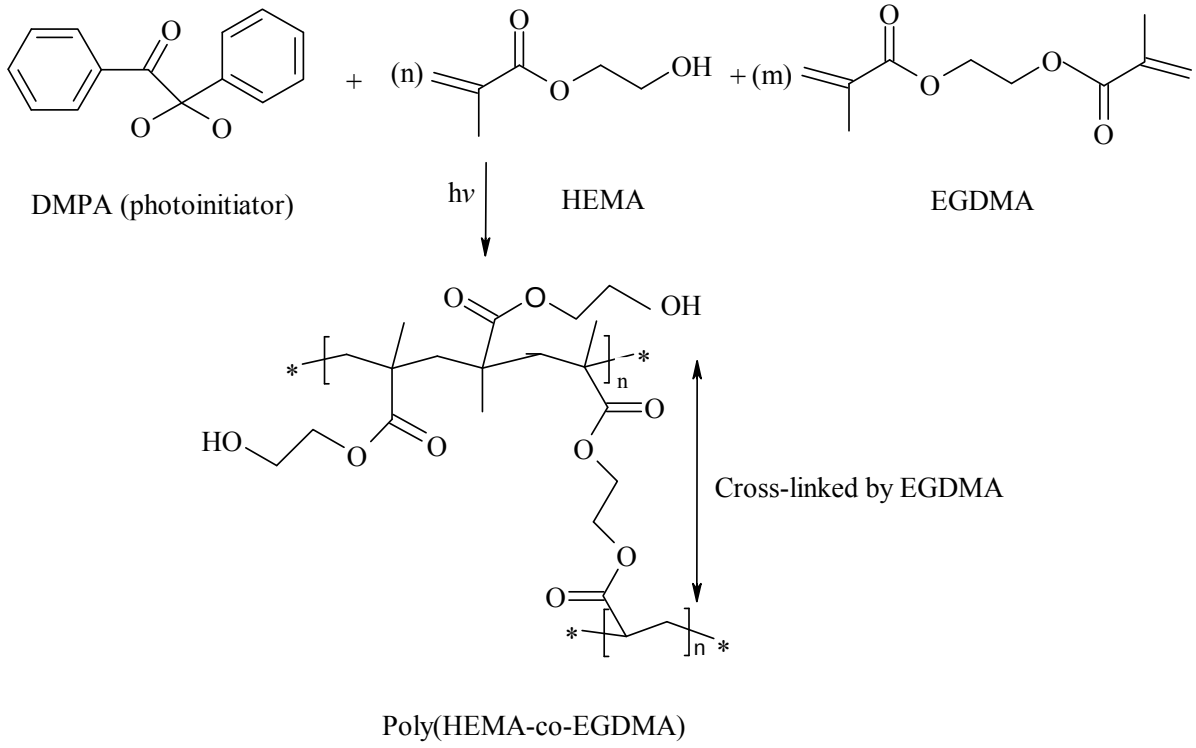

Figure 5-2 Synthesis of poly(HEMA-co-EGDMA) by photopolymerisation

Porosity in poly(HEMA-co-EGDMA) was introduced using two solid porogens: i) silica particles ii) ammonium chloride (NH_4Cl) particles.

i) *Poly(HEMA-co-EGDMA) Synthesis with Silica as Porogen*: Silica particles of 36 μm and 94 μm diameter were used for porogen studies. SU8 and glass-laminate sheet moulds of height 250 μm were filled with silica particles and fused using silane for 30 minutes. The moulds were then filled with a mixture of HEMA, EGDMA and DMPA as prepared above and exposed to UV light through a photomask. The polymerised monoliths were developed using 1 x 10^{-3} mol cm^{-3} NaOH as an etching agent.

ii) *Poly(HEMA-co-EGDMA) Synthesis with NH_4Cl particles as Porogen*: NH_4Cl particles of size 60 μm, 100 μm, and 160 μm were prepared using a pulveriser and particle sieve. The particle size distribution was obtained using a laser light scattering particle sizer. The glass-laminate sheet moulds were filled with approximately 1 g of NH_4Cl particles that were subsequently fused using humidification (95% *RH*). The humidification time

depended on the volume of NH_4Cl used and was approximately between 10 to 15 minutes for 0.055 cm and 0.07 cm height moulds. The fused NH_4Cl particles containing moulds were filled with a mixture of HEMA, EGDMA and DMPA (as described above) and polymerised using UV light, using a photomask. The polymer monolith was developed using deionised water to dissolve NH_4Cl particles. Figure 5-3 below illustrates a schematic of the steps involved in photopolymerisation using NH_4Cl as porogen.

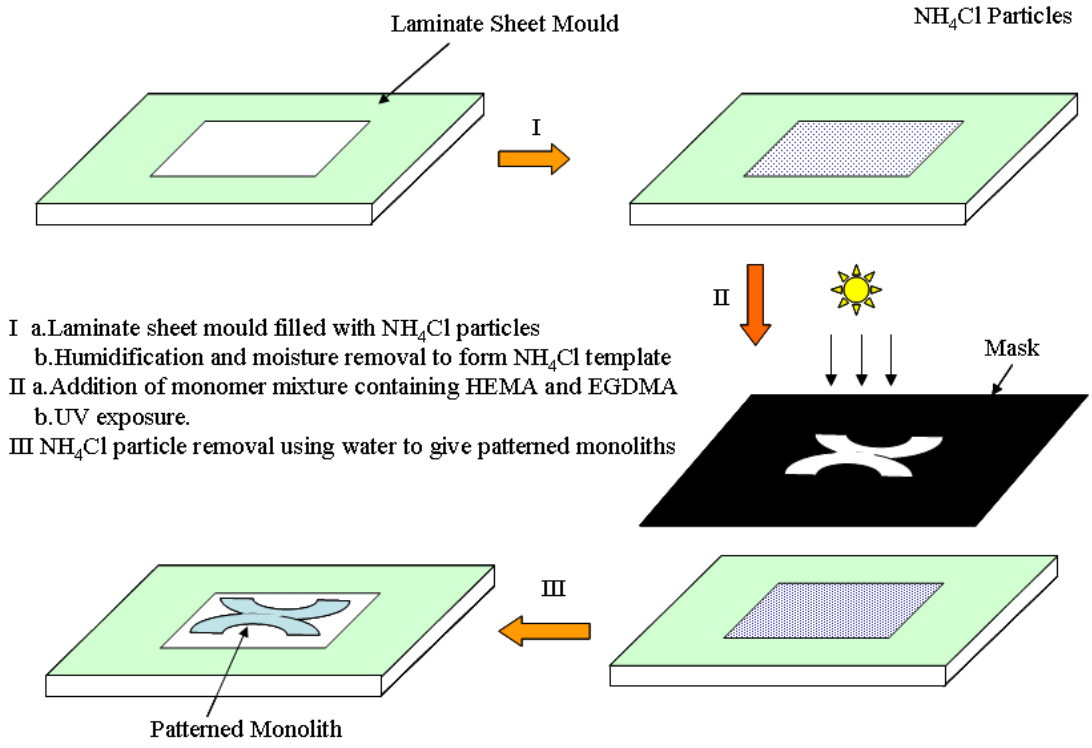

Figure 5-3 Schematic of preparation of NH_4Cl template and *in situ* photopolymerisation of monomers HEMA and EGDMA

3.) *Monolith Characterisation*

Poly(HEMA-co-EGDMA) monoliths were characterised using BET adsorption, Mercury (Hg) porosimetry, laser particle size analyser and scanning electron microscopy (SEM) (refer Section 5.3.1.1).

5.2.1.2 Flow System

1.) *Monolith Fabrication inside Mesochannel*

Mesochannels of width (w) 0.15 cm, length (l) 2.5 cm and height (h) 0.055 cm or 0.07 cm were fabricated for pressure drop studies by micromachining glass wafers. A polymer monolith of length (L) 1 cm was patterned inside the channel by the process discussed above with NH_4Cl particles (d_p = 60 μm, 100 μm and 160 μm) as porogen. Glass capillaries (i.d. = 0.162 cm) formed the inlet and outlet and were sealed using epoxy resin.

2.) *Hydrodynamic Characterisation-Experimental and Analytical*

Hydrodynamic characterisation was carried out using pressure drop measurement. The fluid (water) flow was controlled using two syringe pumps with typical flow rates between 1.7 x 10^{-5} cm^3 s^{-1} and 3.3 x 10^{-2} cm^3 s^{-1}. The pressure drop at various flow rates was measured using a pressure drop sensor (Pneumatic Hand-held Manometer). Bed permeability was calculated using Darcy's correlation for flow through porous bed, which is expressed as [43]:

$$V_f = \frac{-\kappa A \Delta P}{\mu L} \qquad (5.1)$$

Where, V_f (cm^3 s^{-1}) is the total volume flow rate, κ (cm^2) is permeability of the medium, A (cm^2) is the cross-sectional area to flow, ΔP (kPa) is the pressure drop, L (cm) is the length of monolith and μ (Pa s) is the dynamic viscosity.

Analytical pressure drop calculations were performed using Hagen-Poiseulle equation for laminar flow in straight tubes. The equation is only valid for laminar flow which assumes the capillary model, where porous material is regarded as a bundle of tangled tubes of uneven cross-section [18, 44, 45]. The equation is given as.

$$\frac{\Delta P}{L} = \frac{8\mu V_{pore}}{r_H^2} \tag{5.2}$$

Where $\Delta P/L$ (Pa cm^{-1}) is pressure gradient, V_{pore} (cm s^{-1}) is pore velocity {pore velocity (V_{pore}) = superficial velocity (V_s)/bed voidage (ε)}, r_H (cm) is hydraulic radius of pore, and η (Pa s) is viscosity of water.

5.2.2 Electrochemically Polymerised Conducting Monolith Details

5.2.2.1 Polymer Synthesis

Bulk electrochemical polymerisation of pyrrole (Pr) over gold electrodes was performed using cyclic voltammetry (CV), by sweeping the voltage from -0.8 to +1.0 V. Figure 5-4 below illustrates the electrochemical polymerisation scheme. A 0.4 x 10^{-3} mol cm^{-3} pyrrole solution was prepared in 0.1 x 10^{-3} mol cm^{-3} phosphate buffer saline (PBS) as background electrolyte. A platinum mesh, silver wire and a gold electrode (1 cm x 2 cm) were used as counter, reference and working electrodes respectively. Cyclic voltammetry was performed at a scan rate of 0.2 V s^{-1}. Micropatterned structures of polyPr were obtained by using patterned gold electrodes (fabricated using photolithography-refer Section 2.3) of various shapes as template.

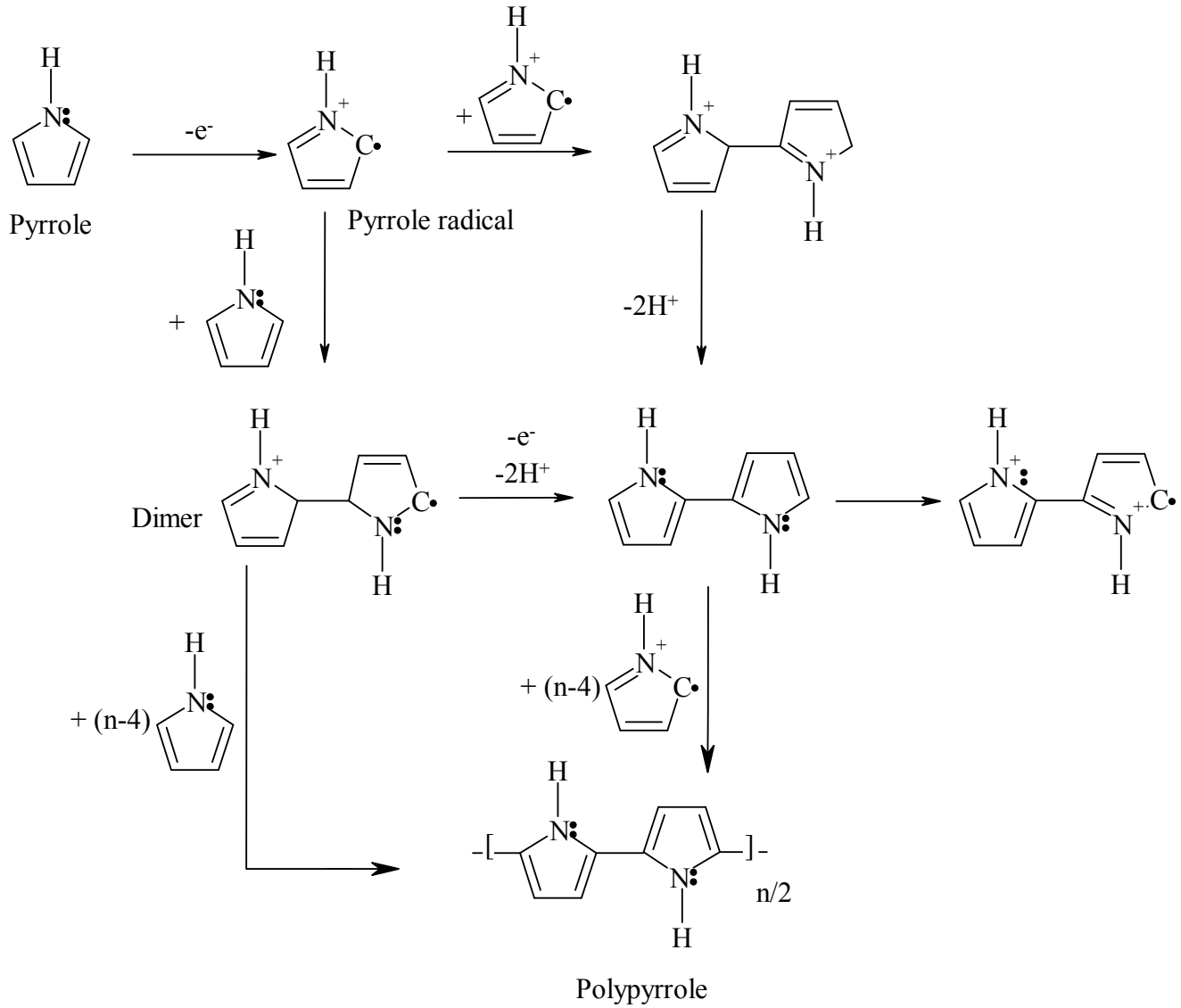

Figure 5-4 Synthesis of polypyrrole by electrochemical polymerisation

Porosity in polyPr was introduced using the following three techniques.

i) NH_4Cl Template

ii) Poly(HEMA-co-TEGDA) Template

iii) Electrochemical Polymerisation of Two Monomers

i) *NH_4Cl Template Technique:* Three bands of 1 cm x 2 cm gold electrodes were fabricated on a glass wafer using photolithography. A heat laminate film was positioned and sealed over the electrodes to act as a mould. The mould was filled with approximately 0.5 g of

NH_4Cl particles (d_p = 100 μm), spread uniformly across the exposed electrodes, and humidified (95% *RH*) for 10-15 minutes. The three electrodes were then used as working, counter and reference electrodes. PolyPr was electrochemically synthesised on the working electrode, by slowly injecting 0.4 x 10^{-3} mol cm^{-3} pyrrole solution (in 0.1 x 10^{-3} mol cm^{-3} PBS) into the NH_4Cl template on the glass wafer, by performing CV (-0.8 to +1.0 V) at a scan rate of 0.2 V s^{-1}. A drawback of this method was the dissolution of NH_4Cl template, once it got saturated with aqueous pyrrole solution over time.

ii) *Poly(HEMA-co-TEGDA) Template:* In this method, poly(2-hydroxyethyl methacrylate-co-tetraethyleneglycol diacrylate) (poly(HEMA-co-TEGDA)) was used as a polymer matrix template for electrochemical polymerisation of pyrrole monomer. The polyPr_poly(HEMA-co-TEGDA) composites thus obtained had improved mechanical properties. Like the first method, three bands of gold electrode evenly covered with NH_4Cl within a laminate film mould were prepared. To fabricate polyPr_poly(HEMA-co-TEGDA) composites, a monomer mixture of HEMA, cross-linker TEGDA and pyrrole was prepared in a volume(%) composition of 80:10:10. 1 volume(%) of photoinitiator dimethoxyphenyl acetophenone (DMPA) was added to this monomer mixture. TEGDA is similar to EGDMA as a cross-linker. However it has better swelling properties in aqueous system than EGDMA. This is useful, as an aqueous based pyrrole solution was used during electrochemical polymerisation process [46]. The monomer mixture was added to the mould containing NH_4Cl, just enough to saturate NH_4Cl, and was UV polymerised for 60 seconds. After UV light exposure, NH_4Cl particles were etched away using deionised water. The electrode with poly(HEMA-co-TEGDA) template was then electrochemically polymerised with 0.4 x 10^{-3} mol cm^{-3} pyrrole solution (in 0.1 x 10^{-3} mol cm^{-3} PBS), by performing CV at a scan rate of 0.2 V s^{-1}. The

schematic of the fabrication procedure has been illustrated in Figure 5-5.

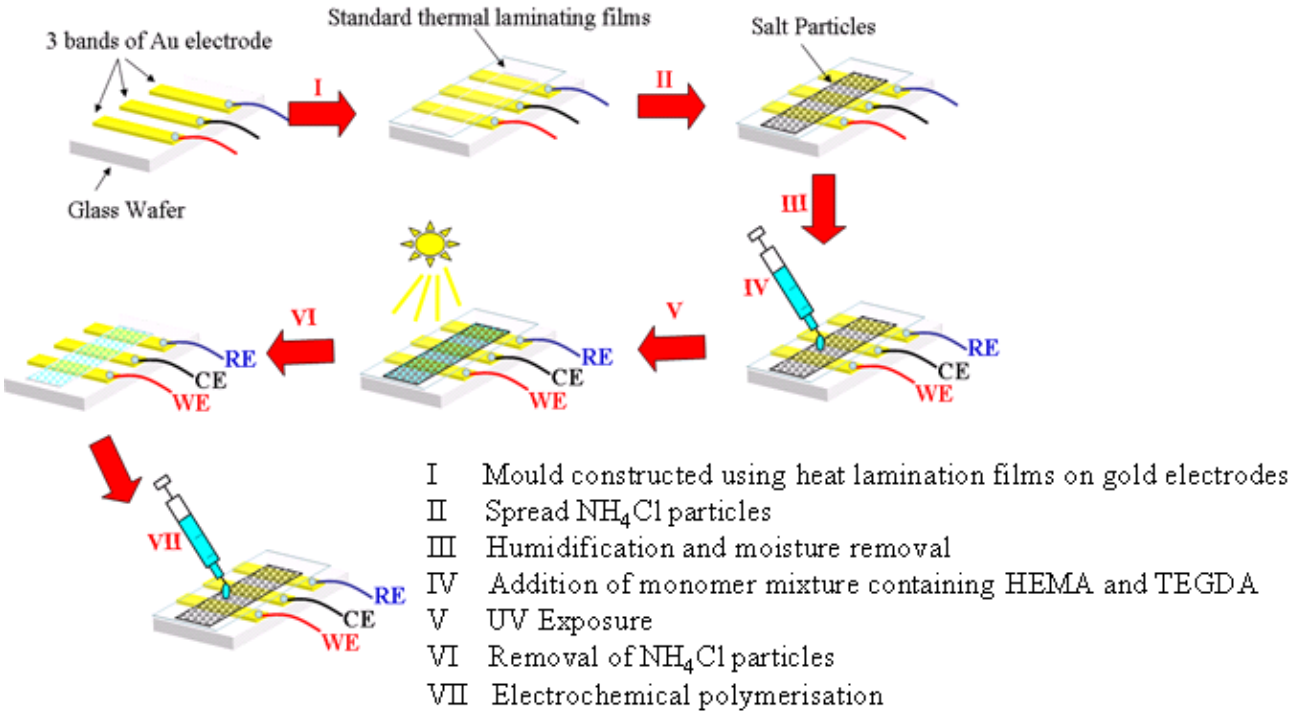

Figure 5-5 Schematic of NH_4Cl template preparation and *in situ* electrochemical polymerisation of pyrrole

iii) *Electrochemical polymerisation of Two Monomers:* The same design of glass wafer, with three gold band electrodes as described above was used. A solution containing 0.4 x 10^{-3} mol cm^{-3} pyrrole and 2.5 x 10^{-3} mol cm^{-3} methylene blue (MB) in 0.1 x 10^{-3} mol cm^{-3} phosphate buffer saline aqueous solution was prepared. The electrochemical polymerisation was performed using CV (-0.8 to +1.0 V) at a scan rate of 0.025 V s^{-1}. The influence of number of scans was investigated. After polymerisation, the polyPr and poly(MB) composite film (polyPr_MB) was immersed in acetone for 48 hours to remove the poly(MB) and reveal the porous structure.

5.2.2.2 Electrochemical Analysis of N,N,N',N'-Tetramethyl-P-Phenylenediamine (TMPD) using Conducting Polymers

Six 0.03 cm x 0.135 cm gold microelectrodes were fabricated using standard photolithographic procedure, detailed in Chapter 2. They were then used as substrates to synthesise six polyPr

composite electrodes. Table 5-1 below lists all the electrodes used during the experiments.

Electrode Description	**Electrode Abbreviation**
Gold electrode	Au
Gold electrode deposited with a bulk pyrrole film	Bulk PolyPr_Au
Gold electrode deposited with a porous polypyrrole film using a NH_4Cl template	Porous PolyPr_NH_4Cl_Au
Gold electrode deposited with a porous polypyrrole film using a poly(HEMA-co-TEGDA) template	Porous PolyPr_Poly(HEMA-co-TEGDA)_Au
Gold electrode deposited with a porous polypyrrole film obtained from a polypyrrole/ poly(methylene blue) composite film	Porous PolyPr_MB_Au
Gold electrode deposited with a bulk pyrrole film with platinum deposited onto the polypyrrole film	Bulk PolyPr_Au_Pt
Porous PolyPr_MB_Au with platinum deposited onto the polypyrrole film.	Porous PolyPr_MB_Au_Pt

Table 5-1 Electrodes fabricated for electrochemical analysis of N,N,N′,N′-tetramethyl-p-phenylenediamine

The conditions for electrochemical polymerisation of pyrrole were maintained to be the same in all electrode materials. A total of 20 cyclic voltammetry cycles were used to fabricate all polyPr films. The electrodes were characterised using CV at scan rates of 0.025, 0.05, 0.1, 0.02 and 0.400 V s^{-1}. A mixture of 1 x 10^{-6} mol cm^{-3} N,N,N′,N′-tetramethyl-p-phenylenediamine (TMPD) and 0.1 x 10^{-3} mol cm^{-3} tetrabutylammonium perchlorate (TBAP) was prepared in acetonitrile. A platinum basket was used as a counter electrode and silver/silver chloride was used as a reference electrode.

The electrochemical reactions that drive the production of current in fuel cells do not occur without the use of platinum catalyst [47]. Therefore the electrochemical response of the polyPr films, when coated with platinum, was also studied. The platinum was deposited using the electroplating procedure described in Appendix 3 (A.3.1), following the completion of the polyPr procedure.

5.3 RESULTS AND DISCUSSION

The objective of this chapter was to develop and fabricate micropatterned photo and electrochemically polymerised monoliths and characterise the monoliths by using physical, hydrodynamic and electrochemical techniques. The following section has been divided into two parts: (1) Photopolymerised monolith studies and (2) Electrochemically polymerised monolith studies.

5.3.1 Photopolymerised Monolith Studies

5.3.1.1 Batch System – Effect of Porogen and UV Time

The monoliths synthesised from poly(HEMA-co-EGDMA) were made porous using the following two porogens (i) silica particles (ii) NH_4Cl particles. Silica particles were first chosen as the solid porogen because they are inexpensive and are available in wide range of particle diameters. UV polymerisation time measured for features of width 250 μm, obtained through a photomask, is tabulated in Table 5-2.

Average Silica Particle Diameter d_p (μm)	**UV Exposure Time** t (s)	
	h=0.025 cm	h =0.055 cm
36	9	24
94	5	12

Table 5-2 UV polymerisation time variation with silica particle diameter

Elaborate microfabricated monolith structures with cross-sectional dimensions up to 125 μm could be made using silica particles as a porogen. To illustrate this, Figures 5-6a,b show monolithic structures fabricated on a glass plate using an unsealed glass-laminate sheet mould of height 0.055 cm (550 μm). These structures also show that it was possible to obtain well defined and sharp features using silica (94 μm diameter) as porogen. Monolithic structures were also obtained in sealed SU8 moulds of height 0.025 cm (250 μm) (see Figure 5-7a-c) where,

(i) Figure 5-7a illustrates micropatterned monolithic obstructions of width 250 μm and 500 μm spaced at 1100 μm to increase the path length, inside a SU8 2100 channel of width 1100 μm.

(ii) Figure 5-7b illustrates a porous monolith membrane of width 250 μm formed along the length of a closed macrochannel that separates two parallel fluid flow channels of width 450 μm each.

(iii) Figure 5-7c illustrates two porous monolith plugs of length 800 μm positioned 1000 μm apart, inside a microchannel of width 300 μm.

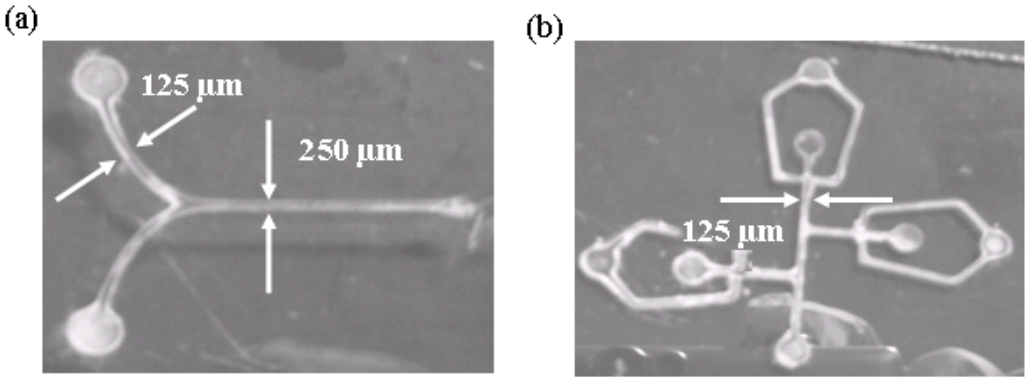

Figure 5-6 Examples of micropatterned poly(HEMA-co-EGDMA) monoliths fabricated using 94 µm silica particles as porogen fabricated inside an unsealed glass-laminate sheet mould, prepared using standard photolithographic techniques

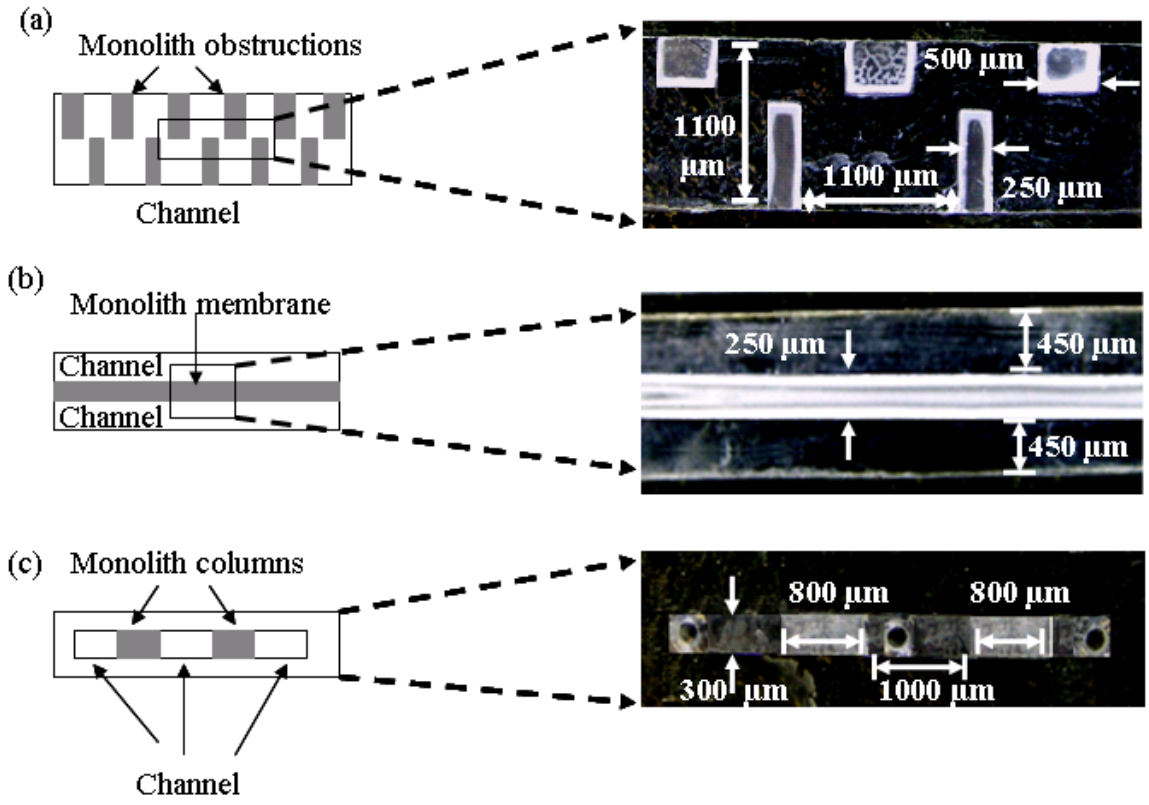

Figure 5-7 Schematic and SEM images of micropatterned poly(HEMA-co-EGDMA) monoliths fabricated using 94 µm silica particles as porogen inside a sealed SU8 2100 channel on glass. Images show (a) a set of patterned monolith obstructions to increase path length, (b) a monolithic porous membrane of width 250 µm separating two channels of width 450 µm and (c) two monoliths of length 800 µm separated by 1000 µm

Although monoliths fabricated using silica particles as porogen could be fabricated and positioned accurately, it proved difficult to remove all the silica particles during the etching stage, as many were completely encapsulated within poly(HEMA-co-EGDMA) (see Figure 5-8). Incomplete etching of the silica particles resulted in high pressure drops (>1000 kPa cm^{-1}) in the monolithic channel. Hence an alternative technique, involving the use of a water soluble salt as a porogen, was developed.

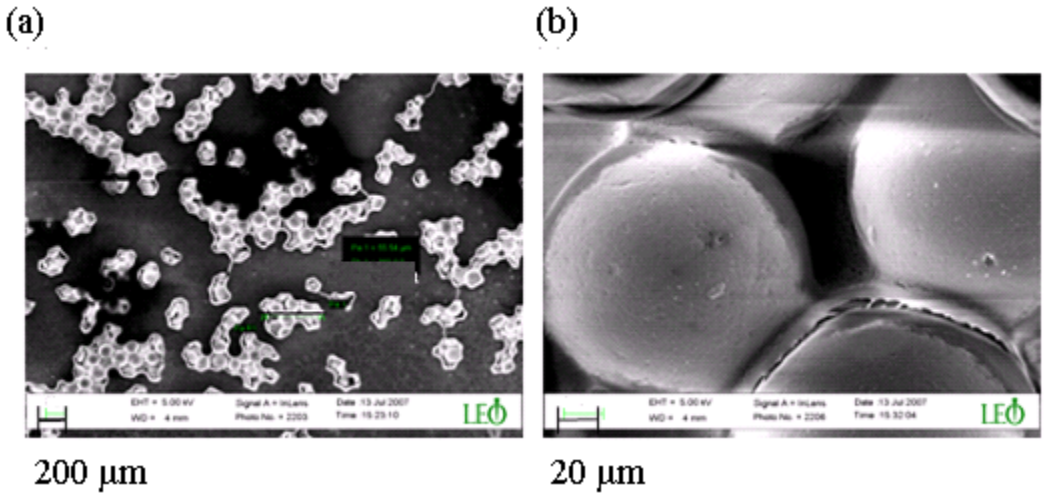

Figure 5-8 (a) SEM image of poly(HEMA-co-EGDMA) monolith with silica particles used as porogen (b) High magnification SEM image showing the complete encapsulation of silica particles by poly(HEMA-co-EGDMA)

NH_4Cl was chosen as an alternative solid porogen, due to the high solubility of NH_4Cl particles in water and their ability to fuse easily under humid conditions. Unlike silica particles, NH_4Cl particles fused under 95% *RH* conditions to form a rigid template. After polymerisation, the NH_4Cl template could be readily etched away by water to leave a porous monolith. Like silica particles, UV polymerisation time was measured for features of width 250 µm, obtained through a photomask, and is tabulated in Table 5-3.

Average Salt Particle Diameter d_p (μm)	**Surface Area (BET)** a ($m^2\ g^{-1}$)	**Average Pore Diameter (Hg Porosimetry)** d_{pore} (μm)	**Average Pore Diameter (SEM)** d_{pore} (μm)	**UV Exposure Time** t (s)		**Permeability** k (x 10^{-12} m^2)	
				h=0.055 cm	h=0.07 cm	h=0.055 cm	h=0.07 cm
60	6.1	55	50	18	35	1.9	2.17
100	4.4335	95	80	10	20	4.171	6.348
160	2.9301	149	140	5	10	6.987	12.215

Table 5-3 Physical characterisation data of micropatterned poly(HEMA-co-EGDMA) monolith (width 0.025 cm, and height 0.055 cm, 0.07 cm) fabricated inside a glass-laminate sheet mould (width 2 cm, length 3 cm, height 0.055 cm, 0.07 cm) using NH_4Cl particles (d_p = 60 μm, 100 μm and 160 μm) as porogen

As can be seen in Figure 5-9, it was possible to obtain well defined micro features of poly(HEMA-co-EGDMA) monolith of desired dimensions inside glass-laminate sheet moulds, with NH_4Cl as a porogen. Using this method, the pore size could also be varied by changing the salt particle size (refer Table 5-3). The variation in pore size due to different NH_4Cl particle size was also evident from the SEM images of poly(HEMA-co-EGDMA) monoliths shown in Figure 5-10. The monolith porosities measured using Hg porosimetry were found to be in the range of 38-55 %. Laser particle size, BET adsorption and Hg porosimetry data have been reported in Appendix 3 (A.3.2).

The physical and chemical properties of the polymer monolith were compared with commercially available glycidyl methacrylate-ethylene glycol dimethacrylate (GMA-EGDMA) monolith disks. The 12 mm diameter GMA-EGDMA monolith discs had porosity in the range of 60% and BET surface area of 7.19 $m^2\ g^{-1}$ for pore size of approximately 10 μm [18].

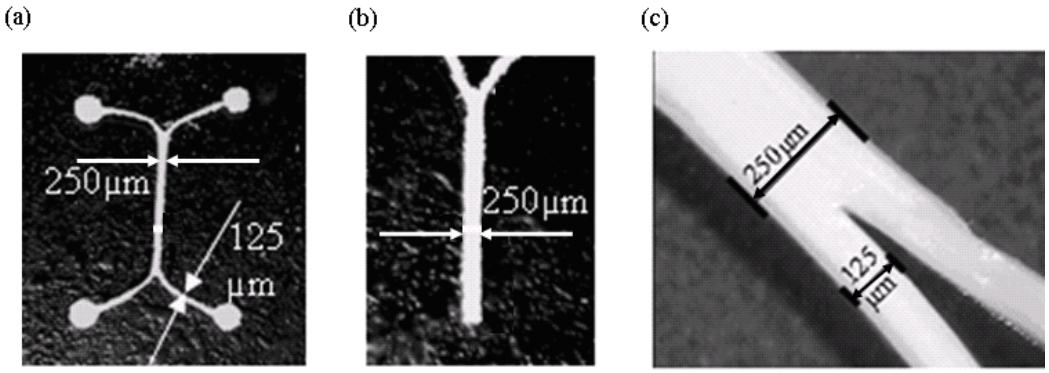

Figure 5-9 High resolution images of porous micropatterned poly(HEMA-co-EGDMA) monoliths fabricated using standard photolithographic techniques with NH_4Cl as porogen, inside an unsealed glass-laminate sheet mould. Images show (a) a two inlet - two outlet monolith channel, (b) a two inlet – one outlet monolith channel and (c) a two inlet monolith channel at higher magnification

Although the solid porogen method worked well for particle sizes of 30 µm and more, for particle sizes below 10 µm it proved difficult to etch away the solid porogen (salt or silica), thus resulting in high pressure drops (>1000 kPa cm^{-1}) and monolith blockage.

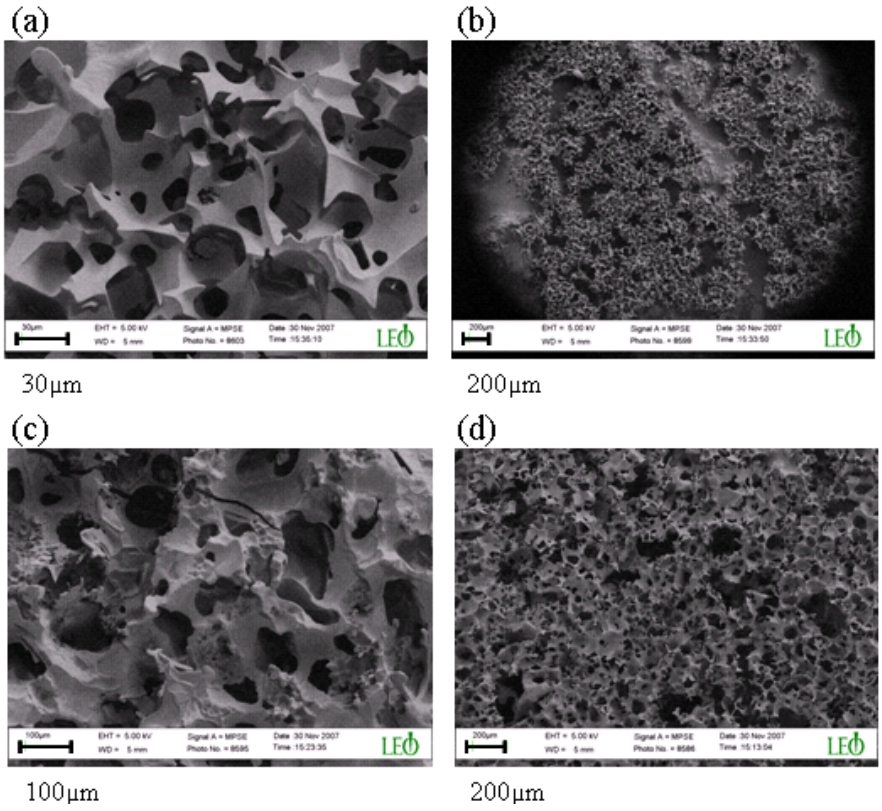

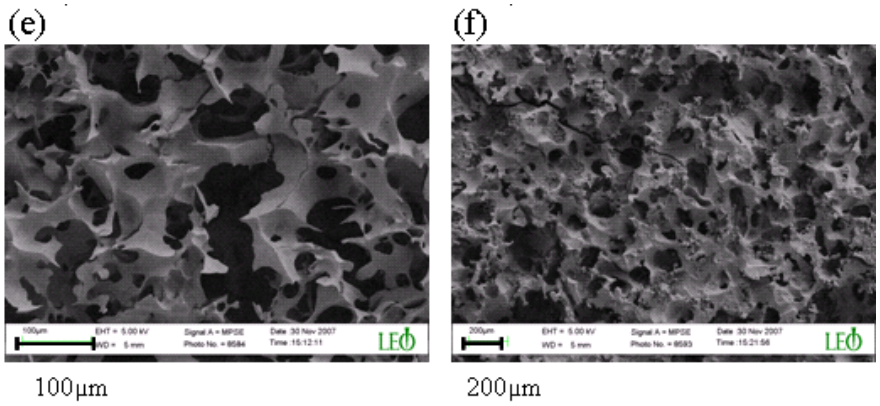

Figure 5-10 High and low magnification SEM images of porous monoliths formed using NH_4Cl as porogen of dimensions (a-b) 60 µm, (c-d) 100 µm, (e-f) 160 µm

5.3.1.2 Flow System - Pressure Drop Studies

From the batch system studies, it was clear that NH_4Cl salt as a porogen gave reproducible results with different particle diameters (above 30 µm) and was easy to dissolve during development stage. Hence NH_4Cl particles were used as porogen during fabrication of poly(HEMA-co-EGDMA) monoliths inside mesochannels. Pressure drop studies were carried out in these monolithic mesochannels (Figure 5-11) by flowing water at various flow rates, as described in Section 5.2.1.2.

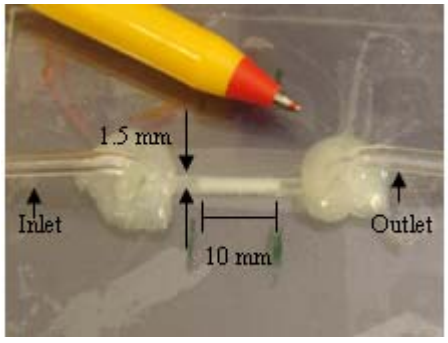

Figure 5-11 Schematic of monolith fabricated using NH_4Cl particles as porogen, inside a mesochannel micromachined in glass

Linear variation of pressure drop (per unit length of monolith) with total volumetric flow rate was observed for flow rates in the range of 1.67 x 10^{-4} cm^3 s^{-1} to 8.33 x 10^{-3} cm^3 s^{-1} (refer Figure 5-12). Such behaviour is characteristic of laminar flow according to Darcy's law. Bed permeability (*k*),

calculated using Darcy's correlation, is tabulated in Table 5-3 for NH_4Cl particle dimensions of 60, 100 and 160 µm. Figure 5-12a,b shows the decrease in the pressure gradient with increase in pore dimensions, as expected (pressure gradient is inversely proportional to the square of pore diameter), for channel heights of 0.055 cm (550 µm) and 0.07 cm (700 µm). Also illustrated in Figure 5-12a,b is the variation of pressure gradient with different channel heights. A considerable decrease in pressure drop per unit monolith length, with increase in cross sectional area was noticed.

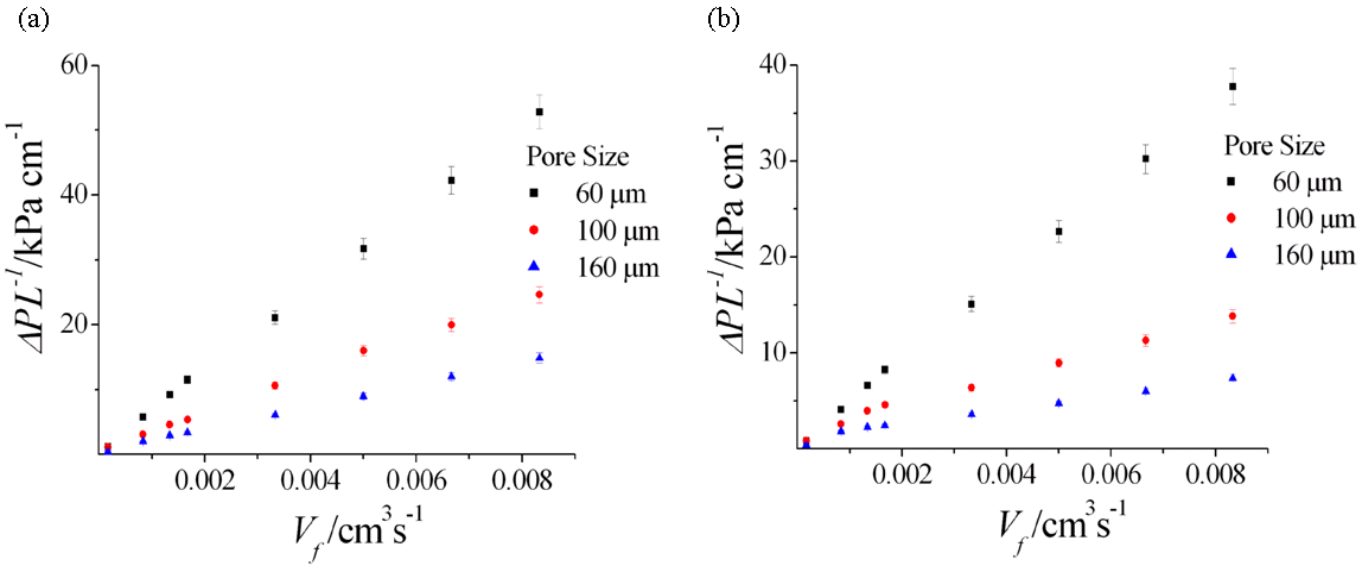

Figure 5-12 Plot of experimental pressure drop per unit length of monolith against total volume flow rates of water passed through a 1 cm long monolith fabricated inside a glass mesochannel of length (*l*) 2.5 cm, width (*w*) 0.15 cm and height (a) 0.055 cm, (b) 0.07 cm, using NH_4Cl as porogen (d_p = 60 µm, 100 µm and 160 µm)

The experimental pressure drop data for different pore diameter and channel heights was compared with analytical values, calculated using Hagen-Poiseulle equation (refer Section 5.2.1.2) for laminar flow, by plotting them against superficial velocity. Although the trends were similar, there was however a slight deviation of analytical values from experimental data (refer Figure 5-13). This could be due to non idealities of the porous media such as difference in pore size and shape, tortuousity of pores or pore connectivity, which are not accounted for in the Hagen-Poiseulle equation. A plot of pressure gradient versus square of pore size is presented in Appendix 3 (A.3.3).

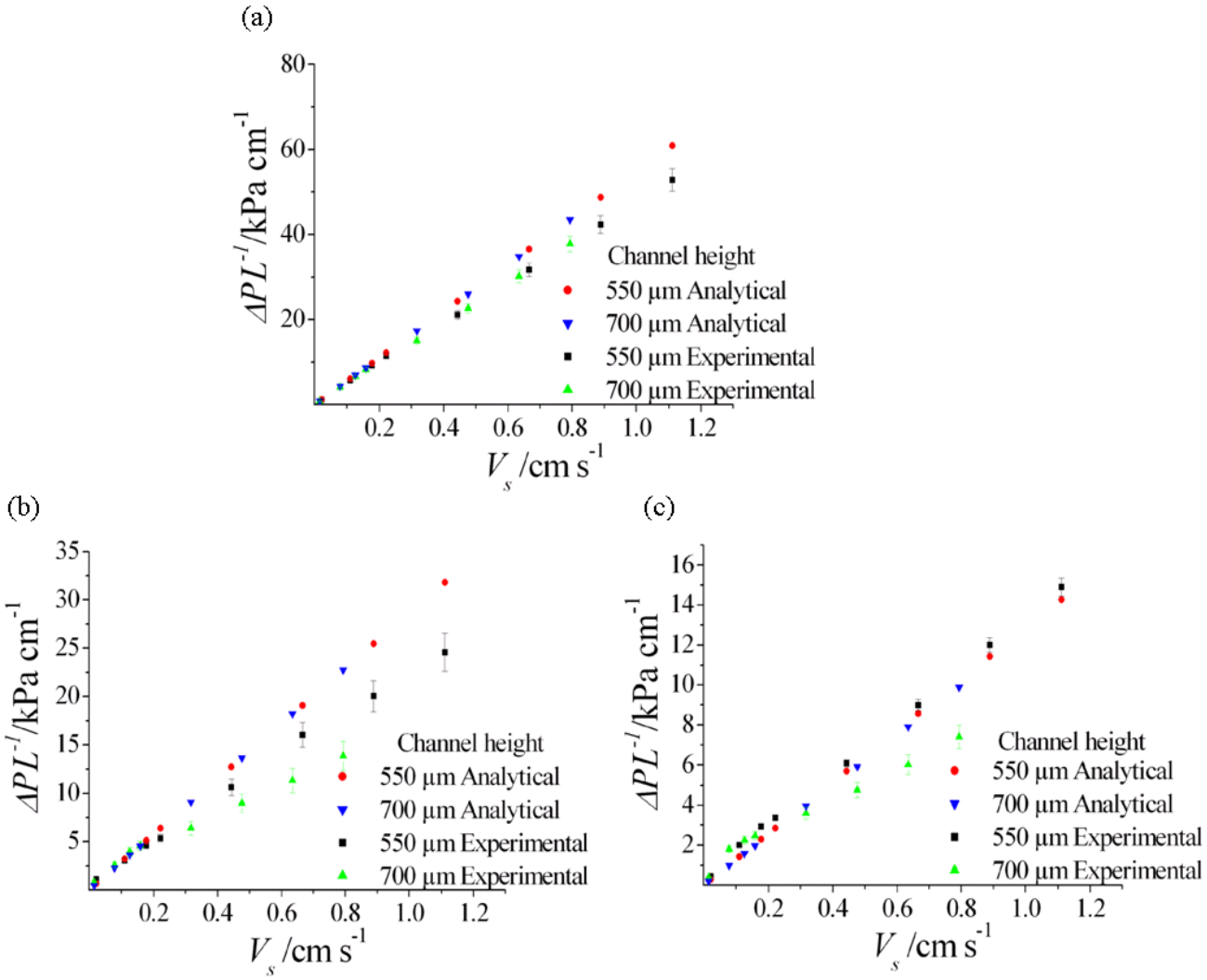

Figure 5-13 Plot of analytical and experimental pressure drop per unit length of monolith against superficial velocity through a 1 cm long monolith, fabricated inside a glass mesochannel (*l* = 2.5 cm, *w* = 0.15 cm, *h* = 0.055, 0.07 cm) using NH_4Cl particles (as porogen) of diameter (a) 60 µm (b) 100 µm and (c) 160 µm

5.3.2 Electrochemically Polymerised Monolith Studies

5.3.2.1 Polymer Synthesis

As described in Section 5.2.2.1, polypyrrole (polyPr) was synthesised by sweeping the voltage from -0.8 to +1 V 20 times. The voltammograms (refer Figure 5-14) obtained for pyrrole polymerisation demonstrated a quasi-reversible trend with broad reduction (-0.3 to -0.2 V) and oxidation peaks (0.5 to 0.7 V). The increase in the oxidation peak (anodic) current with increasing number of scans could be explained by the increase in active electrode surface area with each scan due to the formation of

subsequent layer of polyPr film. The potential, at which the reduction peak occurs, appears to shift with increasing scans; this is indicative of a slow electron transfer process. The change in electrode surface, due to deposition of polyPr, may affect the electron transfer at the electrode [48, 49].

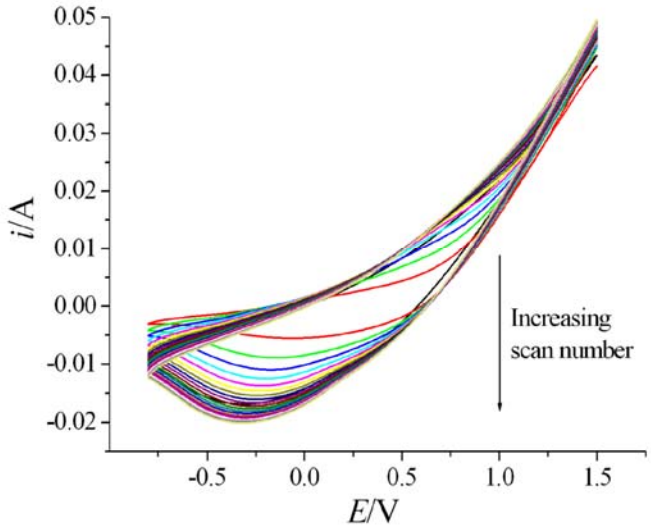

Figure 5-14 Cyclic voltammograms of pyrrole electrochemical polymerisation recorded in 0.4 x 10^{-3} mol cm^{-3} pyrrole monomer and 0.1 x 10^{-3} mol cm^{-3} PBS at a scan rate of 0.2 V s^{-1} for 20 scans on a gold electrode

Electrochemical bulk pyrrole polymerisation was used to fabricate polyPr on micropatterned electrodes of dimensions as low as 100 µm. Illustrated in Figure 5-15 are the micropatterned polyPr monoliths obtained over gold electrode template at a scan rate of 0.2 V s^{-1}. It was evident that by combining photolithography (for electrode fabrication) with electrochemical technique, polyPr monoliths of known shapes, size and at desired location could be obtained.

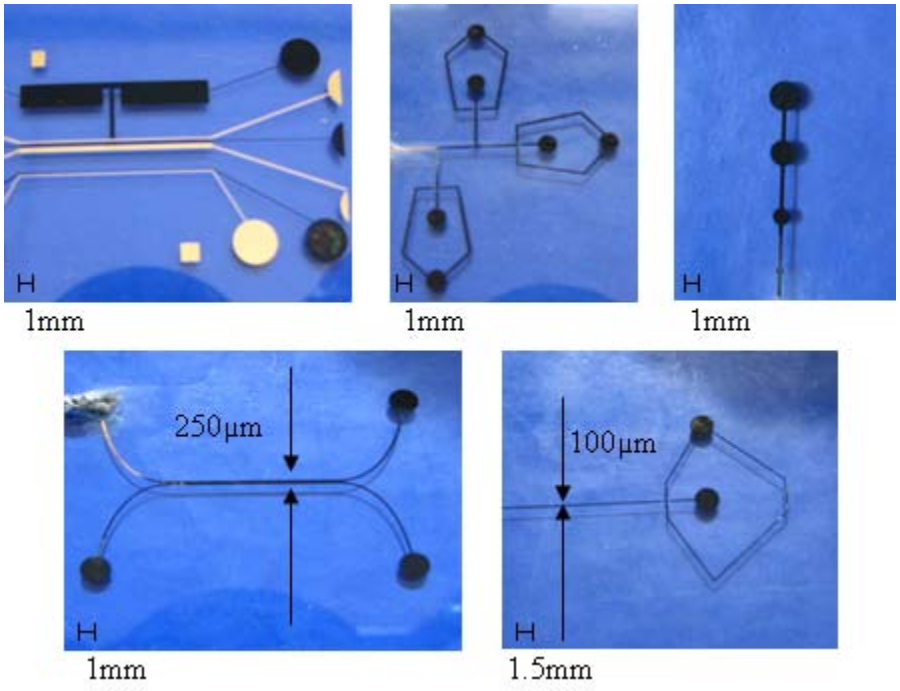

Figure 5-15 Micropatterned polypyrrole structures synthesised using gold microelectrode template

As discussed in the Section 5.2.2.1, three methods were used to introduce pores into the polymer structure: (i) NH_4Cl template, (ii) Poly(HEMA-co-TEGDA) template and (iii) Electrochemical polymerisation of two monomers.

(i-ii) *NH_4Cl or Poly(HEMA-co-TEGDA) Template*: The cyclic voltammograms obtained whilst using NH_4Cl or the poly(HEMA-co-TEGDA) template exhibited similar characteristics to those observed during the bulk polyPr formation. In both the cases, broad reduction and oxidation peaks were observed. Sample voltammograms obtained, when using NH_4Cl and poly(HEMA-co-TEGDA) as a template, to synthesise polyPr at a scan rate of 0.2 V s^{-1} are illustrated in Figure 5-16.

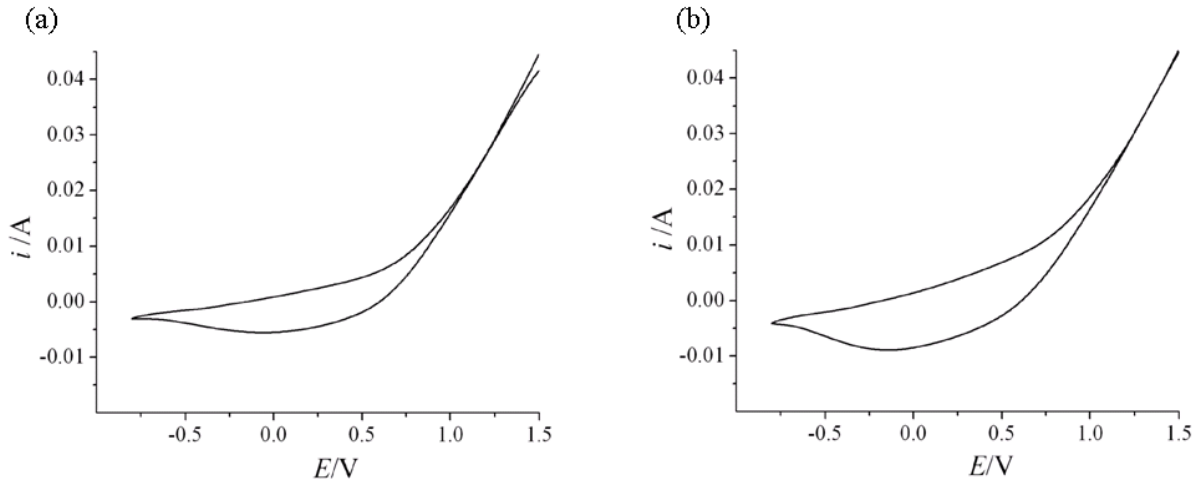

Figure 5-16 Sample cyclic voltammograms of pyrrole electrochemical polymerisation recorded in 0.4 x 10^{-3} mol cm^{-3} pyrrole monomer and 0.1 x 10^{-3} mol cm^{-3} PBS at a voltage scan rate of 0.2 V s^{-1} on a gold electrode using (a) NH_4Cl template and (b) poly(HEMA-co-TEGDA) template

It was observed that the use of the NH_4Cl salt template did not affect the electrochemical polymerisation process. Figure 5-17 shows the progressive formation of a polyPr film using gold electrodes and a salt template. It is clear from the appearance of the black band that polyPr was formed around the salt template.

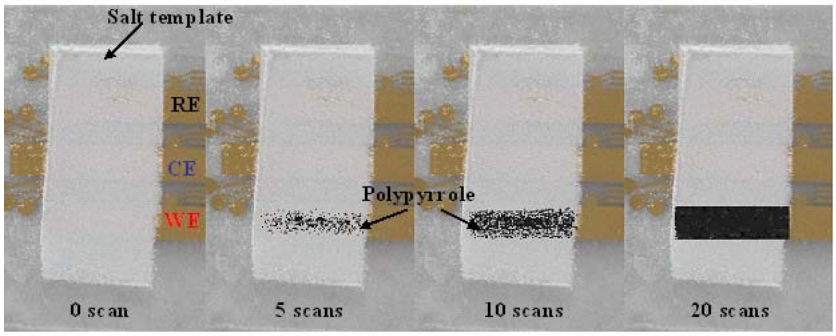

Figure 5-17 Formation of polypyrrole within a salt template using cyclic voltammetry (20 scans)

However, when using the poly(HEMA-co-TEGDA) template method, polyPr did not seem to form uniformly within the porous poly(HEMA-co-TEGDA) template even after conducting the polymerisation for more than one hour. This method could be improved by using either a bi-functionalised pyrrole monomer, having UV polymerisable part on one end and oxidative polymerisable part on the other, as discussed by Guiseppi-Elie *et al*. or by using two-monomer

system, one of which can be selectively dissolved [46]. The second method is reported in following section.

(iii) *Electrochemical Polymerisation of Two Monomers*: An alternative method to introduce pores into the polymer was to electrochemically polymerise a mixture of two monomers and then use solvent extraction to selectively remove one of the polymers [40]. A mixture of pyrrole and methylene blue was polymerised using cyclic voltammetry (-0.76 to +0.8 V). Figure 5-18 shows the cyclic voltammograms obtained at a scan rate of 0.025 V s^{-1}. The appearance of a cathodic peak (~ -0.1 V) and anodic peak (~ -0.2 V) are attributed to methylene blue electrochemical polymerisation. The second cathodic peak (~ 0.6 V) is consistent with the pyrrole oxidation observed in Figure 5-18. The anodic peak current was again seen to increase with increasing number of scans. This was due to the increase in active electrode surface area with the growing polymer film.

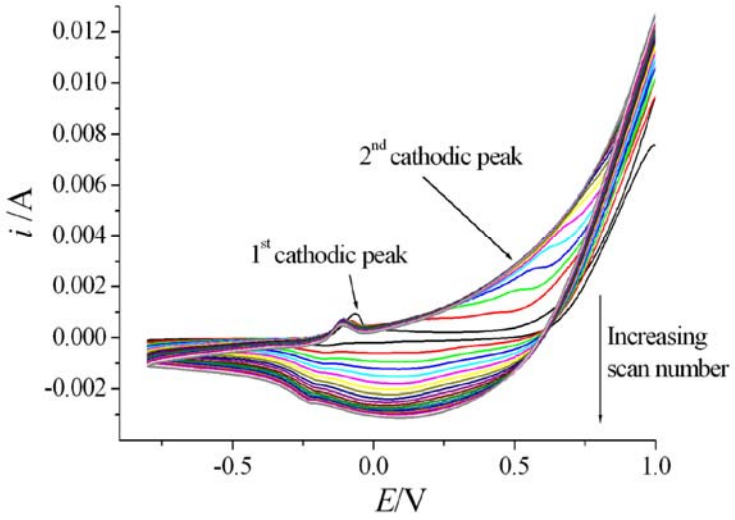

Figure 5-18 Cyclic voltammograms of pyrrole and methylene blue electrochemical polymerisation recorded in a mixture of 0.4 x 10^{-3} mol cm^{-3} pyrrole and 2.5 x 10^{-6} mol cm^{-3} methylene blue in 0.1 x 10^{-3} mol cm^{-3} PBS at a scan rate of 0.025 V s^{-1} on a gold electrode

In order to determine the success of the methods used to introduce pores in the polymer structure, physical and electrochemical characterisation techniques were used, which are described below.

5.3.2.2 Characterisation Studies

i.) *Physical Characterisation:* In order to assess the morphology of the porous polyPr film, SEM was used. Figure 5-19 (a-d) illustrates the different morphologies for polyPr monoliths obtained using poly(HEMA-co-TEGDA) template method and by dissolving methylene blue method. Pore size in case of poly(HEMA-co-TEGDA) templates were determined by salt particle size (refer Figure 5-19a,b). In case of poly Pr_MB method, the average pore diameters of the samples were noted to be 35 µm at a scan rate of 0.025 V s^{-1} as seen in Figure 5-19c,d.

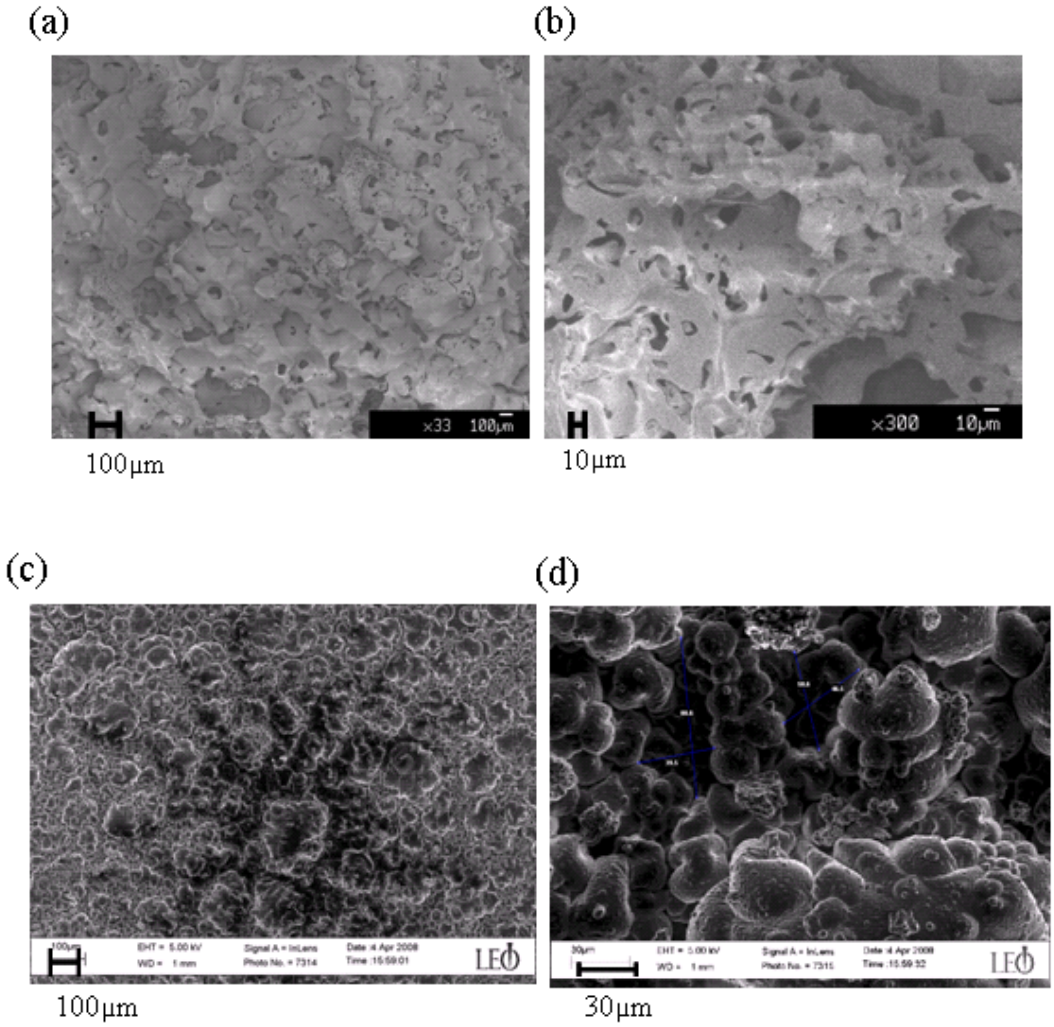

Figure 5-19 SEM images showing pore structure of (a-b) porous polyPr_poly(HEMA-co-TEGDA) films and (c-d) porous polyPr_MB films

ii) *Electrochemical Characterisation*: After synthesising and studying electrochemical polymerisation of pyrrole, electrochemical one-electron oxidation of N,N,N′,N′-tetramethyl-p-phenylenediamine (TMPD) was carried out to characterise the six different polymer-gold composite electrodes fabricated as described in Section 5.2.2.2. The current response from these electrodes was compared with pure gold electrode, in order to determine the suitability of these conducting polymers as electrode material in applications such as sensors and fuel cells.

Figure 5-20 shows sample voltammograms and their corresponding Randles-Sevcik plots (peak current versus square root of scan rate) obtained for polyPr made using NH_4Cl template. The peak current was found to be directly proportional to the square root of the voltage scan rate as described by the Randles-Sevcik equation (refer Section 1.5.5).

The linear relationship observed between the peak current and square root of the voltage scan rate indicates that the electrochemical system (TMPD) is still reversible and polypyrrole acts like any standard metal electrode. Voltammograms for rest of the electrodes are reported in Appendix 3 (A.3.4).

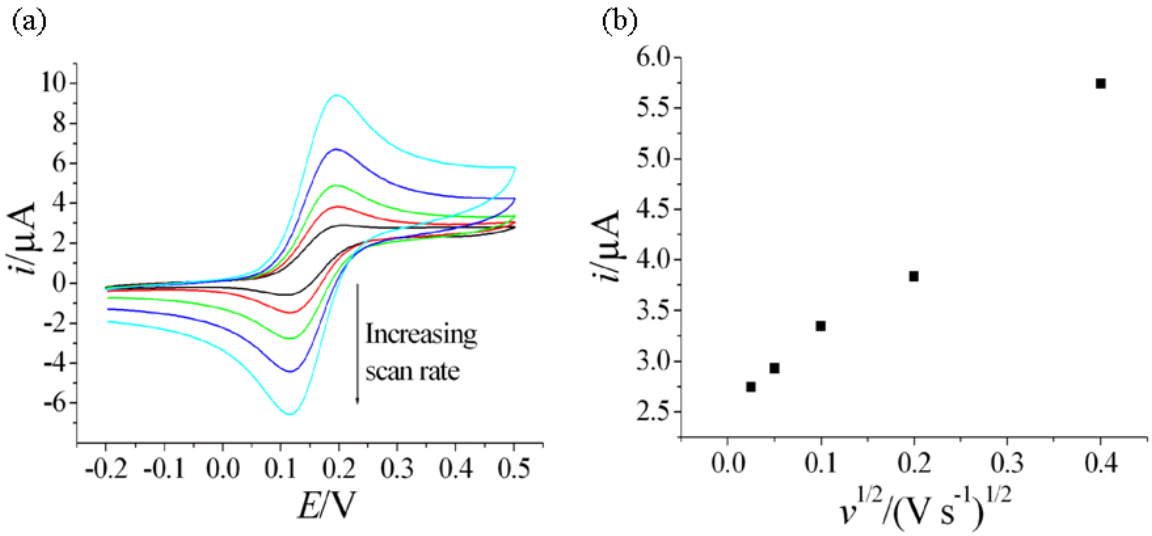

Figure 5-20 Sample cyclic voltammograms and corresponding Randles-Sevcik plot of 1 x 10^{-6} mol cm^{-3} TMPD + 0.1 x 10^{-3} mol cm^{-3} TBAP in acetonitrile solution obtained using porous polyPr_NH_4Cl_Au as working electrode and at scan rates of 0.025, 0.05, 0.1, 0.2 and 0.4 V s^{-1}

Using the slope of the Randles-Sevcik plot and the equation itself, the experimental electrode surface area could be estimated by using $n = 1$, $D = 5 \times 10^{-5}$ cm^2 s^{-1} and $C = 1 \times 10^{-6}$ mol cm^{-3}. All the polyPr films had an increased surface area compared to the plain gold electrode, as reported in Table 5-4. In addition to this, it is also apparent that the introduction of pores to the polyPr film increased the active electrode surface area.

Electrode Material	***A*** (mm^2)
Au	0.3577
Bulk PolyPr_Au	0.4021
Porous PolyPr_NH_4Cl_Au	0.4133
Porous PolyPr_Poly(HEMA-co-TEGDA)_Au	0.5023
Porous PolyPr_MB_Au	1.0743
Bulk PolyPr_Au_Pt	2.8311
Porous PolyPr_MB_Au_Pt	2.9992

Table 5-4 Electrode surface area (*A*) calculated from the Randles-Sevcik equation

Figure 5-21 compares the cyclic voltammograms obtained on each electrode material at a set scan rate of 0.4 V s^{-1}. It clearly illustrates that the use of a porous polyPr film increases the electrode surface area without a significant deterioration of the electrochemical response. The greatest increase in electrode surface area was observed with the polyPr film produced using solvent extraction techniques. The effect of coating the polyPr with platinum is also demonstrated in Figure 5-21. The presence of platinum increases the peak current as well as enhances the electrochemical response, indicating that the electron transfer kinetics is faster. Consequently, the use of a porous polyPr film produced by the solvent extraction technique and coated in platinum should provide a suitable electrode material for applications in fuel cells.

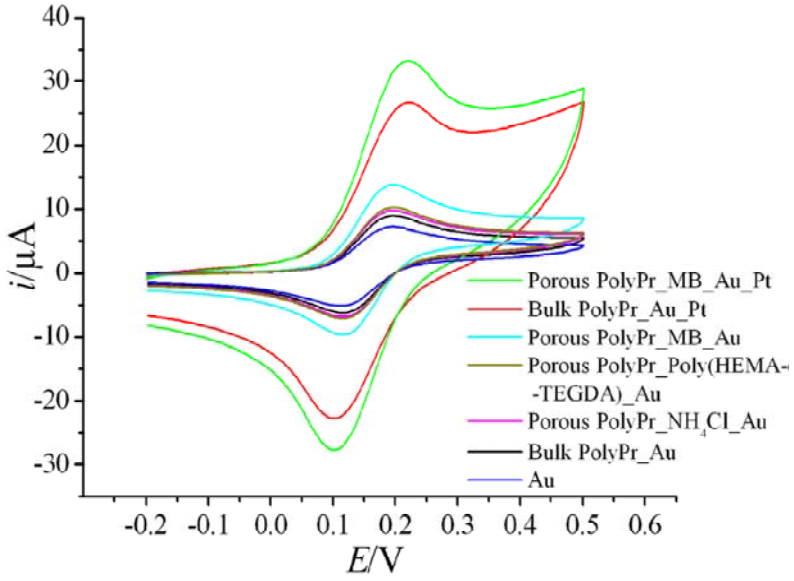

Figure 5-21 Cyclic voltammograms obtained for 1 x 10^{-6} mol cm^{-3} TMPD+ 0.1 x 10^{-3} mol cm^{-3} TBAP in acetronitrile solution for electrode material of bulk polyPr_Au, porous polyPr_NH_4Cl_Au, porous polyPr_poly(HEMA-co-TEGDA)_Au, porous polyPr_MB_Au, bulk polyPr_Au_Pt, porous polyPr_MB_Au_Pt and Au electrode at a scan rate of 0.4 V s^{-1}

5.4 CONCLUSIONS

Poly(HEMA-co-EGDMA) and polyPr monolithic features of micro- and meso-scale dimensions were developed and fabricated for analytical applications including chromatographic separations and electrochemical detection.

In the first half of the results section, a method to micropattern poly(HEMA-co-EGDMA) monoliths was developed and discussed in detail. Studies were carried out to understand the effect of UV polymerisation time and porogen size on the resolution of the photopatterned monoliths in batch. The use of two solid porogens, silica and NH_4Cl salt, was studied and results demonstrated the advantages of using NH_4Cl salt as a more practical porogen due to its solubility and ease of etching. NH_4Cl salt was used to fabricate poly(HEMA-co-EGDMA) monoliths inside glass mesochannels. Pressure drop studies demonstrated the laminar flow regime inside the porous

networks and the experimental results were shown to be in qualitative agreement with standard models for flow through porous media.

In the second half of the results section, fabrication of micropatterned structures of conducting polyPr monoliths, synthesised using electrochemical polymerisation technique, was described. Various methods to introduce porosity into polyPr were discussed. The polyPr composite electrodes thus fabricated, were characterised by studying electrochemical response of TMPD and their current responses were compared with the one obtained from standard gold electrode. The studies identified polyPr as a suitable material for the aforementioned applications due to its ability to be micropatterned, high conductivity as well as porous structure.

In the next chapter, an application of modified poly(HEMA-co-EGDMA) monoliths for developing and fabricating meso-chromatography columns, for separation and purification of low volume and expensive proteins, has been demonstrated.

5.5 REFERENCES

[1] Goral, V. N.; Zaytseva, N. V.; Baeumner, A. J. *Lab Chip*, **2006**, 6, 414–421.

[2] Chovan, T.; Guttman, A. *Trends Biotechnol.* **2002**, 20 (3), 116-122.

[3] Schiewe, B.; Staudt-Bickel, C.; Vuin, A.; Wegner, G. *Chem. Phys. Chem.* **2001**, 2, 211.

[4] Martin, P. M.; Matson D. W.; Bennett, W. D. *Chem. Eng. Commun.* **1999**, 173**,** 245.

[5] Dittrich, P. S.; Manz, A. *Nature* **2006**, 5, 211-218.

[6] Zhang, C.; Xu, J.; Ma, W.; Zheng, W. *Biotechnol. Adv.* **2006**, 24 (3), 243-284.

[7] Choban, E. R.; Markoski, L. J.; Wieckowski, A.; Kenis, P. J. A. *J. Power Sources* **2004**, 128, 54–60

[8] King, J. W.; Hill, Jr, H. H.; Lee, M. L. *Analytical Supercritical Fluid Chromaography In: Physical Methods of Chemistry* **1993**, Eds. Rossiter, B. W.; Baetzold, R. C., John Wiley & Sons, Canada, 2nd Edition, pp. 1.

[9] Tabeling, P.; Cheng, S. *Introduction to Microfluidics*, **2005**, Oxford University Press.

[10] Ocvirk, G.;Verpoorte, E.; Manz, A.; Grasserbauer, M.; Widmer, H. M. *Anal. Methods Instrum.* **1995**, 2, 74–82.

[11] Andersson, H.; Jonsson, C.; Moberg, C.; Stemme, G. *Electrophoresis* **2001**, 22, 3876–82.

[12] Liao, J-L.; Chen, N.; Ericson, C.; Hjerten, S. *Anal. Chem.* **1996**, 68**,** 3468–72.

[13] He, B.; Regnier, F. *J. Pharm. Biomed. Anal.* **1998**, 17, 925–32.

[14] Floyd, T. M.; Schmidt, M. A.; Jensen, K. F. *Procs. Micro Tot. Anal. Sys.* **2001**, 277.

[15] Svec, F.; Frechet, J. M. J. *Chem. Mater* **1995**, 7, 707–15.

[16] Hahn, R.; Panzer, M.; Hansen, E.; Mollerup, J.; Jungbauer, A. *Sep. Sci Tech.* **2002**, 37, 1545–1565.

[17] Hahn, R; Jungbauer, A. *Anal. Chem.* **2000**, 72, 4853–4858.

[18] Mihelic, I.; Nemec, D.; Podgornik, A.; Koloini, T.; *J. Chromatogr. A*, **2005**, 1065, 59-67.

[19] Chuda, K.; Jasik, J.; Carlier, J.; Tabourier, P.; Druon, C.; Coqueret, X. *Rad. Phy. Chem.* **2006**, 75, 26– 33.

[20] Chao-Hsiang, W.; Louis, S.; Jaromir, R.; Bruce, Z. *Analyst* **2001**, 126 (3), 291-297.

[21] Srinivasa, B. **2008**, WIPO Patent No.WO 2008/010005 A1.

[22] Oriel, P.; *Enzyme Microb. Technol.* **1988**, 518, 10.

[23] Dufaud, O.; Favre, E.; Sadtler, V. *J. Appl. Polym. Sci.* **2002**, 967, 83.

[24] Simms, H. M.; Brotherton, C. M.; Good, B. T.; Davis, R. H.; Anseth, K. S.; Bowman, C. N. *Lab Chip* **2005**, 151, 5.

[25] Moorthy, J.; Beebe, D. J. *Lab Chip* **2003**, 62, 3.

[26] Krajnc, P.; Leber, N.; Stefanec, D.; Kontrec, S.; Podgornik, A. *J. Chromatogr. A* **2005**, 1065, 69–73.

[27] Duan, J.; Liang, Z.; Yang, C.; Zhang, J.; Zhang, L.; Zhang, W.; Zhang, Y. *Proteomics* **2005**, 6 (2), 412-419.

[28] Stejskal, J.; Gilbert, R. J. *Pure Appl. Chem.* **2002,** 74 (5), 857–867.

[29] Cowie, J. M. G. *Polymers: Chemistry and Physics of Modern Materials* **1991**, Stanley Thornes Ltd., UK, 2nd Edition, pp. 52-81.

[30] Kerbouc'h, P.; Lebaudy, P.; Lecamp, L.; Bunel, C. *Thermochimica Acta* **2004**, 410 (1-2), 73-78.

[31] Chanda, M. *Introduction to Polymer Science and Chemistry: A Problem Solving Approach* **2006,** Taylor and Francis Group, LLP, Boca Raton, pp. 315-340.

[32] Simms, H. M.; Brotherton, C. M.; Good, B. T.; Davis, R. H.; Ansethab, K. S.; Bowman, C. N. *Lab Chip* **2004**, 5, 151–157.

[33] Lai, Y.; Wilson, A.; Zantos, S. *Contact Lenses. In Kirk-Othmer Concise Encyclopedia of Chemical Technology* **1999**, Ed. Kroschwitz, J., Wiley, New York, pp. 528–530.

[34] Carlier, J.; Chuda, K.; Arscott, S.; Thomy1, V.; Verbeke1, B.; Coqueret, X.; J. Camart, C.; Druon, C.; Tabourier, P. J. *Micromech. Microeng.* **2006**, 16, 2211-2219.

[35] Chandrasekhar, P. *Conducting Polymers, Fundamentals and Applications: A Practical Approach* **1999,** Kluwer Academic Publishers, USA, pp. 102.

[36] Saveant, J. M. *J. Phys. Chem.* **1991**, 95, 10158.

[37] Yeom, J.; Mozsgai, G. Z.; Flachsbart, B. R.; Choban, E. R.; Asthana, A.; Shannon, M. A.; Kennis, P. J. A. *Sens. Acts. B: Chemical* **2005**, 107, 882-891.

[38] Litster, S.; McLean, G. *J. Power Sources* **2004**, 130, 61-76.

[39] Wang L-X.; Li X-G.; Yang Y-L. *React. Funct. Polym.* **2001**, 47, 125-139.

[40] Li, L.; Yan, F.; Xue, G. *J. Appl. Polym. Sci.* **2004**, 91, 303-307.

[41] Borovkov, V. I.; Velizhanin, K. A. *Chem. Phy. Lett.* **2004**, 394, 441-445.

[42] Hacioğ lu, B.; Berchtold, K. A.; Lovell, L. G.; Nie, J.; Bowman, C. N. *Biomat.* **2002**, 20, 4057-4064.

[43] Whitaker, S. *Flow in Porous Media I: A Theoretical Derivation of Darcy's Law. In Transport in Porous Media 1* **1983**, Kluwer Academic Publishers, USA, pp. 3-25.

[44] Viklund, C.; Svec, F.; Frchet, J. M. J.; Irgum, K. *Chem. Mater.* **1996**, 8 (3), 744-750.

[45] Juntar, I.; Koloini, T.; Krajnc, P.; Nemec, D.; Podgornik, A.; Strancar, A. *J. Chromatogr. A* **2007**, 1144, 48-54.

[46] Guiseppi-Elie, A.; Brahim, S.; Slaughter, G.; Ward, K. R. *IEEE Sensors Journal* **2005**, 5, 345.

[47] Li, L.; Yan, F.; Xue, G. *J. Appl. Poly. Sci.* **2004**, 91, 303-307.

[48] Chao-Hsiang, W.; Louis, S.; Jaromir, R.; Bruce, Z. *Analyst* **2001**, 126 (3), 291-297.

[49] Vernitskaya, T. V.; Efimov, O. N. *Russian Chemical Reviews* **1997**, 66 (5), 443 - 457.

Chapter 6

Immobilised Metal Affinity Meso-Chromatography for Histidine Tag Protein Purification

6.1 INTRODUCTION

There is a high demand for meso and micro-litre volume analytical devices in fine chemical industries and research laboratories, due to the high cost of biochemical reagents [1]. By combining photopolymerisation with photolithography, as described in Chapter 5, it is possible to fabricate patterned monolithic microreactors that can handle reagent volumes at micro-scale [2]. The technique described in this chapter has the potential to considerably broaden the scale and scope of scientific research, by enabling effective separation and concentration of valuable biological products from a very small volume of feedstock. In the following sections, an analytical method known as immobilised metal affinity chromatography was investigated at meso-scale and the performance of meso-chromatography column was quantified by selective adsorption of histidine tag proteins [3]. In addition to allowing rapid quantification of column performance, the fluorescent properties of the proteins enabled the monitoring and mapping of regions of protein adsorption and desorption.

6.1.1 Monolithic Microchannel - Advantages and Applications

The limited availability of materials during the early phases of development of biological product can hinder progress towards the preclinical trials [4, 5]. In many cases, the quantity of product that is available after laboratory scale fermentation is not adequate for conventional operations, and so purified product is not obtained. Microfluidics and monolithic materials are two important platform technologies that offer potential solutions. Microfluidics enables very small volumes to be processed precisely in a short time [6]. Monolithic polymers are a new class of solid phase material that overcomes problems of column packings that are particularly acute at very small scale [7, 8].

The use of monoliths within microchannel devices has developed a lot of interest in applications such as micro-separations, micro-mixing, micro-purification and micro-filtration [9-11]. Within the monolithic network of channels, the transport of a solute to the monolith surface is primarily by convection instead of diffusion, as occurs in conventional porous adsorption media. Hence they could also be used at the industrial scale for quick on-line analysis of process performance, in terms of reaction selectivity or conversion [12]. West and coworkers have described a method to isolate nucleic acids by using an amine terminated monolith inside a microchannel [13]. The advantage of using such a device is that it could replace the multiple rounds of amplification process of target sequence by PCR and could also process volumes as small as 3 µl in couple of seconds, giving extremely purified samples with high concentration during elution. Gao *et al.* have reported a trypsin modified polyvinylidiene fluoride (PVDF) membrane, in a poly(dimethylsiloxane) (PDMS) microfluidic chip, that enables protein digestion in 3–10 minutes [14]. Peterson *et al.* have developed a methacrylate based monolith for tryptic digestion of myoglobin in approximately 11 seconds [15]. Recently microfluidics has also been touted as a useful tool for performing proteomics. Freire and coworkers have demonstrated and reviewed the use of membranes or monoliths inside microfluidic devices for proteome profiling [16].

One purification process of industrial importance that would offer a new platform for analysis of biological reagents, if miniaturised, is immobilised metal affinity chromatography (IMAC). Porath *et al.* developed IMAC for protein purification, separation and isolation [17, 18]. IMAC is based on interaction between metal ion and biological reagent of interest [18]. Since its inception, IMAC has been explored for various applications, from protein purification to refolding inside the polymer matrix, evaluation of protein folding status, protein surface topography studies and biosensor development [3]. Biacore Life Sciences (GE Healthcare) has developed this technology further by fabricating a sensor for kinetic measurements and determination of binding constants in protein analysis. The sensor works on interaction between a metal chelating ligand (*e.g.* nitrilotriacetic acid) and an analyte such as histidine tag proteins [19]. Histidine tag (his tag) proteins are proteins with a long chain of histidine residues (six (his_6) or eight (his_8)) attached to the C-terminal or N-terminal of the protein of interest (*e.g.* GroES protein with six consecutive histidines) [19]. Another well known application of IMAC is in separation of 6-histaminylpurine tag oligonucleotides. Min *et al.* reported a straightforward method by which they produced long single stranded deoxyribonucleic acid (DNA) molecules using the polymerase chain reaction (PCR) in combination with IMAC. They demonstrated that a tag consisting of six successive 6-histaminylpurine (H) residues (H_6 tag) endows a deoxyribonucleic acid (DNA) strand with selective retentivity onto a nickel-nitriloacetic acid (Ni^{2+}-NTA) agarose chromatography matrix, which could then be recovered by elution using imidazole [20]. However in most of these applications, large amounts of reagents are required during processing and purification.

By combining monolithic polymers with microfluidic devices, efficient and rapid immobilised metal affinity chromatographic processing is possible at the micro-scale, thus reducing the total operational costs. In this chapter, a meso-chromatography column was fabricated and its performance at IMAC was assessed. The theory on IMAC process and parameters used to quantify it has been described in detail below.

6.2 IMMOBILISED METAL AFFINITY CHROMATOGRAPHY-THEORY

Immobilised metal affinity chromatography (IMAC) as mentioned above, is a well documented, efficient, and reliable separation process that is widely used at the lab-scale [21]. Like any other chromatography, a mobile phase containing reagent(s) of interest (adsorbate) is passed through a stationary phase (adsorbent), which can selectively separate the reagents. The separation principle of IMAC is based on the exploitation of a selective binding interaction between an electron donating group of the reagent (*e.g.* his tag on protein) with an immobilised metal ion having free or accessible coordination sites [18]. The metal ion is immobilised using metal chelating agents covalently bound to the polymer matrix (adsorbent).

Many chelating agents have been developed in the past for various applications [22]. They can be classified as monodenate, bidentate or multidentate ligand, based on the number of electron donating groups that can form bonds with a single metal ion. Multidentate chelating compounds are most commonly used chelating groups in IMAC, which provides the strength of the complex formed by the protein, metal ion and chelating group. Iminodiacetic acid (IDA) is a standard and the most commonly used metal chelating ligand for immobilisation of metal ions in IMAC [22-24]. It has three electron donating groups (tridentate), one nitrogen atom and two short chain carboxyl groups. Developed by Hochuli *et al.*, nitriloacetic acid (NTA) is another extensively used IMAC chelator [25].

One of the commonly used IMAC polymer matrix (stationary phase) in industry is agarose bead, to which the metal chelating ligand (IDA) is covalently attached [26]. On addition of metal ions, the tridentate chelating agent (IDA) forms strong complexes with the metals ions such as Cu^{2+} or Co^{2+}. The immobilised metal ion still has free coordination sites to bind to either the protein of interest or the displacer solvent (eluent). The ligand-metal complex bound polymer is then used for protein

separation where the metal binding group of protein (*e.g.* his tag) forms a complex with the metal ion on the polymer. The protein that does not have this group passes the column without any interaction. There could be some non specific binding with the polymer itself which can be avoided or minimised by using a buffer containing low concentration of displacer component such as imidazole. Finally to remove the bound protein, a buffer containing high concentration of displacer is used, where by the displacer molecule displaces the protein and form a more favourable complex with the metal ion [27]. The process is depicted in Figure 6-1a.

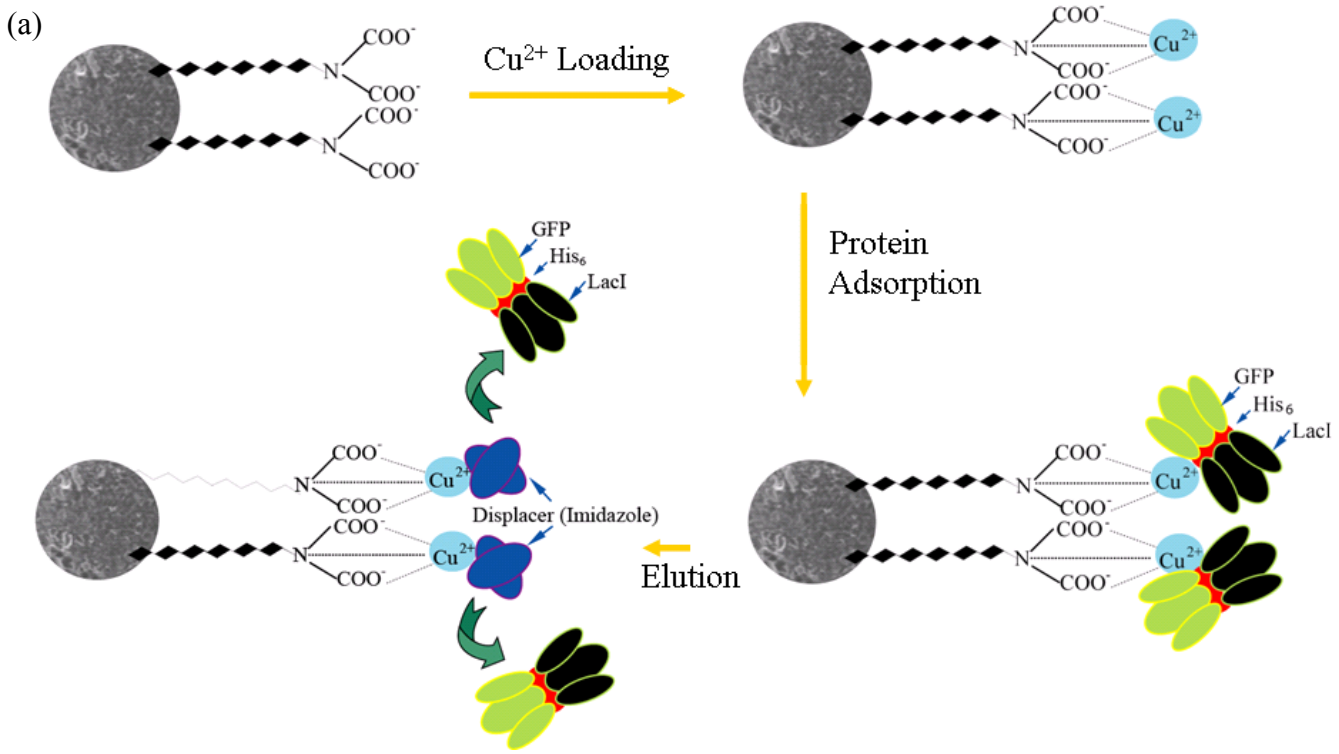

(b)

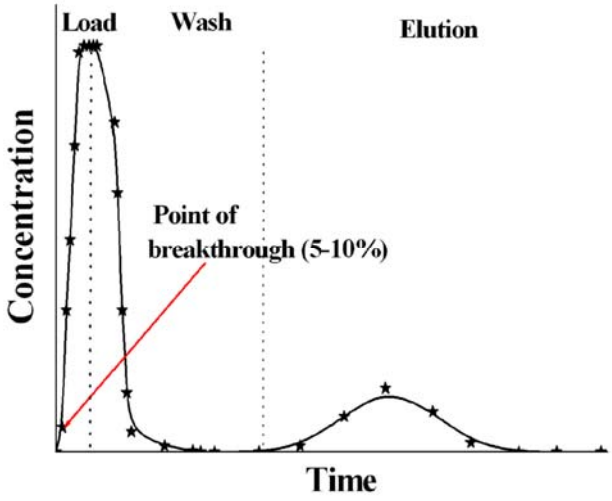

Figure 6-1 (a) Schematic of histidine tag protein binding to immobilised metal affinity chromatography (IMAC) resin (b) Sample breakthrough, wash and elution curve for IMAC operation

Figure 6-1b above shows a typical breakthrough curve for loading, wash and elution stages of IMAC [28].

In IMAC, the polymer performance can be quantified using the following four quantities:

1. *Metal Ion Capacity (MIC)*: Metal ion or metal chelation capacity is the total amount of metal ion that is immobilised on the monolith at equilibrium *i.e.* prolonged incubation. The quantity is measured as per unit volume of monolith and is dependent on the retention strength of metal ion [29]. Different metal ions exhibit different retention strengths based on the principles of hard and soft acids and bases. Their order of retention strength as chelated by IDA follows Cu^{2+}>Ni^{2+}>Co^{2+} [17, 21].
2. *Equilibrium Binding Capacity (EBC)*: EBC or saturated capacity of a column is the amount of target protein the column can bind, if every available binding site is utilised. This is determined by loading a large excess of target protein either at very slow flow rates or after prolonged incubation in a closed system. In practice, the saturated capacity is never available under process conditions using packed columns [30].

3. *Dynamic Binding Capacity (DBC)*: DBC of chromatography media is the amount of target protein the media will bind under actual flow conditions before significant breakthrough of unbound protein occurs [30]. DBC is calculated usually at roughly 5-10% breakthrough [31]. As this parameter reflects the impact of mass transfer limitations that may occur as flow rate is increased, it is much more useful in predicting real process performance than a simple determination of saturated capacity. For most of the industrial chromatography media, its value is lower than EBC.

   In general, DBC will decrease as the residence time decreases, however the rate at which it decreases can vary greatly from media to media. An ideal media would have efficient mass transfer properties across the range of flow rates being used [30].

4. *Langmuir Adsorption Isotherms*: They are curves that describe the fraction of the surface area of the adsorbent (monolith) covered with monolayer of adsorbate (solute), as a function of the concentration (at equilibrium) of the solute in the contacting liquid phase [32]. Langmuir isotherm is expressed as:

$$q^* = q_m \frac{k_D[C^*]}{1 + k_D[C^*]} \qquad (6.1)$$

   Where q^* (µg ml^{-1}) is the concentration of protein adsorbed on the adsorbent, q_m (µg ml^{-1}) is the maximum capacity of adsorbent, k_D (µg ml^{-1}) is Langmuir adsorption constant, which is the measure of affinity of adsorbate for adsorbent, and [C^*] (µg ml^{-1}) is the equilibrium concentration of the adsorbate. Langmuir isotherms are useful in industries in determining the optimum conditions of operations, to achieve maximum adsorbent capacity utilisation.

This chapter has been divided into two main sections. In the first section, the development and synthesis of IDA-functionalised porous methacrylate-polymer matrix has been reported. Physical

characterisation techniques were used to verify the presence of IDA on the polymer [33]. The MIC and EBC were measured under physiological conditions in a batch system. In the second section, the DBC of the polymer matrix was calculated at various flow rates in a fixed bed meso-chromatography column. The meso-chromatographic platform was finally used to purify protein from crude cell lysate. The purified protein was analysed using sodium dodecyl sulfate-polyacrylamide gel electrophoresis (SDS PAGE) [34]. During meso-chromatography, laser scanning confocal microscopy was used to identify locations within the monolith where protein adsorption and desorption occurred and to study the channeling effects [35].

6.3 EXPERIMENTAL

6.3.1 Microfabrication

Two types of moulds were prepared on glass wafers for polymer synthesis. Macro moulds (length 5 cm, height 0.025 cm, width 5 cm) were prepared using heat lamination method for batch experiments and mesochannel moulds (length (*l*) 2.5 cm, height (*h*) 0.07 cm and width (*w*) 0.155 cm) were prepared using micromachining for flow experiments [36]. The moulds were then silanised using 3-aminopropyltrimethoxysilane to aid hydrogen binding between polymer and glass. The silane adhesion between polymer and substrate proved to be satisfactory at reasonably high pressures of 1000 kPa cm^{-1} [2, 37]. The moulds were filled with NH_4Cl particles (porogen) and humidified (95% *RH*), to form a fused NH_4Cl particle template. NH_4Cl particles of diameter 100 μm were prepared using a pulveriser and particle sieve and the particle size distribution was obtained using laser scattering particle sizer. The porosity obtained using mercury porosimetry was around 38-45% and BET surface area was approximately 4.4 m^2 g^{-1}. More details on polymer synthesised using variety of porogens is presented in Chapter 5.

6.3.2 Polymer Synthesis

The monomers used during the photopolymerisation reaction were 2-hydroxyethyl methacrylate (HEMA), cross-linker ethyleneglycol dimethacrylate (EGDMA) and disodium 2,2'-{[2-hydroxy-3-(prop-2-en-1-yloxy)propyl]imino}diacetate (HPIDA). Monomer, HPIDA, has a covalently bound metal ion chelant (iminodiacetic acid). Iminodiacetic acid (IDA) is a tridentate ligand and chelates metal ions such as Cu^{2+}, very strongly. Cu^{2+} was selected due to its high retention strength as seen in Section 6.2. However IDA does not undergo copolymerisation, so it was reacted with the epoxy group of allyglycidyl ether (AGE), by following a protocol similar to that patented by Chen *et al.* to obtain HPIDA [38]. HPIDA can take part in polymerisation through the carbon-carbon π bond. HPIDA monomer solution was characterised using hydrogen nuclear magnetic resonance (^{1}H NMR) technique. Its synthesis is explained in detail below.

IDA dissolved in 0.2 M sodium carbonate was reacted with AGE in 1:1 molar ratio at pH 10. Sodium carbonate (Na_2CO_3) was used as a catalyst to speed up the reaction and drive it to completion. The solution was heated gradually to a temperature of 50-60 ^oC in an oil bath. The reaction was carried out for over 8 hours to ensure complete conversion. A dark yellow viscous aqueous solution containing HPIDA was obtained. A schematic of the reaction is given in Figure 6-2 below.

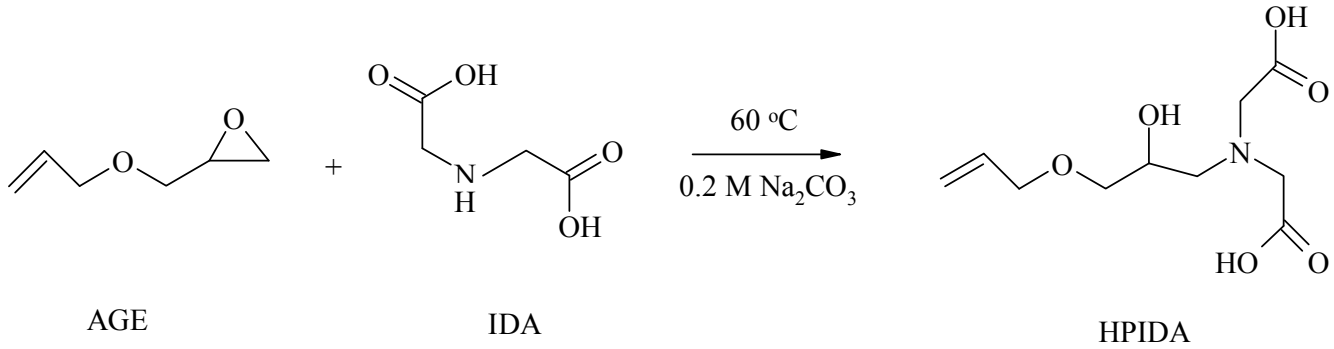

AGE IDA HPIDA

Figure 6-2 Reaction scheme for disodium 2,2'-{[2-hydroxy-3-(prop-2-en-1-yloxy)propyl]imino}diacetate synthesis

Nine monomer mixture samples were prepared by mixing HEMA (*x* ml) and HPIDA (*y* ml). The volume ratio of *x* to *y* was varied from 0.5 to 5 whilst keeping the total comonomer volume constant at 3 ml (refer Table 6-1). 2 ml of cross-linker was added to each of the nine monomeric mixtures. 1 volume(%) 2,2-dimethoxy 2-phenyl acetophenone (DMPA) was also added as photoinitiator. The monomer mixture samples were added to NH_4Cl template (refer Section 6.3.1) and exposed to ultraviolet (UV) light source for 2 minutes for complete polymerisation to give tertiary-amine metal-ion-chelating poly(HEMA-co-EGDMA-co-HPIDA). The poly(HEMA-co-EGDMA-co-HPIDA) samples thus obtained were etched using deionised water to dissolve NH_4Cl particles and reveal its porous structure. The reaction scheme is illustrated in Figure 6-3 below.

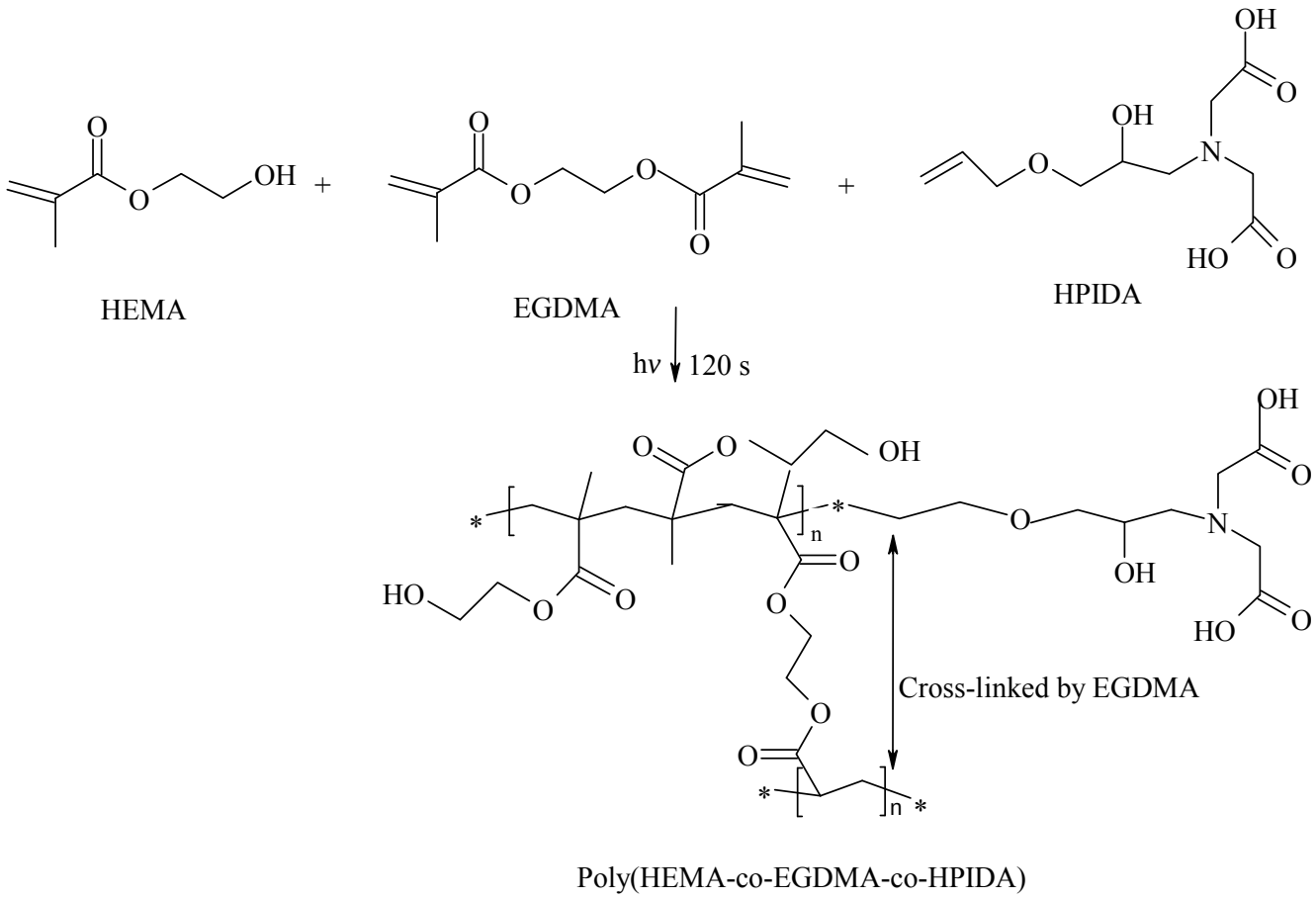

Figure 6-3 Reaction scheme for poly(HEMA-co-EGDMA-co-HPIDA) synthesis

Poly(HEMA-co-EGDMA-co-HPIDA) samples were analysed using Fourier transform infrared spectroscopy (FTIR), solid state nitrogen nuclear magnetic resonance (^{15}N NMR) analysis and elemental analysis.

HEMA (*x*)		**HPIDA (*y*)**		**EGDMA**	
Volume (ml)	Volume (%)	Volume (ml)	Volume (%)	Volume (ml)	Volume (%)
1	20	2	40	2	40
1.5	30	1.5	30	2	40
1.8	36	1.2	24	2	40
2	40	1	20	2	40
2.07	41.4	0.93	18.6	2	40
2.14	42.8	0.86	17.2	2	40
2.2	44	0.8	16	2	40
2.3	46	0.7	14	2	40
2.4	48	0.6	12	2	40
2.45	49	0.55	11	2	40
2.5	50	0.5	10	2	40

Table 6-1 Volume of 2-hydroxyethyl methacrylate, disodium 2,2'-{[2-hydroxy-3-(prop-2-en-1-yloxy)propyl]imino}diacetate and ethyleneglycol dimethacrylate in the monomer mixture, used for synthesising poly(HEMA-co-EGDMA-co-HPIDA)

Poly(HEMA-co-EGDMA-co-HPIDA) for batch and flow analysis of proteins was prepared with a comonomer composition of 41.4:18.6:40 (HEMA:HPIDA:EGDMA) by volume(%). Poly(HEMA-co-EGDMA-co-HPIDA) monoliths were also characterised using scanning electron microscopy (SEM), environmental scanning electron microscopy (ESEM) and laser confocal microscopy.

6.3.3 Quantification of Immobilised Metal Ions

1 ml of all nine porous poly(HEMA-co-EGDMA-co-HPIDA) samples prepared above (refer Table 6-1), were cleaned thoroughly with 10 ml of 1 M sodium chloride (NaCl) solution, 10 ml of 2% Tween 20 and 10 ml of methanol to remove any unpolymerised residual monomer and organic impurities. They were loaded with 1 ml of 50 mM copper(II) sulphate solution to enable Cu^{2+}-polymer binding. It was followed by another thorough wash with an aqueous solution of 1 M sodium chloride, 250 mM sodium phosphate and 300 mM imidazole to remove any loosely bound Cu^{2+}. The metal ion capacity (MIC) was determined by eluting the Cu^{2+} with 1 ml of 0.1 M ethylenediaminetetraacetic acid (EDTA) and assayed using UV spectrometer at 730 nm. Standard calibration curve for known concentration of Cu^{2+} in EDTA solution was generated and used to calculate the total amount of metal ions removed from the charged poly(HEMA-co-EGDMA-co-HPIDA) samples. Sample measurements were in triplicate. The polymer samples were rinsed in deionised water after each step described above.

6.3.4 Protein Expression and Purification

Two his tag proteins (LacI-His_6-GFP, α-Synuclein-His_8-YFP) were used in all the binding studies. LacI-His_6-GFP protein was synthesised by transforming LacI-His_6-GFP plasmid DNA in BL21 (*E. Coli*) gold competent cells as described by Darby *et al*. [39]. Briefly, the LacI-His_6-GFP plasmid DNA construct was transformed in BL21 gold competent cells and a single fresh colony was used to inoculate LB media supplemented with 50 μg ml^{-1} ampicillin. Protein was expressed constitutively

at 30 ºC overnight and the resulting culture was centrifuged at 4000 rpm. The pellets were stored at -80 ºC until necessary. LacI-His_6-GFP lysates were prepared by resuspending the pellets in phosphate buffer (PBS) and lysed by sonication (4 x 3 seconds at maximum power) and then incubated on ice for two minutes. The process was repeated four times. The lysed cells were centrifuged at 19000 rpm and the supernatant was recovered. The supernatant was purified using a commercial Histrap FF column (GE Healthcare). Before loading the column with LacI-His_6-GFP cell lysate, the column was equilibrated according to manufacturer's manual. The LacI-His_6-GFP cell lysate was then fed into the Histrap FF column and washed with a wash buffer (50 mM Tris HCl, 10 mM Imidazole, 300 mM NaCl, pH 7.4) to remove any non specific bound protein [40]. The protein was then eluted using the elution buffer (50 mM Tris HCl, 130 mM Imidazole, 300 mM NaCl, pH 7.4) and dialysed using the dialysis (equilibrium) buffer (50 mM Tris HCl, 130 mM NaCl, pH 7.4). The yield of protein obtained after this was approximately 12 $\mu g\ ml^{-1}$ of soluble LacI-His_6-GFP in the culture media. The protein obtained was analysed using SDS PAGE and comassie protein assay stain for purity [34]. Another his tag protein, α-Synuclein-His_8-YFP, was used to confirm the selectivity of poly(HEMA-co-EGDMA-co-HPIDA) for his tag and also study the difference in binding characteristic with increase in number of histidine residues. α-Synuclein-His_8-YFP protein was kindly gifted by the Department of Chemistry at the University of Cambridge (UK). α-Synuclein-His_8-YFP was cloned in frame in the vector PET41C (Novagen) using specific primers and NdeI/HindIII restriction sites. This vector adds an octarepeat of his residues at the C-terminus of the exogenous gene under the control of the T7 promoter. The Synuclein-His_8-YFP construct was expressed recombinantly in *E. Coli* and purified by affinity chromatography using Ni-NTA-Agarose as per supplier's instructions (Invitrogen), followed by size exclusion chromatography using a Superdex S75 column (GE Healthcare). Purity of both the proteins was higher than 90% as measured by SDS PAGE.

6.3.5 Protein Binding Capacity - Batch Analysis

0.25 ml of Cu^{2+} immobilised poly(HEMA-co-EGDMA-co-HPIDA) sample (positive control) was equilibrated using 9 ml of wash buffer. 3 ml of pre-purified LacI-His_6-GFP of concentration 500 μg ml^{-1} in 50 mM Tris HCl was then loaded to this positive control sample. The polymer-protein system was shaken gently for 20 minutes to equilibrate the binding of LacI-His_6-GFP to Cu^{2+} bound to the polymer. After equilibration, poly(HEMA-co-EGDMA-co-HPIDA) sample was washed for 20 minutes successively with wash buffer (108 x monolith volume) and elution buffer (56 x monolith volume). After each stage (loading, wash and elution), samples of the retentate were collected, filtered using 0.45 μm filters and the amount of LacI-His_6-GFP in the samples was measured using Bradford analysis [41]. The Bradford calibration graphs were generated using standard bovine serum albumin (BSA) protein in equilibrium, wash and elution buffer (refer Appendix 4 (A.4.1)). The following two negative controls were also performed on poly(HEMA-co-EGDMA-co-HPIDA):

i) Cu^{2+} negative control, where LacI-His_6-GFP was loaded to poly(HEMA-co-EGDMA-co-HPIDA) with no Cu^{2+} chelated/immobilised.

ii) Non his tag protein negative control, where copper chelated poly(HEMA-co-EGDMA-co-HPIDA) was loaded with β-Lactoglobulin (500 μg ml^{-1}, Mw: 18 kDa).

All other experimental conditions for negative control remained the same, as described above for positive control.

Two 0.25 ml poly(HEMA-co-EGDMA-co-HPIDA) samples (as synthesised before) were loaded with 3 ml of 9.5 μg ml^{-1} of LacI-His_6-GFP (274 kDa) and α-Synuclein-His_8-YFP (30 kDa) for his tag selectivity studies. Images of poly(HEMA-co-EGDMA-co-HPIDA) samples at various stages (loading, wash, elution) were collected using laser confocal microscopy.

Langmuir Adsorption Isotherms: Eight samples of poly(HEMA-co-EGDMA-co-HPIDA) (0.05 ml) were loaded with 0.5 ml of LacI-His_6-GFP of concentrations 0.025, 0.09, 0.12, 0.15, 0.55, 0.7, 1 and 1.5 mg ml^{-1} and equilibrated for 20 minutes. Similarly eight samples of poly(HEMA-co-EGDMA-co-HPIDA) (0.005 ml) were loaded with 0.16 ml of α-Synuclein-His_8-YFP of concentrations 0.085, 0.12, 0.22, 0.5, 0.75, 1, 1.4, 1.7 and 2.2 mg ml^{-1} and equilibrated for 20 minutes. All samples were then washed and eluted using the protocol described above for positive control.

6.3.6 Protein Binding Capacity - Flow Analysis

A glass mesochannel (l = 2.5 cm, w = 0.155 cm, h = 0.07 cm) was fabricated and filled with 100 μm NH_4Cl particles as the porogen (refer Section 6.3.1). It was then filled with a monomeric mixture of HEMA:HPIDA:EDGMA in the volume(%) composition of 41.4:18.6:40 and photopolymerised for 10 seconds using UV light. The length (L) of poly(HEMA-co-EGDMA-co-HPIDA) monolith inside the mesochannel was restricted to 1.5 cm using a computer aided designed photomask. The polymer was developed using deionised water for 12 hours. Glass capillaries (i.d. = 0.162 cm) were used as inlets and outlets and sealed using epoxy resin. The pressure drop was measured using a standard differential pressure drop sensor. Fluid flow inside mesochannels was controlled using two syringe pumps, with typical flow rates between 0.017 μl s^{-1} and 33 μl s^{-1}.

The column was prepared by loading it first with Cu^{2+} and then equilibrating using wash buffer. The column was then loaded with LacI-His_6-GFP (170 μg ml^{-1}) at flow rates of 1.5 μl s^{-1} (residence time, τ = 2.7 s), 0.66 μl s^{-1} (τ = 6.2 s), 0.47 μl s^{-1} (τ = 8.77 s) and 0.3 μl s^{-1} (τ = 13.7 s) and then washed with 5 column volumes (0.135 ml) of wash buffer to remove any non-specifically bound protein. Finally the immobilised protein was eluted using another 5 column volumes of elution buffer, as used for Histrap FF columm (refer Section 6.3.4). During all these stages, samples of 20 μl were collected at an interval of every 10 seconds during load stage and 0.5 to 1 minute during wash and elution stages. The concentration of protein was calculated using Bradford analysis. The

same experiments were also performed with α-Synuclein-His_8-YFP (170 μg ml^{-1}) at a flow rate of 0.47 μl s^{-1} (τ = 8.77 s). The protein obtained was analysed using SDS PAGE and silver stain using Silver Snap kit II protocol (Invitrogen).

Amount of protein fed to the column at a given time *t* (s) was calculated using the following equation [42]:

$$q_d = V_f \left[C\right]_o t \tag{6.2}$$

Where q_d (μg) is the amount of protein loaded at a given time in a flow through meso-chromatography column, V_f (μl s^{-1}) is the total volume flow rate and $[C]_o$ (μg ml^{-1}) is initial concentration of protein during the loading stage. A graph of normalised concentration of protein ($[C]/[C]_o$, where $[C]$ is concentration of protein measured at the outlet of the column at time *t*, was plotted against q_d, to determine dynamic binding capacity at 10 % of the total breakthrough concentration.

6.3.7 Confocal Analysis

The poly(HEMA-co-EGDMA-co-HPIDA) monolith inside a mesochannel fabricated in Section 6.3.6 was also analysed using laser confocal microscopy at various lengths, during loading, washing and elution stages. The meso-chromatography column was loaded with the protein LacI-His_6-GFP (170 μg ml^{-1}) at a flow rate of 0.3 μl s^{-1} (residence time, τ = 13.7 s) and confocal images were taken at various times to show the progression of the adsorbed protein front through a particular field of view. The field of view represented a 0.2 cm length of monolith that was positioned 0.3 cm from the entrance to the monolith. Other confocal microscopy observations were made after the adsorbed protein front had passed through the field of view, by moving the microscope along the axis of the monolith until breakthrough was observed. LacI-His_6-GFP was

then kept in the monolith overnight to ensure equilibrium binding. After 12 hours, the column was washed with 5 column volumes (0.135 ml) of buffer solution and then eluted using another 5 column volumes of elution buffer.

6.3.8 Cell Lysate Purification

2 ml LacI-His_6-GFP cell lysate, prepared as described in Section 6.3.4, was fed into the meso-chromatography column (l = 2.5 cm, w = 0.155 cm, h = 0.07 cm, L = 1.5 cm) at a flow rate of 1.33 µl s^{-1} and then washed and eluted using 5 column volumes (0.135 ml) of wash and 5 column volumes of elution buffer respectively. Samples of volume 20 µl were collected at an interval of approximately 1 minute during elution stage.

6.4 RESULTS AND DISCUSSION

The objective of this work was to synthesise metal ion chelating polymer, poly(HEMA-co-EGDMA-co-HPIDA), and optimise its metal ion capacity and protein binding capacity in batch system in order to develop a novel meso-chromatography column for quick downstream on-line analysis. The monolith inside the mesochannel was synthesised by photopolymerisation. The length of the monolith could be adjusted using a photomask and pore size could be changed by changing the NH_4Cl particle size, thereby rendering better control over total pressure drop. The meso-chromatography columns thus prepared were used to study the selective binding of his tag proteins and variation of binding capacity with flow rate.

6.4.1 Batch System Analysis

A polymer monolith to perform IMAC operations was developed. Experiments were performed in batch to determine the metal ion capacity and protein binding capacity of poly(HEMA-co-EGDMA-co-HPIDA) and to study various factors affecting the binding capacities.

6.4.1.1 Polymer Development Chemistry

A new comonomer HPIDA was prepared as described in Section 6.3.2 and photopolymerised with HEMA and cross-linker EGDMA to obtain poly(HEMA-co-EGDMA-co-HPIDA). Poly(HEMA-co-EGDMA-co-HPIDA) thus obtained had an IDA molecule covalently bound to the backbone of the polymer chain. In all the experiments, iminodiacetic acid (IDA) molecule on the polymer chain was used as a metal ion chelating agent.

All nine poly(HEMA-co-EGDMA-co-HPIDA) samples, prepared by following the protocol described in Section 6.3.2, were analysed for tertiary amine group using FTIR and ^{15}NMR, and for the presence of nitrogen using elemental analysis, in order to test the validity of the polymer reaction explained above. Figure 6-4a,b illustrates the FTIR obtained for poly(HEMA-co-EGDMA-co-HPIDA) sample with monomer ratio of 41.6:18.6:40 (HEMA:HPIDA:EGDMA) by volume(%). As it is evident from Figure 6-4b, a new peak corresponding to tertiary amine was observed at a wave number of 1586 cm^{-1} with FTIR analysis. This peak was absent in poly(HEMA-co-EGDMA) (refer Figure 6-4a). Also ^{15}N NMR analysis for the same poly(HEMA-co-EGDMA-co-HPIDA) sample showed a peak (refer Figure 6-5b) at around 290 ppm, which was absent in standard poly(HEMA-co-EGDMA) as seen in Figure 6-5a. This peak also corresponds to tertiary amine group. The FTIR for rest of the samples were similar to the ones reported in Figure 6-4b. Elemental analysis of the sample further proved the presence of nitrogen. The elemental composition measured for 1.73 g of the polymer sample described above was C: 57.3%, H: 7.4% and N: 0.1%.

The HPIDA monomer mixture prepared by following the protocol described in Section 6.3.2 was analysed using ^{1}H NMR (refer Appendix 4 (A.4.2)). Using the amount of nitrogen obtained from elemental analysis for poly(HEMA-co-EGDMA-co-HPIDA), mass of HPIDA in the poly(HEMA-co-EGDMA-co-HPIDA) sample was calculated as 0.0225 g (ml of monolith)$^{-1}$. The volume(%) of HPIDA in the HPIDA monomer solution was calculated as 12.2%. The low percentage of HPIDA

can be due to the presence of monomer glyceryl allyl ether (GAE), which is formed preferentially over HPIDA by hydrolysis of AGE [38]. GAE does not react with IDA during the HPIDA synthesis reaction. However, it still remains in the HPIDA monomer solution that was used during photopolymerisation and undergoes copolymerisation, thus reducing the amount of HPIDA in the polymer.

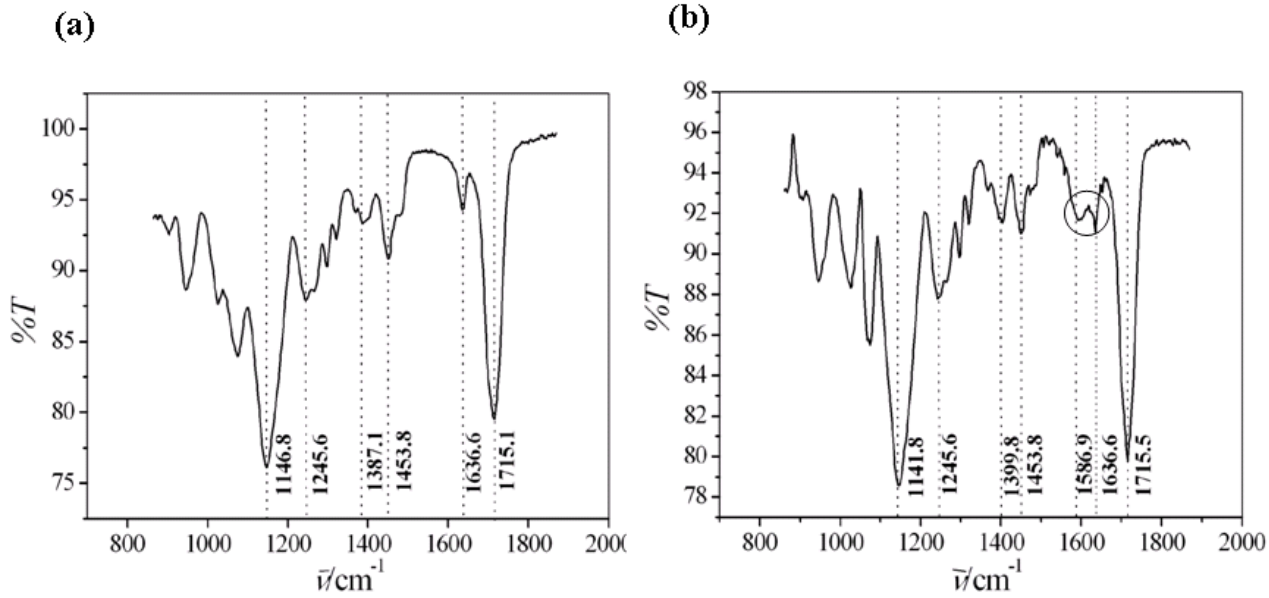

Figure 6-4 (a) FTIR spectra of poly(HEMA-co-EGDMA) (b) FTIR spectra of poly(HEMA-co-EGDMA-co-HPIDA) with a new peak at 1586 cm^{-1} for tertiary amine

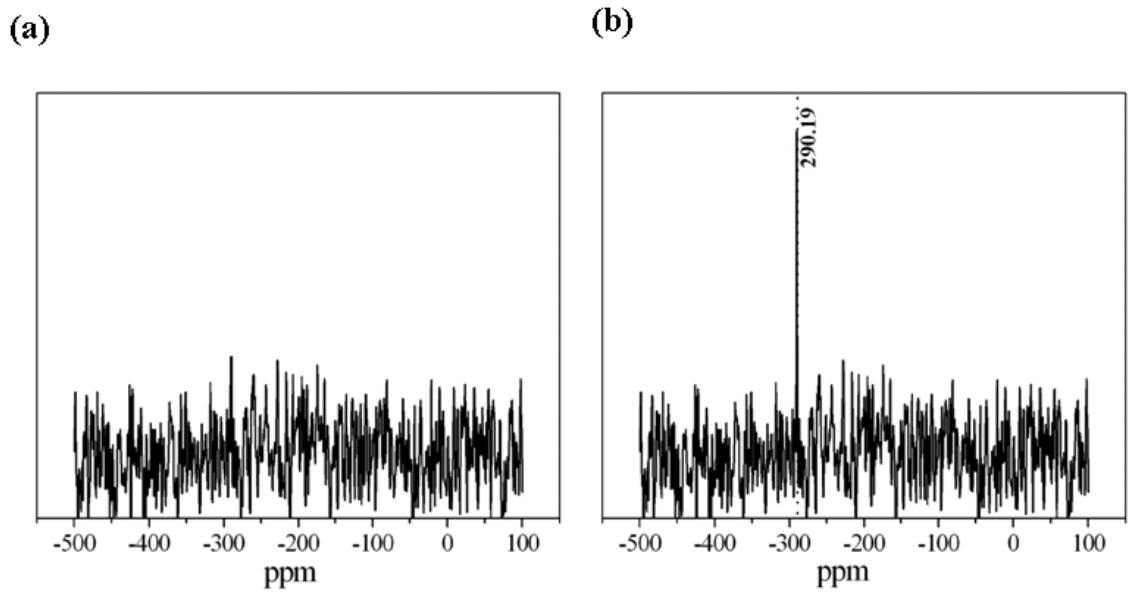

Figure 6-5 (a) ^{15}N-NMR spectra of poly (HEMA-co-EGDMA) (b) ^{15}N-NMR spectra of poly (HEMA-co-EGDMA-co-HPIDA) with a peak at 290 ppm for tertiary amine groups

Experiments were carried out to study the effect of amount of comonomers (HPIDA and HEMA) on the metal ion capacity (MIC) (refer Figure 6-6). The amount of Cu^{2+} immobilised was calculated using calibration curves obtained from UV absorption spectroscopy (Appendix 4 (A.4.3)). Figure 6-6 illustrates the effect of HEMA:HPIDA volume ratio (V_{HEMA}/V_{HPIDA}) on the MIC of poly(HEMA-co-EGDMA-co-HPIDA). MIC increased proportionally with HEMA:HPIDA volume ratio and reached a maximum of 2.42 μmol (ml of monolith)$^{-1}$ at a volume ratio of 2.22. Further increase in the amount of HPIDA decreased the capacity. At low HEMA concentrations of 10-20 vol% in total monomer mixture the formation of a poly(HEMA-co-HPIDA) gel with a low metal ion capacity was favoured. With these gels Cu^{2+} was bound weakly and most of it was removed by washing with an aqueous solution of 1 M NaCl, 250 mM sodium phosphate and 300 mM imidazole. Increase in the amount of HEMA to 40 vol% in the monomer mixture resulted in the formation of monolithic structures with structural rigidity [43]. With these monoliths Cu^{2+} bound more strongly and the metal ion binding capacity increased to 2.42 μmol (ml of monolith)$^{-1}$. Further increase in the amount of HEMA to 50 vol% in total monomer mixture produced impermeable poly(HEMA-co-HPIDA). The monomer composition corresponding to maximum metal ion binding capacity was HEMA 41.4 vol%, HPIDA 18.6 vol% and EGDMA 40 vol% and this was selected for the fabrication of monoliths for the protein binding experiments.

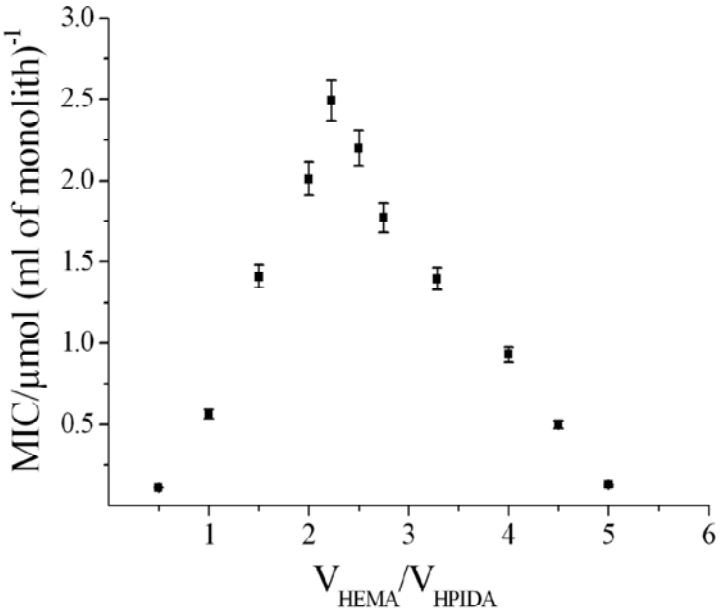

Figure 6-6 Plot of copper(II) chelation capacity against volume ratio of HEMA to HPIDA

6.4.1.2 Protein Analysis with Poly(HEMA-co-EGDMA-co-HPIDA)

1.) ***Protein Binding Studies:*** A his tag protein, LacI-His_6-GFP, was used to calculate the protein binding capacity of the Cu^{2+} loaded poly(HEMA-co-EGDMA-co-HPIDA) developed in Section 6.3.2, in batch process. Figure 6-7 shows a logarithmic plot of the total protein amount in the supernatant during loading with LacI-His_6-GFP ($[C]_o$ = 500 µg ml^{-1}), washing the monolith with wash buffer and eluting the bound protein using elution buffer. Only LacI-His_6-GFP loaded on Cu^{2+} immobilised monolith was recovered during the elution stage, whereas LacI-His_6-GFP did not bind to monoliths in the absence of Cu^{2+}. Similar experiments were also performed, as described in Section 6.3.5, with another protein, β-Lactoglobulin, that did not contain a his tag. Only a very low level of β-Lactoglobulin ($[C]_o$ = 500 µg ml^{-1}) was detected in the eluate, consistent with a low degree of non-specific binding (refer Figure 6-7).

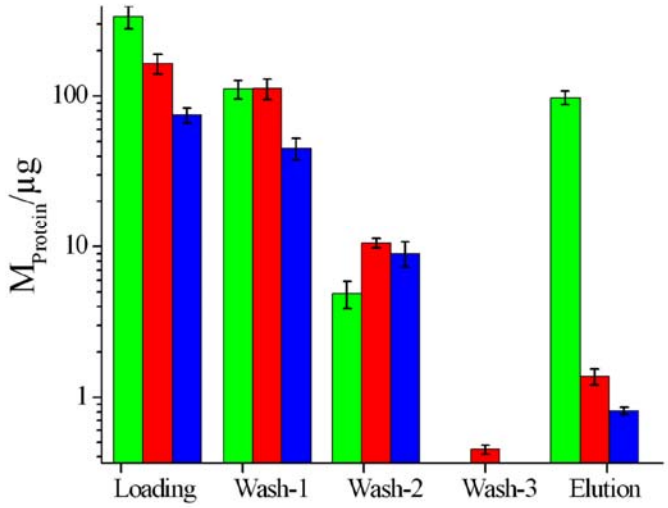

Figure 6-7 Study of amount of protein collected at loading, wash and elution stages of polymer-protein binding analysis. 500 µg ml^{-1} LacI-His$_6$-GFP (positive control); 500 µg ml^{-1} LacI-His$_6$-GFP without charging the polymer with Copper(II) ions (negative control); 500 µg ml^{-1} β-Lactoglobulin (negative control)

Batch protein binding studies were carried out with another his tag protein to confirm the selectivity of Cu^{2+} immobilised poly(HEMA-co-EGDMA-co-HPIDA) monoliths. Figure 6-8 shows the comparison for LacI-His$_6$-GFP and α-Synuclein-His$_8$-YFP adsorption on poly(HEMA-co-EGDMA-co-HPIDA) at a concentration of 9.5 µg ml^{-1}. The higher protein binding capacity of poly(HEMA-co-EGDMA-co-HPIDA) for α-Synuclein-His$_8$-YFP, as expected, was due to the presence of eight histidine residues compared to only six in LacI-His$_6$-GFP. α-Synuclein-His$_8$-YFP hence bound strongly to the Cu^{2+} and did not get washed away during the two wash stages.

Another factor contributing to the low amounts of LacI-His$_6$-GFP being bound to poly(HEMA-co-EGDMA-co-HPIDA) monolith could be the steric hindrance or difference in accessibility of histidine tags for metal interaction [44]. LacI-His$_6$-GFP has been reported to exist as a tetrameric protein with a total molecular weight of 274 kDa whereas α-Synuclein-His$_8$-YFP is a comparatively smaller molecule with molecular weight of 30 kDa.

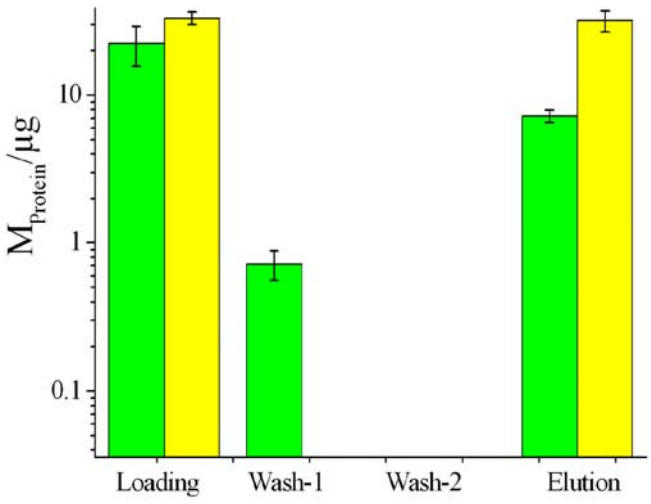

Figure 6-8 Comparative study of amount of his tag protein collected at various stages of polymer-protein capacity analysis for Laci-His_6-GFP and α-Synuclein-His_8-YFP in batch. 9.5 µg ml^{-1} LacI-His_6-GFP; 9.5 µg ml^{-1} α-Synuclein-His_8-YFP

2.) ***Langmuir Adsorption Isotherms:*** The affinity of his tag proteins was also studied using Langmuir adsorption isotherms. Langmuir adsorption isotherms for two his tag protein, LacI-His_6-GFP and α-Synuclein-His_8-YFP, were obtained by following the protocol described in Section 6.3.5 (refer Figure 6-9 and Figure 6-10). The k_D (Langmuir adsorption constant) and q_m (maximum protein adsorbed) values obtained for LacI-His_6-GFP were 174.5, 347.35 µg ml^{-1} and that for α-Synuclein-His_8-YFP were 6.17, 743.7 µg ml^{-1} respectively. The extremely low value of k_D for α-Synuclein-His_8-YFP as compared to LacI-His_6-GFP confirms the high affinity of α-Synuclein-His_8-YFP for the metal ion and fast kinetics of the polymer-protein adsorption reaction as compared to LacI-His_6-GFP.

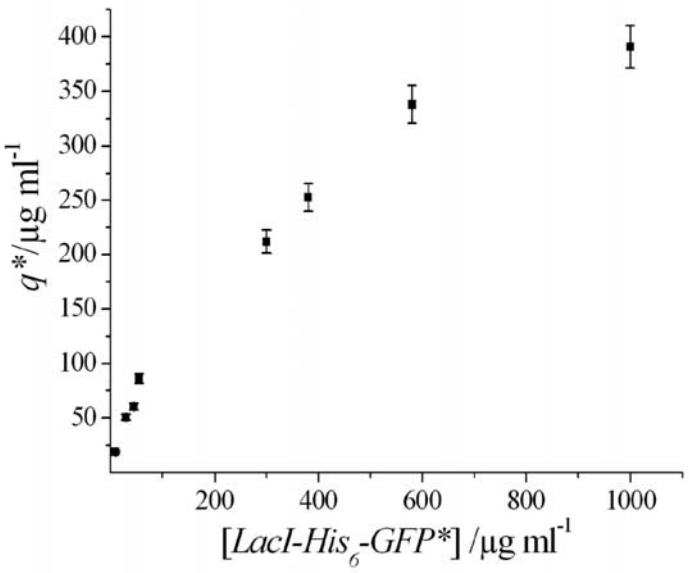

Figure 6-9 Plot of amount of adsorbed LacI-His_6-GFP against equilibrium concentration of LacI-His_6-GFP (k_D = 174.5 µg ml^{-1} and q_m = 347.3 µg ml^{-1})

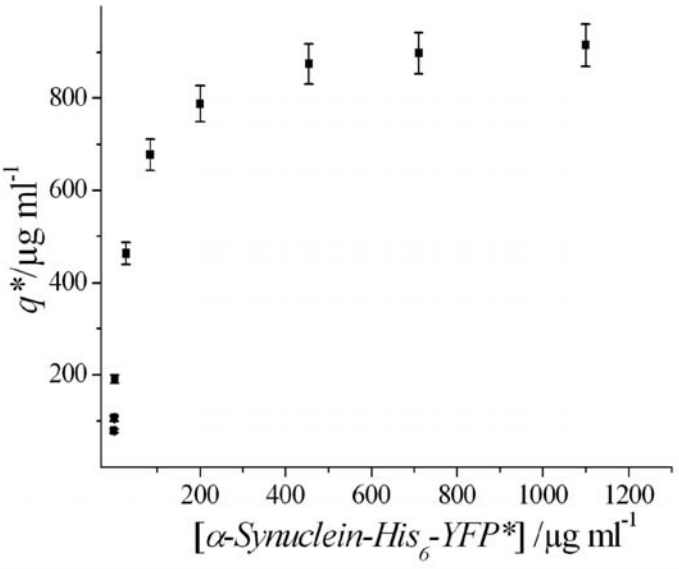

Figure 6-10 Plot of amount of adsorbed α-Synuclein-His_8-YFP against equilibrium concentration of α-Synuclein-His_8-YFP (k_D= 6.17 µg ml^{-1} and q_m = 743.7 µg ml^{-1})

3.) ***Confocal Microscopy Studies:*** Laser confocal microscopy imaging was employed as another test to study the his tag protein adsorption/desorption on poly(HEMA-co-EGDMA-co-HPIDA) at various stages of operation described below. Figure 6-11 illustrates confocal microscopy images

showing (a) α-Synuclein-His_8-YFP fluorescence and (b) LacI-His_6-GFP fluorescence, superimposed on the optical transmission image of a section of porous poly(HEMA-co-EGDMA-co-HPIDA) (i) prior to protein adsorption, (ii) after protein adsorption, (iii) after buffer wash to remove excess unbound protein and (iv) after eluting the adsorbed protein using elution buffer.

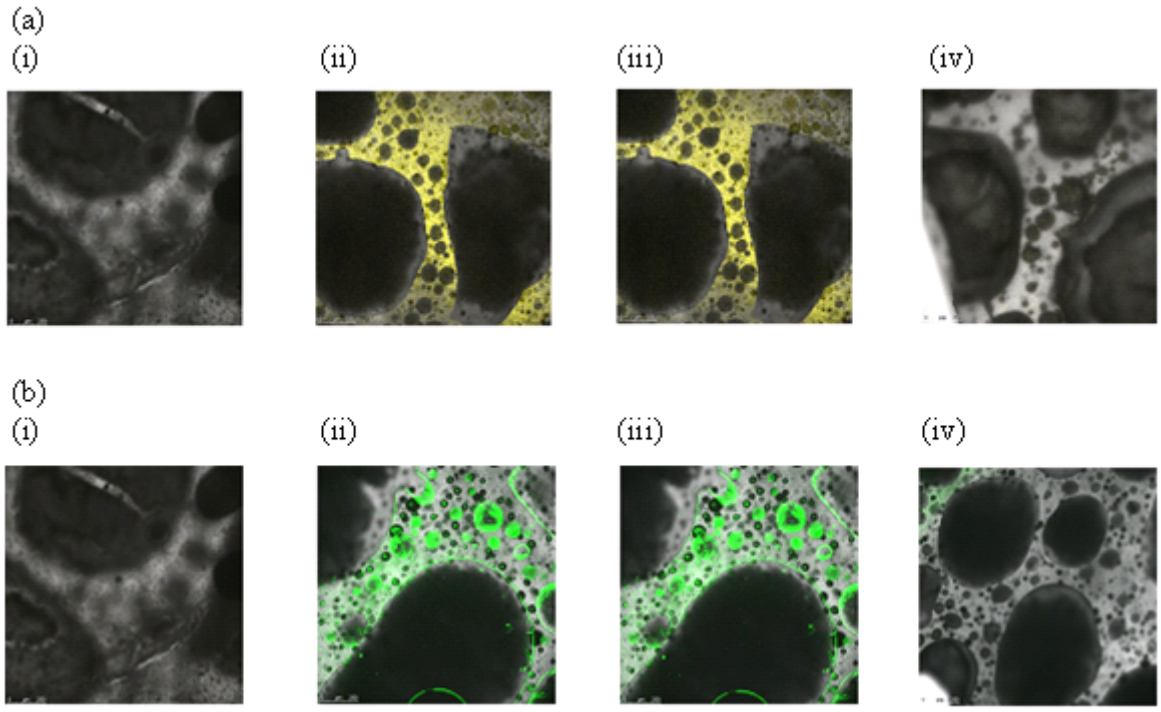

Figure 6-11 Confocal microscopy images showing (a) α-Synuclein-His_8-YFP, (b) LacI-His_6-GFP fluorescence superimposed on the optical transmission image of a section of porous poly(HEMA-co-EGDMA-co-HPIDA) monolith (NH_4Cl as porogen) at various stages of batch protein adsorption experiment through a field of view. Images show: (i) prior to protein adsorption (ii) after protein adsorption (iii) after wash and (iv) after elution.

The values of metal ion capacity and protein binding capacity obtained for LacI-His_6-GFP and α-Synuclein-His_8-YFP with poly(HEMA-co-EGDMA-co-HPIDA) were compared with commercial GE healthcare Histrap FF resin (refer Table 6-2) of diameter 34 µm. The Histrap FF resin were characterised for its MIC and EBC in batch using similar protocol as described in Section 6.3.3 and Section 6.3.5. Poly(HEMA-co-EGDMA-co-HPIDA) monolith appeared to be quite low in both metal ion and protein binding capacities, approximately by a factor of 10, for both LacI-His_6-GFP and α-Synuclein-His_8-YFP. This can be explained due to two reasons:

i) Highly porous network of agarose beads, rendering high surface area compared to poly(HEMA-co-EGDMA-co-HPIDA) as illustrated in Figure 6-12.

ii) Due to low volume percentage of HPIDA in the HPIDA monomer solution prepared (refer Section 6.4.1.1). The HPIDA monomer solution can be purified using distillation, solvent extraction to overcome this issue (*Future Work*).

Specifications	**HisTrap FF Column Resin** (*GE Healthcare*)	**Poly(HEMA-co-EGDMA-co-HPIDA) Monolith**
Chelating group	Iminodiacetic acid	Iminodiacetic acid
Matrix	Highly cross-linked agarose	Highly cross-linked polymer
Particle size	34 μm (extremely porous)	Monolith (porosity introduced using 100 μm NH_4Cl particles)
Metal ion capacity (Cu^{2+})	12.07 μmol (ml of resin)$^{-1}$	2.417 μmol (ml of monolith)$^{-1}$
Binding capacity		
LacI-His_6-GFP (274 kDa)	3.580 mg (ml of resin)$^{-1}$	0.391 mg (ml of monolith)$^{-1}$
α-Synuclein-His_8-YFP (30 kDa)	8.849 mg (ml of resin)$^{-1}$	0.910 mg (ml of monolith)$^{-1}$

Table 6-2 Comparison of properties of poly(HEMA-co-EGDMA-co-HPIDA) monolith synthesised by photopolymerisation with commercial Histrap FF column specifications obtained from GE Healthcare

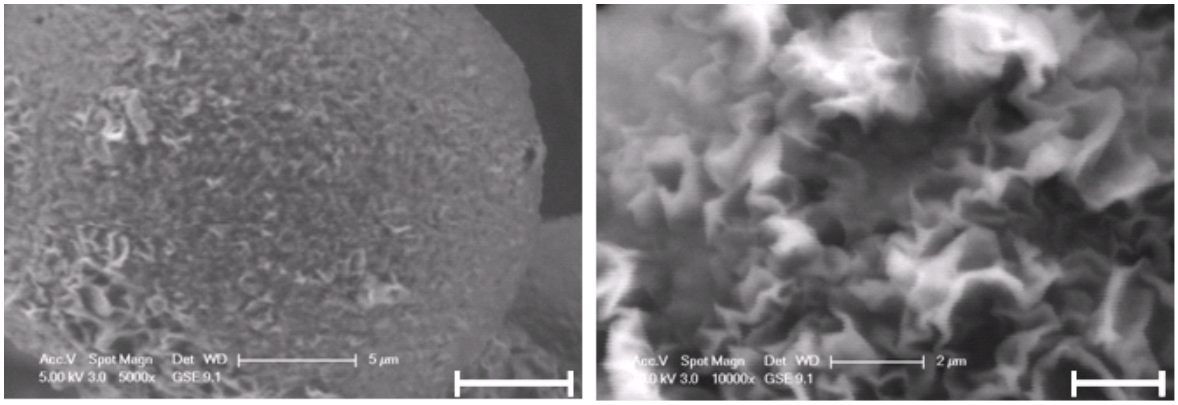

Figure 6-12 ESEM images illustrating the surface morphology of 34 µm diameter agarose beads used in GE Histrap FF columns

6.4.2 Flow System Analysis

The IMAC polymer developed in batch system was now used to fabricate poly(HEMA-co-EGDMA-co-HPIDA) monoliths inside mesochannels, with pores of diameter 100 µm. The protein binding characteristics were studied in hydrodynamic system by flowing his tag proteins at various flow rates. Laser confocal analysis was used to study the adsorption and desorption characteristics of fluorescent his tag proteins in a meso-chromatography column.

6.4.2.1 Protein Analysis with Poly(HEMA-co-EGDMA-co-HPIDA)

A meso-chromatography column was fabricated from photopolymerised poly(HEMA-co-EGDMA-co-HPIDA) monolith inside a glass mesochannel, as discussed in Section 6.3.6. The reason to use photopolymerisation was to obtain micropatterned structures of known dimensions inside the channel (refer Chapter 5). Pressure drop calculated across the 1.5 cm monolith, with 100 µm pores inside the mesochannel, was around 4 kPa cm^{-1} at a flow rate of 1.8 µl s^{-1} (see Figure 6-13).

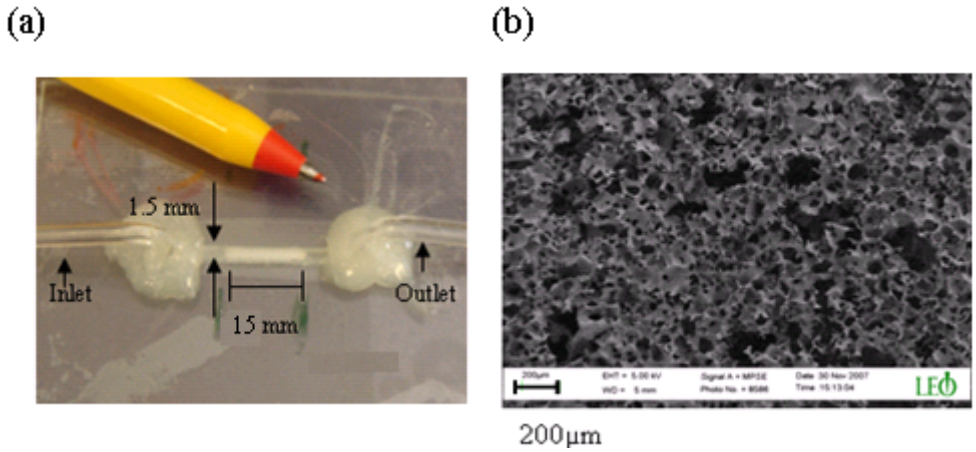

Figure 6-13 (a) Micropatterned poly(HEMA-co-EGDMA-co-HPIDA) monolith (*L* = 1.5 cm) inside a mesochannel (*l* = 2.5 cm, *w* = 0.155 cm, *h* = 0.07 cm) (b) SEM image of poly(HEMA-co-EGDMA-co-HPIDA) monolith formed using NH_4Cl as porogen (d_p = 100 µm)

The meso-chromatography column was fed with LacI-His_6-GFP (170 µg ml^{-1}) at flow rates of 0.3, 0.47, 0.66 and 1.5 µl s^{-1} to calculate the DBC as a function of flow rate. A shift in the load, wash and elution curves with decreasing flow rates (increasing residence time) was observed as illustrated in Figure 6-14a-c. EBC was also calculated by leaving the column overnight with protein. DBC values for LacI-His_6-GFP, measured as 10% of breakthrough value (refer Figure 6-14d), were found to be constant at 0.319 mg (ml of monolith)$^{-1}$ for low flow rates of 0.3 and 0.47 µl s^{-1} and comparable to the EBC of 0.37 mg (ml of monolith)$^{-1}$. At higher flow rates of 0.66 and 1.5 µl s^{-1}, DBC was calculated as 0.154 and 0.148 mg (ml of monolith)$^{-1}$ respectively. Due to the continuous porous network of channels inside monolith, the rate of adsorption in meso-chromatography is no longer pore diffusion limited, allowing dynamic binding capacities to be comparable to the equilibrium ones at lower flow rates.

The flow experiments explained above were repeated using α-Synuclein-His_8-YFP (170 µg ml^{-1}) at a flow rate of 0.47 µl s^{-1}, as illustrated in Figure 6-15. The equilibrium and dynamic binding capacities of α-Synuclein-His_8-YFP were found to be almost double at a flow rate of 0.47 µl s^{-1}, compared to LacI-His_6-GFP as reported in Table 6-3.

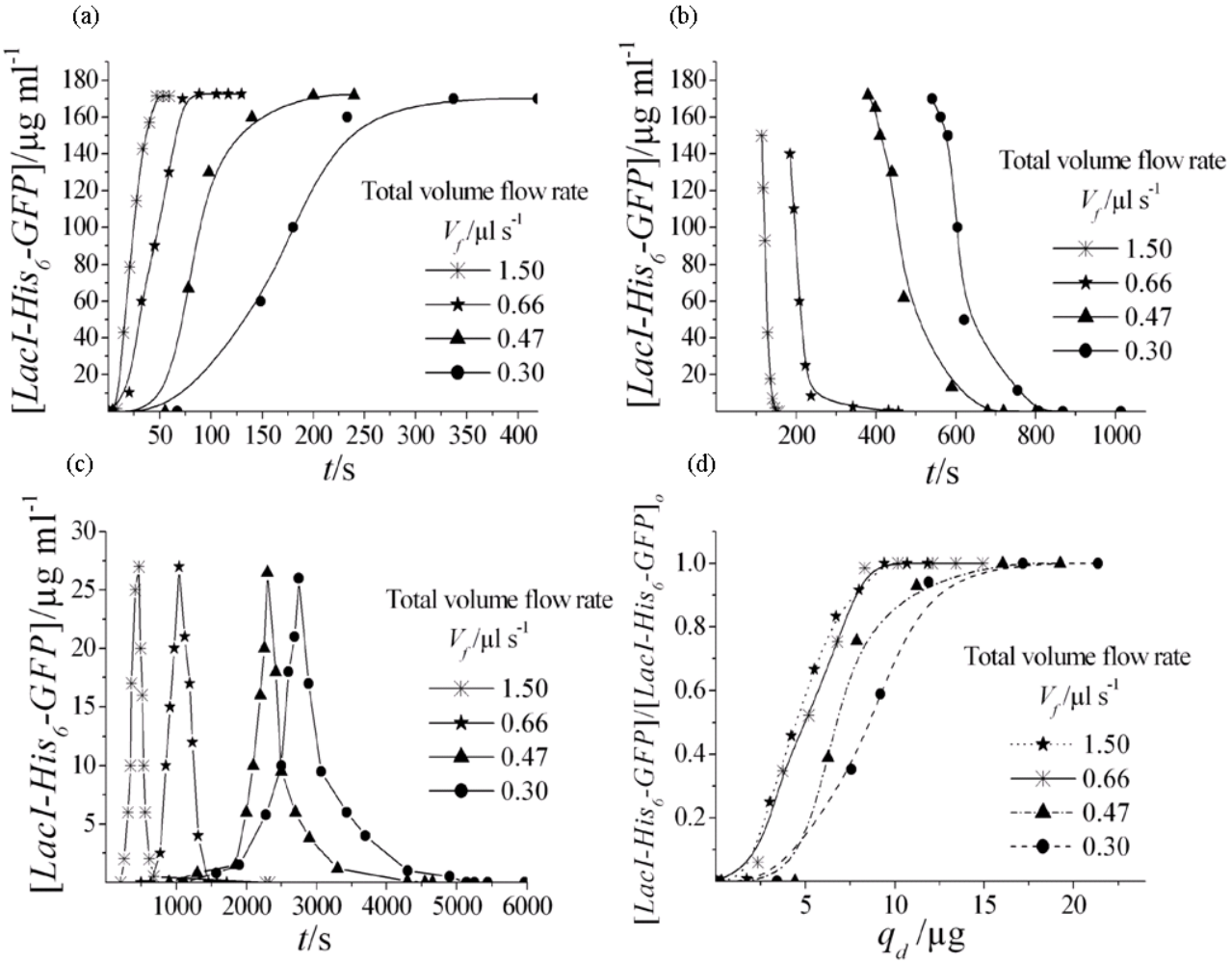

Figure 6-14 (a-c) Plot of LacI-His_6-GFP concentrations against time at flow rates of 0.3, 0.47, 0.66 and 1.5 µl s^{-1} for (a) Loading (b) Wash and (c) Elution stages (d) Plot of normalised concentration of LacI-His_6-GFP against amount of protein adsorbed

The amount of protein bound to the monolith in meso-chromatography column was also calculated from area under the elution curves (Figures 6-14c, Figure 6-15), for all the flow rates. It was noted to be constant at 5.5 µg (0.34 mg (ml of monolith)$^{-1}$) for LacI-His_6-GFP and 9 µg (0.55 mg (ml of monolith)$^{-1}$) for α-Synuclein-His_8-YFP.

Sample Protein	**Equilibrium Binding Capacity** mg (ml of monolith)$^{-1}$	**Dynamic Binding Capacity** mg (ml of monolith)$^{-1}$
LacI-His_6-GFP	0.370	0.319
α-Synuclein-His_8-YFP	0.802	0.543

Table 6-3 Comparison of equilibrium and dynamic binding capacities of poly(HEMA-co-EGDMA-co-HPIDA) for his tag proteins, LacI-His_6-GFP and α-Synuclein-His_8-YFP, passed through a meso-chromatography column (*l* = 2.5 cm, *w* = 0.155 cm, *h* = 0.07 cm, *L* = 1.5 cm). Dynamic binding capacity was calculated at 10% breakthrough and at a flow rate of 0.47 µl s^{-1}

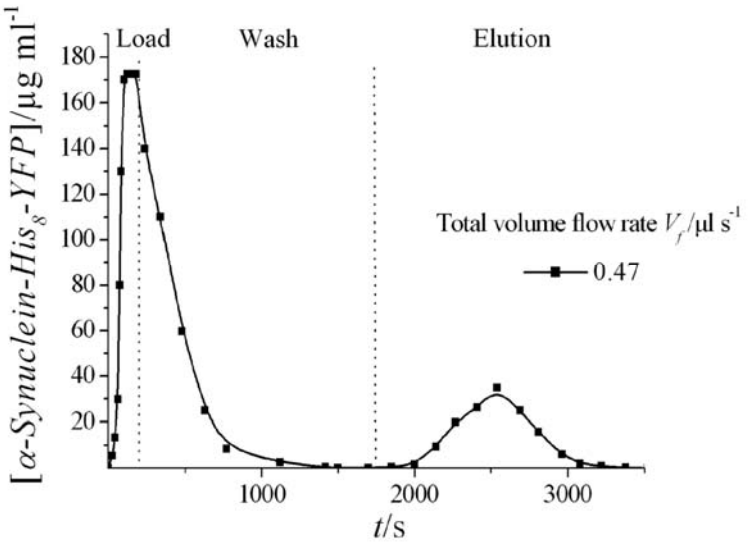

Figure 6-15 Plot of outlet concentration of α-Synuclein-His_8-GFP against time in a meso-chromatography column (*l* = 2.5 cm, *w* = 0.155 cm, *h* = 0.07 cm, *L* = 1.5 cm) at a flow rate of 0.47 µl s^{-1}

SDS PAGE gel analysis was performed to confirm the protein adsorption and desorption at various stages of meso-chromatography operation. Figure 6-16a describes a SDS PAGE silver stain gel for LacI-His_6-GFP when fed to the column at a flow rate of 0.66 µl s^{-1} with (i) lane M illustrating the progression of marker protein through the gel, (ii) lane L illustrating the progression of protein sample that was used to load the meso-chromatography column, (iii) lane W-1,W-2,W-3, W-4 describing the progression of samples collected during washing stage at times 184 s, 208 s, 237 s

431 s (iv) lane E-1, E-2 describing the progression of sample collected during the elution stage at times 1040 s, 1190 s. LacI-His_6-GFP was detected roughly at 70 kDa instead of 240 kDa because the addition of reducing agent (dithiothreitol) during SDS PAGE analysis reduces the sulphide linkages, thus separating tetramer into monomer. Similarly Figure 6-16b describes a SDS PAGE silver stain gel for α-Synuclein-His_8-YFP when fed at a flow rate of 0.47 μl s^{-1} with (i) lane M illustrating the progression of marker protein through the gel, ii) lane L illustrating the progression of protein sample that was used to load the meso-chromatography column, (iii) lane W-1,W-2,W-3 describing the progression of samples collected during washing stage at times 239 s, 476 s, 1132 s and (iv) lane E-1 describing the progression of sample collected during the elution stage at 2532 s.

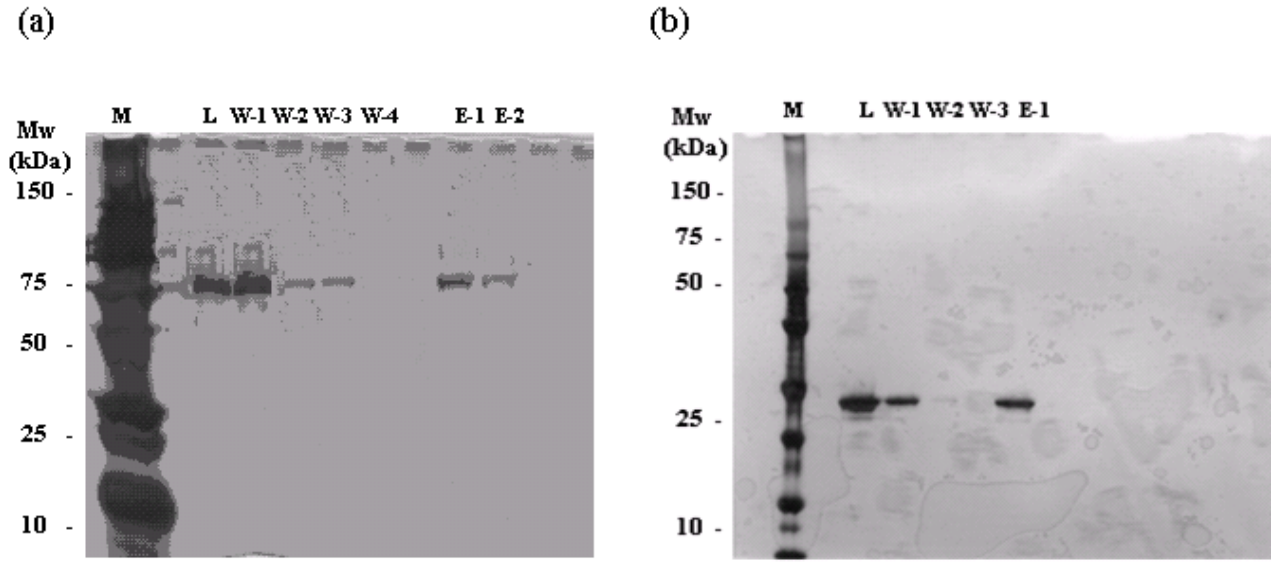

Figure 6-16 (a) SDS PAGE silver stain gel obtained for fractions of LacI-His_6-GFP operation sample collected at following stages of operation. L: loading, W-1: wash fraction at time 184 s, W-2: wash fraction at time 208 s, W-3: wash fraction at time 237 s, W-4: wash fraction at time 431 s and E-1: elution fraction at time 1040 s, E-2: elution fraction at 1190 s, (b) SDS PAGE silver stain gel obtained for fractions of α-Synuclein-His_8-YFP sample collected at following stages of operation. L: loading, W-1: wash fraction at time 239 s, W-2: wash fraction at time 476 s, W-3: wash fraction at time 1132 s, E: elution at 2532 s

The load, wash, elution curves and SDS PAGE gel analysis confirmed the working of the new IMAC poly(HEMA-co-EGDMA-co-HPIDA) meso-chromatography column, with both the his tag proteins, LacI-His_6-GFP and α-Synuclein-His_8-YFP, in a continuous operation.

6.4.2.2 Confocal Analysis

Confocal analysis was carried out inside the meso-chromatographic columns, as described in Section 6.3.7, to study the moving protein front in the column (refer Figure 6-17). Figure 6-17b-d show the progressive movement of the adsorbed LacI-His_6-GFP protein front through the field of view during loading. Figure 6-17e shows that the protein remained bound to the monolith in the field of view after washing with buffer, but was removed completely following elution (refer Figure 6-17f). There was no channelling observed during the whole process.

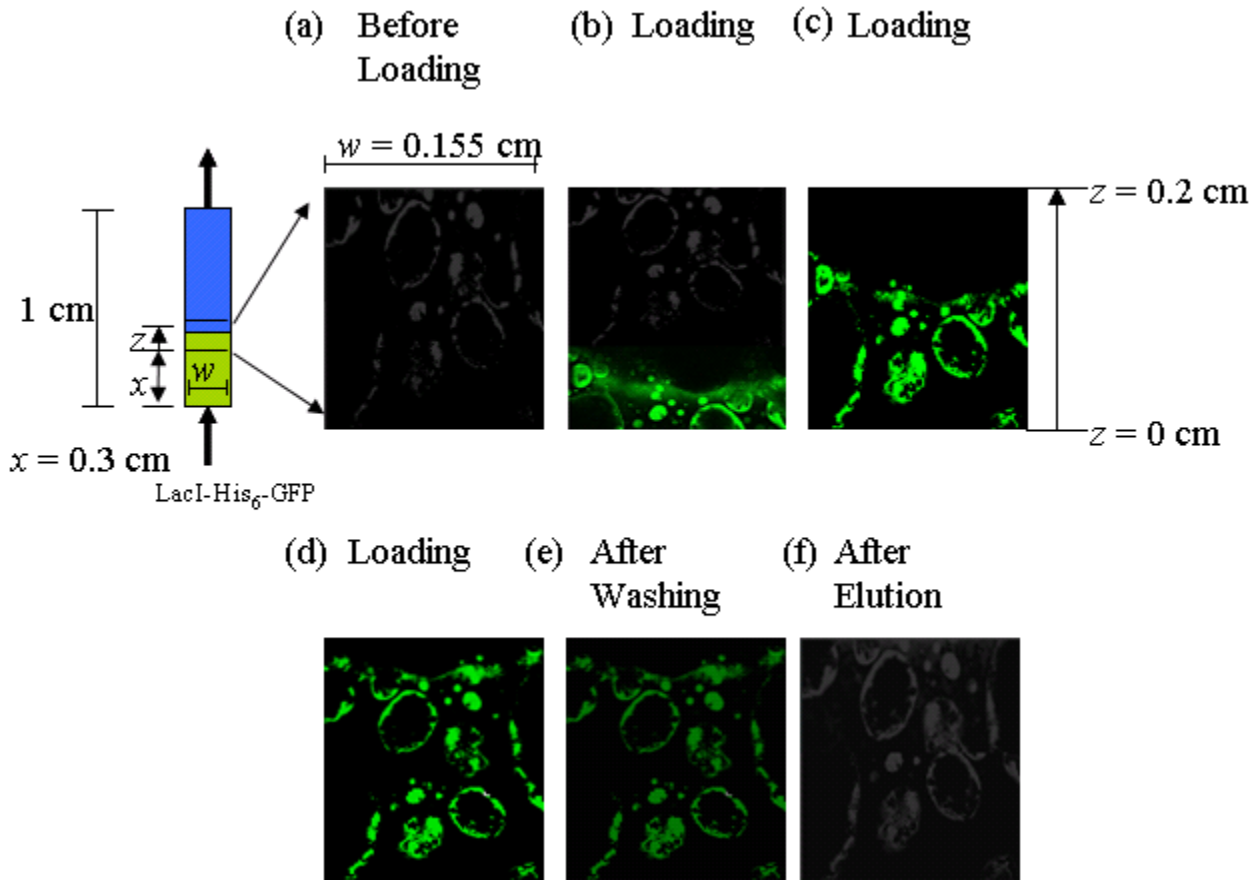

Figure 6-17 Confocal microscopy images showing LacI-His_6-GFP fluorescence superimposed on the optical transmission image of a section of porous poly(HEMA-co-EGDMA-co-HPIDA) monolith (NH_4Cl as porogen) at various stages of meso-chromatography. Images show: (a) prior to loading LacI-His_6-GFP at z = 0 cm, (b-d) during loading when the front of adsorbed protein had progressed to (b) z = 0.05 cm, (c) z = 0.11 cm, (d) z = 0.2 cm, (e) after washing and (f) after elution

6.4.2.3 Cell Lysate Analysis

LacI-His_6-GFP cell lysate obtained during the protein preparation process, as described in Section 6.3.4, also contains other proteins as well as insoluble and soluble impurities. Purification of LacI-His_6-GFP from the cell lysate was carried out inside the meso-chromatography column (l = 2.5 cm, w = 0.155 cm, h = 0.07 cm, L = 1.5 cm) by a similar approach, as discussed in Sections 6.3.4 and Section 6.3.6. Figure 6-18 illustrates the elution curve obtained for pure LacI-His_6-GFP at a flow rate of 1.33 µl s^{-1}.

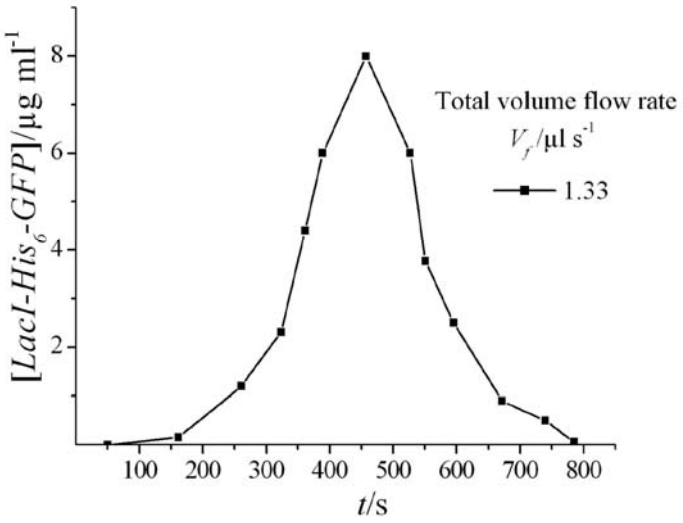

Figure 6-18 Plot of LacI-His_6-GFP cell lysate concentration against time at 1.33 µl s^{-1} for the elution stage

A SDS PAGE silver stain analysis (lane E1) confirmed the purification step, as can been seen in the Figure 6-19. Only one band corresponding to LacI-His_6-GFP monomer was obtained, however the strength of the band was low due to poor yield of LacI-His_6-GFP during the meso-chromatographic cell lysate purification process. The yield of LacI-His_6-GFP was 2.67 µg from 2 ml of lysate.

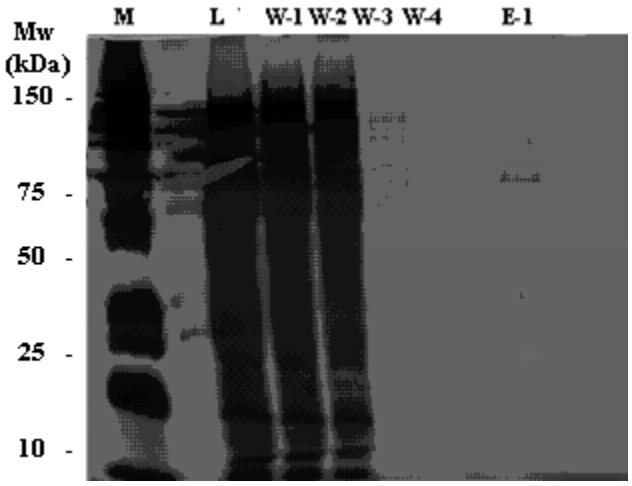

Figure 6-19 SDS PAGE silver stain gel obtained for fractions of sample collected at three main stages of operation. L: loading, W-1: first wash fraction, W-2: second wash fraction, W-3: third wash fraction, W-4: fourth wash fraction, E: elution

Although this proves that cell lysate could be purified directly inside the mesochannel using low volumes, occasionally the meso-chromatography column was found to get blocked due to residue or cells fragments in the cell lysate. Therefore a better separation of cell fragments and other insoluble wastes from soluble LacI-His_6-GFP in the cell lysate, prior to feeding into the meso-chromatography column, would give better protein yields. Nonetheless, an on-line system of growing cells *in situ*, followed by protein synthesis and then protein purification on one single chip, could be an attractive alternative for a quick analysis in areas such as pharmacology. Also in industries where broth is prepared in large quantities and final concentration is critical, a quick analysis of broth at various times could help the engineers decide when to stop the reaction and save operating cost and time.

6.5 CONCLUSIONS

In this chapter, the development and fabrication of a meso-chromatography column for application in IMAC was demonstrated successfully. A new metal chelating ligand (IDA) bound monomer, HPIDA, was synthesised which was further used to synthesise poly(HEMA-co-EGDMA-co-HPIDA) monolith. Poly(HEMA-co-EGDMA-co-HPIDA) monolith was optimised for metal

chelation capacity (2.42 μmoles (ml of monolith)$^{-1}$) using Cu^{2+} and also for protein binding capacity using LacI-His_6-GFP (0.391 mg (ml of monolith)$^{-1}$ and α-Synuclein-His_8-YFP (0.91 mg (ml of monolith)$^{-1}$. The metal ion and protein binding capacities were compared with commercially available resin and were seen to differ by a factor of 10, but the ability to fabricate them *in-situ* in a micro-flow device, their reduced diffusional mass transfer resistance and their ability to handle some solids containing feed streams offer other advantages.

Batch studies confirmed that only his tag proteins could bind to poly(HEMA-co-EGDMA-co-HPIDA) monolith strongly and remained adsorbed during the wash stage. The non his tag proteins, such as β-Lactoglobulin, did not bind to the column. The negative control for Cu^{2+} binding was demonstrated, where no LacI-His_6-GFP binding was observed in the absence of Cu^{2+} ions. Laser confocal microscopy optically demonstrated the loading, wash and elution operations in a batch analysis.

Experiments were also carried out in flow systems with LacI-His_6-GFP and α-Synuclein-His_8-YFP. Dynamic binding capacities of LacI-His_6-GFP and α-Synuclein-His_8-YFP were calculated at varying flow rates and were noted to be constant at low flow rates. They were also comparable with the equilibrium binding capacities at lower flow rates. Laser confocal microscopic analysis showed a steady moving protein front in the column without any channeling. SDS PAGE analysis showed clear band of protein during elution, hence confirming the working of the meso-chromatography column. Purification of LacI-His_6-GFP from its cell lysate was demonstrated inside the meso-chromatography column.

Further optimisation is needed; nevertheless it was shown that meso-chromatography columns would be useful in future for application in quick downstream analysis in fermentation and protein purification.

6.6 REFERENCES

[1] Nguyen, N.-T.; Wereley, S. T. *Fundamentals and Applications of Microfluidics* **2002**, Artech House, Norwood, ISBN 1-58053-343-4, pp.401.

[2] Carlier, J.; Chuda, K.; Arscott, S.; Thomy, V.; Verbeke, B.; Coqueret, X.; Camart, J. C.; Druon, C.; Tabourier, P. *J. Micromech. Microeng.* **2006**, 16, 2211-2219.

[3] Wilchek, M.; Chaiken, I. *An Overview of Affinity Chromatography In: Affinity Chromatography-Methods and Protocols. Methods in Molecular Biology* **2000** Ed. Bailon, P.; Ehrlich, G. K.; Fung, W-J.; Berthold, W., Humana Press, Totowa Volume 147, pp. 1-7.

[4] Weigl, B. H.; Yager, P. *Science* **1999**, 283, 346-347.

[5] Cunningham, D. D. *Anal. Chim. Acta* **2001**, 429, 1-18.

[6] Peterson, D. S.; Rohr, T.; Svec, F.; Fréchet, J. M. J. *Anal. Chem.* **2002**, 74, 4081–4088.

[7] Svec, F.; Frechet, J. M. J. *Chem. Mater* **1995**, 7, 707–15.

[8] Liao, J-L.; Chen, N.; Ericson, C.; Hjerten, S. *Anal. Chem.* **1996**, 68**,** 3468–72.

[9] He, B.; Tan, L.; Regnier, F. *Anal Chem.* **1999**, 71, 1464-1468.

[10] Davies, M. I.; Lunte, C. E. *Chem. Soc. Rev.* **1997**, 26, 215-222.

[11] Kaplan**,** B.; Shtrasburg**,** S.; Pras, M. *J. Clin. Path.* **2003**, 56, 86-90.

[12] Yoon, S. K.; Choban, E. R.; Kane, C.; Tzedakis, T.; Kenis, P. J. A. *J. Am. Chem. Soc.* **2005**, 127, 10466.

[13] West, J. A. A.; Satterfield, B. C. *In: Microchip-Based Assay Systems: Methods and Applications, Series: Methods in Molecular Biology* **2007**, Ed. Floriano, P. N., Human press Inc., New Jersey, Vol. 385, pp. 9-21.

[14] Gao, J.; Xu, J.; Locascio, L. E.; Lee, C. S. *Anal. Chem.* **2001**, 73, 2648–2655.

[15] Peterson, D. S.; Rohr, T.; Svec, F.; Fréchet, J. M. J. *Anal. Chem.* **2002**, 74, 4081–4088.

[16] Freire, S. L. S.; Wheeler, A. R. *Lab Chip.* **2006**, 6, 1415-1423.

[17] Hellferich, F. *Nature* **1961**, 189, 1001.

[18] Porath, J.; Carlsson, J.; Olsson, I.; Belfragge, G. *Nature* **1975**, 258, 598-599.

[19] Nieba, L.; Nieba-Axmann, S. E.; Persson, A.; Hamalainen, M.; Edebratt, F.; Hansson, A.; Lidholm, J.; Magnusson, K.; Karlsson, A. F.; Plückthunv, A.; *Anal. Biochem.* **1997**, 252, 217-228.

[20] Min, C.; Verdine, G. L.; *Nucleic Acids Res.* **1996**, 24, 3806.

[21] Arnold, F. H. *Bio/Technol.* **1991**, 9, 151-156.

[22] Wong, J. W.; Albright, R. L.; Wang, N.-H. *Sep. Purif. Methods* **1991**, 20, 49.

[23] Ueda, E. K. M.; Gout, P. W.; Morganti, L. J.; *Chromat. A* **2003**, 988, 1-23.

[24] Lindgren, G. E. *Am. Biotechnol. Lab.* **1994**, 12, 263.

[25] Hochuli, E.; Bannwarth, H.; Döbeli, R.; Gentz, R.; Stüber, D. *BioTech.* **1988**, 6, 1 321–1325.

[26] Armisen, P.; Mateo, C.; Cortés, E.; Barredo, J. L.; Salto, F.; Diez, B.; Rodes, L.; García, J. L.; Fernandez-Lafuente, R.; Guisan, J. M. *J. Chromatogr. A* **1999**, 848, 61.

[27] Kagedal, L. *In: Protein Purification: Principles, High Resolution Methods, and Applications* **1998,** Ed. Janson, J.-C.; Ryden, L, Wiley, New York, 2nd Edition, pp. 311.

[28] Subramanian A. *General Considerations in Preparative Affinity Chromatography In: Handbook of Affinity Chromatography* **2006**, Ed. Hage, D. S., Taylor and Francis Group, Boca Raton, 2nd Edition, Vol. 92, pp. 287.

[29] Sutton, R. M. C.; Hill, S. J.; Jones, P**.** *J. Chromat. A* **1996**, 739, 81-86**.**

[30] Hage, D. S.; Xuan, H.; Nelson, M. A. *Application an Elution in Affinity Chromatography In: Handbook of Affinity Chromatography* **2006**, Ed. Hage, D. S., Taylor and Francis Group, Boca Raton, 2nd Edition, Vol. 92, pp. 287.

[31] Kemp, G. D. *Process Development: When to start Where to Stop In: Bioseparation and Bioprocessing: A Handbook* **2007**, Ed. Subramanian, G., Wiley-VCH, 2nd Edition, Vol.1, pp. 3.

[32] Langmuir, I. *Phys. Rev.* **1916**, 8, 149–176.

[33] Cheremisinoff , N. P. *Polymer Characterization: Laboratory Techniques and Analysis* **1996**, Noyes Publications, New Jersey.

[34] Shapiro, A. L.; Viñuela, E.; Maizel, J. V. Jr. *Biochem. Biophys. Res. Commun.* **1967**, 28 (5), 815-820.

[35] McCabe, W. L.; Smith, J. C.; Harriott, P. *Unit Operations of Chemical Engineering* **2001**, McGraw-Hill, New York, 6th Edition, pp. 157 - 161.

[36] Becker, H.; Locascio, L. E. *Talanta* **2002**, 56, 267-287.

[37] Kickelbick, G. *J. Sol-Gel Sci. Technol.* **2008**, 46, 281-290.

[38] Chen, F.; Carey, W. S. **1990**, US Patent No. 4913880

[39] Darby, R. A. J.; Hine, A. V. *The FASEB Journal***. 2005**, 19, 801-803.

[40] Ren, D.; Penner, N. A.; Slentz, B. E.; Inerowicz, H. D.; Rybalko, M.; Regnier, F. E. *J. Chromatogr*. **2004**, 1031, 87.

[41] Bradford, M. M. *Anal. Biochem.* **1976**, 72, 248-254.

[42] Ghose, S.; Hubbard, B.; Cramer, S. M. *Biotechnol. Bioeng.* **2007**, 96 (4), 768-779.

[43] Chuda, K.; Jasik, J.; Carlier, J.; Tabourier, P.; Druon, C.; Coqueret, X. *Rad. Phys. Chem.* **2006**, 75, 26–33.

[44] Spitznagel, T. M.; Clark, D. S. *Bio/Technol.* **1993**, 11, 825.

Chapter 7

Conclusions

This thesis has described the design, development and applications of micro analytical devices. The use of micro analytical devices enables the precise, quick and on-line measurements in process analytics.

Chapter 3 described the development of an electrochemical micro-biosensor (EMB) for application in cofactor detection and analysis. It was divided into two sections. The first section investigated the electrochemical response of cofactors, flavin adenine dinucleotide (FAD), flavin mononucleotide (FMN) and Vitamin B_{12} using four different electrode materials - gold, platinum, glassy carbon, boron doped diamond, in batch. Out of the four electrodes, boron doped diamond electrode (BDDE) gave the most well defined and reproducible voltammograms in comparison to the other three and also had a wider potential window to work in. This was due to high resistance to adsorption of biological reagents on the electrode surface during electrochemical reaction, as reported in the literature. The second section described the fabrication of an electrochemical micro-biosensor with integrated BDDE. The EMB was characterised qualitatively and quantitatively, using one-electron oxidation of potassium ferrocyanide at room temperature. Electrochemical study of flavin mononucleotide and nicotinamide adenine dinucleotide was performed inside the EMB using linear sweep voltammetry. The transport limited current as a function of the cube root of

volume flow rate was shown to give a linear response, which is consistent with studies shown for traditional channel electrodes and electrochemical microreactors. The experimental data was validated qualitatively and quantitatively by use of two-dimensional numerical simulation of the concentration profile under hydrodynamic conditions.

Chapter 4 described the application of hydrodynamic focusing within electrochemical microreactor for (bio)chemical sensing. Experimental studies examining the effects of focusing ratio, lead-in length and total volume flow rate on the electrolysis response observed were carried out and compared to results predicted numerically, using a finite difference model. Regimes where diffusional broadening of the reagent stream may affect the current response were identified. The diffusional broadening was low at high flow rates and hence electron transfer at the electrode occurs at the same rate as if the entire channel were filled with reactant. In contrast, diffusional broadening due to considerable lead-in lengths and high focusing ratios affect the concentration of reagents at the electrode surface at low flow rates, resulting in slower electron transfer. The experimental data was validated using a pseudo-two dimensional steady state backward implicit numerical model and a good qualitative agreement between the numerical and experimental approaches was observed.

Chapter 5 detailed the development and synthesis of poly(2-hydroxy ethyl methacrylate-co-ethyleneglycol dimethacrylate) and polypyrrole monolithic features, of micro and meso-scale dimensions, for analytical applications including chromatographic separations and electrochemical detection. This chapter was divided into two sections. The first section investigated a method to micropattern poly(HEMA-co-EGDMA) monoliths. The micropatterned poly(HEMA-co-EGDMA) monoliths were hydrodynamically characterised by measuring the pressure drop. The experimental data was compared with analytical values, calculated using a standard model for flow through porous bed and was found to be in good agreement. The second section described an

electrochemical method to fabricate micropatterned structures of conducting polymer: polypyrrole. The polypyrrole monoliths thus fabricated, were characterised by studying the electrochemical response of N,N,N',N'-tetramethyl-P-phenylenediamine (TMPD) and their current response was compared with the one obtained from standard metal electrodes. Both photopolymerised and electrochemical polymerised monoliths were also studied using physical characterisation techniques such as BET, mercury porosimetry and scanning electron microscopy.

Chapter 6 described the application of photopolymerised monoliths, described in Chapter 5, in the development of an immobilised metal affinity meso-chromatography column. Poly(HEMA-co-EGDMA) monoliths were modified by adding a new metal chelating ligand (iminodiacetic acid) bound monomer, disodium 2,2'-{[2-hydroxy-3-(prop-2-en-1-yloxy)propyl]imino}diacetate (HPIDA), during the polymerisation reaction. Poly(HEMA-co-EGDMA-co-HPIDA) thus obtained was optimised for metal chelation capacity (2.42 μmoles (ml of monolith)$^{-1}$) using copper(II) ion and also for protein binding capacity using LacI-His_6-GFP (0.391 mg (ml of monolith)$^{-1}$ and α-Synuclein-His_8-YFP (0.91 mg (ml of monolith)$^{-1}$, in batch. The metal and protein binding capacities were compared with commercially available resin. Batch studies confirmed that only histidine tag proteins could bind to the poly(HEMA-co-EGDMA-co-HPIDA) monolith strongly and remained adsorbed during the wash stage. Experiments were also carried out in hydrodynamic systems with LacI-His_6-GFP and α-Synuclein-His_8-YFP. Dynamic binding capacities of LacI-His_6-GFP and α-Synuclein-His_8-YFP calculated at varying flow rates were found to remain constant. The meso-chromatography column was also used to demonstrate the purification of LacI-His_6-GFP cell lysate. A single band for the purified protein was observed using SDS PAGE analysis.

Chapter 8

Future Work

The previous chapters described the development, fabrication and application of different micro analytical devices. Analytical techniques such as electrochemical detection and chromatography were studied separately using these devices. These techniques can also be performed on one single platform by making use of a micro-total analytical system. A micro-total analytical system (μTAS), as discussed in Chapter 1, offers the potential for highly efficient and simultaneous processing of a large number of (bio)chemical reagents in medical diagnostics (*e.g.* immunoassays), synthetic chemistry (*e.g.* rapid screening) and reaction monitoring (*e.g.* electrochemical detection). This chapter reviews the further applications of micro-total analytical systems in biotechnological research.

There is currently a growing interest in fine chemical companies and applied research groups to develop lab-on-a-chip technology. One such application of pharmaceutical importance that needs to be studied in detail is the *in situ* regeneration of expensive cofactors, such as reduced nicotinamide adenine dinucleotide (NADH), during the conversion of pyruvate to L-lactate (refer Chapter 3 for reaction scheme). Two new techniques could be employed to study this reaction further. The first technique involves hydrodynamically focusing the pyruvate stream over boron doped diamond electrode surface (refer Chapter 3 for advantages of boron doped diamond over other electrode

materials), immobilised with NADH. This would allow continuous electrochemical regeneration of NADH over the electrode. The pyruvate/L-lactate mixture can then be separated downstream using ligand exchange micro-chromatography. Figure 8-1 depicts a schematic of the two processes carried out on one single chip.

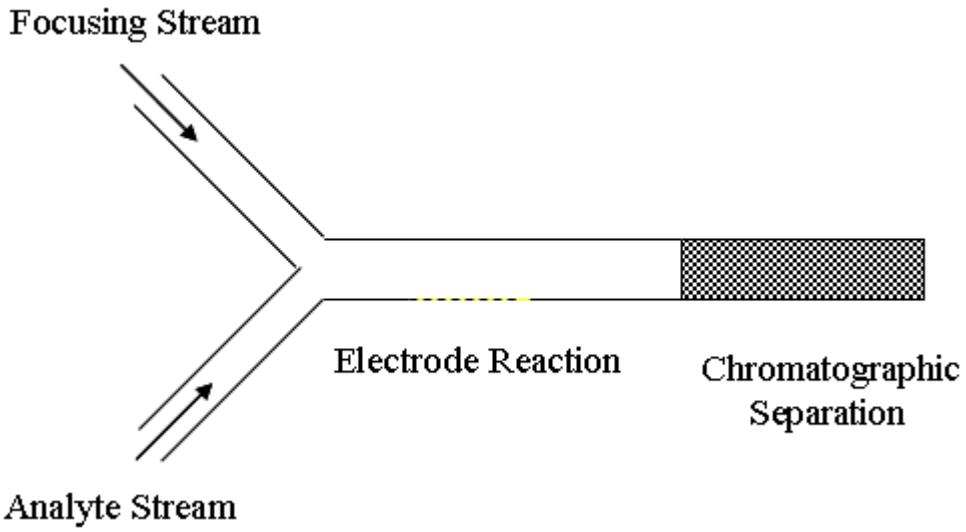

Figure 8-1 Schematic of reagent mixing, electrochemical reaction and chromatographic separation inside a micro-total analytical system

The second method involves chemical regeneration of NADH (as opposed to electrochemical) by immobilising NADH on a monolithic (*e.g.* poly(2-hydroxyethyl methacrylate)) microchannel, with subsequent downstream separation of pyruvate from L-lactate. The reaction scheme is shown in Figure 8-2.

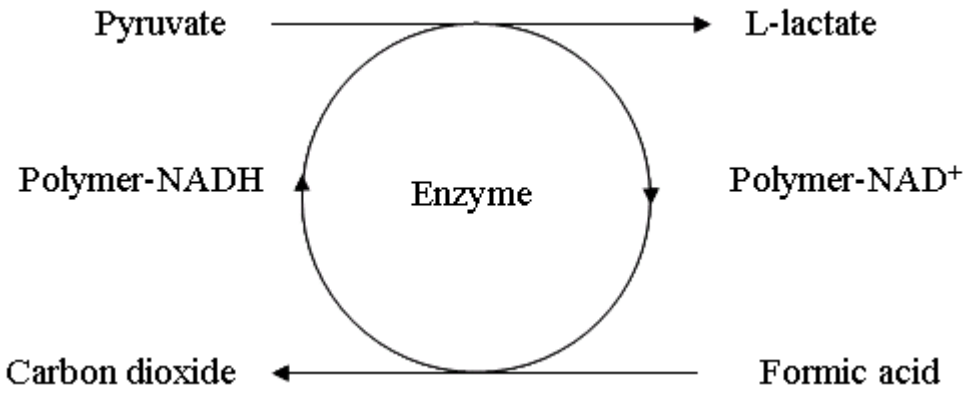

Figure 8-2 Schematic of polymer immobilised NADH regeneration

The biocatalytic reaction can then be simulated using Lattice Boltzmann Method, since it is more sensitive to irregular geometries. Further quantitative investigation can also be performed by using laser confocal microscopy. By passing an electroactive fluorescent analyte over an electrode surface at various flow rates and focusing ratios, concentration profile, total analyte conversion and product selectivity can be quantified.

The development of a μTAS that can perform the entire process of recombinant histidine (his) tag protein production, purification and concentration on a single chip also warrants further study. A μTAS consisting of four chambers can be fabricated, in which the first chamber could be used to carry out bacterial cell production. The second chamber would allow the expression and release of the desired his tag protein from the cells and the third chamber would enable purification of protein from the crude lysate using affinity chromatography. The final chamber would be used to concentrate the his tag protein solution using a photopatterned polymer membrane inside a microchannel. This would allow the investigation of various factors that affect the expression of his tag protein in a bacterial cell, on a single platform, making the whole process quicker and more effective. Analogous to the affinity purification of proteins, plasmid DNA can also be isolated directly from a bacterial crude lysate, as an initial purification step.

APPENDIX 1

A.1.1 The Thomas Algorithm

As described in Chapter 2, the Thomas Algorithm is used to solve the simultaneous equations resulting from backward implicit finite difference approach.

The algorithm solves the following equation:

$$\{d\} = [T]\{u\} \tag{A.1.1}$$

Where the matrix, T, can be written as $[T] = \begin{bmatrix} b_1 & c_1 & & & 0 \\ a_2 & b_2 & c_2 & & \\ & \ddots & \ddots & \ddots & \\ & & a_{j-2} & b_{j-2} & c_{j-2} \\ 0 & & & a_{j-1} & b_{j-1} \end{bmatrix}$

The algorithm factorises Equation A.1.1 into an upper $[T_U]$ and lower $[T_L]$ matrix:

$$[T] = [T_L][T_U] = \begin{bmatrix} \alpha_1 & & & & 0 \\ \alpha_2 & \alpha_2 & & & \\ & \ddots & \ddots & & \\ & & \alpha_{j-2} & \alpha_{j-2} & \\ 0 & & & \alpha_{j-1} & \alpha_{j-1} \end{bmatrix} \begin{bmatrix} 1 & \beta_1 & & & \\ & 1 & \beta_2 & & \\ & & \ddots & \ddots & \\ & & & 1 & \beta_{j-2} \\ & & & & 1 \end{bmatrix} \tag{A.1.2}$$

Where

$$\alpha_1 = \beta_1$$
$$\beta_1 = \frac{c_1}{\alpha_1}$$
$$\alpha_j = b_j - a_j \beta_{j-1}$$
$$\beta_j = \frac{c_j}{\alpha_j}$$

A solution for vector $\{f\}$ is found using:

$$[T_L]\{f\} = \{d\} \tag{A.1.3}$$

Therefore the elements of $\{f\}$ are given by

$$f_1 = \frac{d_1}{\alpha_1}$$
$$f_j = \frac{d_j - a_j f_{j-1}}{\alpha_j} \qquad j = 2,3,.....J-1 \tag{A.1.4}$$

$\{f\}$ is then used for the final calculation of$\{u\}$:

$$[T_U]\{u\} = \{f\} \tag{A.1.5}$$

Where

$$u_{J-1} = f_{J-1}$$
$$u_j = f_j - \beta_j u_{j+1} \qquad j = J-2,\ J-3, \ldots 1$$

Combing Equations A.1.4 and A.1.5 gives:

$$([T_L][T_U])\{u\} = \{d\} \tag{A.1.6}$$

APPENDIX 2

A.2.1 Effect of Scan Rate

As described in Section 3.5.1, using the three electrode configuration, cyclic voltammetry (CV) was performed at six different scan rates (0.02, 0.05, 0.1, 0.2, 0.3 and 0.4 V s^{-1}). Described below are cyclic voltammograms and the corresponding Randles-Sevcik plots (peak current versus square root of scan rate) obtained for flavin adenine dinucleotide (FAD), flavin mononucleotide (FMN) and Vitamin B_{12} over glassy carbon electrode (GCE), gold electrode (GE) and platinum electrode (PE). Experimental conditions are described in detail in Section 3.4.

1.) *Response for FAD*:

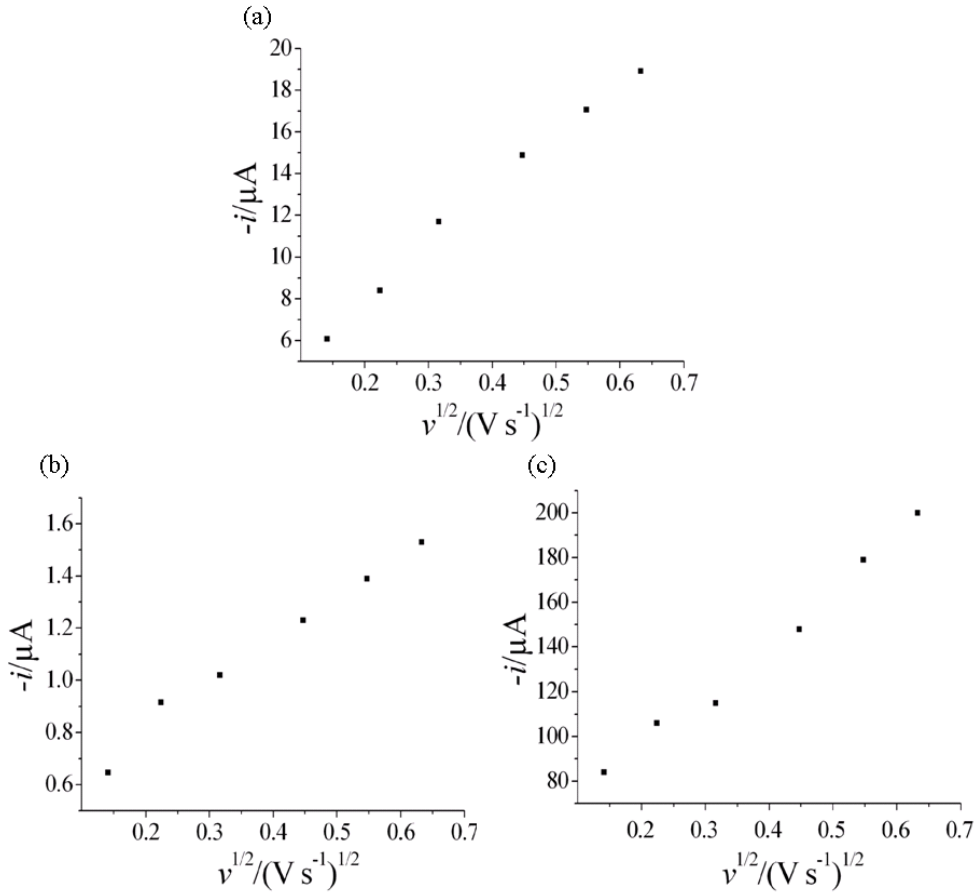

Figure A.2-1 Randles-Sevcik plots of 0.6 x 10^{-6} mol cm^{-3} FAD solution over GCE, GE and PE

2.) *Response for FMN*:

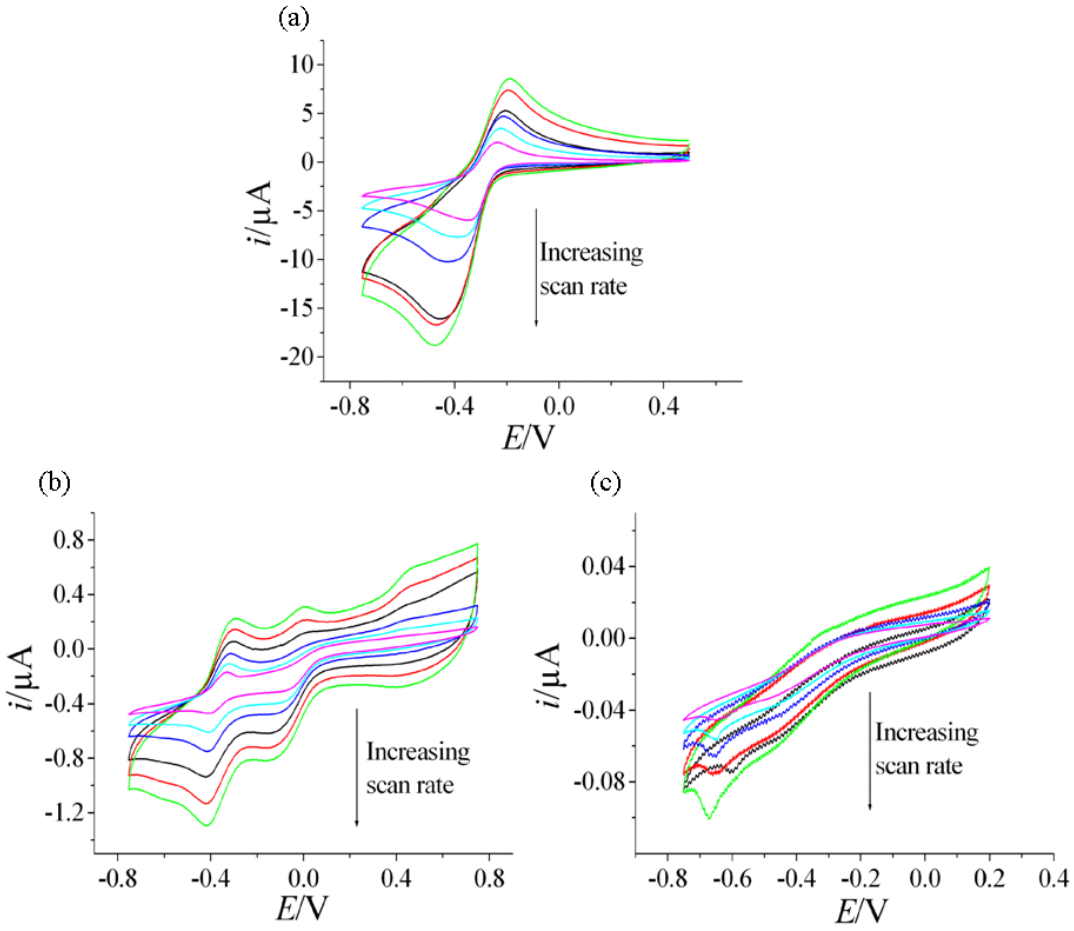

Figure A.2-2 Sample cyclic voltammograms of 0.6 x 10^{-6} mol cm^{-3} FMN solution at scan rates (ν) of 0.02, 0.05, 0.1, 0.2, 0.3 and 0.4 V s^{-1} over (a) GCE (b) GE and (c) PE.

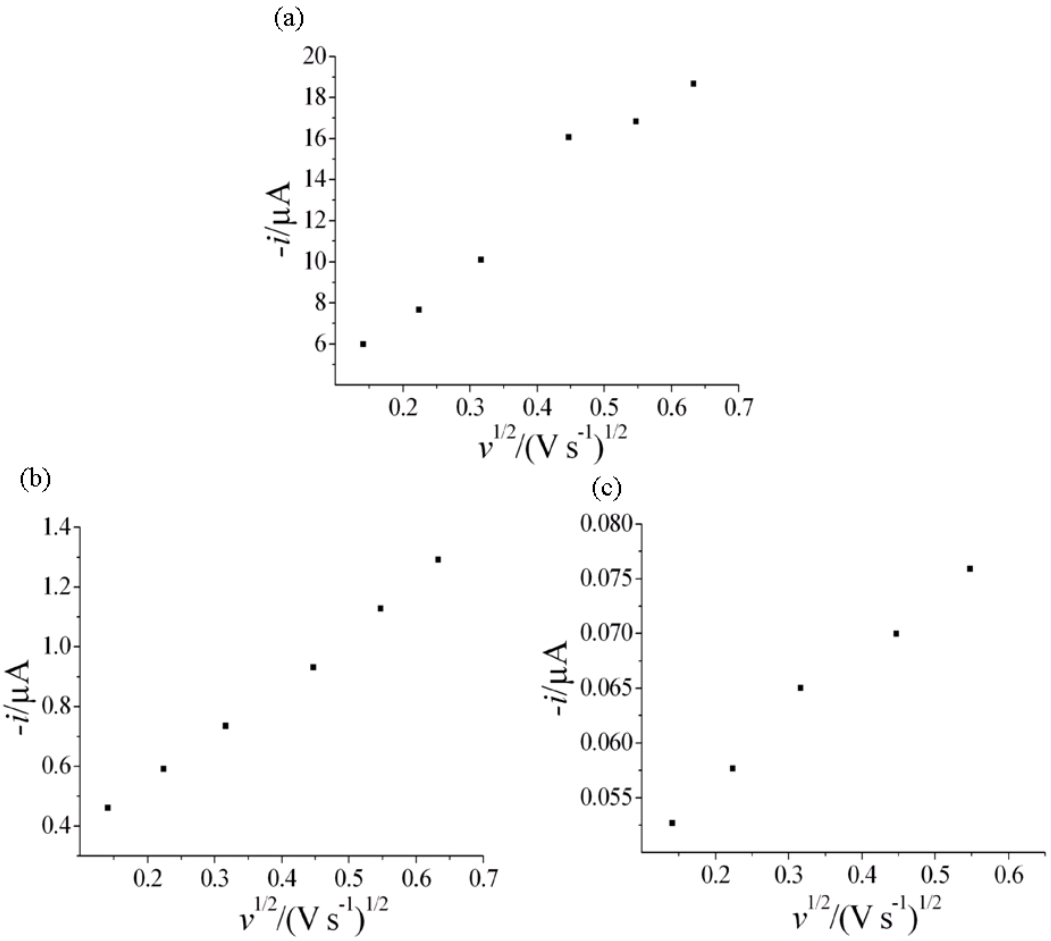

Figure A.2-3 Randles-Sevcik plots of 0.6 x 10^{-6} mol cm^{-3} FMN solution over GCE, GE and PE

3.) *Response for Vitamin B_{12}*:

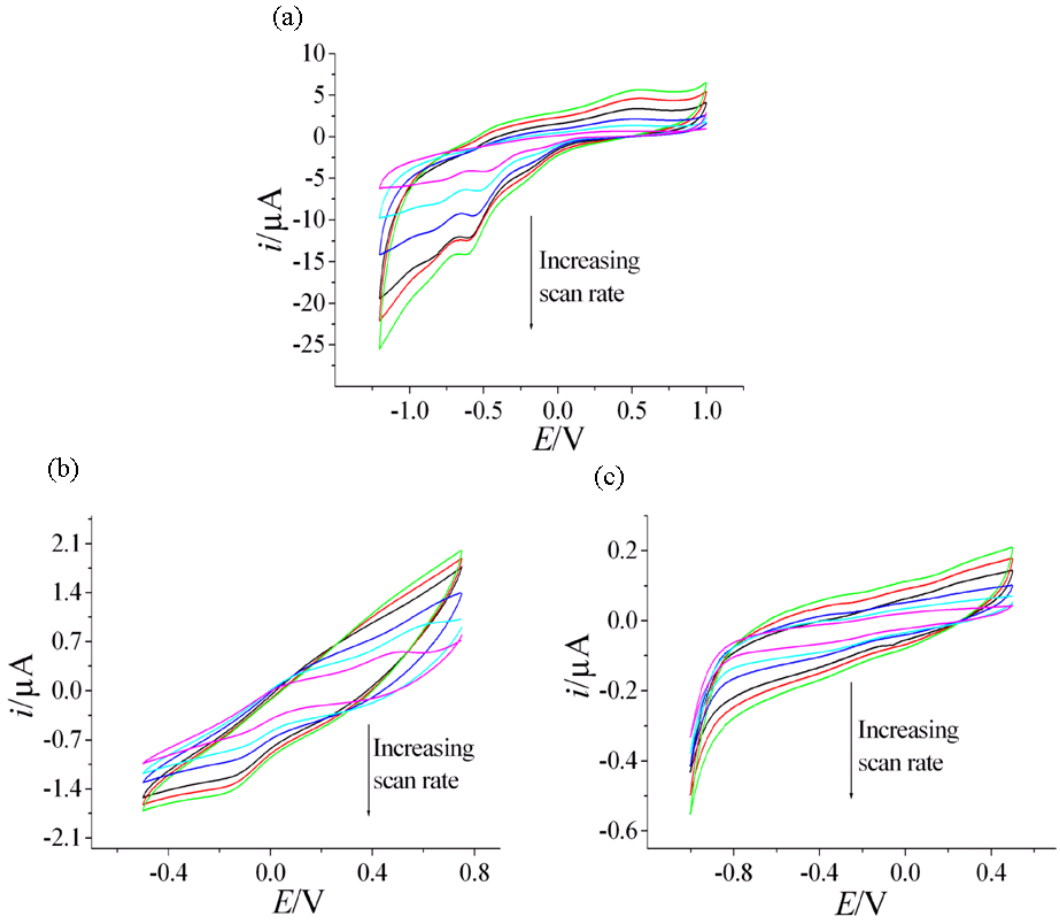

Figure A.2-4 Sample cyclic voltammograms for 0.6 x 10^{-6} mol cm^{-3} Vitamin B_{12} solution at scan rates (v) of 0.02, 0.05, 0.1, 0.2, 0.3 and 0.4 V s^{-1} over (a) GCE (b) GE and (c) PE

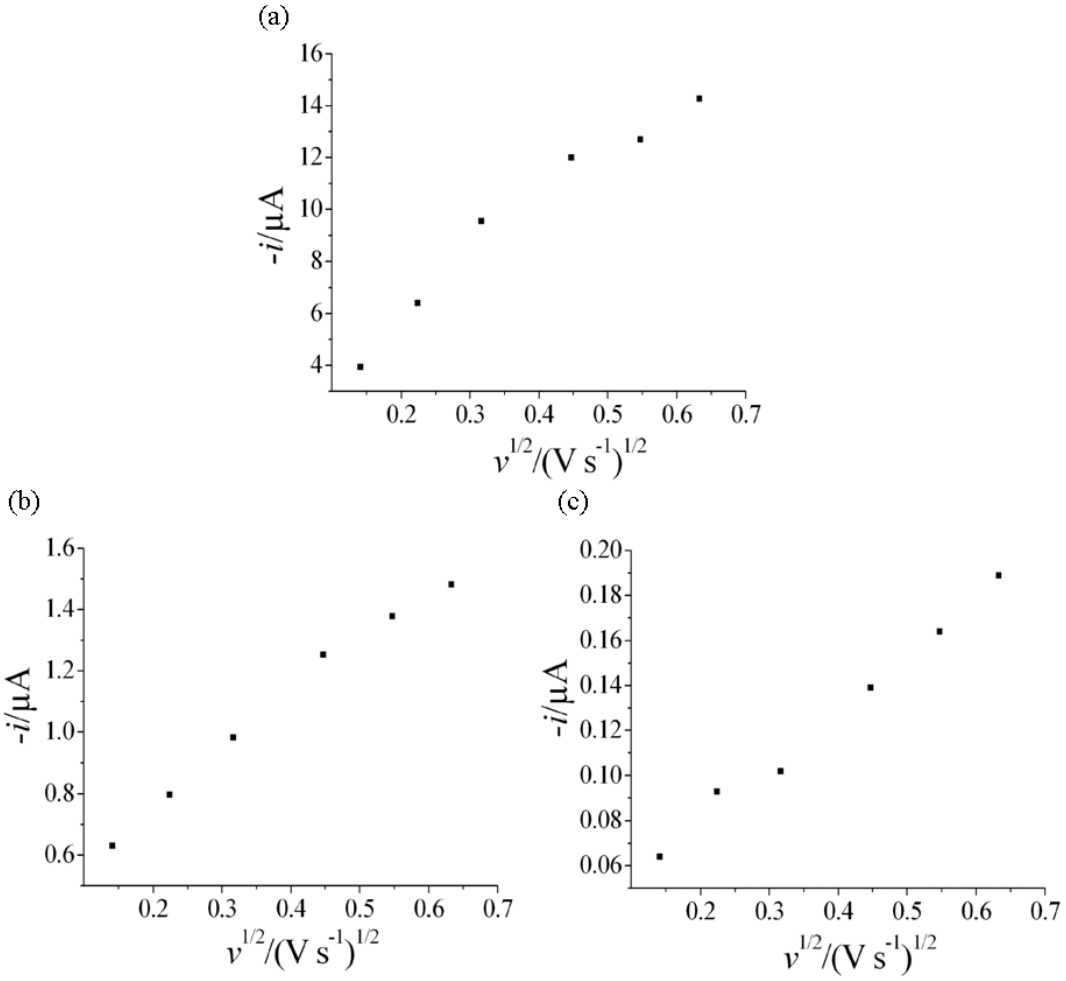

Figure A.2-5 Randles-Sevcik plots of 0.6 x 10^{-6} mol cm^{-3} Vitamin B_{12} solution over GCE, GE and PE

A.2.2 Effect of Concentration

Figure A.2-6, Figure A.2-7, Figure A.2-8 and Figure A.2-9 below illustrate the cyclic voltammograms obtained for four different concentrations (0.4, 0.6, 0.8 and 1.0 x 10^{-6} mol cm^{-3}) of cofactors FAD, FMN, and Vitamin B12 over BDDE, GCE, GE and PE respectively. Experimental conditions are described in Section 3.4.

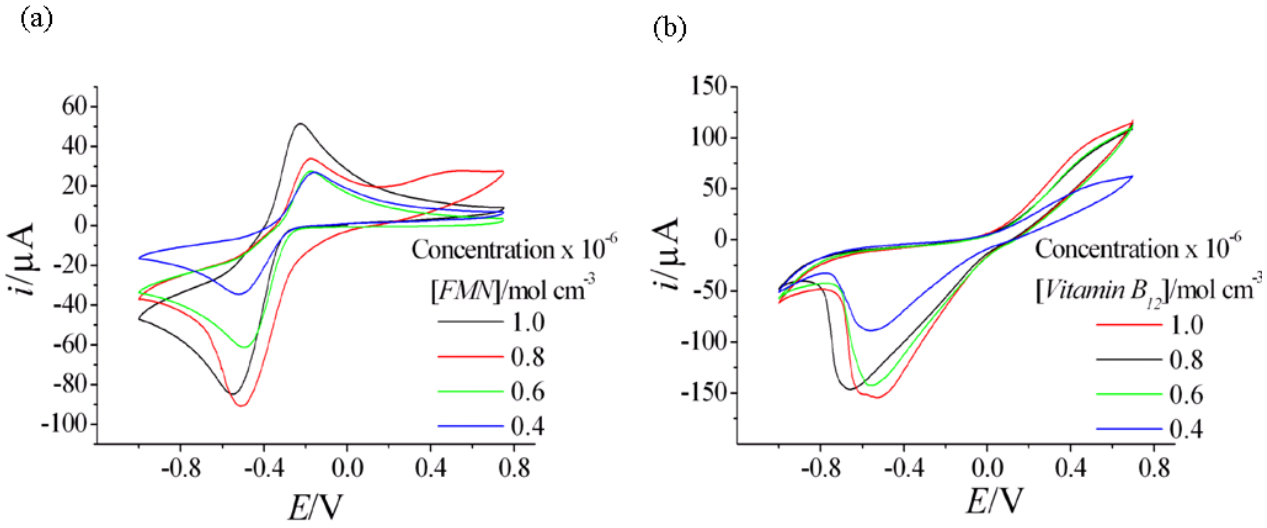

Figure A.2-6 Cyclic voltammograms of cofactors (a) FMN and (b) Vitamin B_{12} over BDDE at a scan rate of 0.4 V s^{-1} and for concentrations of 0.4, 0.6, 0.8 and 1 x 10^{-6} mol cm^{-3}

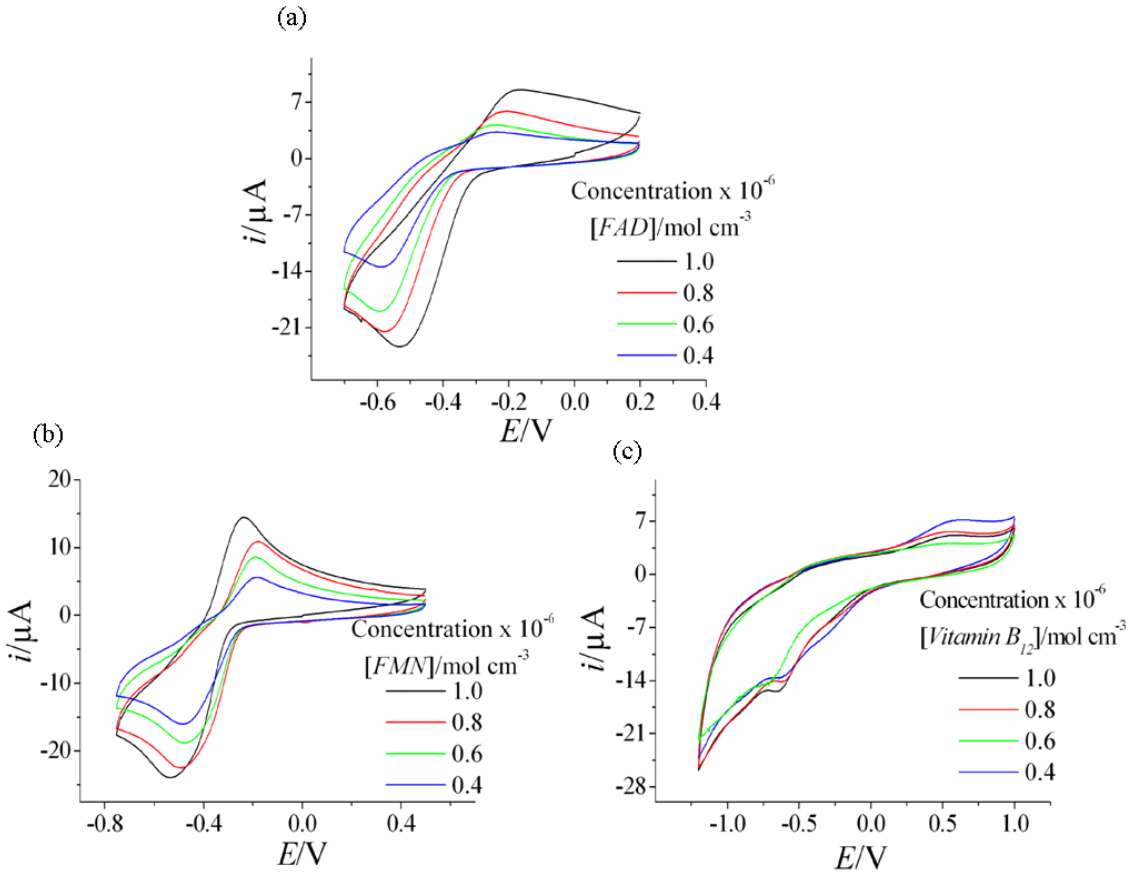

Figure A.2-7 Cyclic voltammograms of cofactors (a) FAD (b) FMN and (c) Vitamin B_{12} over GCE at a scan rate of 0.4 V s^{-1} and for concentrations of 0.4, 0.6, 0.8 and 1 x 10^{-6} mol cm^{-3}

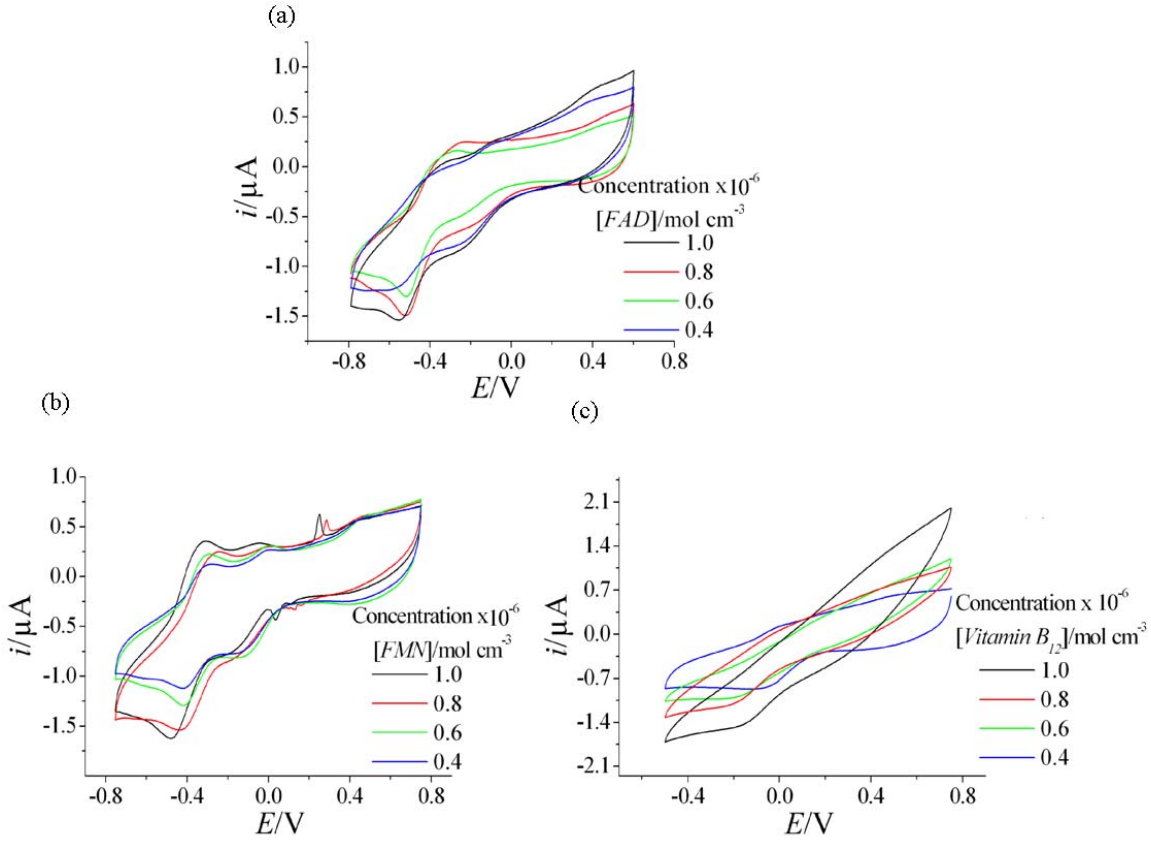

Figure A.2-8 Cyclic voltammograms of cofactors (a) FAD (b) FMN and (c) Vitamin B_{12} over GE at a scan rate of 0.4 V s^{-1} and for concentrations of 0.4, 0.6, 0.8 and 1 x 10^{-6} mol cm^{-3}

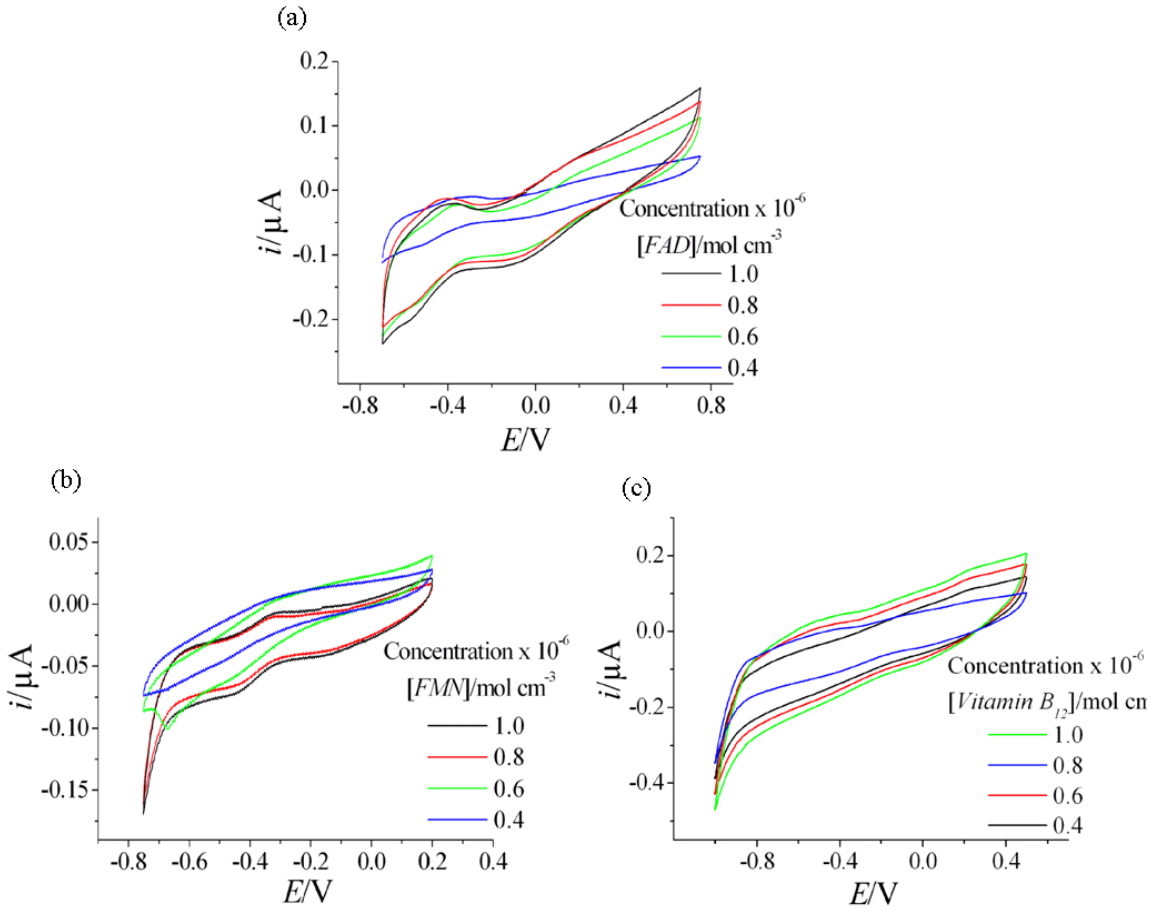

Figure A.2-9 Cyclic voltammograms of cofactors (a) FAD (b) FMN and (c) Vitamin B_{12} over PE at a scan rate of 0.4 V s^{-1} and for concentrations of 0.4, 0.6, 0.8 and 1 x 10^{-6} mol cm^{-3}

A.2.3 Diffusion Coefficient Calculation Using Randles-Sevcik Equation

Diffusion coefficients of potassium ferricyanide, potassium ferrocyanide and nicotinamide adenine dinucleotide reduced (NADH) in aqueous system were calculated using Randles-Sevcik equation for reversible system (refer Section 1.5.5) by obtaining series of cyclic voltammograms. A potentiostat with three-electrode configuration was used. The working electrode was rectangular boron doped diamond electrode (BDDE) of area 10 x 10^{-2} cm^2 and the counter was a platinum mesh. The pseudo-reference electrode used was standard Ag/AgCl electrode.

Solutions of 1 x 10^{-6} mol cm^{-3} potassium ferricyanide and 1 x 10^{-6} mol cm^{-3} potassium ferrocyanide were prepared in 0.1 x 10^{-3} mol cm^{-3} potassium chloride (background electrolyte) and a solution of 60 x 10^{-9} mol cm^{-3} NADH was prepared in 0.1 x 10^{-3} mol cm^{-3} phosphate buffer (pH 7.4) in a 100 ml beaker. All three electrodes were immersed in the solution and cyclic voltammograms were obtained for varying scan rates. Figure A.2-10a and Figure A.2-11a illustrate the voltammograms obtained by sweeping the potential between -0.5 to +0.7 V for 1 x 10^{-6} mol cm^{-3} potassium ferrocyanide at scan rates of 0.06, 0.08, 0.1, 0.2, 0.3 and 0.4 V s^{-1}, and for 1 x 10^{-6} mol cm^{-3} potassium ferricyanide at scan rates of 0.01, 0.05, 0.08, 0.1, 0.2, and 0.3 V s^{-1}. Figure A.2-12a illustrates the voltammograms obtained by sweeping the potential between 0 to +0.8 V for 60 x 10^{-9} mol cm^{-3} NADH at scan rates of 0.01, 0.03, 0.05, 0.07 and 0.1 V s^{-1}. Figure A.2-10b, Figure A.2-11b and Figure A.2-12b demonstrate linear variation of reduction/oxidation peak current with square root of scan rates. Slopes obtained from these graphs were used in the Randles-Sevcik equation to calculate the diffusion coefficients of potassium ferrocyanide, potassium ferricyanide and NADH in aqueous solution. The diffusion coefficient values thus calculated were 6.5 x 10^{-6} cm^2 s^{-1}, 6.77 x 10^{-6} cm^2 s^{-1} and 2.9 x 10^{-5} cm^2 s^{-1} respectively.

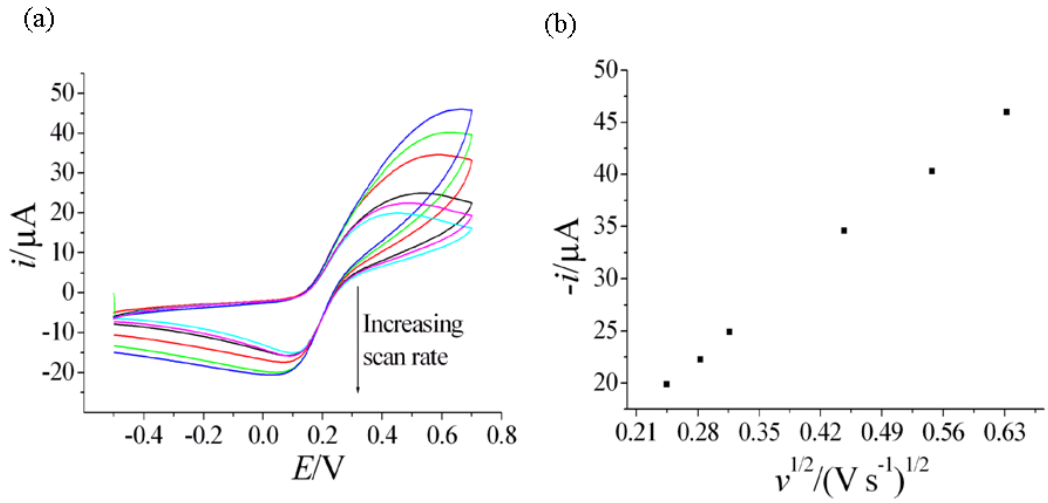

Figure A.2-10 (a) Sample cyclic voltammograms and (b) the corresponding Randles-Sevcik plot obtained for 1 x 10^{-6} mol cm^{-3} potassium ferrocyanide in 0.1 x 10^{-3} mol cm^{-3} potassium chloride as background electrolyte at scan rates of 0.06, 0.08, 0.1, 0.2, 0.3 and 0.4 V s^{-1}

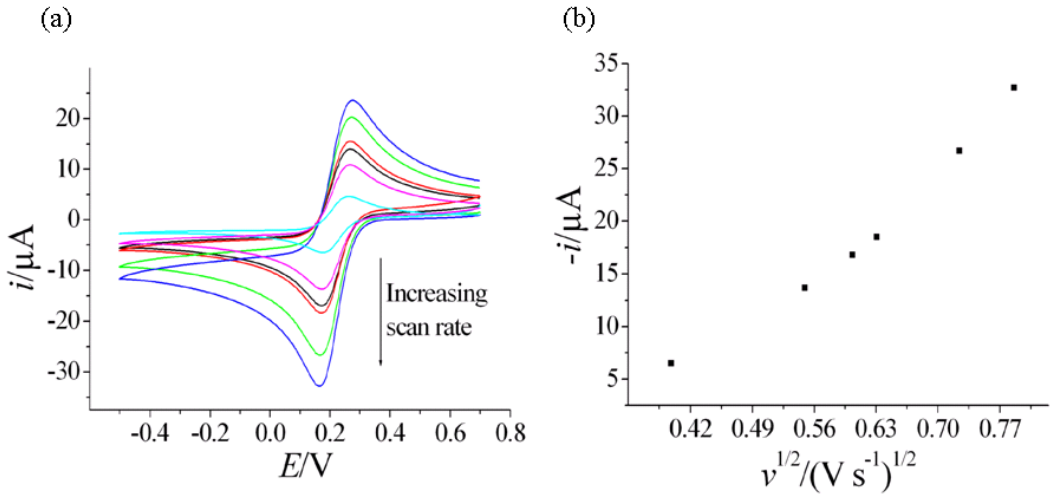

Figure A.2-11 (a) Sample cyclic voltammograms and (b) the corresponding Randles-Sevcik plot obtained for 1 x 10^{-6} mol cm^{-3} potassium ferricyanide in 0.1 x 10^{-3} mol cm^{-3} potassium chloride as background electrolyte at scan rates of 0.01, 0.05, 0.08, 0.1, 0.2 and 0.3 V s^{-1}

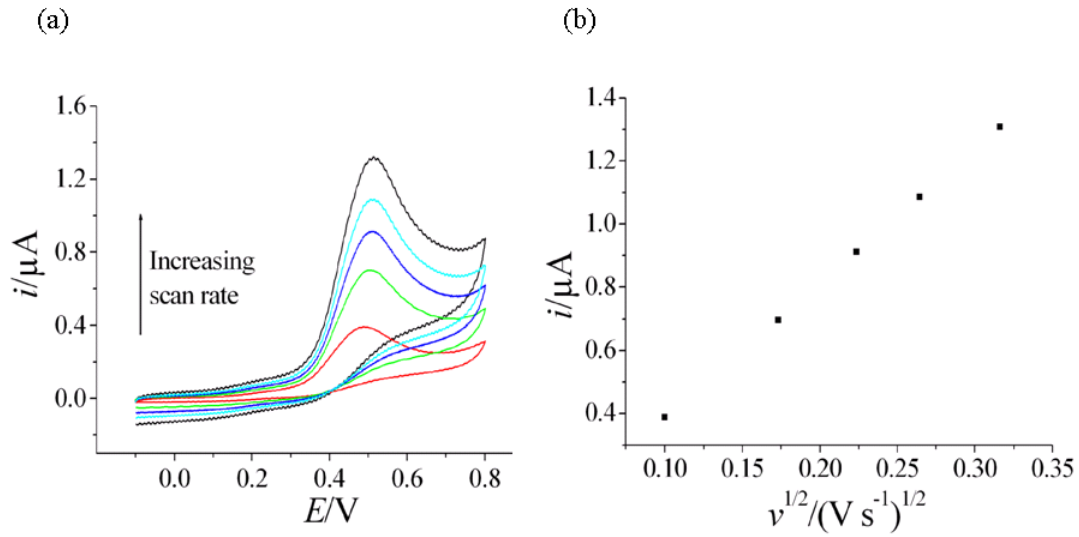

Figure A.2-12 (a) Sample cyclic voltammograms and (b) the corresponding Randles-Sevcik plot for 60 x 10^{-9} mol cm^{-3} NADH solution in 0.1 x 10^{-3} mol cm^{-3} phosphate buffer at scan rates (v) of 0.01, 0.03, 0.05, 0.07 and 0.1 V s^{-1} over BDDE

APPENDIX 3

A.3.1 Platinum Deposition

Platinum deposition method was used to fabricate platinum electrodes and deposit platinum on porous conducting electrodes such as polypyrrole. Platinum deposition procedure consisted of two stages: 1.) Preparation of platinum plating solution, 2.) Electrochemical platinum plating.

1.) *Preparation of Platinum Plating Solution*

To prepare a solution of 100 cm^3 platinum plating solution, 12 g of disodium hydrogen phosphate dihydrate was mixed with 1.8 g of diammonium hydrogen phosphate in deionised water. The pH was adjusted to 6.5-7.5 using sodium hydroxide solution (10% w/v) or phosphoric acid. 0.5 g of platinum slurry (Platinum diamminedinitrite (Pt P salt)) was then added to this solution and heated to 90 ^oC to dissolve it completely. The Pt P salt was not allowed to dry out as the salt is explosive in its solid state.

2.) *Electrochemical Platinum Plating*

The platinum plating solution prepared above was placed in a 500 cm^3 clean beaker and put into a water bath. A clean thermometer was placed into the platinum solution along with three electrodes: Ag/AgCl reference electrode, Pt mesh counter electrode and the working electrode that was required to be electroplated (gold, conducting polymer). The experiment was conducted at 90-93 ^oC using a potentiostat. The voltage was stepped from 0 to -0.9 V for 150 seconds, for a consistent thick film. The electrodes thus obtained were thoroughly cleaned with deionised water.

A.3.2 Physical Characterisation Data

1.) *Laser Particle Size Measurement*

The NH_4Cl salt particles of different size, prepared using a pulveriser and particle sieve as described in Chapter 5 were analysed for their particle size distribution using a commercial particle sizer. Figure A.3-1 below illustrates the particle size distribution for 60, 100 and 160 µm NH_4Cl particles. The particles were dispersed in an organic solvent (Toluene) before injecting them into the laser particle size analyser.

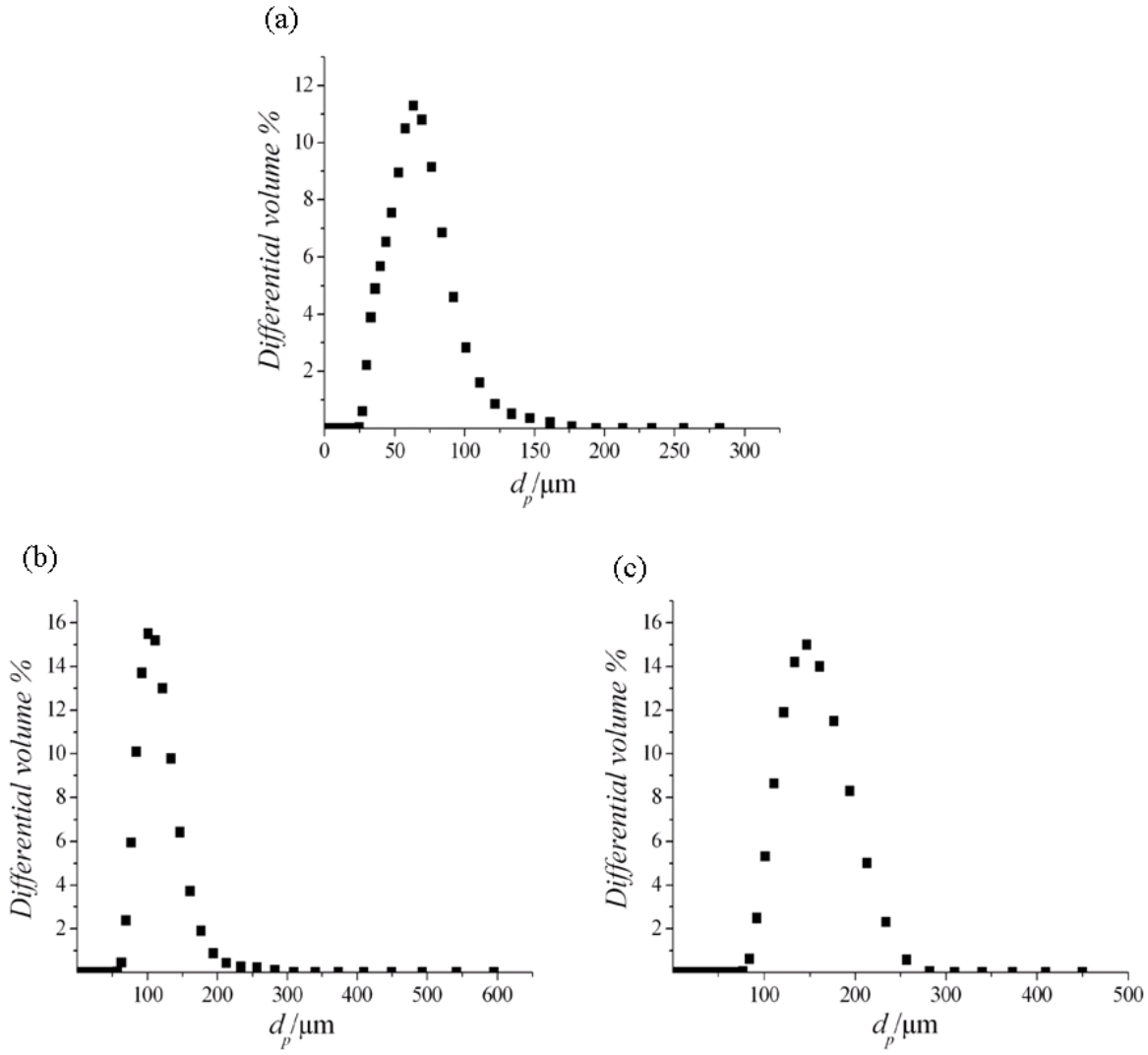

Figure A.3-1 Particle size distribution curves for NH_4Cl particles of diameter (a) 60 µm, (b) 100 µm, (c) 160 µm

2.) *BET Adsorption*

The monoliths synthesised in Chapter 5 and Chapter 6 were analysed using BET adsorption for the pore surface area. Figure A.3-2 shows the BET adsorption isotherms obtained for poly(2-hydroxyethyl methacrylate-co-ethyleneglycol dimethacrylate) monoliths synthesised using NH_4Cl salt particles of diameter 60, 100 and 160 µm as porogen. The BET surface area calculated using these isotherms was 6.1, 4.43 and 2.93 $m^2\ g^{-1}$ for poly(HEMA-co–EGDMA) monoliths with pore dimensions of approximately 60, 100 and 160 µm respectively.

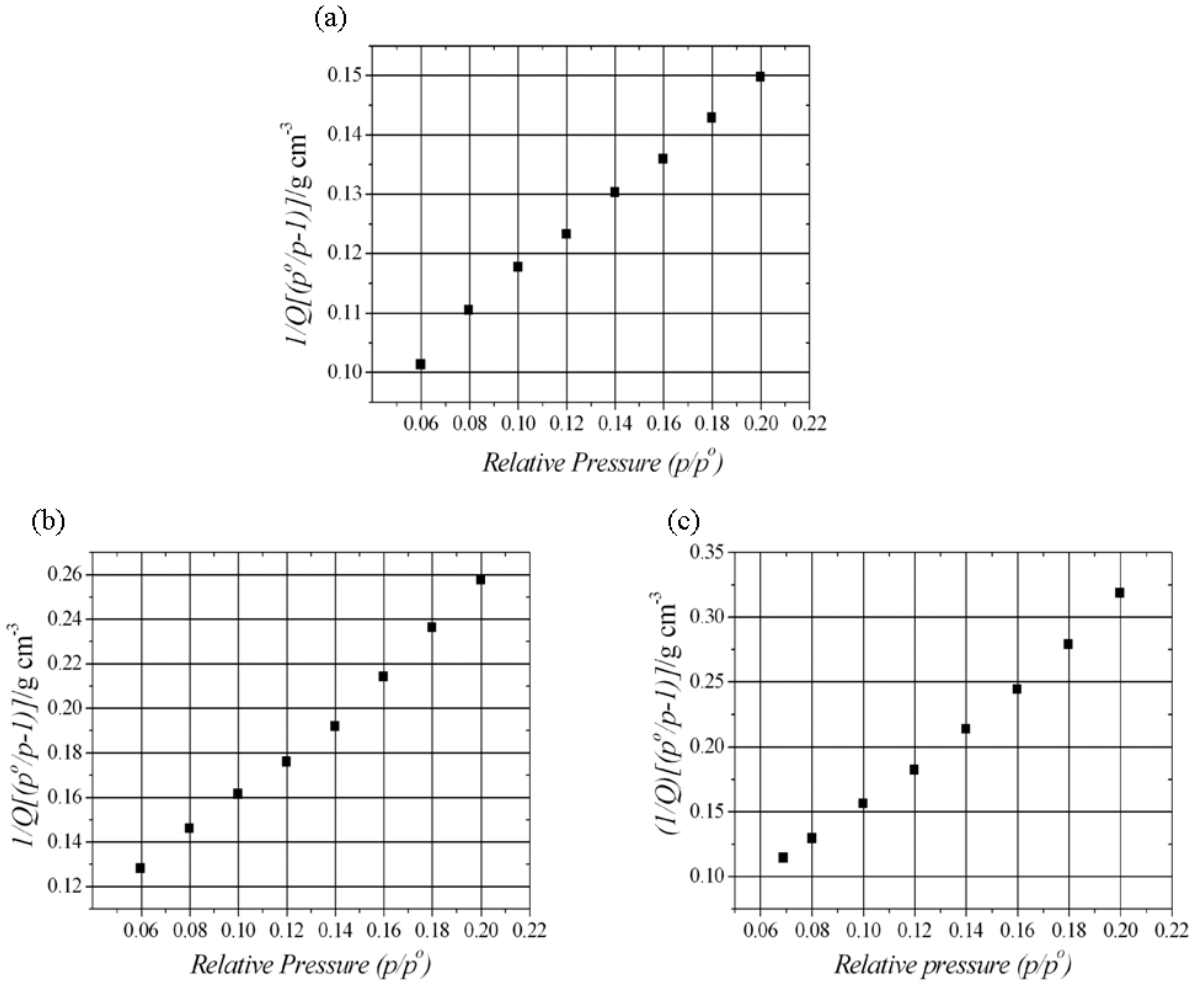

Figure A.3-2 BET adsorption plots for poly(HEMA-co-EGDMA) monoliths synthesised using porogen as NH_4Cl particles of diameter (a) 60 µm, (b) 100 µm, (c) 160 µm

3.) *Mercury Porosimetry*

The pore size and porosity of the monoliths described in Chapter 5 and Chapter 6 was measured using mercury (Hg) porosimetry. Figure A.3-3 illustrate the pore size distribution of poly(HEMA-co-EGDMA) monoliths synthesised using NH_4Cl salt particles of diameter 60, 100 and 160 µm as porogen. The porosity measured using this technique varied between 38-45%.

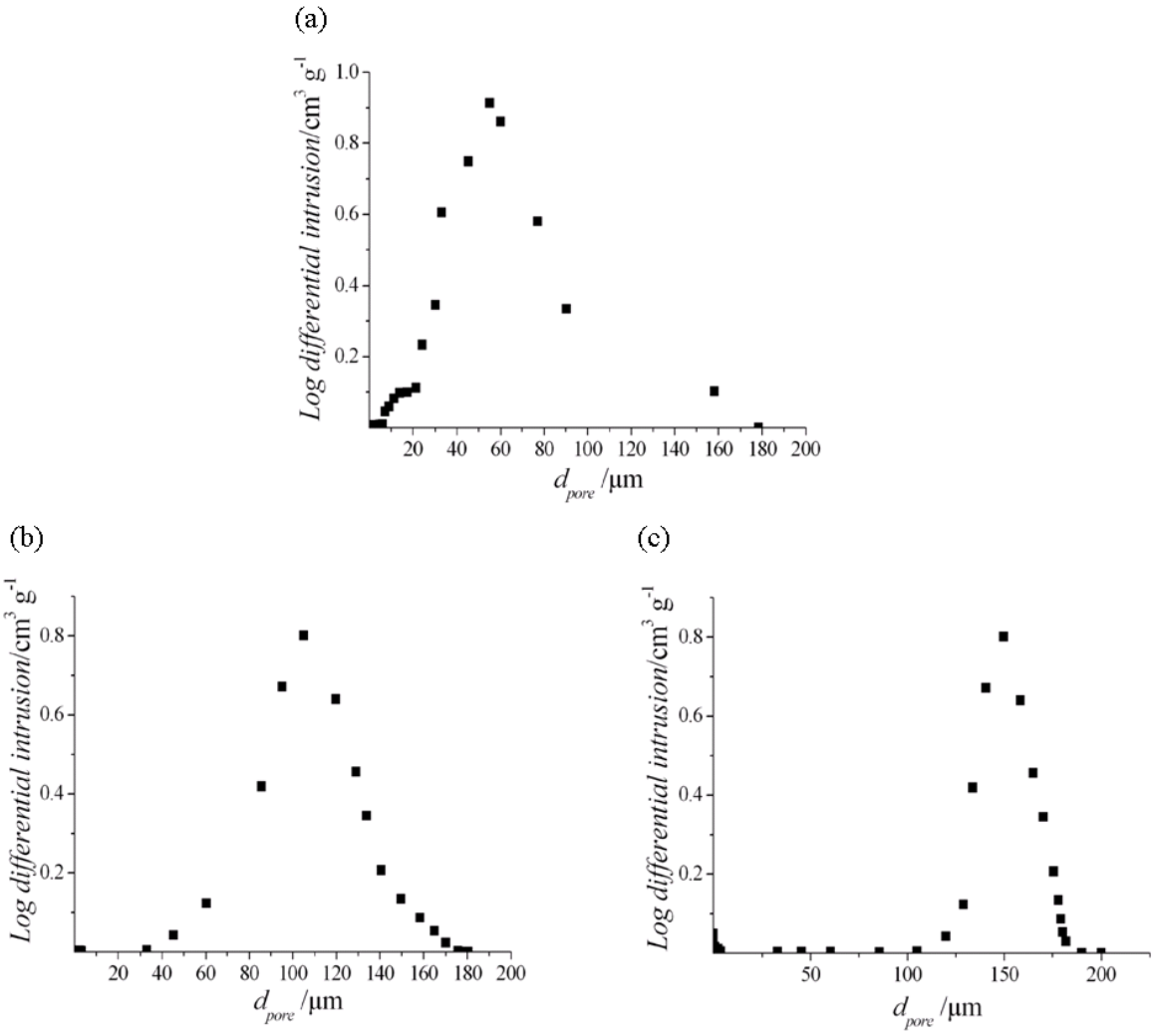

Figure A.3-3 Pore size distribution curves for poly(HEMA-co-EGDMA) monoliths synthesised using porogen as NH_4Cl particles of diameter (a) 60 µm, (b) 100 µm, (c) 160 µm

A.3.3 Pressure Drop Studies

Pressure drop studies were carried out inside the mesochannels to understand the flow characteristic by flowing water at various volume flow rates, as described in Section 5.3.1.2. Figure A.3-4 below illustrates the variation of pressure gradient with square of pore diameter.

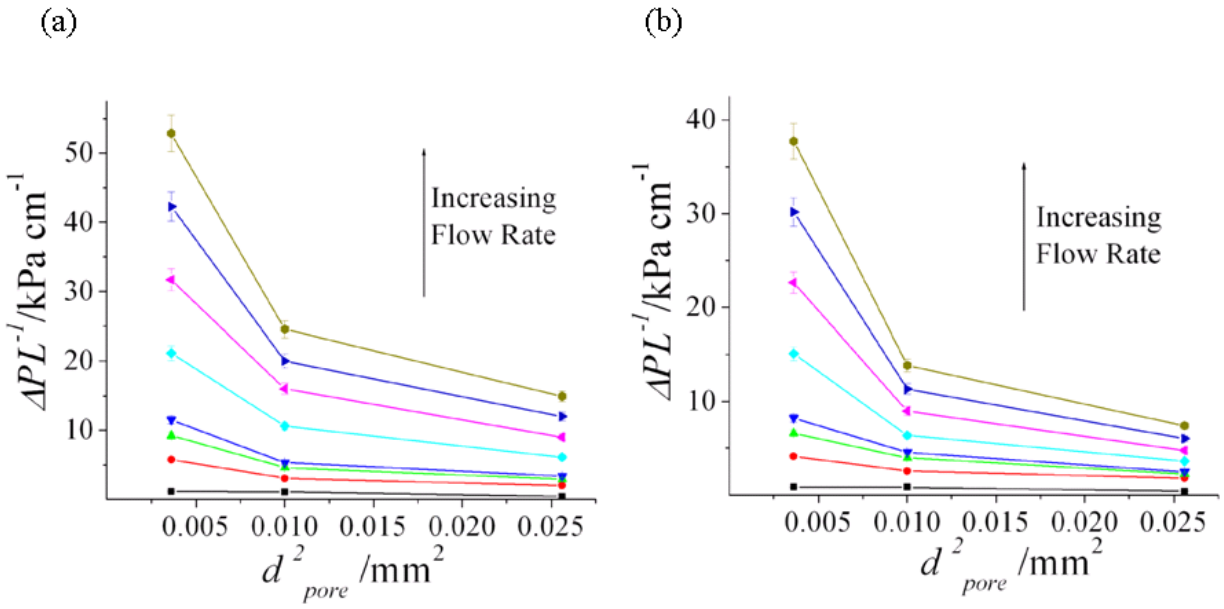

Figure A.3-4 Plot of experimental pressure drop per unit length of monolith against square of pore diameter at various total volume flow rates (0.00017, 0.00083, 0.00133, 0.00167, 0.0033, 0.005, 0.00667 and 0.0083 cm^3 s^{-1}) of water passed through a 1 cm long monolith fabricated inside a glass mesochannel of length (*l*) 2.5 cm, width (*w*) 0.15 cm and height (a) 0.055 cm, (b) 0.07 cm, using NH_4Cl as porogen

A.3.4 Electrochemical Analysis of N,N,N′,N′-tetramethyl-p-phenylenediamine

Electrochemical one-electron oxidation of N,N,N′,N′-tetramethyl-p-phenylenediamine (TMPD) was carried out to characterise the six different polymer-gold electrode composites fabricated as described in Section 5.2.2. Figure A.3-5 shows cyclic voltammograms and their corresponding Randles-Sevcik plots obtained for various electrode materials including (a-b) Au, (c-d) Bulk PolyPr_Au, (e-f) Porous PolyPr_Poly(HEMA-co-TEGDA)_Au, (g-h) Porous PolyPr_MB_Au, (i-j) Bulk PolyPr_Au_Pt and (k-l) Porous PolyPr_MB_Au_Pt. The peak current was found to be directly proportional to the square root of the voltage scan rate as described by the Randles-Sevcik equation (refer Section 1.5.5).

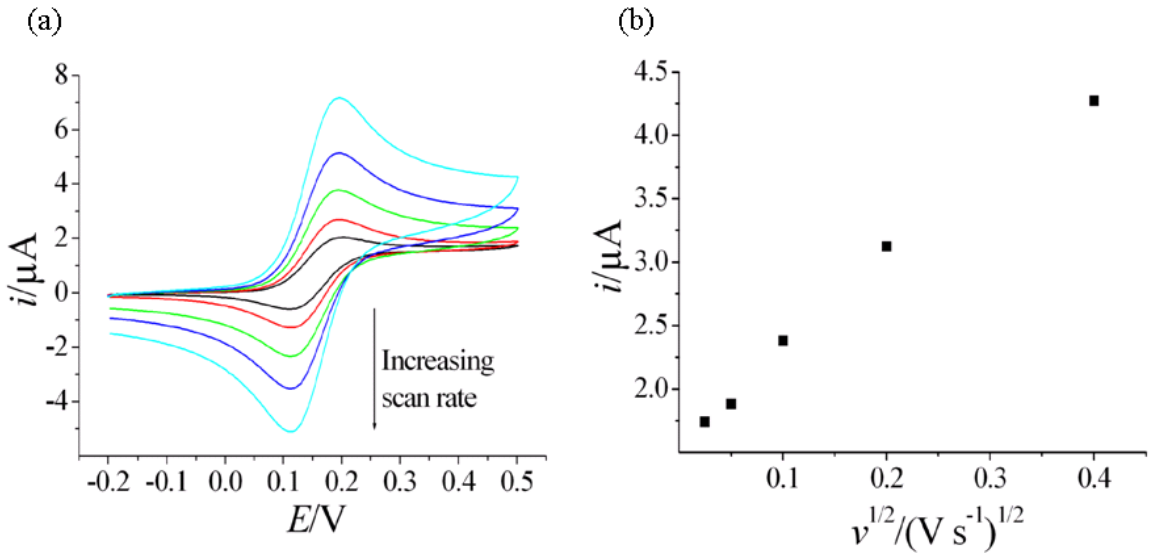

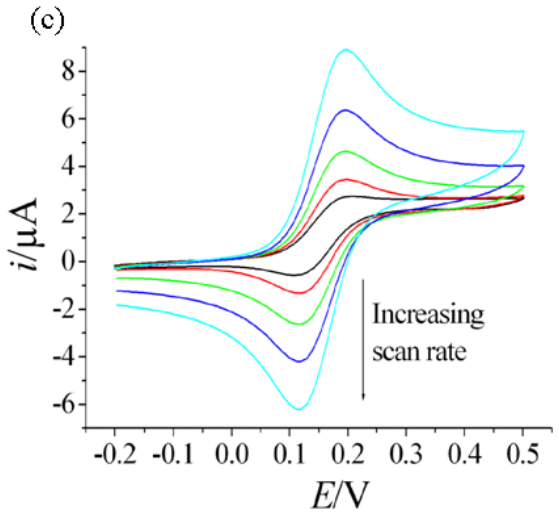
(c)
i/μA
E/V
Increasing
scan rate

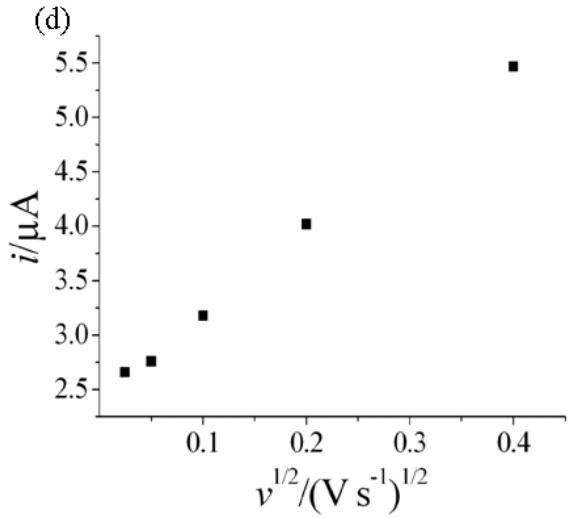
(d)
i/μA
v^1/2/(V s^-1)^1/2

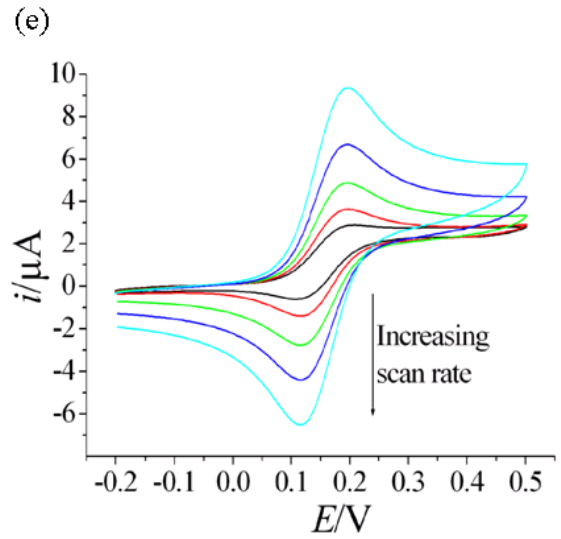
(e)
i/μA
E/V
Increasing
scan rate

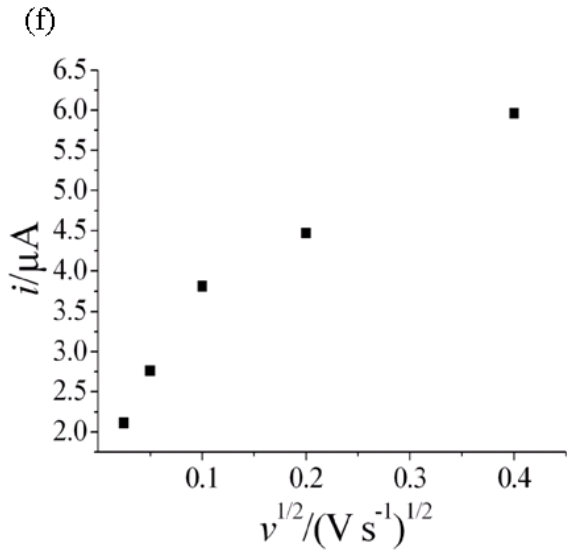
(f)
i/μA
v^1/2/(V s^-1)^1/2

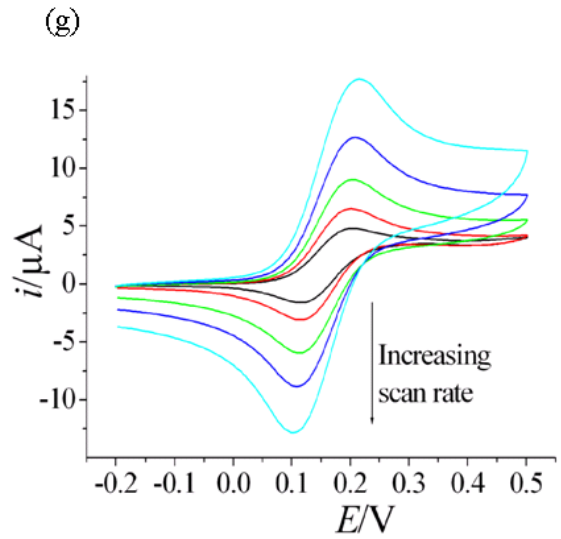
(g)
i/μA
E/V
Increasing
scan rate

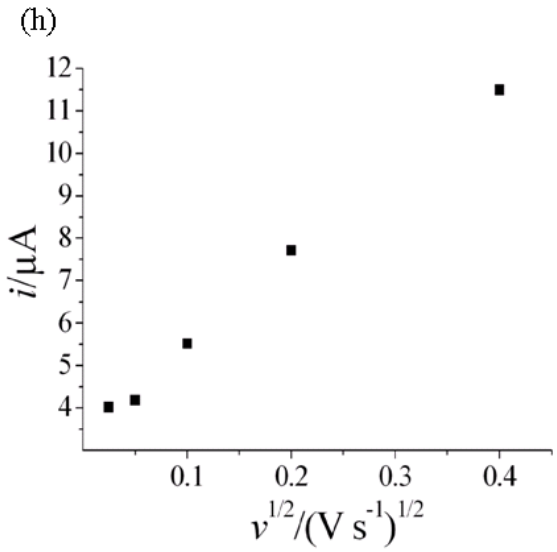
(h)
i/μA
v^1/2/(V s^-1)^1/2

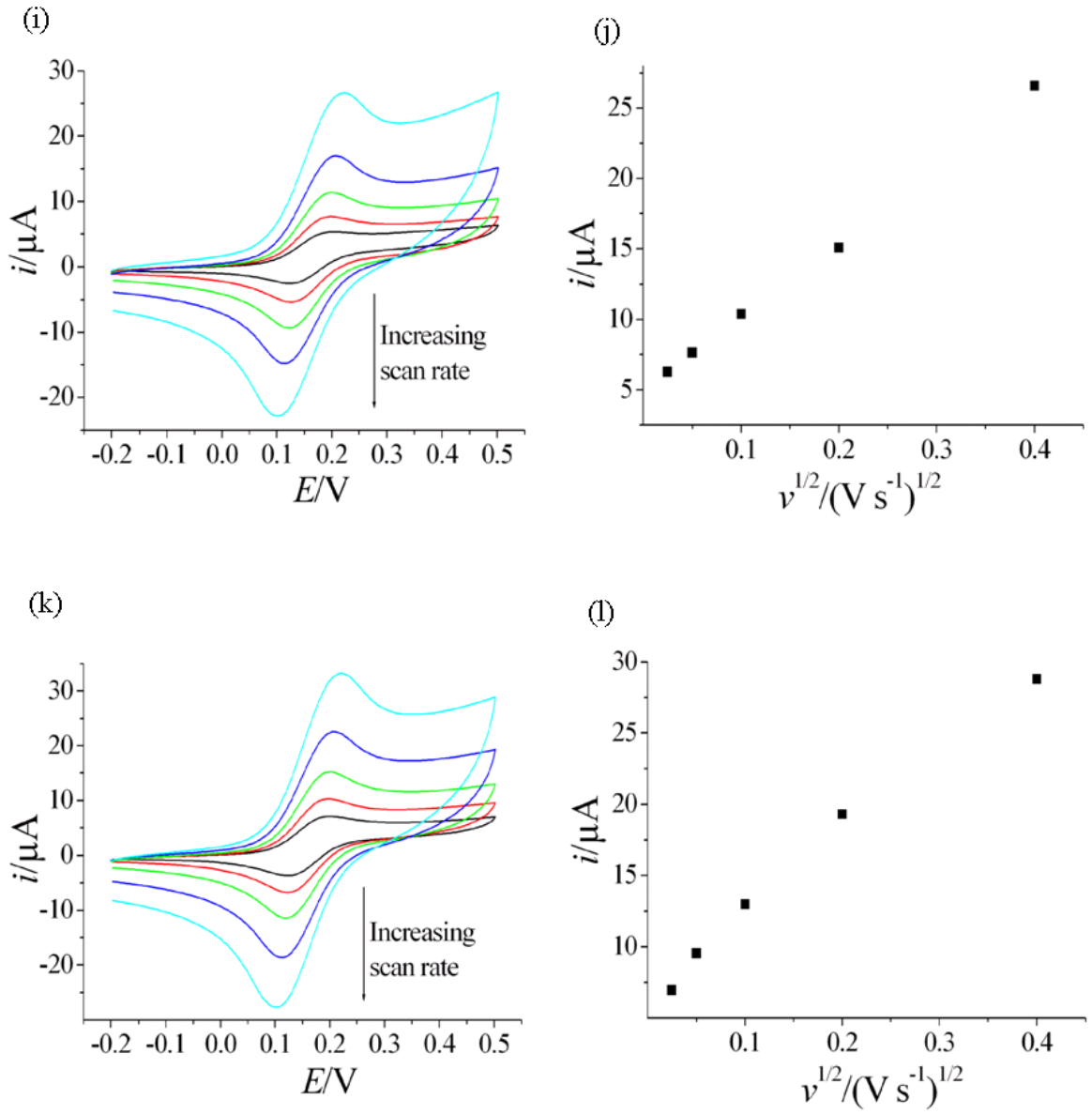

Figure A.3-5 Sample cyclic voltammograms and the corresponding Randles-Sevcik plots of 1 x 10^{-6} mol cm^{-3} TMPD + 0.1 x 10^{-3} mol cm^{-3} TBAP in acetonitrile solution at scan rates of 0.025, 0.05, 0.1, 0.2 and 0.4 V s^{-1} over various electrode material including (a-b) Au, (c-d) Bulk PolyPr_Au, (e-f) Porous PolyPr_Poly(HEMA-co-TEGDA)_Au, (g-h) Porous PolyPr_MB_Au, (i-j) Bulk PolyPr_Au_Pt, (k-l) Porous PolyPr_MB_Au_Pt

APPENDIX 4

A.4.1 Bovine Serum Albumin Calibration Plots

The concentration of protein during the loading, wash and elution stages of chromatography was measured using standard bovine serum albumin (BSA) calibration plots. Figure A.4-1 below illustrates the plots of absorbance at 590 nm versus various concentrations of BSA, using background solution as dialysis (equilibrium), wash and elution buffer.

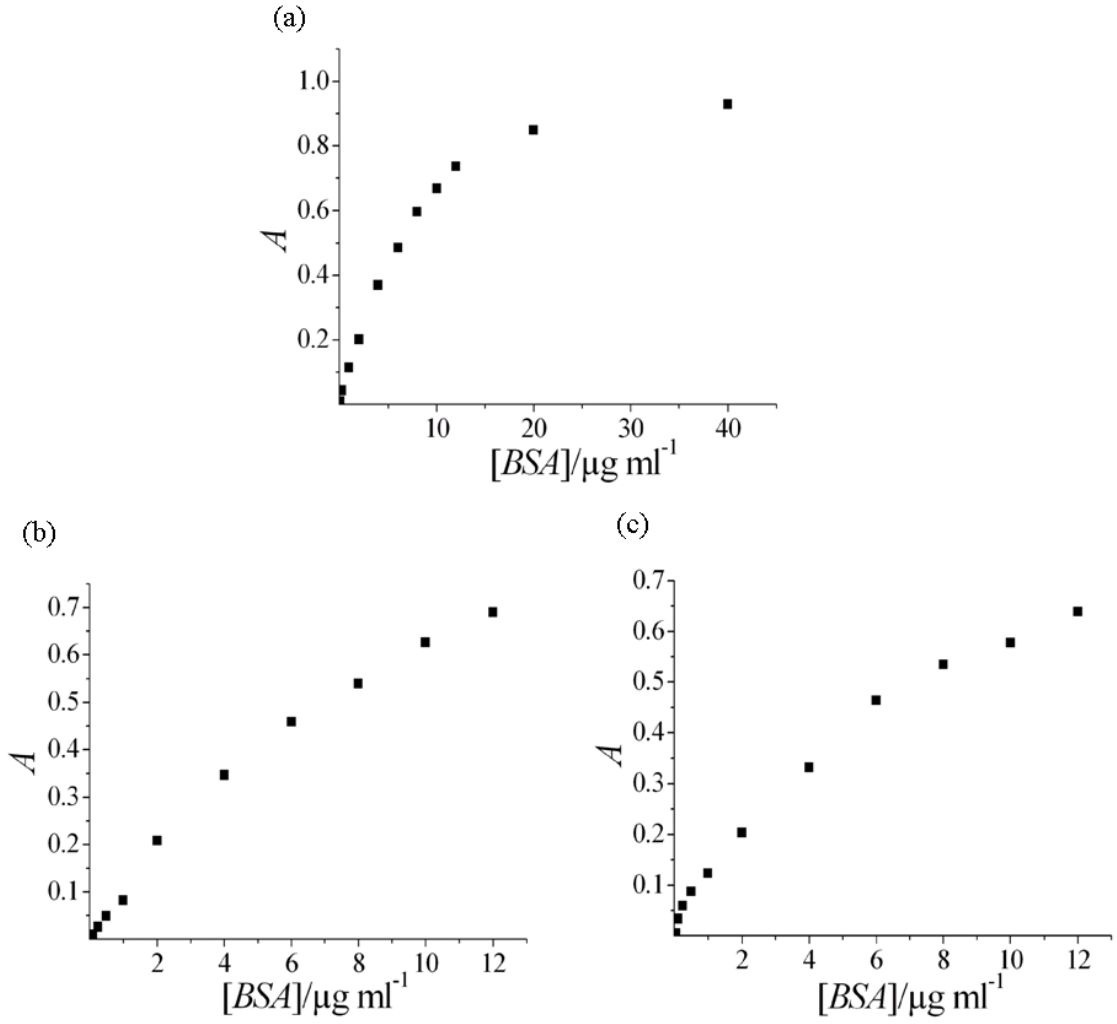

Figure A.4-1 Plot of absorbance against standard Bovine Serum Albumin concentration for working curve calibration using background solution as (a) dialysis (equilibrium) buffer, (b) wash buffer and (c) elution buffer

A.4.2 ^{1}H NMR Data for HPIDA Monomer Solution

As mentioned in Section 6.3.2, disodium 2,2'-{[2-hydroxy-3-(prop-2-en-1-yloxy)propyl]imino} diacetate (HPIDA) was synthesised by chemical reaction between allyl glycidyl ether (AGE) and iminodiacetic acid (IDA) as described by Chen *et al.* in their patent. The HPIDA monomer solution thus prepared was analysed using ^{1}H NMR to detect the presence of HPIDA in the solution (refer Figure A.4-2 and Figure A.4-3).

(1) *^{1}H NMR: HPIDA Monomer Solution*

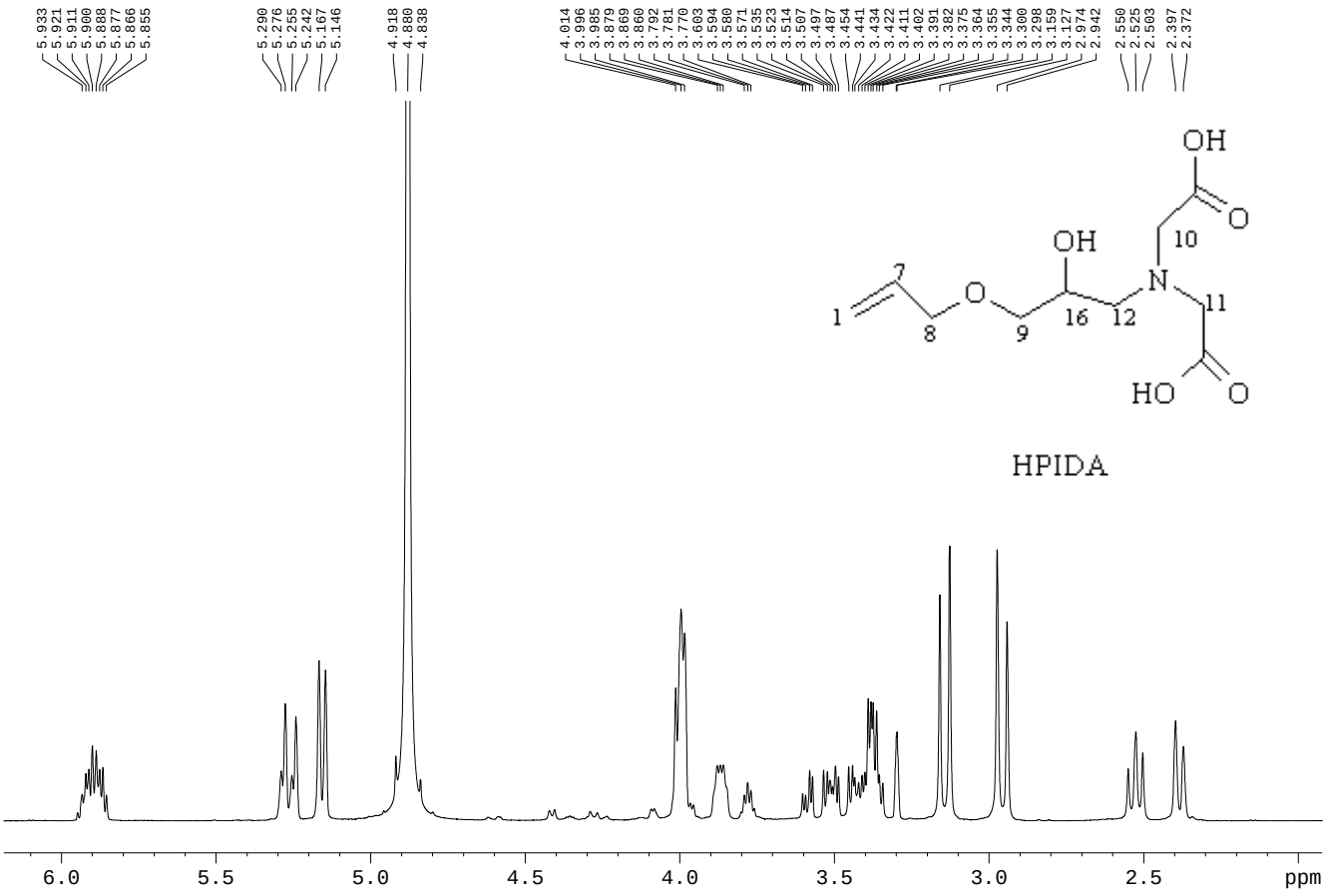

Figure A.4-2 ^{1}H NMR spectra for HPIDA monomer solution

The solvent used for ^{1}H NMR analysis was deuteriated methanol (MeOD).

5.040 (1, 1H, dd, J=10.677, J=1.323), 4.980 (1, 1H, dd, J=16.501, J=1.323), 5.885 (7, 1H, ddt, J=16.501, J=10.677, J=6.047), 3.838 (8, 2H, d, J=6.047), 3.515 (9, 2H, d, J=5.316), 3.539 (10, 2H), 3.539 (11, 2H), 2.871 (12, 2H, d, J=4.737), 3.880 (16, 1H, tt, J=5.316, J=4.737)

(2) *^{1}H NMR: AGE*

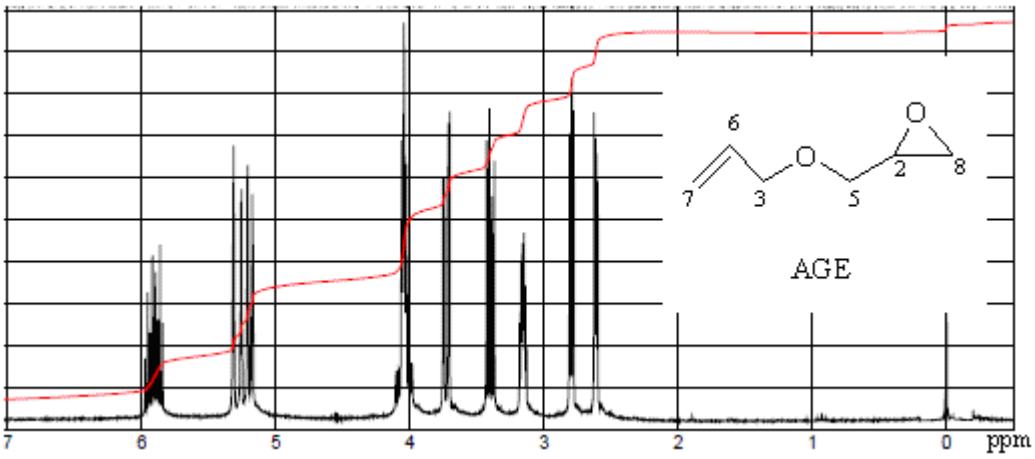

Figure A.4-3 ^{1}H NMR spectra for allyl glycidyl ether solution [Sigma Aldrich]

The solvent used for ^{1}H NMR analysis was deuteriated chloroform ($CDCl_3$).

3.007 (2, 1H, ddt, J=8.060, J=7.690, J=5.222), 3.893 (3, 2H, d, J=5.222), 3.886 (5, 2H, d, J=6.066), 5.774 (6, 1H, ddt, J=17.236, J=10.657, J=6.066), 5.039 (7, 1H, dd, J=10.657, J=1.427), 4.980 (7, 1H, dd, J=17.236, J=1.427), 2.960 (8, 1H, dd, J=7.690, J=4.144), 3.001 (8, 1H, dd, J=8.060, J=4.144).

A.4.3 Copper(II) Ion Calibration Plots

The amount of Cu^{2+} immobilised on poly(HEMA-co-EGDMA-HPIDA) monoliths, described in Chapter 6, was calculated using calibration curves obtained from UV absorption spectroscopy for copper(II) sulphate solution, at various concentrations. Figure A.4-4a illustrates the UV absorption curve for copper(II) sulphate solution at various wavelengths and Figure A.4-4b shows a plot of absorbance versus concentration of Cu^{2+} ions in copper(II) sulphate solution.

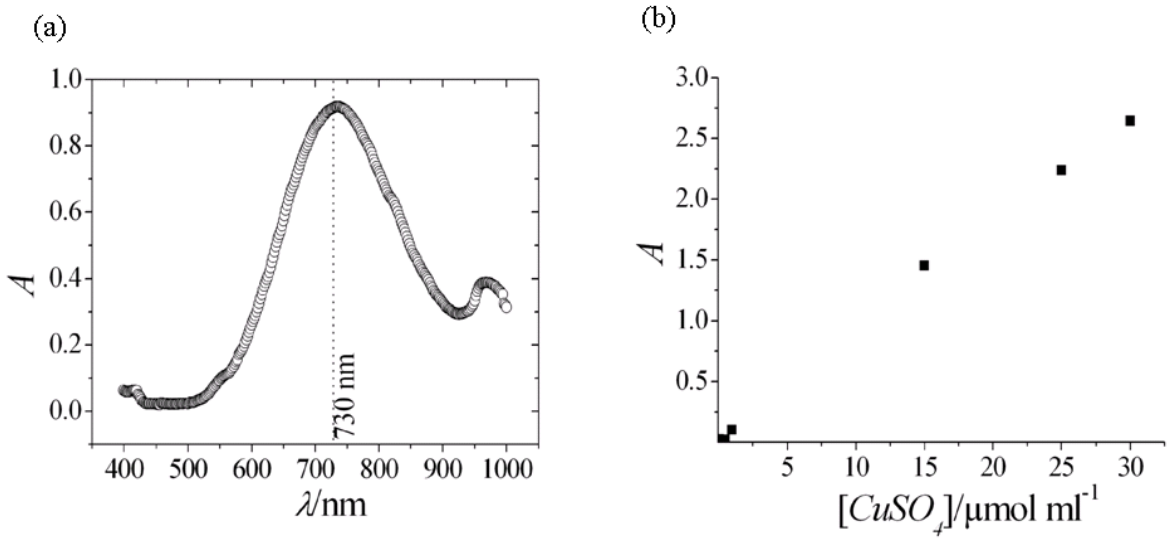

Figure A.4-4 (a) UV absorption curve for 10 mM $CuSO_4$ and (b) Plot of absorbance against concentration of $CuSO_4$